

1997

Exploring aluminum-rich intermetallics with experiment and theory

Karen Jane Nordell
Iowa State University

Follow this and additional works at: <https://lib.dr.iastate.edu/rtd>

 Part of the [Inorganic Chemistry Commons](#), and the [Physical Chemistry Commons](#)

Recommended Citation

Nordell, Karen Jane, "Exploring aluminum-rich intermetallics with experiment and theory" (1997). *Retrospective Theses and Dissertations*. 12227.
<https://lib.dr.iastate.edu/rtd/12227>

This Dissertation is brought to you for free and open access by the Iowa State University Capstones, Theses and Dissertations at Iowa State University Digital Repository. It has been accepted for inclusion in Retrospective Theses and Dissertations by an authorized administrator of Iowa State University Digital Repository. For more information, please contact digirep@iastate.edu.

INFORMATION TO USERS

This manuscript has been reproduced from the microfilm master. UMI films the text directly from the original or copy submitted. Thus, some thesis and dissertation copies are in typewriter face, while others may be from any type of computer printer.

The quality of this reproduction is dependent upon the quality of the copy submitted. Broken or indistinct print, colored or poor quality illustrations and photographs, print bleedthrough, substandard margins, and improper alignment can adversely affect reproduction.

In the unlikely event that the author did not send UMI a complete manuscript and there are missing pages, these will be noted. Also, if unauthorized copyright material had to be removed, a note will indicate the deletion.

Oversize materials (e.g., maps, drawings, charts) are reproduced by sectioning the original, beginning at the upper left-hand corner and continuing from left to right in equal sections with small overlaps. Each original is also photographed in one exposure and is included in reduced form at the back of the book.

Photographs included in the original manuscript have been reproduced xerographically in this copy. Higher quality 6" x 9" black and white photographic prints are available for any photographs or illustrations appearing in this copy for an additional charge. Contact UMI directly to order.

UMI

A Bell & Howell Information Company
300 North Zeeb Road, Ann Arbor MI 48106-1346 USA
313/761-4700 800/521-0600

Exploring aluminum-rich intermetallics with experiment and theory

by

Karen Jane Nordell

**A dissertation submitted to the graduate faculty
in partial fulfillment of the requirements for the degree of
DOCTOR OF PHILOSOPHY**

Major: Inorganic Chemistry

Major Professor: Gordon J. Miller

Iowa State University

Ames, Iowa

1997

Copyright © Karen Jane Nordell, 1997. All rights reserved.

UMI Number: 9737740

**UMI Microform 9737740
Copyright 1997, by UMI Company. All rights reserved.**

**This microform edition is protected against unauthorized
copying under Title 17, United States Code.**

UMI
300 North Zeeb Road
Ann Arbor, MI 48103

**Graduate College
Iowa State University**

**This is to certify that the Doctoral dissertation of
Karen Jane Nordell
has met the dissertation requirements of Iowa State University**

Signature was redacted for privacy.

Major Professor

Signature was redacted for privacy.

For the Major Program

↗

Signature was redacted for privacy.

For the Graduate College

~ to my parents ~

*“A little wonder is worth tons of knowledge in truly
knowing what the universe means.”*

- George MacDonald

TABLE OF CONTENTS

CHAPTER 1: INTRODUCTION AND MOTIVATION	1
Hume-Rothery Phases	2
Zintl Phases	3
Preview of Research Projects	7
CHAPTER 2: THE SYNTHESIS AND CHARACTERIZATION OF TERNARY TRIELIDES FORMING A TERNARY VARIANT OF THE NaZn₁₃ STRUCTURE	11
Introduction	11
Experimental	12
Synthesis	12
Structure Determination	13
Physical Measurements	14
Theoretical Calculations	15
Results	15
BaCu ₅ Al ₈	15
Structure Description	16
Magnetic Susceptibility Measurements	20
Phase Width: Synthetic Investigation	20
Phase Width: Theoretical Investigation	23
Substitutional Derivatives of BaCu ₅ Al ₈	24
Conclusions	30
CHAPTER 3: ELECTRONIC STRUCTURE CALCULATIONS ON TERNARY ALUMINIDE SYSTEMS FORMING THE NaZn₁₃ AND ThMn₁₂ STRUCTURES	31
Introduction	31
Electronic Structure Calculations of BaCu _x Al _{13-x}	32
Coloring Calculations	32
Phase Width: Theoretical Investigation	37
Electronic Structure Calculations of YCu ₄ Al ₈ (ThMn ₁₂ structure)	43
YCu ₄ Al ₈ : Structure Description	45
Extended Hückel Calculations on YCu ₄ Al ₈	50
Ordering of Copper and Aluminum in YCu ₄ Al ₈	52
Conclusions on the Ordering of YCu ₄ Al ₈	60
Phase Width: Theoretical Investigation	62

Calculations on YCu_xAl_{13-x} to Investigate the Role of the Cation in $NaZn_{13}$	66
Conclusions	67
CHAPTER 4: QUATERNARY ALUMINIDES	69
Introduction	69
Synthesis and Results	69
Conclusions	77
CHAPTER 5: TERNARY RARE EARTH-GOLD-ALUMINIDES FORMING STRUCTURAL VARIANTS OF $BaAl_4$	78
Introduction	78
$Ln_3Au_2Al_9$ ($Ln = Sm, Gd, Tb, Dy, Yb$) - New Ternaries Forming the α - La_3Al_{11} Structure	82
Synthesis and Characterization	82
$Dy_3Au_2Al_9$: Structure Solution	84
Physical Measurements	84
$Dy_3Au_2Al_9$ - Structure Description	89
Electronic Structure Calculations on $Ln_3Au_2Al_9$	90
$EuAu_{0.75}Al_{3.75}$ - A Disordered Ternary Derivative of $BaAl_4$	94
Synthesis and Structure Solution	94
Structure Description	94
Electronic Structure Calculations on $EuAuAl_3$	97
Conclusions	101
CHAPTER 6: STRUCTURE SORTING BY <i>VEC</i> USING SECOND MOMENT SCALING	104
Introduction	104
Structure Types Chosen for Second Moment Scaling	106
Practical Considerations of the Second Moment Scaling Calculations	115
Second Moment Scaling of Aluminum-Rich Compounds Using Ge Parameters	117
Results	117
Second Moment Scaling Calculations Using Ga Parameters	120
Second Moment Scaling of Two $CaCu_5$ Derivatives: Th_2Ni_{17} vs. Th_2Zn_{17}	122
$BaAl_4$ vs. α - La_3Al_{11}	127

CuAl ₂ vs. ThMn ₁₂ and Cu ₅ Zn ₈ vs. BaCu ₅ Al ₈	128
Conclusions	128
CHAPTER 7: THE SYNTHESIS AND STRUCTURE OF TERNARY ALUMINIDES FORMING THE BaCd₁₁, ErZn₅, Th₂Ni₁₇ and Th₂Zn₁₇ STRUCTURES	132
EuAg ₅ Al ₆ – BaCd ₁₁ Structure Type	132
Synthesis	132
Structure Solution	132
Structure Description	134
Tb ₃ Ag ₁₀ Al ₅ – ErZn ₅ Structure	138
Synthesis and Physical Measurements	138
Structure Solution	141
Structure Description	141
Ln ₂ Ag _x Al _{17-x} – Th ₂ Ni ₁₇ vs. Th ₂ Zn ₁₇	146
Structure Descriptions	146
Synthesis and Characterization	152
Results	154
Conclusions	156
CHAPTER 8: AAu₆Al₆ AND APd₄Al₉ (A = Ba, Sr, Eu, La) TETRAGONAL VARIANTS OF BaCu₅Al₈	158
Introduction	158
APd ₄ Al ₉ (A = Ba, Sr, Eu)	158
Synthesis and Structure Solution	158
Structure Description	162
AAu ₆ Al ₆ (A = Ba, Sr, Eu, La)	164
Synthesis and Structure Solution	164
Conclusions	169
CHAPTER 9: GENERAL CONCLUSIONS	170
APPENDIX A: REACTION COMPOSITION AND PRODUCT IDENTIFICATION	172

APPENDIX B: SUMMARY OF SINGLE CRYSTAL REFINEMENTS ON VARIOUS TERNARY ALUMINIDES	176
APPENDIX C: REFINED LATTICE PARAMETERS FROM POWDER X-RAY PATTERNS	180
APPENDIX D: ELECTRONIC STRUCTURE, SUPER- CONDUCTIVITY, AND SUBSTITUTION PATTERNS IN Tl_5Te_3	182
REFERENCES CITED	219
ACKNOWLEDGMENTS	224

CHAPTER 1

INTRODUCTION AND MOTIVATION

Solid state chemists spend a great deal of time trying to understand the complex set of variables which relate a compound's composition and its observed structure. Some of these variables include atomic size, electronic configuration, and electronegativity. Many classification schemes and sets of 'rules' have been proposed to separate groups (or classes) of compounds from a larger family of structures based on some unifying characteristic or criterion. For example, Wade's Rules account for the structure and bonding within deltahedral clusters by counting pairs of electrons available for terminal (exo-) and skeletal bonding.^[1] Another example is the Darken-Gurry method for predicting the extent of solid solubility in alloy systems based on the differences in size and electronegativities of the elements involved.^[2] There have been several classification schemes proposed based on the idea of valence electron concentration per atom (*vec*) which have proved useful for explaining the observation of certain intermetallic structure types. The Brewer-Engel Model correlates hexagonal close-packed (hcp), cubic close-packed (ccp) and body-centered cubic (bcc) packed structures, with the number of s and p valence electrons.^[3] This model uses primarily the valence electron configurations and structure types of the elements to relate bcc with one valence electron per atom (*ve*)(i.e. Na), hcp with two *ve* (i.e. Zn), and ccp with 3 *ve* (i.e. Al). Perhaps the two most well-known classes of solid state materials for which the ideas of valence electron concentration are critical, are the Hume-Rothery electron phases and the Zintl phases.

Main group intermetallics can be classified into three groups based on their (*vec*); the Hume-Rothery phases with $vec < 2$, the classical Zintl phases with $vec > 4$, and compounds with *vec* between 2 and 4, whose structures cannot be rationalized by any simple electron counting rules. (Note: the *vec* as applied to the classical Zintl phases is counted as the number of valence electrons per post-transition (or anionic) atom, not per 'all' atoms as in the Hume-Rothery phases.) Compounds within these three classes display a rich variety of

structures and compositions ranging from close-packed structures with wide phase widths to valence compounds containing some covalent two-center, two-electron bonds.^[4] The Hume-Rothery electron phases are well-known intermetallics whose structures are correlated with narrow ranges of *vec* between 1 and 2 (i.e. CuZn = 3 ve / 2 atoms, *vec* = 1.5). The classical Zintl phases are another class of intermetallic compounds formed between electropositive metals and main group elements from groups 13-17, whose structures are determined by the octet rule. Since the ideas of Hume-Rothery and Zintl, as well as the two classes of intermetallic materials which bear their names, provide a foundation and in part the motivation for the research and results to be discussed in this thesis, a brief review is appropriate.

Hume-Rothery Phases

In 1926 William Hume-Rothery published a paper based on his thesis research on intermetallic compounds in which he made the observation that for CuZn, Cu₃Al and Cu₅Sn, which all form the β -brass structure, the ratio of valence electrons to atoms was 3:2 (*vec* = 1.5).^[5-6] Hume-Rothery's observation was a breakthrough in the study of intermetallics. Following this initial investigation by Hume-Rothery, A. J. Bradley completed extensive work on the γ -brass structures in the Cu-Zn, and Cu-Al systems, and determined that for the γ -types Cu₅Zn₈, Cu₉Al₄ and Cu₃₁Sn₈, the valence electron to atom ratio was 21:13 (*vec* = 1.61).^[7] Later, Arne Westgren and Gösta Phragmén established that the hexagonal ϵ phases that form in many binary Cu, Ag and Au systems all had the valence electron to atom ratio of 7:4, (*vec* = 1.75).^[8] J. D. Bernal suggested that these phases be called electron compounds, but they are often referred to as Hume-Rothery phases.^[9] Many of the structures of the Hume-Rothery phases are very complex, making these simple counting rules even more elegant and useful. Table 1.1 includes the structure types and electron phases with their respective ranges in *vec*. The silver - zinc phase diagram^[10] contains three of the most well known Hume-Rothery phases, β -brass (AgZn, *vec* = 1.5), γ -brass (Ag₅Zn₈, *vec* = 1.61), and the ϵ -phase (AgZn₃, *vec* = 1.75).

Table 1.1: Summary of the electron phases with $1.0 < vec < 2.0$.^[11]

Phase Type	Structure	<i>vec</i> range
α	f.c.c.	1.00 - 1.42
β	b.c.c.	1.36 - 1.59
μ	cubic	1.40 - 1.54
γ	b.c.c.	1.54 - 1.70
δ	cubic	1.55 - 2.00
ξ	h.c.p.	1.32 - 1.83
ϵ	h.c.p.	1.65 - 1.89
η	h.c.p.	1.93 - 2.0

Zintl Phases

In 1929 Eduard Zintl published a short paper entitled “Salt-like Compounds of Sodium and their Transition to Intermetallic Phases”.^[12] This publication marked the introduction of what has come to be known as the “Zintl concept”,^[13] which Roald Hoffmann calls “the single most important theoretical concept in solid state chemistry of this century”.^[14] In the years following that first paper, Zintl carried out many experiments involving anions and polyanions of the groups 14-17 elements (S^{2-} , Sn_9^{4-}) in liquid ammonia, and performed structural investigations of intermetallic materials using X-ray diffraction. Zintl made the observation that many of the intermetallic compounds he studied did not behave like typical Hume-Rothery phases, and in some cases exhibited salt-like behavior. Some of the compounds formed between an electropositive metal and a main group metal had higher melting points than either elemental component, were poorer electrical conductors and were more brittle than typical alloy phases.^[15] Zintl’s analysis of the structures of these compounds was based on the idea that the electropositive metal donates its valence electrons to the electronegative main group metal, and that the octet rule can be used to rationalize the connectivity within the anionic main group network. A beautiful example demonstrating the simplicity and usefulness of this concept is NaTl. With the transfer of an electron from Na, the Tl’s become formally Tl⁻ anions, now with four valence electrons. Employing the octet rule, a tetravalent species would be expected to be in a 4-

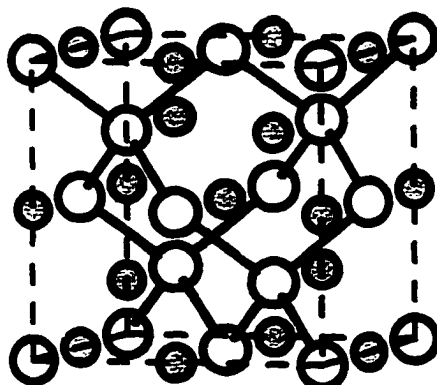


Figure 1.1: The structure of NaTl in which the Na atoms (gray) donate their electron to the Tl atoms (white) which form a diamond network.

coordinate environment, and indeed the Tl ions in NaTl form a diamond-type network with the Na^+ counterions packed in the voids, (see Figure 1.1). Through the study of many intermetallic materials formed between main group metals and electropositive metals, Zintl showed that many compounds containing elements from groups 14-17 formed structures which could be likewise rationalized using the octet rule. However, compounds formed with group 13 elements often adopted alloy structures with wider homogeneity widths, and followed no simple counting rules. The “Zintl border” separates groups 13 and 14.

Broadly defined, both Hume-Rothery and Zintl phases are intermetallic materials, however, the differences between these two classes are striking. It is not clear though, how intermetallic phases whose *vec*'s are between the “extremes” defined by the Hume-Rothery phases and the classical Zintl phases (i.e. compounds with $2 \leq \text{vec} \leq 4$), should be classified.

In order to explore the connection between *vec* and structure type for the compounds which lie in this intermediate *vec* region, we have focused on the synthesis, characterization and electronic structure investigations of new ternary aluminum-rich intermetallics. Many intermetallics present chemists with complex structural challenges such

as fractional and mixed site occupancies, site preferences, vacancy ordering and structural phase transitions. In addition to careful crystallography, electronic structure calculations are an essential tool for understanding the structures and bonding of these compounds. There are several reasons why this investigation of aluminum-rich phases is important to chemists, (1) careful systematic study of the composition (i.e phase width) and electronic structure of new aluminides adds valuable information to the larger collection of intermetallic compounds with *vec* between 0 to 8, including the Hume-Rothery and Zintl phases, and (2) while the structures of many binary and ternary aluminides have been identified, there are many more as-yet unexplored systems with intermediate *vec*'s which hold exciting possibilities for unique structures and physical properties. The Hume-Rothery phases are metallic compounds, and the traditional Zintl phases, in which the atoms in the anionic network obey the octet rule, are usually semiconductors or insulators. Aluminum-rich compounds, whose structures and bonding are not easily rationalized with electron counting rules, may have unexpected and desirable physical properties, such as high temperature metallic conductivity, high strength alloys, thermoelectrics, and superconductivity. ^[16-19]

Aluminides are a challenging group of compounds for a variety of reasons, mainly due to unique features of aluminum itself. The rich cluster chemistry of boron, gallium and the lower group 13 members has not been as forthcoming for aluminum.^[20] Even though the Zintl border separates groups 13 and 14, there are well documented Zintl phases formed with the lower group 13 members, but relatively few aluminum-rich Zintl phases.^[21] In combination with the alkali and alkaline earth metals, Ga, In and Tl form many phases containing isolated clusters and anionic frameworks whose connectivity can be rationalized by the octet rule.^[22] In contrast, binary and ternary aluminides containing electropositive metals (and/or transition metals) adopt structure types like the Laves phases, CaCu_5 , and other close packed intermetallic structures.^[22-23] In fact, the formation of several aluminum-rich phases has been correlated to certain narrow ranges of *vec* from 1 - 3, with some success.^[22] While there isn't a definitive explanation for the differences observed in

aluminides versus compounds containing the lower group 13 elements, several observations about aluminum itself provide insight.

Despite its position directly under boron and above gallium, in many respects aluminum has a very different behavior than the other group 13 elements. Aluminum, an fcc metal, has the lowest room temperature resistivity of any of the group 13 elements, $2.65 \times 10^{-6} \Omega\text{-cm}$, versus boron $1.8 \times 10^6 \Omega\text{-cm}$, gallium $\sim 27 \times 10^{-6} \Omega\text{-cm}$,^[26] indium $8.37 \times 10^{-6} \Omega\text{-cm}$, and Tl $18.0 \times 10^{-6} \Omega\text{-cm}$.^[24-25] Aluminum has the lowest electronegativity of any group 13 element (B:2.0, Al:1.5, Ga:1.6, In:1.7, Tl:1.8).^[26] In fact, Greenwood and Earnshaw report that for trends in both ionization energies and decreasing stability of the highest oxidation state, boron and aluminum fit nicely above the group 3 metals (Sc, Y, La and Ac), rather than above Ga, In and Tl.^[26] Despite aluminum's resemblance to the late transition metals (such as Cu and Ag) in its elemental structure and metallic properties, it does not have a d-core or high lying accessible d-orbitals like Ga, In and Tl (which in the same ways do *not* resemble the late transition metals). One of the consequences of the d-core for the heavier group 13 elements is that their valence s and p orbitals lie lower in energy than those of Al (i.e. Al: $3s = -12.30 \text{ eV}$, $3p = -6.50 \text{ eV}$, Ga: $4s = -14.58 \text{ eV}$, $4p = -6.75 \text{ eV}$).^[27] All of these factors combine to make the structures and properties of aluminum containing materials rather unpredictable, but possibly exciting.

Aluminum has been an important component for lightweight materials applications for many decades. Recently however, aluminum has played an integral role in the young but growing exploration and development of quasicrystalline materials.^[28] Many of the stable icosahedral and dodecahedral quasicrystalline phases are aluminum-rich compounds such as $\text{Al}_{70}\text{Pd}_{21.5}\text{Mn}_{8.5}$. Quasicrystals are an exciting new class of materials with unique and rather unexpected bulk and surface properties, not to mention the fundamental interest in the structures and synthesis of these non-classically crystalline compounds. Careful study of aluminides containing icosahedral units (whose symmetry is lowered to conform to classical crystallography), could provide valuable information in the search for new quasicrystalline compounds.

Preview of Research Projects

Chapter 2: The synthesis and characterization of ternary trieleides forming a ternary variant of the NaZn_{13} structure

The ternary compound, $\text{BaCu}_x\text{Al}_{13-x}$ ($5 < x < 6$), forms the NaZn_{13} structure,^[29] in which Ba atoms are surrounded by a ${}^3[\text{Cu}(\text{Cu}_y\text{Al}_{12-y})]$ ($4 < y < 5$) cubic framework of Cu-centered icosahedra with randomly arranged copper (ca. 33%) and aluminum (ca. 67%) atoms. This structure is a network of stuffed icosahedra and snub cubes which are packed in a CsCl arrangement. BaCu_5Al_8 has a *vec* of 2.38 and has elemental components commonly found in both Zintl and Hume-Rothery phases, making it a 'bridge' between the two families. This project consisted of the investigation of the phase width of $\text{BaCu}_x\text{Al}_{13-x}$ ($0 < x < 13$), a careful examination of the electronic structure and bonding within the metallic Cu-Al framework, and the exploration of other combinations of elements which form this same structure. BaCu_5Al_8 is an example of a ternary aluminide whose *vec* maximizes the bonding within the ${}^3[\text{Cu}_5\text{Al}_8]$ network as observed in its overlap populations. One of the important aspects of this synthetic effort was the progression from Cu to Ag to Au, and consideration of the effects of systematically changing the transition metal on the products and structures observed.

Chapter 3: Electronic structure calculations on ternary aluminide systems forming the NaZn_{13} (BaCu_5Al_8) and ThMn_{12} (LnCu_4Al_8) structures

The preparation of the ternary aluminides began with the synthesis of BaCu_5Al_8 and SrCu_6Al_7 , and then expanded to LnCu_6Al_7 systems (Ln = rare earth metals). While EuCu_6Al_7 and LaCu_6Al_7 are isostructural with BaCu_5Al_8 , all the other rare earth elements, in combination with copper and aluminum do not form the NaZn_{13} structure; rather, they form the ThMn_{12} structure. According to *Pearson's Handbook of Crystallographic Data for Intermetallic Phases*, 122 ternary aluminides form the ThMn_{12} structure type, with compositions; LnM_4Al_8 , LnM_5Al_7 , or LnM_6Al_6 , (where Ln = rare earth or actinide element, and M = Cr, Mn, Fe, Cu).^[29-32] The *vec* for these compounds are calculated based on the

number of electrons per framework atom, not including the alkaline earth or rare earth atoms. For example, the *vec* of BaCu_5Al_8 is $(2 + 5 + 24)/13 = 2.38$, and for DyCu_4Al_8 the *vec* is $(3 + 4 + 24) / 12 = 2.58$. Many of the ternary aluminides forming the ThMn_{12} and NaZn_{13} structure types have *vec*'s between 2 and 2.6. This chapter will include a careful examination of both of these structures, the bonding within the two Cu-Al networks, the differences in size and symmetry of the polyhedra surrounding the large electropositive metal atoms (i.e. Ba, La) in each structure, and the electronic structures of representative ternary aluminides in both structures, using extended Hückel calculations. These calculations were designed to illuminate some of the factors influencing the formation of either of these structures for a particular composition.

Chapter 4: Quaternary Aluminides

The synthesis of new ternary aluminum-rich intermetallics with alkaline earth and rare earth metals as electropositive electron donating atoms was discussed in chapter 2, and the role of these metal atoms in directing the formation of either the ThMn_{12} or NaZn_{13} structure was discussed in chapter 3. With the observation of the ThMn_{12} structure for LnCu_5Al_7 ($\text{Ln} = \text{Y, Ce, Pr, Nd, Sm, Gd, Tb, Dy, Ho, Er, Tm, Yb, Lu}$), and the NaZn_{13} structure for AeCu_6Al_7 ($\text{Ae} = \text{Ba, Sr, Eu, La}$), the synthesis of quaternary systems of mixed cations was carried out to explore whether the products would be a mixture of two different phases, or a single phase with mixed cations. Quaternary reactions of alkaline earth and rare earth silver aluminides were also carried out. $\text{AeAg}_{5.5}\text{Al}_{7.5}$ ($\text{Ae} = \text{Ba, Sr}$) are isostructural with BaCu_5Al_8 , but EuAg_5Al_6 forms the BaCd_{11} structure, and $\text{La}_2\text{Ag}_x\text{Al}_{17-x}$ systems either form the $\text{Th}_2\text{Zn}_{17}$ or $\text{Th}_2\text{Ni}_{17}$ structure types.

Chapter 5: Ternary rare earth - gold - aluminides forming structural variants of BaAl_4

A series of rare earth-gold-aluminides has been investigated, yielding insights into the importance of *vec* and atomic size as factors which influence the formation of various BaAl_4 structural derivatives. For the larger rare earth atoms (La...Eu), the ternary gold compounds

LnAuAl_3 ($\text{Ln} = \text{La}, \text{Sm}, \text{Eu}$) form a variant of BaAl_4 . The smaller rare earth atoms ($\text{Sm} \dots \text{Yb}$), form the new compounds, $\text{Ln}_3\text{Au}_2\text{Al}_9$ ($\text{Ln} = \text{Sm}, \text{Gd}, \text{Tb}, \text{Dy}, \text{Yb}$), which crystallize in the α - $\text{La}_3\text{Al}_{11}$ structure type, another variant of BaAl_4 . Electronic structure calculations were used to investigate the arrangements of Au and Al atoms within the frameworks of these structures. There is an energetic preference for heteronuclear Au - Al contacts, rather than homonuclear Al - Al or Au - Au contacts within these structures. The indications this has on the phase widths of these compounds, and the importance of the *vec* was examined.

Chapter 6: Structure sorting by *vec* using second moment scaling

In chapters 3 and 5, extended Hückel calculations were used extensively to investigate the electronic structures of several of these aluminides. These calculations are a powerful tool for comparing differences in overlap populations, Mulliken populations, Fermi energies and total energies for different arrangements of atoms within a given structure. However, one weakness of the Hückel calculations is their energetic bias toward structures in which the atoms are more highly coordinated. For this reason, without very careful treatment, it is difficult (if not impossible) to use the calculated total energies from a Hückel program as a basis for comparing the relative stability of similar compounds which form different structures. In recent years the method of moments, and in particular second moment scaling (*sms*), has been used successfully to minimize the effects of this bias in the Hückel total energies, and to allow for more accurate comparisons.^[33] Second moment scaling, which will be discussed in chapter 6, was used to investigate the relationship between the formation of ternary aluminides in various structure types within narrow ranges of *vec* between 0 and 4. While the number of structure types to consider could potentially be very large, the structure types selected were the following: NaZn_{13} , ThMn_{12} , BaCd_{11} , $\text{Th}_2\text{Ni}_{17}$, $\text{Th}_2\text{Zn}_{17}$, CaCu_5 , MoAl_{12} , SrCo_2Al_9 , K_4Si_{23} , BaAl_4 and α - $\text{La}_3\text{Al}_{11}$, because all of these structure types (except MoAl_{12}) have been encountered in my synthetic work. In many cases the calculated and observed ranges of *vec* were similar.

Chapter 7: The synthesis and structure of ternary aluminides forming the BaCd₁₁, ErZn₅, Th₂Ni₁₇ and Th₂Zn₁₇ structures

The synthesis and structural characterization of several new ternary intermetallics forming variants of the BaCd₁₁, ErZn₅, Th₂Ni₁₇ and Th₂Zn₁₇ structures are reported. LnAg₅Al₆ (Ln = La and Eu) form the tetragonal BaCd₁₁ structure, in which the silver and aluminum atoms build a closely packed network around the rare-earth cations. Gd₃Ag₁₀Al₅ forms a ternary derivative of the ErZn₅ structure.

Both Th₂Ni₁₇ and Th₂Zn₁₇ are variations of the CaCu₅ structure, in which some of the cationic positions have been replaced by pairs of transition metal atoms. The Th₂Zn₁₇ ($R\bar{3}m$) and Th₂Ni₁₇ (P6₃/mmc) structures are closely related and most easily described as two different arrangements of dimers and cations. There are many rare earth - silver - aluminum compounds reported in both of these two structures, with the aluminum-rich compounds (i.e. Ln₂Ag₇Al₁₀) forming the Th₂Ni₁₇ structure, and the silver-rich systems (i.e. Ln₂Ag₉Al₈) forming the Th₂Zn₁₇ structure.^[34-39] However, there has not been a systematic investigation of the ternary composition and structure type relationship. Using both synthesis and electronic structure calculations, a careful investigation of a series of La₂Ag_xAl_{17-x} was carried out to investigate the factors which drive the formation of both these structures.

Chapter 8: AeAu₆Al₆ and AePd₄Al₉ (Ae = Ba, Sr, Eu, La): tetragonal variants of BaCu₅Al₈

AeAu₅Al₈ and AePd₄Al₉ (Ae = Ba, Sr, Eu) form tetragonal variants of the NaZn₁₃ structure. These compounds have presented crystallographic challenges due to the poor quality of the majority of single crystals. However, based on the best refinements of the single crystal data, and the powder diffraction evidence, these new structures will be presented.

CHAPTER 2

THE SYNTHESIS AND CHARACTERIZATION OF TERNARY
TRIELIDES FORMING A TERNARY VARIANT OF THE
NaZn₁₃ STRUCTURE

Introduction

In order to explore the connection between *vec* and structure type for the compounds which lie between the Hume-Rothery phases ($vec < 2$) and the Zintl phases ($vec > 4$), we have focused on the synthesis, characterization and electronic structure of new ternary aluminum-rich intermetallics with $2 < vec < 4$. Many binary and ternary compounds in which a group 13 metal (Al, Ga, In, Tl) is a major component have *vec* near 3. While many of the intermetallics involving the trielide metals are not easily classified by any set of simple counting rules, this has not discouraged extensive synthetic efforts and structural characterization of binary and ternary phases containing aluminum, gallium and indium, many of which have *vec* near three. *Pearson's Handbook of Crystallographic Data for Intermetallic Phases* contains many trielide phases in a multitude of structure types such as: BaAl₄, K₄Si₂₃, WAl₁₂, SrCo₂Al₉, CaCu₅, Th₂Ni₁₇, Th₂Zn₁₇, BaHg₁₁, Th₆Mn₂₃, MgCu₂, MgZn₂, and ThMn₁₂.^[4, 40] I encountered many of these structure types in my synthetic explorations of ternary aluminides, and many of them are subjects of further discussions in this thesis. The largest group of ternary aluminides reported in *Pearson's Handbook of Crystallographic Data for Intermetallic Phases*^[40] forming a single structure type are those adopting the ThMn₁₂ structure (122 compounds). Many ternary rare earth (Ln), transition metal (M) aluminides with the general formula LnM_xAl_{12-x} (where $4 < x < 6$; Ln = Y, Ce - Lu, Th, U; M = Cr, Mn, Fe, Cu), have been characterized in this tetragonal variant of CaCu₅.^[4,30-32] This body-centered tetragonal structure contains a $\infty^3[M_xAl_{12-x}]^{n-}$ network, surrounding the Ln atoms by 20-vertex polyhedra. This ThMn₁₂ structure and the LnCu_xAl_{12-x} ($4 < x < 6$) compounds will be discussed in detail in chapter 3. These rare-earth-copper-aluminum ternaries have *vec*'s between 2 and 2.6, and therefore fall well within the *vec* region of interest.

We began with ternary systems in which the three components were a blend of both Zintl and Hume-Rothery phases, including an electropositive alkaline earth metal, a late transition metal and a trielide metal (Al, Ga, In). The first ternary characterized was BaCu_5Al_8 , which forms the NaZn_{13} structure type, in which the Ba atoms are surrounded by a network of interconnected, centered icosahedra, composed of copper and aluminum atoms. Several $\text{MCu}_x\text{Al}_{13-x}$ ($M = \text{Ca, Sr, La, Ce, Pr, Nd, Sm, Eu; } 5 < x < 7$) compounds have been reported forming the NaZn_{13} structure.^[29,34,41-42] To our knowledge, however, a systematic examination of these compounds, including their compositions, phase widths, atomic distributions, and electronic structures has not been reported. In this paper we report the results of our investigation of the composition, structure, phase width and electronic structure of many ternary aluminides which form the NaZn_{13} structure type.

Experimental

Synthesis

The synthesis of the ternary aluminide phases was carried out in a water-cooled, argon filled arc melting furnace. The samples were prepared from the elements in a glove box using foil as a wrapping which served as both a convenient way to keep the smaller pieces of metal or powder contained within the sample for arc melting, and to keep the more reactive metals protected from air exposure as the samples were quickly transferred from the box into the arc melting furnace chamber. The elemental sources were as follows, Ba and Sr rod (Johnson-Matthey, 99.5%), Cu (Johnson-Matthey, 99.5%) and Ag (Alfa, 99.9%) powders, Au wire (Aesar, 99.95%), Ga ingots (Alfa, 99.99%), In ingots (Alfa, 99.0%), Sn shot (Balzers, 99.99%), rare earth ingots (Y, La, Ce, Sm, Eu, Gd, Tb, Dy, Ho, Er, Yb) (Materials Preparation Center 99.0%) and Al foil. Some of the reactions, particularly those with gallium and indium, were carried out in tube furnaces with the reactants loaded into Al_2O_3 crucibles which were then sealed in evacuated fused silica jackets. But, most of the samples were melted and often remelted several times in the arc melting furnace with a titanium or zirconium getter to further purify the atmosphere. The arc

melted buttons were silvery with a dulled luster on the outer surface, but shiny silver and metallic looking in the inside. The buttons were easily broken into smaller pieces or ground into fine black powders for Guinier X-ray powder patterns which were taken immediately after arc melting to identify crystalline phases in the products. Samples were wrapped in Nb foil (0.025 mm, Alfa, 99.8%) and sealed in evacuated fused silica tubes for annealing at temperatures ranging from 600 - 1100°C depending on the compositions of the products. The Guinier X-ray powder patterns for the annealed products contained sharper lines than the initial post arc melting patterns, indicating improved crystallinity. However, for most of the products the positions and relative intensities of the lines did not change, indicating no change in the structure upon annealing. Powder patterns observed from products ground and handled exclusively in the glove box were identical to those of products handled in the air. The surfaces exposed are assumed to be passivated instantaneously, and oxidation of the bulk materials is not observed.

Single crystal data were collected on crystals selected from both pre-annealed and post-annealed products. Single crystals were generally loaded in air on glass fibers in epoxy, but many crystals were loaded in capillaries in the glove box. All of the single crystals chosen had an irregular shape and a shiny silver metallic appearance. After a satisfactory single crystal solution revealed the composition of the crystal, that stoichiometry was loaded for another reaction in an attempt to prepare single phase material for physical property measurements.

Structure Determination

Structural analysis of the products was carried out using both powder and single crystal X-ray diffraction. An Enraf-Nonius Guinier camera (Cu $K\alpha_1$ with Si internal standard) was used for powder diffraction analysis and lattice parameters were refined using measured line positions from the films. Single crystal data were collected on a Siemens P4 diffractometer at 298 ± 2 K (Mo $K\alpha_1$). Peaks located from a rotation photo were used to obtain a unit cell whose orientation matrix was refined using a group of 25 -50 reflections in

the 2θ range 10° to 30° . Most data sets were collected with $2\theta_{\max}$ either 45° , 50° or 60° , the latter was used to refine mixed occupancies on a single site more precisely. Lorentz and polarization corrections were applied to the data sets as well as a semi-empirical absorption correction based on collected azimuthal scans. The structures were solved by direct methods and refinement calculations were performed on a Digital Equipment Micro VAX 3100 computer using the SHELXTL-PLUS programs.^[43] Note: the refinement was on F^2 for all reflections except for those with very negative F^2 or those flagged by the user for potential systematic errors. Weighted R-factors (wR) and all goodnesses of fit (S) are based on F^2 , conventional R-factors (R1) are based on F, with F set to zero for negative F^2 . The observed criterion of $F^2 > 2\sigma(F^2)$ is used only for calculating $R_{\text{factor obs.}}$ and is not relevant to the choice of reflections for refinement. R-factors based on F^2 are statistically about twice as large as those based on F, and R- factors based on all data will be even larger.
[43]

Physical Measurements

Magnetic susceptibility tubes were prepared in the glove box by grinding 20 - 40 mg of product and loading it into a fused silica tube packed tightly between two rods, or by gluing a small piece of product inside a plastic straw. Magnetic susceptibility measurements were performed using a SQUID magnetometer, from 6 - 300K at a field strength of 3 Tesla.

Samples for X-ray photoelectron spectroscopy (XPS) were prepared and mounted in the glove box. XPS measurements of core binding energies and sample surface composition were carried out on PHI 5500 Multi-Technique Surface Analysis Equipment. This technique provides binding energies of electrons ejected from the atoms in the sample, and from those energies one gains information about the chemical environment of the elements in the structure. The surface of the material can be analyzed as received without any surface cleaning, in which case the material is always covered with an aluminum-rich oxide layer. The surface can be etched with a beam of electrons for a period of several minutes which effectively cleans the surface and exposes "fresh" sample which can be analyzed and will

reflect more accurately the composition of the "bulk" material. This compositional analysis has been carried out on many of these ternary aluminide samples.

Samples for scanning electron microscopy (SEM) were mounted in air on carbon paste to provide good contact with the sample holder surface and to avoid charging. The SEM and in situ energy dispersive spectroscopy (EDS) compositional analysis were carried out in a JEOL 6100 Scanning Electron Microscope.^[44] Microscopy was carried out on powder samples, crystals and larger pieces of arc melted buttons from both pre- and post-annealed products. Using EDS the elemental components of each sample can be identified and a qualitative composition can be analyzed. Without rigorous analysis of standards, however, accurate compositions from EDS are not easily acquired. For some products which contained multiple crystalline phases, as identified by powder X-ray analysis, regions of different phases were seen and their compositions confirmed by EDS. For example, observation of a cleaved surface of an arc melted button of $\text{EuCu}_5\text{Al}_7\text{Sn}$, showed large smooth looking regions of the sample which only analyzed as containing Eu, Cu and Al, as well as some smaller rougher areas which contained Eu, Cu, Al and Sn. The X-ray powder pattern confirms the presence of EuCu_6Al_7 , as well as elemental Sn.

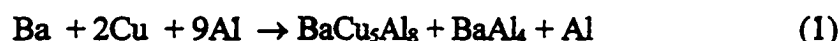
Theoretical Calculations

The electronic structures of many ternary aluminides were evaluated using the tight-binding approximation in the extended Hückel calculations, and these results will be presented in detail in chapter 3.

Results

BaCu₅Al₈

The new ternary compound BaCu_5Al_8 was first identified in the product of reaction (1) which was characterized using both powder and single crystal X-ray diffraction.



A single crystal was chosen from the reaction products of (1) and the structure of the new ternary compound BaCu_5Al_8 was solved; see Table 2.1 for relevant collection parameters and refinement results. BaCu_5Al_8 forms a ternary variant of the NaZn_{13} structure, which is a 3-dimensional network of Cu-centered icosahedra enclosing the Ba atoms in 24-vertex snub cubes. Table 2.2 contains the positional coordinates, isotropic displacement parameters, and site occupancies for BaCu_5Al_8 .

Structure Description

BaCu_5Al_8 forms a ternary variant of the NaZn_{13} structure in which each large face centered cubic unit cell contains 8 formula units, totaling 112 atoms. The structure can be described as a CsCl packing of Ba atoms and Cu1-centered icosahedra as shown in Figure 2.1 (a). The structure contains three positions which are summarized in Table 2.2 for $\text{BaCu}_{5.3}\text{Al}_{7.7}$, and a slice of the structure is shown in Figure 2.1(b). The Ba atoms (8a, large gray circles) are surrounded by 24-vertex snub cubes, and the Cu1 atoms (8b, small black circles) are surrounded by icosahedra, composed of four Cu2 and eight Al atoms (96i, small open circles). The Cu1-centered icosahedra are interconnected by tetracapped tetrahedra (stella quadrangula) such that they are arranged in an alternate pattern with the icosahedra bisecting each cell edge $(1/2, 0, 0)$ rotated 90° from the icosahedra on the corners $(0, 0, 0)$ and the center $(1/2, 1/2, 1/2)$ of the unit cell. There are three polyhedra which are building blocks from which the entire structure can be described: the snub cube, the stuffed icosahedron, and the stella quadrangula, see Figure 2.2 (a), (b) and (c). The snub cubes are nearly spherical polyhedra around each Ba atom whose site symmetry is O (432). The distance from the Ba atoms to each of the 24 atoms of the snub cube is $3.576(1)$ Å. The icosahedra are also nearly spherical polyhedra, centered by Cu1 atoms whose site symmetry is T_h ($m\bar{3}$). The distance from the central Cu1 atom $(0, 0, 0)$ to each of the 12 atoms of the icosahedron is $2.572(1)$ Å. The distances between Al and Cu2 atoms which make up the icosahedral network range from $2.637(1)$ – $2.845(1)$ Å, see Figure 2.2. There are two different distances within a single icosahedron, 6 long distances ($2.845(1)$ Å) and 24 shorter distances ($2.668(1)$ Å), see Figure 2.2 (b). The stella quadrangula also contain interactions

at two distances, 2.637(1) Å, and 2.771(1) Å, see Figure 2.2 (c). While this is a densely packed structure, it cannot be considered a true Frank-Kasper phase because the snub cubes contain 4 membered rings, and not every polyhedron can be described by the packing of tetrahedra.

Table 2.1: A summary of collection parameters and structure refinement results for BaCu_{5.3}Al_{7.7}.

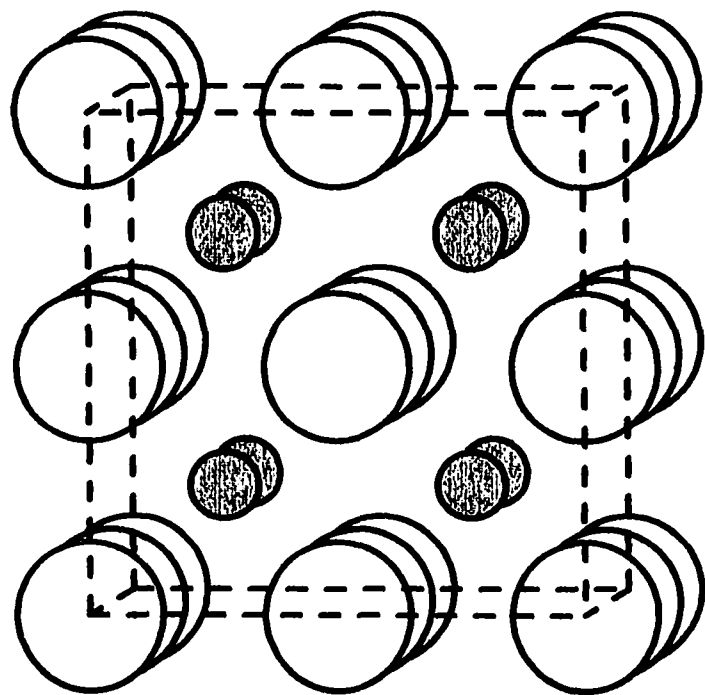
Space Group	Fm $\bar{3}$ c (no. 226)
Unit Cell Dimensions	$a = 12.205(4)$ Å
Volume	1815.8(10) Å ³
Z	8
Density (calc.)	4.977 Mg/m ³
Crystal Size (mm)	0.50 x 0.30 x 0.20
Absorption Coefficient	17.064 mm ⁻¹
Radiation	MoK α ($\lambda = 0.71073$ Å)
Temperature (K)	298(1)
2 θ_{\max}	60.0°
Scan Range (ω)	0.60°
Scan Speed	Variable; 1.0 to 10.0°/min. in ω
Index Ranges	0 $\leq h \leq 12$, -16 $\leq k \leq 16$, -16 $\leq l \leq 16$
Reflections Collected	8415
Independent Reflections	117 ($R_{int} = 0.0532$)
Observed Reflections	115 ($F_o \geq 4.0 \sigma(F_o)$)
Min./ Max. Transmission	0.3495 / 0.9006
Weighting Scheme	$w^{-1} = \sigma^2(F) + 0.0015F^2$
Parameters Refined	14
R Indices ($wR2$)[$F_o \geq 4\sigma(F_o)$] *	R = 0.0186, $wR = 0.0456$
R Indices (R1) (all data) **	R = 0.0188, $wR = 0.0456$
Goof, All Data †	1.158
Data-to-Parameter Ratio	15.1:1
Largest Difference Peak	0.858 e/ Å ⁻³
Largest Difference Hole	-1.244 e/ Å ⁻³

$$* wR2 = [\Sigma[w(F_o^2 - F_c^2)^2] / \Sigma[w(F_o^2)^2]]^{1/2}$$

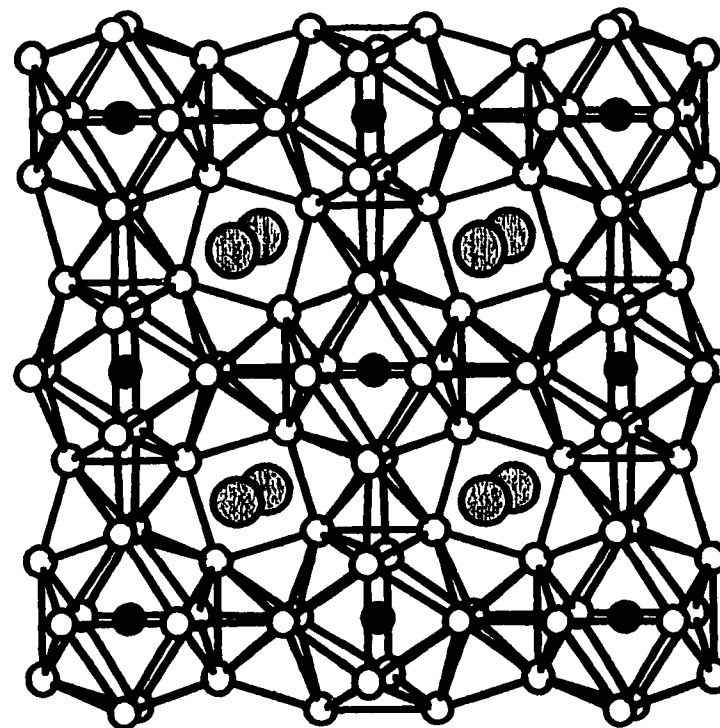
$$** R1 = \Sigma ||F_o| - |F_c|| / \Sigma |F_o|$$

$$† \text{Goof} = S = [\Sigma[w(F_o^2 - F_c^2)^2] / (n - p)]^{1/2}$$

(where n = # of reflections, p = total # of parameters refined)

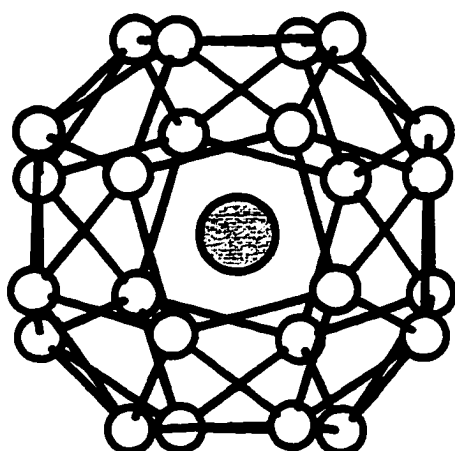


(a)



(b)

Figure 2.1(a) The CsCl packing of Ba atoms (gray circles) and Cu1-centered icosahedra (open circles). (b) A slice of the BaCu_5Al_8 structure. The large gray circles are the Ba atoms (8a), the smaller black circles are the Cu1 atoms (8b), and the small open circles are the Cu2/Al atoms (96i).



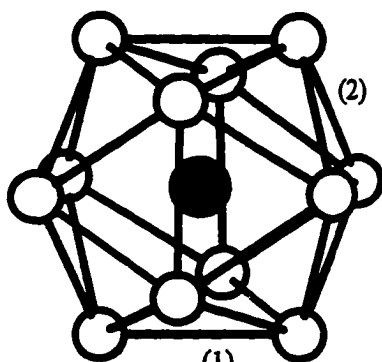
(a)

Ba centered snub cube

Ba - large gray circle
Cu2/Al - small open circles

symmetry of the Ba site = O (432)

Distance from Ba - Cu2/Al = 3.576 (1) Å



(b)

Cu centered icosahedron

Cu1 black circle, Cu2/Al open circles

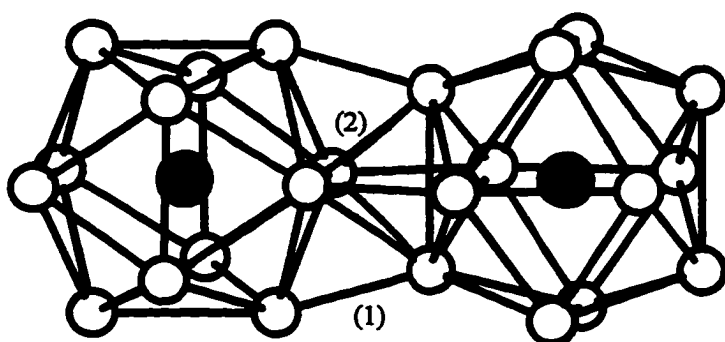
symmetry of the Cu1 site = T_h ($m\bar{3}$)

Distance from Cu1 - Cu2/Al = 2.572(1) Å

Distances from Cu2/Al - Cu2/Al

(1) 2.845(1) Å (x 6)

(2) 2.668(1) Å (x 24)



(c)

Stella Quadrangula

(between two
icosahedra)

Cu2/Al - Cu2/Al

(1) 2.637(1) Å (x 4)

(2) 2.711(1) Å (x 4)

Figure 2.2 (a) The 24-vertex polyhedron around each Ba atom (gray circle), with a distance of 3.576(1) Å to each Cu2/Al atom (open circles). (b) A Cu-centered (black circle) icosahedron, with 12 equivalent distances of 2.572(1) Å to the Cu2/Al atoms (open circles). (c) Two icosahedra are connected by a stella quadrangula, (tetracapped tetrahedron) with two distances of 2.637(1) Å and 2.711(1) Å.

Table 2.2: The positional coordinates and equivalent isotropic displacement coefficients for BaCu_5Al_8 .

Atom	Site	x	y	z	U_{eq}	Site Occ.
Ba	8a	0.25	0.25	0.25	0.0072(5)	1.0
Cu1	8b	0	0	0	0.0148(5)	1.0
Al	96i	0.1166(1)	0.1755(1)	0.0	0.0139(4)	0.643(6)
Cu2	96i	0.1166(1)	0.1755(1)	0.0	0.0139(4)	0.357(6)

Magnetic Susceptibility Measurements

The measured magnetic susceptibilities are shown in Figures 2.3 and 2.4 for BaCu_5Al_8 , and $\text{EuCu}_{6.5}\text{Al}_{6.5}$ respectively. After a diamagnetic core correction was applied, BaCu_5Al_8 showed temperature independent paramagnetism above 100K ($\chi_{\text{TIP}} = 1.0 \times 10^{-4}$ emu/mol), and $\text{EuCu}_{6.5}\text{Al}_{6.5}$ was paramagnetic with an effective moment of 7.82(2) Bohr magnetons ($T > 80\text{K}$), consistent with Eu^{2+} (f^7 , 7.94 B.M.).^[45]

After the synthesis and characterization of BaCu_5Al_8 , several questions guided our further examination of this new intermetallic material; (1) what is the phase width of this compound? (2) can the phase width be explained using electronic structure calculations to examine the bonding within the copper-aluminum framework? and (3) what other ternary (and quaternary) combinations of metals might form isostructural compounds? In the following sections, these three questions will be addressed.

Phase Width: Synthetic Investigation

In the $\text{BaCu}_x\text{Al}_{13-x}$ system, a careful investigation of the phase width was carried out both synthetically and theoretically. Table 2.3 contains the results of efforts to synthesize single phase products by varying the reaction composition for $\text{BaCu}_x\text{Al}_{13-x}$ from $0 \leq x \leq 13$. In all cases except $x = 4, 5$, and 6 , multiple phases were observed in the Guinier X-ray

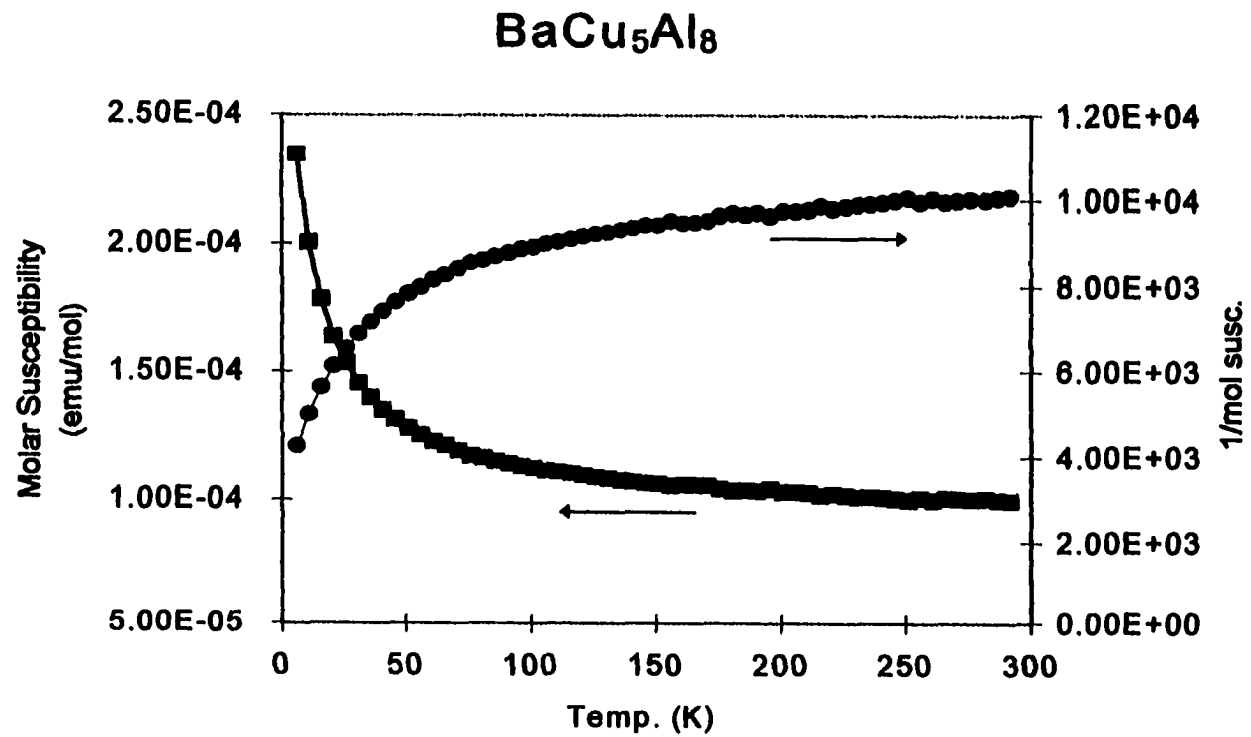


Figure 2.3: The magnetic susceptibility curve for BaCu₅Al₈ from 6 to 300 K at 3 Tesla. BaCu₅Al₈ has a very small paramagnetic signal, which is temperature independent (Pauli paramagnetism) above 100K ($\chi_{\text{TIP}} = 1.0 \times 10^{-4}$ emu/mol).

EuCu_{6.5}Al_{6.5}

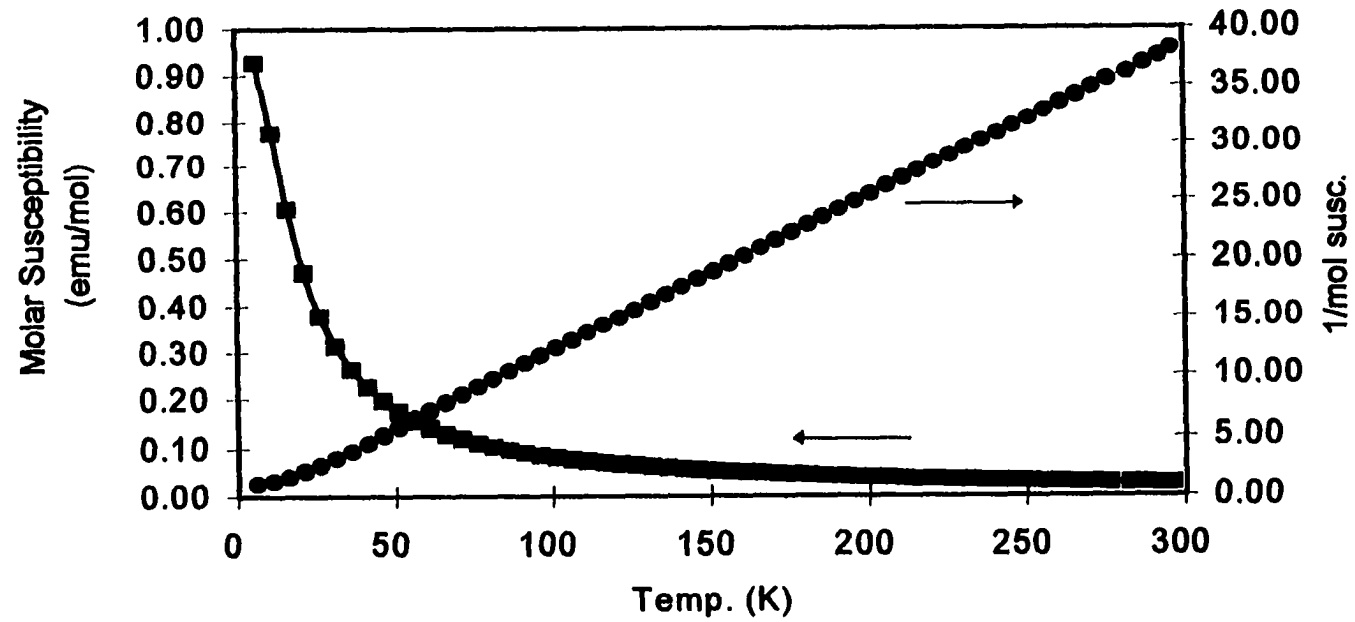
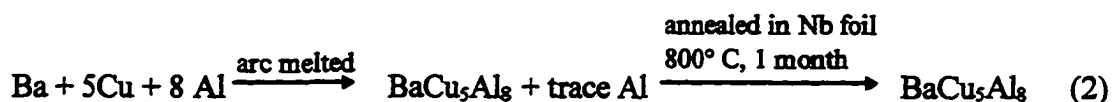


Figure 2.4: The magnetic susceptibility curve for EuCu_{6.5}Al_{6.5} from 6 to 300 K at 3 Tesla. EuCu_{6.5}Al_{6.5} has a large paramagnetic signal with an effective magnetic moment of 7.82(2) Bohr magnetons ($T > 80\text{K}$), consistent with Eu⁺² (f^7 7.94 μ_B).

powder patterns. BaCu_{13} is reported to form the NaZn_{13} structure,^[46] although we could not confirm this.

In order to investigate the variation in composition within a single arc melted button, several single crystals taken from a single reaction product were characterized.



Several crystals were loaded from the annealed product of reaction (2), and three single crystal X-ray data sets were collected and refined with compositions of $\text{BaCu}_{5.40(2)}\text{Al}_{7.60(2)}$, $\text{BaCu}_{5.48(3)}\text{Al}_{7.52(3)}$, and $\text{BaCu}_{5.52(2)}\text{Al}_{7.48(2)}$. Table 2.4 summarizes the results of these three refinements. These results support two important conclusions: (1) these ternary phases $\text{BaCu}_x\text{Al}_{13-x}$ have a fairly narrow phase width between $4 \leq x \leq 6$, and (2) the composition within a certain product button is quite homogeneous.

Phase Width: Theoretical Investigation

These synthetic results lead us to examine how the electronic structure contributes to this narrow phase width. We performed a series of calculations in which the Cu : Al ratio was varied from BaCu_{13} , $\text{BaCu}_{12}\text{Al}$.. BaCuAl_{12} , BaAl_{13} , and considered the total densities of states, Fermi energies, and crystal orbital overlap populations for the bonding in the icosahedral network. The complete results of our investigation of the electronic structure of BaCu_5Al_8 will be presented in chapter 3. It is important to mention that these calculations have been invaluable tools for our exploration and understanding of many aspects of these ternary aluminides. In particular, the electronic structure calculations have aided our examination of the arrangement of copper and aluminum atoms in the icosahedral network, as well as the observed phase width of $\text{BaCu}_x\text{Al}_{13-x}$ (where $4 < x < 6$).

Table 2.3: The synthetic investigation of the phase width of $\text{BaCu}_x\text{Al}_{13-x}$.

Reaction Stoichiometry	Heating Method	Reaction Products
BaCu_{13}	arc welder	BaCu_{13} [46]
BaCu_9Al_4	arc welder	$\text{BaCu}_6\text{Al}_7 + \text{Cu}$
BaCu_6Al_7	furnace and arc welder	BaCu_6Al_7
BaCu_5Al_8	furnace and arc welder	BaCu_5Al_8
BaCu_4Al_9	arc welder	BaCu_4Al_9
$\text{BaCu}_3\text{Al}_{10}$	furnace	$\text{BaCu}_5\text{Al}_8 + \text{CuAl}_2 + \text{Al}$
BaCuAl_{12}	furnace and arc welder	$\text{BaAl}_4 + \text{Al} + \text{trace BaCu}_5\text{Al}_8$
BaAl_{13}	arc welder	$\text{BaAl}_4 + \text{Al}$

Substitutional Derivatives of BaCu_5Al_8

The isostructural ternary trielide-rich phases $\text{AM}_x\text{T}_{13-x}$ ($\text{A} = \text{Ba}, \text{Sr}, \text{La}, \text{Eu}$; $\text{M} = \text{Cu}, \text{Ag}$; $\text{T} = \text{Al}, \text{Ga}, \text{In}$; $5 < x < 6$) were synthesized and characterized using the same methods described earlier. Table 2.5 contains a summary of the reactant compositions, the heating method(s) and the reaction products identified by powder X-ray diffraction. Single crystal X-ray analysis was carried out for those compounds marked with a (*). Table 2.6 contains a summary of single crystal solutions for various ternary aluminide phases forming the NaZn_{13} structure type. Using measured lines from the Guinier X-ray powder patterns, the lattice parameters for these compounds were refined, and are reported in Table 2.7. While the synthetic goal of each reaction was to prepare single phase product, this was not possible in many cases (particularly for the reactions with Ga and In). Therefore the exact compositions for those phases in Table 2.6 marked with a (*) are not known. In order to establish the relationship between the observed lattice parameters and the refined composition of the copper aluminum network, the refined lattice parameters from powder data, were plotted against the refined compositions from the single crystal data. Figure 2.5 contains three graphs of the a lattice parameter vs. composition for the three systems; $\text{BaCu}_x\text{Al}_{13-x}$, $\text{LaCu}_x\text{Al}_{13-x}$ and $\text{EuCu}_x\text{Al}_{13-x}$. The a lattice parameter varies systematically with $\text{MCu}_x\text{Al}_{13-x}$ ($\text{M} = \text{Ba}, \text{Eu}, \text{La}$) composition, decreasing as the Al composition decreases.

Table 2.4: An abbreviated summary of refinement details for three single crystals taken from a single annealed product.

Refined Chemical Formula		(a) BaCu _{5.40} Al _{7.60}	(b) BaCu _{5.48} Al _{7.52}	(c) BaCu _{5.52} Al _{7.48}		
Space Group		Fm $\bar{3}$ c	Fm $\bar{3}$ c	Fm $\bar{3}$ c		
Unit Cell Dimensions		$a = 12.167(1) \text{ \AA}$	12.169(1) \AA	12.168(1) \AA		
Unit Cell Volume		1801.2 (3) \AA^3	1802.0 (3) \AA^3	1801.6 (3) \AA^3		
Reflections Collected		340	342	342		
Independent Reflections		63	63	63		
Observed Reflections		59 ($F_o \geq 2\sigma(F_o)$)	59	59		
R, wR ($F_o \geq 4.0 \sigma(F_o)$)		0.0181, 0.0264	0.0237, 0.0493	0.0162, 0.0288		
R, wR (all data)		0.0222, 0.0281	0.0251, 0.0495	0.0179, 0.0290		
Goof, All Data		0.985	1.300	0.997		
Atom	Site	x	y	z	U _{eq}	Site Occ.
(a) BaCu _{5.40} Al _{7.60}						
Ba	8a	0.25	0.25	0.25	0.0082(6)	1.0
Cu1	8b	0	0	0	0.0113(11)	0.86(2)
Al1	8b	0	0	0	0.0113(11)	0.14(2)
Al2	96i	0.1169(1)	0.1755(1)	0.0	0.0148(7)	0.621(7)
Cu2	96i	0.1169(1)	0.1755(1)	0.0	0.0148(7)	0.379(7)
(b) BaCu _{5.48} Al _{7.52}						
Ba	8a	0.25	0.25	0.25	0.0061(9)	1.0
Cu1	8b	0	0	0	0.014 (2)	0.92(3)
Al1	8b	0	0	0	0.014 (2)	0.08(3)
Al2	96i	0.1169(2)	0.1757(2)	0.0	0.0123(10)	0.621(10)
Cu2	96i	0.1169(2)	0.1757(2)	0.0	0.0123(10)	0.379(10)
(c) BaCu _{5.52} Al _{7.48}						
Ba	8a	0.25	0.25	0.25	0.0077(6)	1.0
Cu1	8b	0	0	0	0.0107(11)	0.85(2)
Al1	8b	0	0	0	0.0107(11)	0.15(2)
Al2	96i	0.1166(1)	0.1754(1)	0.0	0.0148(6)	0.612(7)
Cu2	96i	0.1166(1)	0.1754(1)	0.0	0.0148(6)	0.388(7)

Table 2.5: Reaction composition and product identification for a those ternaries adopting the BaCu₅Al₈ structure. See Appendix 1 for a complete list of reactions.

Reaction Stoichiometry	Heating Method	Reaction Products (by powder x-ray diffraction)
BaAl ₁₃	arc welder	BaAl ₄ + Al
BaCuAl ₁₂	arc welder	BaAl ₄ + Al + BaCu ₅ Al ₈ trace
BaCu ₃ Al ₁₀	arc welder	BaCu ₅ Al ₈ + CuAl ₂ + Al
BaCu ₄ Al ₉	arc welder	BaCu ₄ Al ₉
BaCu ₅ Al ₈	furnace (1120°C) & arc welder	BaCu ₅ Al ₈ *
BaCu ₆ Al ₇	furnace (1125°C) & arc welder	BaCu ₆ Al ₇ *
BaCu ₉ Al ₄	arc welder	BaCu ₆ Al ₇ + Cu
BaCu ₁₃	arc welder	BaCu ₁₃ ^[46]
BaCu ₅ Ga ₈	furnace (600 °C, 950 °C)	BaCu ₆ Ga ₇ + Ga + CuGa ₂
BaCu ₅ In ₈	furnace (600 °C, 950 °C)	BaCu ₆ In ₇ + In
BaAg ₃ Al ₁₀	arc welder	BaAg ₅ Al ₈ + Al
BaAg ₅ Al ₈	arc welder	BaAg ₅ Al ₈ * + trace Al + trace BaAl ₄
BaAg _{5.5} Al _{7.5}	arc welder	BaAg _{5.5} Al _{7.5} *
BaAg ₇ Ga ₆	furnace (1000 °C)	BaAg _x Ga _{13-x} + BaGa ₄
BaAg ₆ In ₇	furnace (1000 °C)	BaAg _x In _{13-x} + In
SrCu ₅ Al ₈	arc welder	SrCu ₆ Al ₇ * + CuAl ₂
SrCu ₆ Al ₇	arc welder	SrCu ₆ Al ₇ *
SrCu ₇ Al ₆	arc welder	SrCu ₇ Al ₆
SrAg ₅ Al ₈	arc welder	SrAg ₆ Al ₇ + Al
SrAg _{5.5} Al _{7.5}	arc welder	SrAg _{5.5} Al _{7.5}
EuCu ₆ Al ₇	arc welder	EuCu ₆ Al ₇ * + CuAl ₂
LaCu ₅ Al ₈	furnace (1125 °C)	LaCu ₆ Al ₇ * + LaAl ₄
LaCu ₆ Al ₇	arc welder	LaCu ₆ Al ₇ *

*single crystal collection and solution

Table 2.6: A summary of single crystal refinements on various ternary aluminide compounds forming the NaZn₁₃ structure.

Refined Composition	<i>a</i> (Å)	# refls. collected	# uniq /obsvd * reflections	2θ _{max} (degrees)	R, wR (F _o ≥ 4σ (F _o))	R, wR all data
1. BaCu _{5.27} Al _{7.73}	12.205 (4)	8415	117 / 115	60.0	0.0186, 0.0452	0.0188, 0.0452
2. BaCu _{5.66} Al _{7.33}	12.134 (1)	560	128 / 110	60.0	0.0290, 0.0710	0.0401, 0.0755
3. BaCu _{6.1} Al _{6.9}	12.061 (1)	164	55 / 45	50.0	0.0143, 0.0300	0.0313, 0.0394
4. BaCu _{5.41} Al _{7.60}	12.167 (1)	340	63 / 59	45.0	0.0181, 0.0264	0.0222, 0.0281
5. BaCu _{5.48} Al _{7.52}	12.169 (1)	342	63 / 59	45.0	0.0237, 0.0493	0.0251, 0.0495
6. BaCu _{5.52} Al _{7.48}	12.168 (1)	342	63 / 59	45.0	0.0162, 0.0288	0.0179, 0.0290
7. BaCu _{6.09} Al _{6.91}	12.084 (1)	980	82 / 82	50.0	0.0219, 0.0542	0.0219, 0.0542
8. SrCu _{6.17} Al _{6.83}	11.980 (1)	904	125 / 111	60.0	0.0315, 0.0674	0.0363, 0.0688
9. SrCu _{6.0} Al _{7.0}	11.980 (1)	466	110 / 96	60.0	0.0442, 0.0927	0.0525, 0.0979
10. LaCu _{5.9} Al _{7.1}	11.965 (1)	904	125 / 113	60.0	0.0170, 0.0398	0.0217, 0.0416
11. LaCu _{6.07} Al _{6.93}	11.913 (1)	324	61 / 59	45.0	0.0163, 0.0329	0.0178, 0.0331
12. LaCu _{6.12} Al _{6.88}	11.916 (1)	324	61 / 59	45.0	0.0236, 0.0563	0.0240, 0.0563
13. LaCu _{6.11} Al _{6.89}	11.915 (1)	427	78 / 73	50.0	0.0223, 0.0420	0.0264, 0.0434
14. EuCu _{6.4} Al _{6.6}	11.928 (1)	894	124 / 117	60.0	0.0218, 0.0554	0.0237, 0.0566
15. EuCu _{6.13} Al _{6.87}	11.936 (1)	324	61 / 59	45.0	0.0204, 0.0436	0.0241, 0.0470
16. EuCu _{5.95} Al _{7.05}	11.940 (1)	324	61 / 59	45.0	0.0165, 0.0353	0.0173, 0.0355
17. BaAg _{5.8} Al _{7.2}	12.665 (1)	874	93 / 88	50.0	0.0433, 0.0813	0.0490, 0.0853
18. BaAg _{5.53} Al _{7.47}	12.677 (1)	517	93 / 89	50.0	0.0222, 0.0501	0.0239, 0.0506

* observed means (F_o ≥ 2σ (F_o))

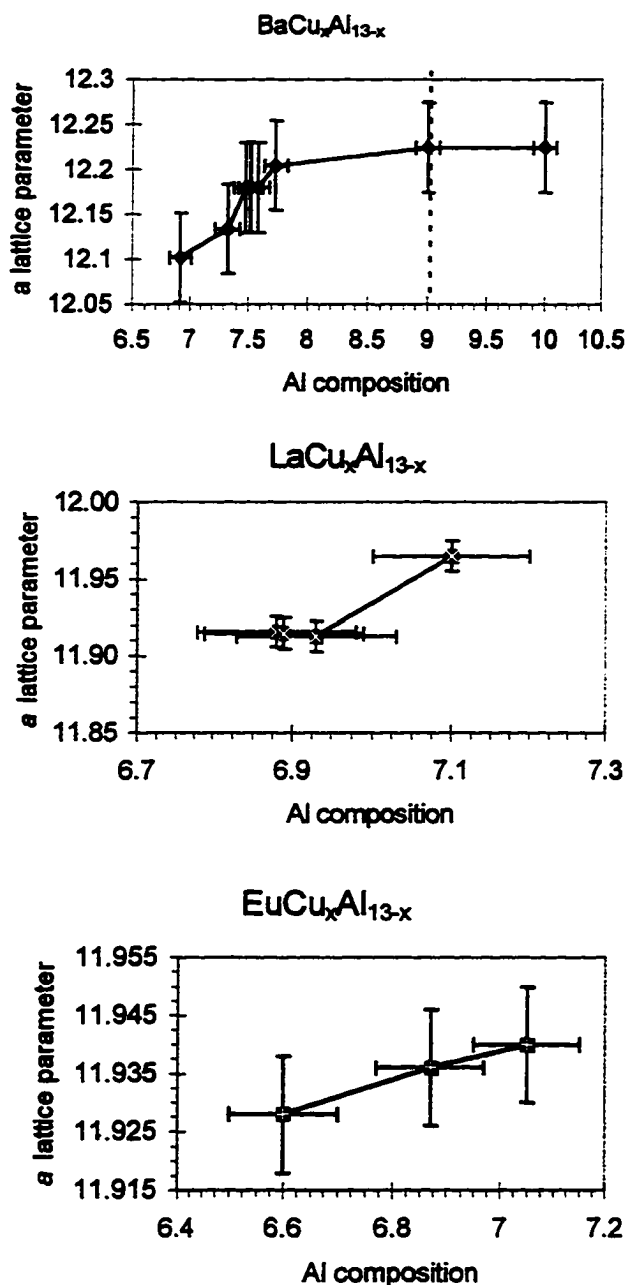


Figure 2.5: The variation of the lattice parameters for the three compounds $\text{BaCu}_x\text{Al}_{13-x}$, $\text{EuCu}_x\text{Al}_{13-x}$ and $\text{LaCu}_x\text{Al}_{13-x}$. The composition, as refined by single crystal data, is plotted versus the measured and refined lattice parameters, with the error bars indicating an uncertainty of ± 0.1 in composition, and ± 0.05 Å in lattice parameter.

Table 2.7: The refined lattice parameters for ternaries forming the NaZn_{13} structure. For those compounds marked with a (*), the composition is approximate, because the reaction product was not single phase, and a single crystal X-ray structure refinement was not obtained.

Composition	Lattice Parameter Å
$\text{BaCu}_{5.3}\text{Cu}_{7.7}$	12.205(4)
BaCu_6Ga_7 *	12.026(2)
BaCu_6In_7 *	12.740(4)
$\text{BaAg}_{5.8}\text{Al}_{7.2}$	12.666(3)
BaAg_6Ga_7 *	12.757(3)
BaAg_6In_7 *	13.442(3)
SrCu_6Al_7	11.975(1)
$\text{SrAg}_{5.5}\text{Al}_{7.5}$ *	12.605(6)
LaCu_6Al_7	11.952(4)
$\text{EuCu}_{6.5}\text{Al}_{6.5}$	11.977(1)

Table 2.5 contains a complete list of those phases which were observed forming the BaCu_5Al_8 structural variant of NaZn_{13} . However, it does not include all the ternary combinations for which phases other than those forming the NaZn_{13} structure were observed. Many ternary reactions with the composition $\text{AM}_x\text{T}_{13-x}$ where $M = \text{Au, Ni, Pd, Co, Fe, Mo, Nb}$, and $T = \text{Si, Sn, Ge}$, were carried out whose products are all included in a complete reaction list in Appendix 1. Several new ternary gold and palladium aluminides which form a tetragonal variant of BaCu_5Al_8 will be presented in chapter 8. The ternary phases reported in this chapter form a variant of the NaZn_{13} structure, but other structure types that were observed and will be discussed in later chapters include; ThMn_{12} ($I4/mmm$), BaCd_{11} ($I4_1/amd$), $\text{Th}_2\text{Ni}_{17}$ ($P6_3/mmc$), $\text{Th}_2\text{Zn}_{17}$ ($R\bar{3}m$), ErZn_5 ($P6_3/mmc$), SrCo_2Al_9 ($P6/mmm$), and variations of BaAl_4 ($I4/mmm$).^[4, 40]

Conclusions

The synthesis and structural characterization of several new ternary derivatives of NaZn_{13} : ACu_5Al_8 ($A = \text{Ba, Sr, Eu, La}$) and $\text{AAl}_5\text{Al}_7.5$ ($A = \text{Ba, Sr}$) was reported. These compounds crystallize in the space group $Fm\bar{3}c$ (No. 226) with lattice parameters near 12 Å, which vary according to the composition of the copper aluminum network. BaCu_5Al_8 contains a ${}^3[\text{Cu}(\text{Cu}_4\text{Al}_8)]^{2-}$ network of interconnected, Cu-centered icosahedra which surround the large Ba atoms in a snub cube. The X-ray diffraction experiments did not suggest any ordering of the 4 Cu and 8 Al atoms within the icosahedra. The ‘coloring’ of these atoms within the network will be discussed in detail in chapter 3. These compounds form with a narrow phase width, and electronic structure calculations designed to explore this phase width will be presented in chapter 3.

CHAPTER 3

ELECTRONIC STRUCTURE CALCULATIONS ON TERNARY ALUMINIDE SYSTEMS FORMING THE NaZn_{13} AND ThMn_{12} STRUCTURES

Introduction

The electronic structures of many ternary aluminides were evaluated using the tight-binding approximation in the extended Hückel calculations.^[48] The extended Hückel method is a one-electron calculation of the orbital energies, considering nearest neighbor orbital overlap. These calculations provide information about the electronic structures of compounds such as the total energies, overlap populations, Mulliken populations, as well as densities of states (DOS) and crystal orbital overlap population (COOP) curves. For a discussion of the extended Hückel method and some examples of its application, please see references [14, 49-51].

For the electronic structure calculations of $\text{BaCu}_x\text{Al}_{13-x}$ the primitive unit cell containing 2 complete centered icosahedra was used. In the majority of the calculations no specific orbital contributions for the electropositive metal atoms (Ba, Sr, La) were included for several reasons. Briefly, in BaCu_5Al_8 , the barium atoms are surrounded by a 24 vertex snub cube of Cu and Al atoms each at a distance of the $3.576(1) \text{ \AA}$, and due to this long distance, the alkaline earth atoms were treated as classical cations, donating two electrons each to the metallic framework. As reported in chapter 2, the magnetic susceptibility measurements of BaCu_5Al_8 and EuCu_6Al_7 support our treatment of the Ba atoms as closed shell Ba^{+2} cations, and the Eu atoms as Eu^{+2} (f^7) cations, well isolated from each other (see Figures 2.3 and 2.4). (Note: In these calculations, since no specific orbitals were included for the Ba atoms, it is more accurate to describe ' BaCu_5Al_8 ' as ${}^3[\text{Cu}_5\text{Al}_8]^{2-}$. For simplicity, however, BaCu_5Al_8 will be used.)

Each calculation considered the precise electron count for the composition ($\text{BaCu}_5\text{Al}_8 = 81e^-$, $\text{Cu}:11(d^{10}s^1)$, $\text{Al}:3$, $\text{Ba}:2$) as well as one fewer electron and one extra

electron per formula unit for comparison. In each calculation, overlap populations and Mulliken populations were used to help examine the bonding and atom distribution within the icosahedral framework. Densities of states (DOS) and crystal orbital overlap population (COOP) curves were determined by summing over a set of k-points (usually 40-60 k-points in the irreducible wedge of the first Brillouin zone). The parameters of the atomic orbitals used in the calculations are given in Table 3.1.

Table 3.1: The atomic orbital parameters for the extended Hückel calculations.^[27]

Element	Atomic Orbital	H_{ii} (eV)	ζ_1	C_1	ζ_2	C_2
Cu	4s	-11.40	2.20			
	4p	-6.06	2.20			
	3d	-14.00	5.95	0.5933	2.30	0.5744
Cu (Charge Iterated Parameters) ^[52]						
	4s	-8.45	2.20			
	4p	-2.98	2.20			
	3d	-10.94	5.95	0.5933	2.30	0.5744
Al	3s	-12.30	1.37			
	3p	-6.50	1.36			
Y	5s	-8.13	1.74			
	5p	-5.13	1.70			
	4d	-8.32	1.56	0.8213	3.55	0.3003
Y (Charge Iterated Parameters) ^[52]						
	5s	-6.78	1.74			
	5p	-4.28	1.70			
	4d	-6.50	1.56	0.8213	3.55	0.3003

Electronic Structure Calculations of $BaCu_xAl_{13-x}$

Coloring Calculations

The X-ray experiment indicated no ordering of the copper and aluminum atoms within the icosahedral network. The position (96i) is fractionally occupied by 35% Cu and

65% Al, which gives an average composition of Cu_4Al_8 for each icosahedron. The question is, how is this network of interconnected icosahedra 'colored'? Or, how do the copper and aluminum atoms arrange themselves over the 12 icosahedral sites? For example, in the hypothetical compound BaCuAl_{12} , (or ${}^3[\text{CuAl}_{12}]^{2-}$) if we stipulate Cu-centered icosahedra, there is only one 'coloring' of the network, i.e. Cu atoms occupy the centers of the two icosahedra in the primitive cell, and Al atoms occupy all 24 icosahedral positions. If however, the composition is $\text{BaCu}_3\text{Al}_{10}$, there is more than one way to 'color' the icosahedra. There are 10 unique ways to 'color' a single Cu_4Al_8 icosahedron. The primitive unit cell of BaCu_5Al_8 contains two complete Cu-centered icosahedra, and the complete cell contains eight. One can imagine the difficulty this presents in the number of calculations which would be necessary in order to consider all of the possible colorings within a single unit cell. In order to examine the variation in total energy, as a function of different 'colorings', two series of calculations were carried out for the composition, BaCu_5Al_8 , (or ${}^3[\text{Cu}(\text{Cu}_4\text{Al}_8)]^{2-}$).

In the first series of calculations, the total energies of 10 unique 'colorings' of a Cu-centered, Cu_4Al_8 icosahedron ($\text{Cu}[\text{Cu}_4\text{Al}_8]^{2-}$), were compared, (see Figure 3.1). In Figure 3.1, the Cu1 atoms (black circles) occupy the centers of the icosahedra, with the four Cu2 atoms (shaded circles) and eight Al atoms (open circles) arranged around the icosahedra. In each of the calculations there were equal numbers of Cu1 - Cu2 and Cu1 - Al bonds, because all of the icosahedra contained 4 Cu2 and 8 Al atoms. The highest energy 'coloring' (1) has the four Cu2 atoms arranged such that two of them have 3 Cu2 - Cu2 contacts (2: 2.668 Å and 1: 2.845 Å), and the other two Cu2 atoms have 2 Cu2 - Cu2 contacts (2: 2.668Å). In contrast, the lowest energy 'coloring' (10) has the four Cu2 atoms as far from one another as possible. Two of the Cu2 atoms have a single Cu2 - Cu2 contact (1: 2.845 Å), and the other two Cu2 atoms do not have any Cu2 - Cu2 contacts. The difference in total energy between the lowest and highest energy configurations is 0.743 eV. The other 8 'colorings' (2-9) have a variety of different Cu2 - Cu2 contacts.

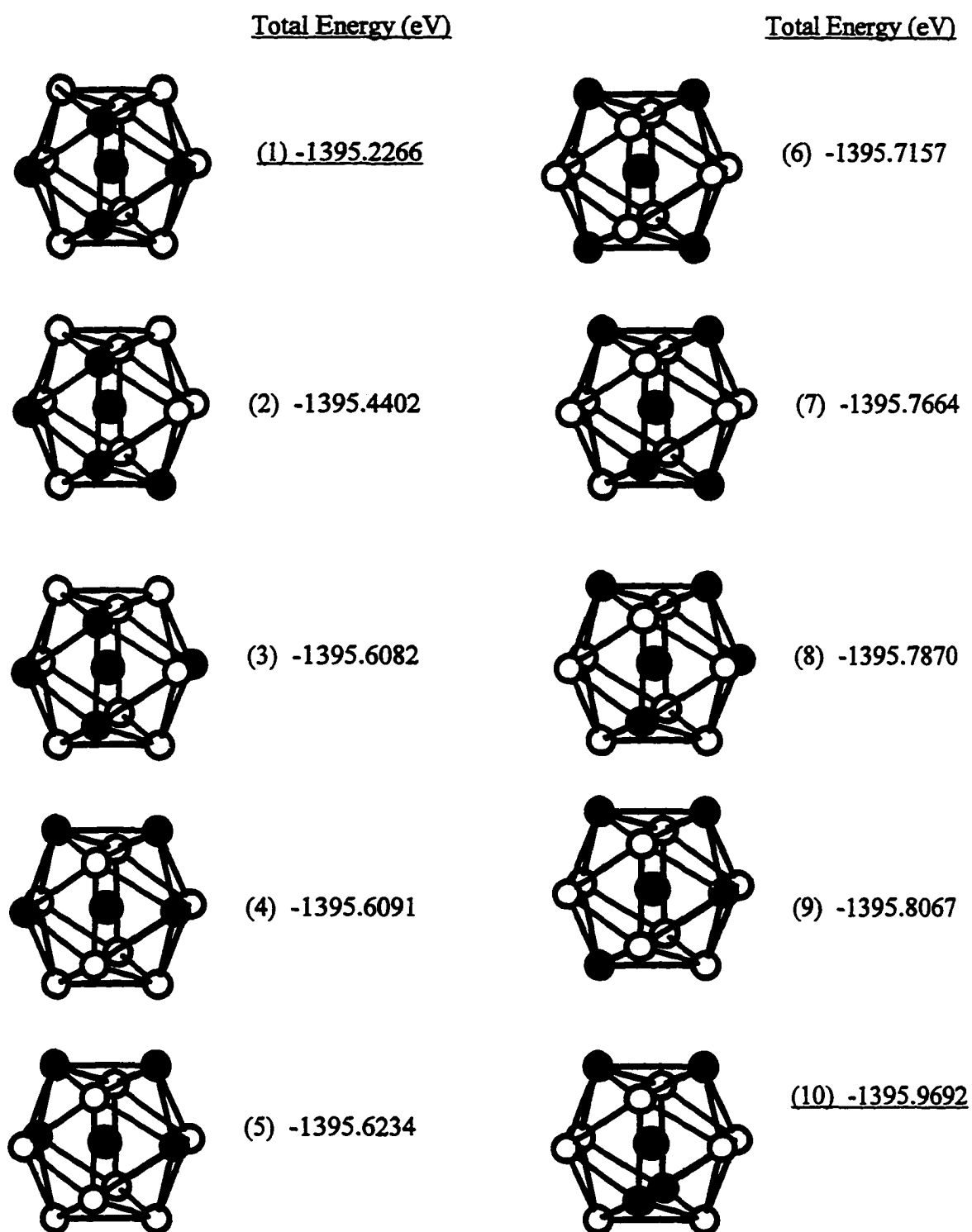


Figure 3.1: The 10 unique ‘colorings’ of a single Cu-centered Cu_4Al_8 icosahedron. The Cu1 and Cu2 atoms are the black circles, and the open circles are the Al atoms. The highest energy configuration (1) has the Cu atoms very close together, and the lowest energy ‘coloring’ (10) has the Cu atoms as far apart as possible.

The primitive unit cell of BaCu_5Al_8 contains two complete Cu1-centered icosahedra (26 atoms), so the second series of calculations was carried out on a variety of 'colorings' of the 24 icosahedral atoms. Figure 3.2 contains the results of calculations on 7 'colorings' of the primitive unit cell of BaCu_5Al_8 , arranged from the highest (1) to the lowest (7) total energy arrangement. In each calculation there are eight Cu1 - Cu2 contacts, and sixteen Cu1 - Al contacts at 2.572 Å. Included in Figure 3.2 are the number of Cu2 - Cu2 contacts within the two icosahedra, for each 'coloring' scheme. There are also Cu2 - Cu2 contacts generated as this primitive cell is extended in three dimensions to neighboring cells, but just considering the Cu2 - Cu2 contacts within the two icosahedra, the fewer the contacts, the lower the total energy. Similar to the results of the calculations with a single icosahedron, the lower energy configurations have Cu2 atoms well separated from each other, and the highest energy 'coloring' (1) has the Cu2 atoms arranged on the stella quadraungula which connect the icosahedra.

From these 'coloring' calculations, it is clear that it is more energetically favorable for the Cu atoms to be well separated from each other. These calculations suggest that the network wants to minimize the number of Cu-Cu interactions, and for this reason, the copper atoms must be spread evenly throughout the network, making the composition of each icosahedron near Cu_4Al_8 . However, the energy differences between colorings 6-10 in Figure 3.1, and colorings 4-7 in Figure 3.2 are small enough to assume that a mixture of several or all of these colorings contributes to the disorder observed in the X-ray diffraction experiment. In chapter 8, BaPd_4Al_9 and SrAu_6Al_6 , two new tetragonal variants of the BaCu_5Al_8 structure will be introduced. Like BaCu_5Al_8 , these are structures containing icosahedra, which are Al-centered in BaPd_4Al_9 , and empty in SrAu_6Al_6 . However, unlike BaCu_5Al_8 , the networks of interconnected icosahedra in BaPd_4Al_9 and SrAu_6Al_6 are not completely disordered. In both compounds some of the icosahedral sites are occupied by only Pd (Au) or Al, and some are mixed. The 'coloring' of the network in BaPd_4Al_9 (see Figure 8.2) most closely resembles coloring (6) in Figure 3.1. The empty ' Au_6Al_6 '

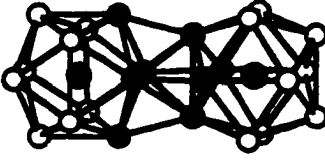
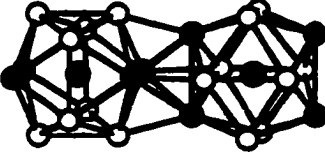
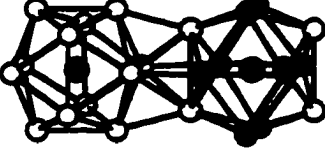
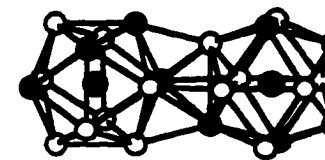
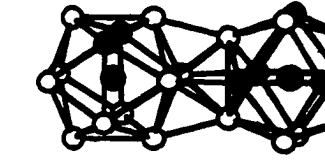
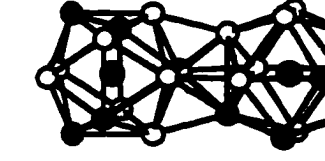
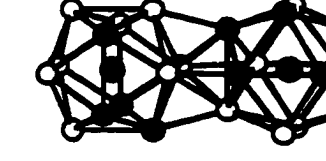
	<u>Total Energy (eV)</u>
	(1) -2105.0488 (highest energy coloring) 17 Cu2 - Cu2 contacts
	(2) -2105.6262 8 Cu2 - Cu2 contacts
	(3) -2106.0835 12 Cu2 - Cu2 contacts
	(4) -2106.1726 6 Cu2 - Cu2 contacts
	(5) -2106.2302 6 Cu2 - Cu2 contacts
	(6) -2106.5238 4 Cu2 - Cu2 contacts
	(7) -2106.5704 (lowest energy coloring) 6 Cu2 - Cu2 contacts

Figure 3.2: Seven 'colorings' of the primitive unit cell of BaCu_5Al_8 arranged from highest energy 'coloring' (1) to lowest energy 'coloring' (7). The calculated total energies, and the number of Cu2 - Cu2 contacts within each arrangement are included.

icosahedra in SrAu_6Al_6 (see Figure 8.4) are colored like numbers (8) and (10) in Figure 3.1, which are two of the lowest energy ‘colorings’.

Phase Width : Theoretical Investigations

Since the single crystal X-ray diffraction experiments indicated no special ordering of the 4Cu and 8Al atoms on the icosahedral (96i) position in BaCu_5Al_8 , we decided to investigate the phase width of this compound using both synthesis and electronic structure calculations. The details of the synthetic efforts to explore the phase width of $\text{BaCu}_x\text{Al}_{13-x}$ ($0 < x < 13$) were discussed in chapter 2, and the results suggest that there is a rather narrow phase width of $\text{BaCu}_x\text{Al}_{13-x}$ where $4 \leq x \leq 6$. In an effort to understand the composition and phase width of this ternary aluminide, electronic structure calculations were performed on a series of compounds with the NaZn_{13} structure in which the Cu : Al ratio was varied from BaCu_{13} , $\text{BaCu}_{12}\text{Al}$, BaCuAl_{12} , BaAl_{13} . Total densities of states, Fermi energies, and crystal orbital overlap populations for the interactions in the icosahedral network were all used to evaluate the electronic structure and stability of these compounds. BaCu_{13} and $\text{BaCu}_x\text{Al}_{13-x}$ ($4 < x < 6$) are known compounds, but the other compounds were merely hypothetical compositions forming the BaCu_5Al_8 structure for the purpose of the calculations. With respect to the earlier discussion of the ‘coloring’ of the network, it is important to mention that the difference in the total energies between two unique ‘colorings’ of BaCu_5Al_8 , is much smaller than the total energy difference between two different compositions (i.e. BaCu_5Al_8 and BaCu_4Al_9). Therefore, in this series of calculations the appropriate number of copper and aluminum atoms were arranged such that a mixture of Cu – Al, Cu – Cu, and Al – Al contacts were generated for the desired composition.

Figure 3.3 contains seven total DOS curves for the compounds BaCu_{13} , BaCu_8Al_5 , BaCu_6Al_7 , BaCu_5Al_8 , BaCu_4Al_9 , $\text{BaCu}_3\text{Al}_{10}$ and BaCuAl_{12} , with the Fermi energies represented by the dashed line. The DOS curves all have a large peak corresponding to the Cu d-orbitals between -15.0 and -13.0 eV, which narrows as the Cu concentration

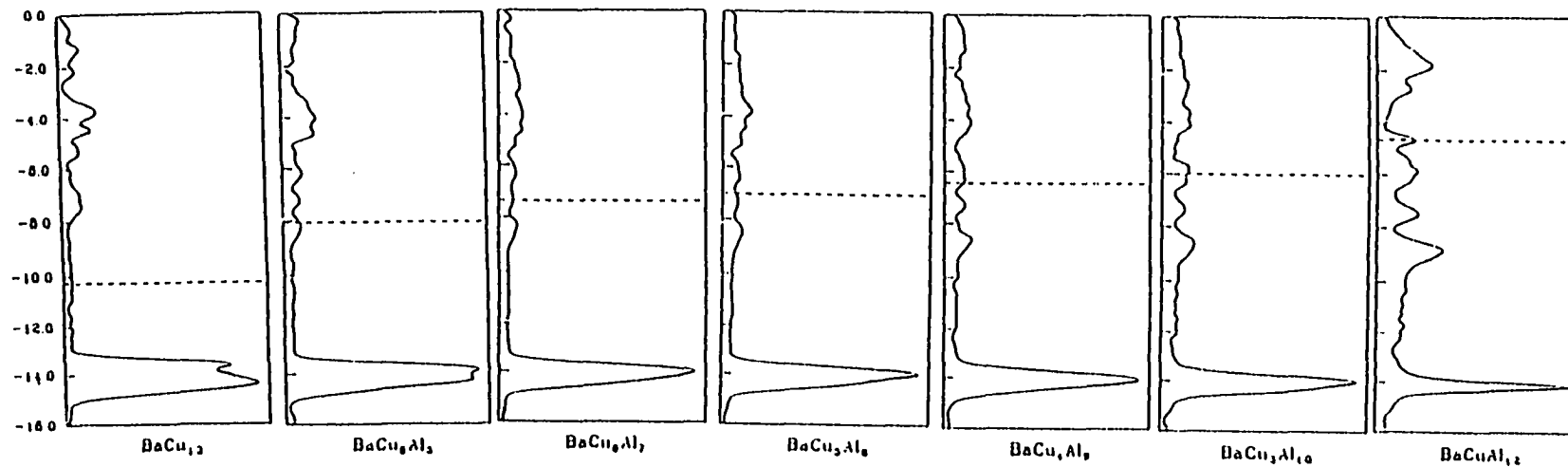


Figure 3.3: The DOS curves for the series of $\text{BaCu}_x\text{Al}_{13-x}$ compounds with the Fermi energies marked with the dotted lines. The curves are plotted as the density of states vs. energy (eV). Notice the Fermi energies increase, and the Cu d-orbital peak at -14.0 eV narrows, as the Al content increases.

decreases. Above this peak, the DOS is dispersed and rather featureless in all of the curves except BaCuAl_{12} . In the BaCuAl_{12} DOS curve, several peaks begin to appear between -9.0 and -4.0 eV, which correspond to areas of high concentration of molecular orbitals in the MO diagram of a single Cu-centered Al_{12} icosahedron, see Figure 3.4.

Table 3.2 contains the Fermi energies, and the overlap populations for the combined interactions between the Cu1 atoms and the Cu2/Al atoms at 2.572 Å. In Table 3.2, the largest overlap population occurs for BaCu_5Al_8 , and gradually gets smaller for both aluminum-rich and copper-rich systems. Figure 3.5 contains the COOP curves for all the interactions between the framework atoms in BaCu_5Al_8 , with the Fermi energy highlighted with the dotted line at -7.03 eV. Figure 3.6 contains the COOP curves for the 2 interactions (1) Cu1 - Al/Cu2 (2.572 Å), and Cu2/Al - Cu2/Al (combination of all interactions 2.637Å, 2.668Å, 2.711Å, 2.845Å). In many of the COOP curves in Figure 3.5, and in both COOP curves in Figure 3.6, the Fermi energy crosses at the point where the overlap character changes from bonding to antibonding, demonstrating the ideal situation that the $[\text{Cu}_5\text{Al}_8]^{2-}$ stoichiometry represents.

Table 3.2: A summary of the extended Hückel results on the series $\text{BaCu}_x\text{Al}_{13-x}$.

Stoichiometry	Fermi Energy (eV)	COOP
		Central Cu1 - Cu2/Al
BaCu_{13}	-10.62	0.0739
BaCu_8Al_5	-8.06	0.1239
BaCu_6Al_7	-7.33	0.1348
<u>BaCu_5Al_8</u>	<u>-7.03</u>	<u>0.1373</u>
BaCu_4Al_9	-6.45	0.1303
$\text{BaCu}_3\text{Al}_{10}$	-6.00	0.1285
BaCuAl_{12}	-4.65	0.1159
BaAl_{13}	-4.35	-

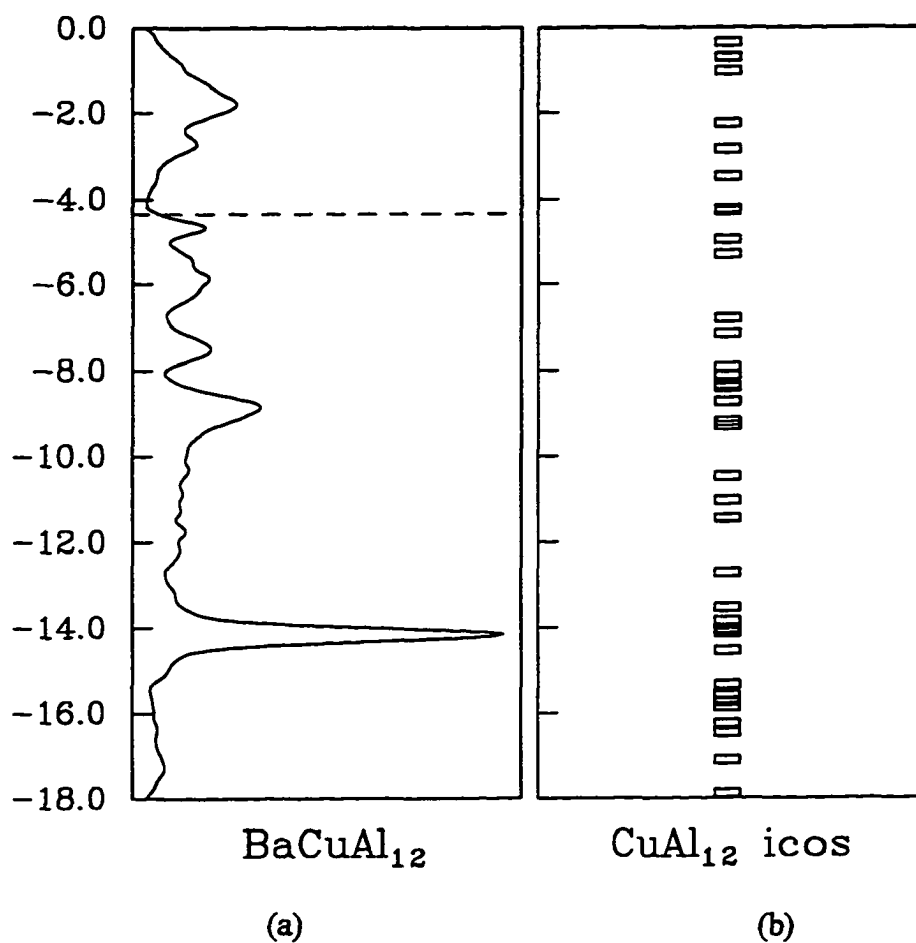


Figure 3.4: (a) The DOS curve for BaCuAl₁₂ with the Fermi energy marked with the dotted line at -4.65eV. The features in this curve resemble the high densities of molecular orbitals in (b), the molecular orbital diagram of a single Cu-centered 'CuAl₁₂' icosahedron.

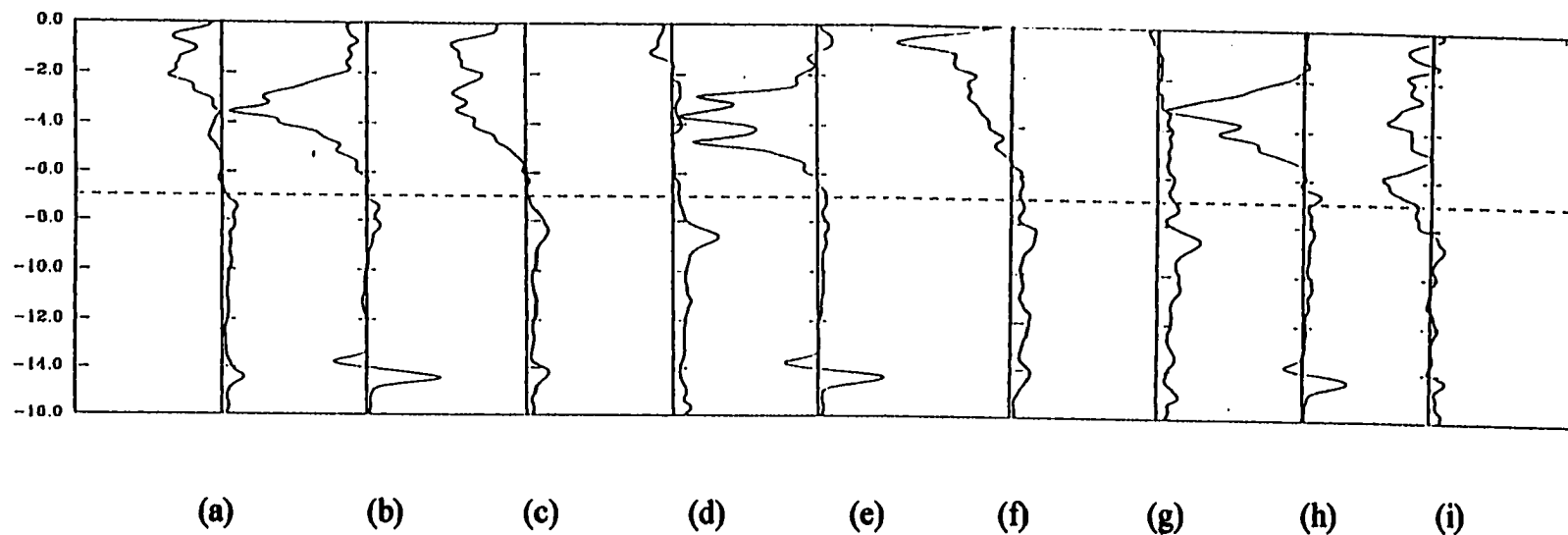


Figure 3.5: All the COOP curves for the copper-aluminum framework interactions in BaCu_5Al_8 . (a) Cu1 - Al, 2.572 Å, (b) Cu1 - Cu2, 2.572 Å, (c) Cu2 - Al, 2.668 Å, (d) Al - Al, 2.668 Å and 2.711 Å, (e) Cu2 - Cu2, 2.668 Å, (f) Cu2 - Al, 2.637 Å, (g) Al - Al, 2.637 Å, (h) Cu2 - Cu2, 2.637 Å, (i) Cu2 - Cu2, Al - Al, Cu2 - Al, 2.845 Å.

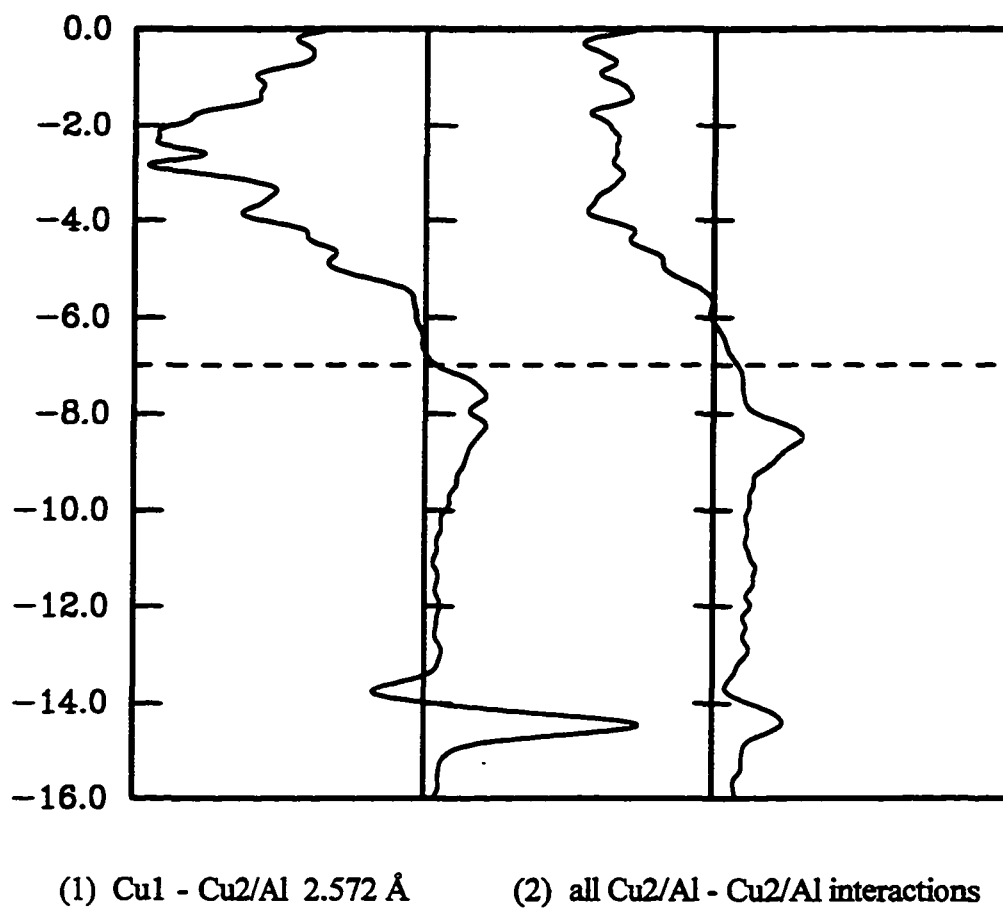


Figure 3.6: The COOP curves for the (1) central to surface Cu1 - Au2/Al interaction in the icosahedra (2.572 Å), and (2) a combination of all the 'surface - surface', Cu2/Al - Cu2/Al interactions, in BaCu₅Al₃. The Fermi energy of -7.03 eV is marked with a dotted line.

When the composition is Cu rich (BaCu_{13} $E_f = -10.62$ eV), the Fermi energy falls well below this crossover, leaving many bonding interactions unfilled. In the case of Al rich ternaries, (BaCuAl_{12} $E_f = -4.65$ eV) the Fermi energy falls above the crossover and many antibonding states are filled. For the three compounds BaCu_4Al_9 , BaCu_5Al_8 and BaCu_6Al_7 , the Fermi energy falls near this crossover, meaning that for these three compounds the electron count is such that the bonding within the Cu-Al framework is maximized, which correlates well with the synthesis of single phase products.

Electronic Structure Calculations of $\text{YCu}_x\text{Al}_{12-x}$ (ThMn_{12} structure)

Many rare earth ternary aluminides form the ThMn_{12} structure, whose similarity in composition and phase width to the alkaline earth and rare earth ternary aluminides which form the NaZn_{13} structure is striking. Table 3.3 includes a list of compounds which form both structure types, and the *vec*'s for each compound. Figure 3.7 is a structure map of ternary aluminides forming the NaZn_{13} and ThMn_{12} structures. The volume per formula unit of the compounds which form the NaZn_{13} is greater than the volume per formula unit of the compounds adopting the ThMn_{12} structure.

Table 3.3: A list of compounds which form either the NaZn_{13} or ThMn_{12} structure. The *vec* is also listed for each compound.

compound	structure	<i>vec</i> / network atom	reference
BaCu_5Al_8	NaZn_{13}	2.38	chapter 2
SrCu_6Al_7	NaZn_{13}	2.23	chapter 2
$\text{CaCu}_{6.5}\text{Al}_{6.5}$	NaZn_{13}	2.15	[34]
$\text{BaAg}_{5.5}\text{Al}_{7.5}$	NaZn_{13}	2.31	chapter 2
LaCu_6Al_7	NaZn_{13}	2.31	[40]
$\text{EuCu}_{6.5}\text{Al}_{6.5}$	NaZn_{13}	2.15	chapter 2
$\text{LnCu}_x\text{Al}_{12-x}$ ($4 < x < 6$)	ThMn_{12}	2.25 - 2.58	[31]
(Ln = Ce, Pr, Nd, Sm, Eu*, Gd, Tb, Dy, Ho, Er, Tm, Yb, Lu, Y)			
LnM_4Al_8	ThMn_{12}	1 - 1.5	[31]
(M = Cr, Mn, Fe: Ln = La*, Ce, Pr*, Nd, Sm, Gd, Tb, Dy, Ho*, Er, Tm, Yb*, Lu, Y)			

* indicated some impurities were present in the products

NaZn₁₃ vs. ThMn₁₂ Structure Map

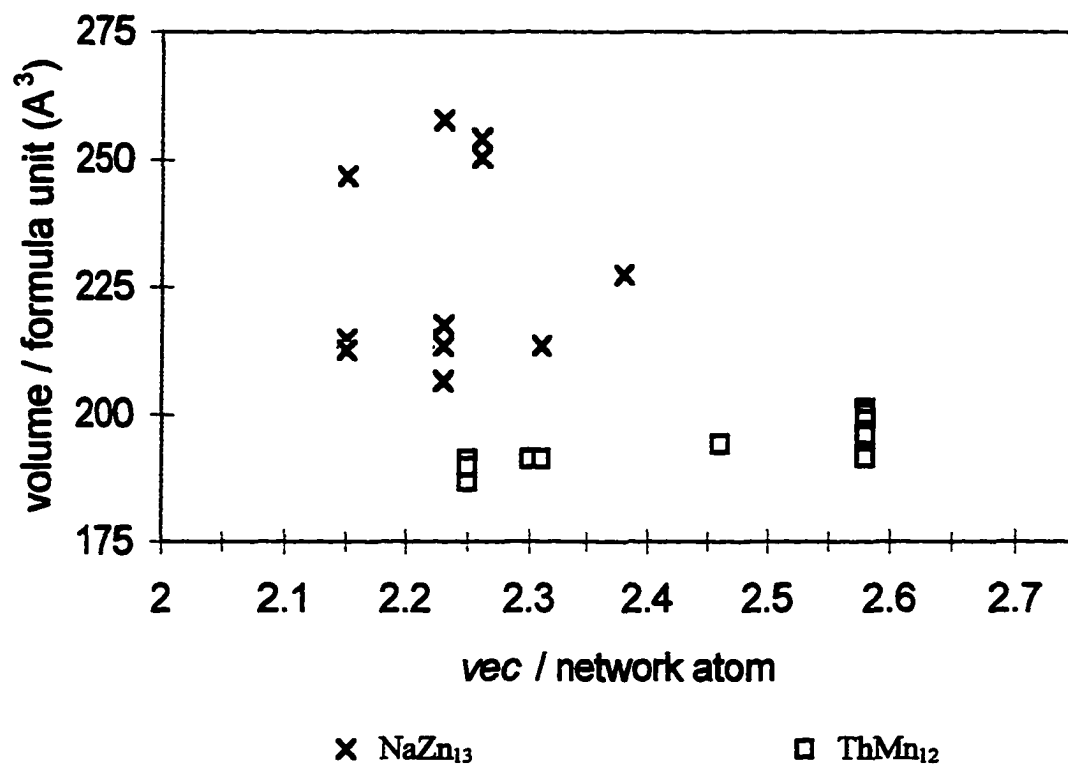


Figure 3.7: A structure map separating ternary aluminides forming the NaZn₁₃ and ThMn₁₂ structures by *vec* / network atom versus volume per formula unit (Å³). The open squares are the aluminides which adopt the ThMn₁₂ structure, while the x's are the aluminides which form the NaZn₁₃ structure. The aluminides which form the NaZn₁₃ structure have a larger volume per formula unit than those compounds forming the ThMn₁₂ structure.

While the similarity in composition between the LnCu_4Al_8 phases and the AeCu_5Al_8 ($\text{Ae} = \text{Ba}, \text{Sr}, \text{Eu}, \text{La}$) phases is noteworthy, it may seem strange however that lanthanum has not been reported to form $\text{LaCu}_x\text{Al}_{12-x}$ ($4 \leq x \leq 6$), with the ThMn_{12} structure. In my experimental investigations of the $\text{La} - \text{Cu} - \text{Al}$ system, I have never observed the formation of the ThMn_{12} structure, rather, I have only observed $\text{LaCu}_x\text{Al}_{13-x}$ ($x = 5 - 6$) which form the NaZn_{13} structure. The challenge presented by these synthetic observations, was to understand the driving forces behind the formation of either of these structures, for compounds which seem so similar. The results of various electronic structure calculations on BaCu_5Al_8 were presented earlier in this chapter. Since this careful examination of the $\text{BaCu}_x\text{Al}_{13-x}$ compounds yielded some valuable insights into the ‘coloring’ of the network, and the balance between the Fermi energies and the overlap populations which maximizes the bonding within the network, similar calculations were performed on the $\text{LnCu}_x\text{Al}_{12-x}$ ($1 < x < 11$) compounds forming the ThMn_{12} structure. Despite their similarities in composition, the LnCu_4Al_8 (ThMn_{12}) structure is very different from the BaCu_5Al_8 (NaZn_{13}) structure, and as a starting point, a discussion of the LnCu_4Al_8 structure is necessary. (Note: In the following discussion of the crystal structure and electronic structure, the representative compound YCu_4Al_8 will be used because Y atomic orbital parameters are included in some of the later calculations. However, because the reported lattice parameters and positional parameters for YCu_4Al_8 are from powder data, the refined parameters from a single crystal solution of HoCu_5Al_7 are used during the discussion of the structure and for the extended Hückel calculations. Since the parameters of HoCu_5Al_7 are very similar to those reported for YCu_4Al_8 , this is not at all unreasonable. As confirmation of this, calculations on ${}^3[\text{Cu}_4\text{Al}_8]^{3-}$ using the two slightly different geometries (as reported YCu_4Al_8 and as refined HoCu_5Al_7) were carried out, and the results were nearly identical.)

YCu_4Al_8 Structure Description

Unlike BaCu_5Al_8 , in which the network of Cu-centered icosahedra does not exhibit a detectable ordering of the 4 copper and 8 aluminum atoms, the network that surrounds the

Y atoms in YCu_4Al_8 is an ordered arrangement of copper and aluminum atoms. In YCu_4Al_8 (YCu_5Al_7 and YCu_6Al_6 are isostructural and will be discussed later) there are three atomic positions each of multiplicity 8 (8f, 8i, and 8j) which form the network surrounding the Y atoms, see Table 3.4.

Table 3.4: The positional parameters for YCu_4Al_8 , forming the ThMn_{12} structure type.

YCu_4Al_8 $I4/mmm$ (No. 139)

$$a = 8.705 (1) \text{ \AA}$$

$$c = 5.128 (1) \text{ \AA}$$

Atom	site sym	x	y	z	occ.
Y	2a	0	0	0	1.0
Cu	8f	0.25	0.25	0.25	1.0
Al1	8i	0.346(4)	0	0	1.0
Al2	8j	0.281(3)	0.5	0	1.0

In YCu_4Al_8 copper atoms occupy position 8f, and aluminum occupies positions 8i and 8j, see Figure 3.8, in which the large open circles are the Y atoms, the dark gray circles are the Cu atoms (8f), the light gray circles are Al1 atoms (8i), and the small open circles are Al2 atoms (8j). For a complete list of the bond distances within the YCu_4Al_8 structure, see Table 3.5. In YCu_4Al_8 , the Y atoms are surrounded by 20-vertex polyhedra composed of 8 Cu atoms (Y - Cu = 3.349Å), 4 Al1 atoms (Y - Al1 = 3.018Å), and 8 Al2 atoms (Y - Al2 = 3.200Å), see Figure 3.9 (a). The symmetry of the Y position (2a) is $4/mmm$ (D_{4h}). The YCu_4Al_8 structure contains chains of Cu-atoms running in the c -direction with a Cu-Cu distance of 2.564 Å. Each Cu atom is surrounded by a 12 vertex polyhedron, composed of 2 Y atoms, 2 Cu atoms, and 8 Al atoms (4:Al1 and 4:Al2), see Figure 3.9 (b). The Al1 atoms form pair-like units which sit inside 20-vertex polyhedra, see Figure 3.9 (c). Alternately, the pairs of Al1 atoms are arranged such that they form chains of edge sharing tetrahedra running in the c -direction, see Figure 3.8, with the pair-like Al1-Al1 contacts highlighted with thicker bonds. The Al2 atoms are surrounded by irregular polyhedra of 10 atoms: 2 Y, 4 Cu, 2 Al1 and 2 Al2 atoms, see Figure 3.9 (d).

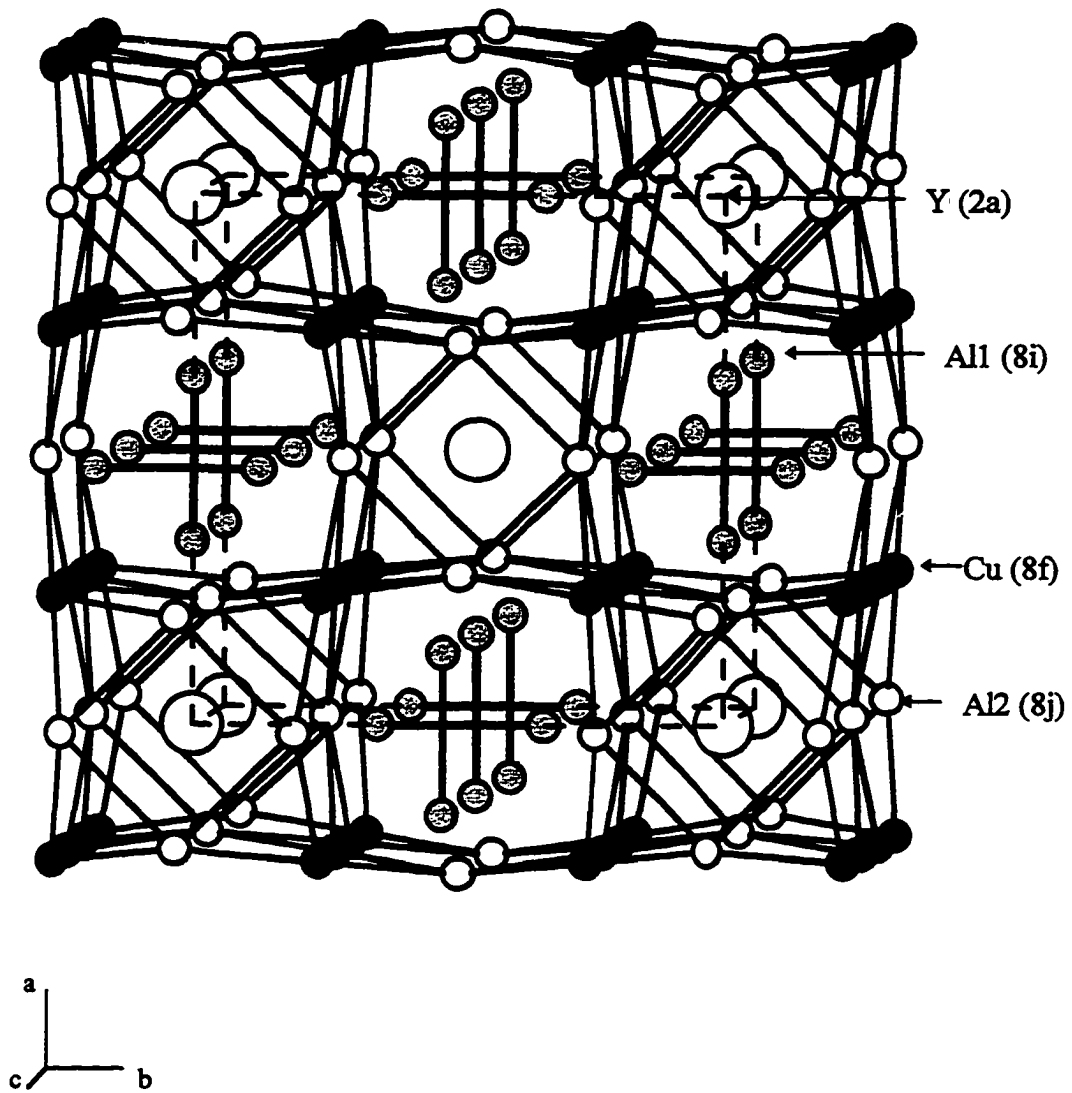
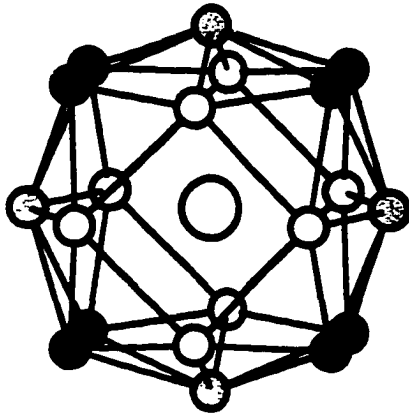


Figure 3.8: The YCu_4Al_8 structure with Y atoms (large open circles), Cu atoms (8f: dark gray circles), Al1 atoms (8i: light gray circles) and Al2 atoms (8j: small open circles). For the compound YCu_4Al_8 , the distances within the framework are listed in Table 3.5.

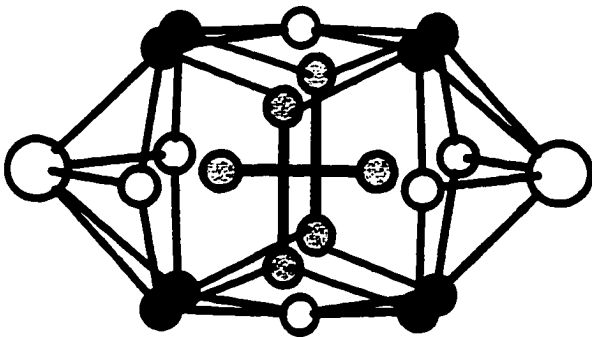


(a) the 20-vertex polyhedron around Y

Y - Cu 3.340 Å (x8)

Y - Al1 3.017 Å (x4)

Y - Al2 3.202 Å (x8)

site symmetry of Y = $4/m\bar{3}m$ (D_{4h})

(b) the 20-vertex polyhedron around the Al1 - Al1 pairs (2.686 Å)

Al1 - Cu 2.665 Å (x4)

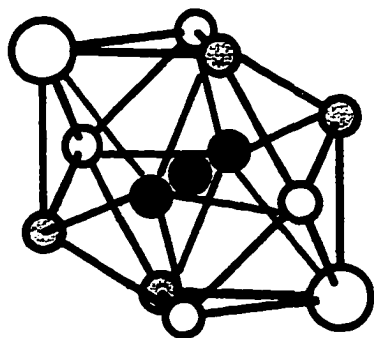
Al1 - Al2 2.798 Å (x2)

Al1 - Al2 2.794 Å (x2)

Al1 - Al1 2.686 Å (x1)

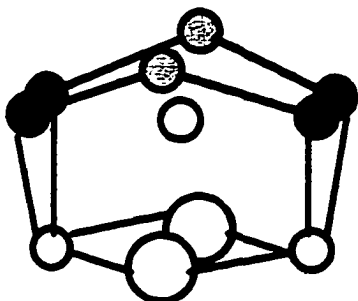
Al1 - Al1 3.195 Å (x4)

Figure 3.9: (a) and (b) The coordination polyhedra around the Y atoms (a) and the Al1 - Al1 'pairs' (b). Distances from the central atoms to the neighboring atoms are given beside each picture. The large open circles are Y atoms, the small open circles are Al2 atoms, the small dark gray circles are Cu, and the small light gray circles are Al1 atoms.



(c) the 12-vertex polyhedron around Cu

Cu - Cu 2.570 Å (x2)
 Cu - Al1 2.665 Å (x4)
 Cu - Al2 2.545 Å (x4)
 Cu - Y 3.349 Å (x2)



(d) the 10-vertex polyhedron around Al2

Al2 - Al1 2.798 Å (x2)
 Al2 - Al1 2.794 Å (x2)
 Al2 - Cu 2.545 Å (x4)
 Al2 - Al2 2.701 Å (x2)
 Al2 - Y 3.200 Å (x2)

Figure 3.9: (c) and (d) The coordination polyhedra around the Cu atoms (c) and the Al2 atoms (d). The distances from the central atom to its neighbors are given beside each picture. The large open circles are Y atoms, the small open circles are Al2 atoms, the small dark gray circles are Cu, and the small light gray circles are Al1 atoms.

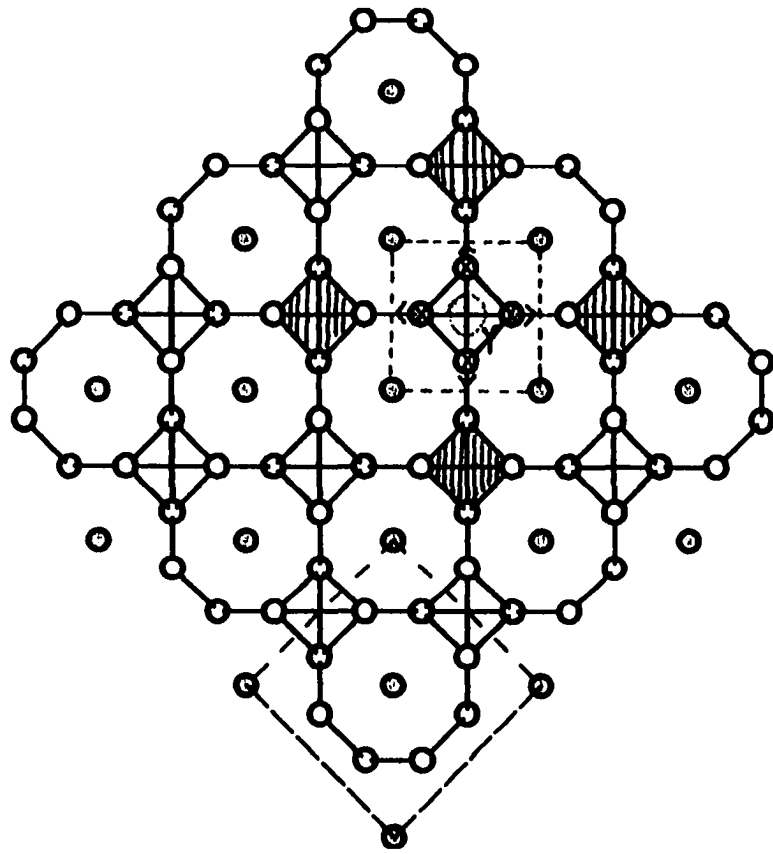
Table 3.5: Distances between the atoms in YCu_4Al_8 , see Figure 3.8.

Atom1	Atom2	distance Å
Y	Cu	3.349(4)
	Al1	3.018(4)
	Al2	3.200(2)
Cu	Al1	2.663(1)
	Al2	2.539(1)
	Cu	2.564(1)
Al1	Al1	2.668(7)
	Al2	2.792(2)
	Al2	2.779(2)
Al2	Al2	2.708(4)

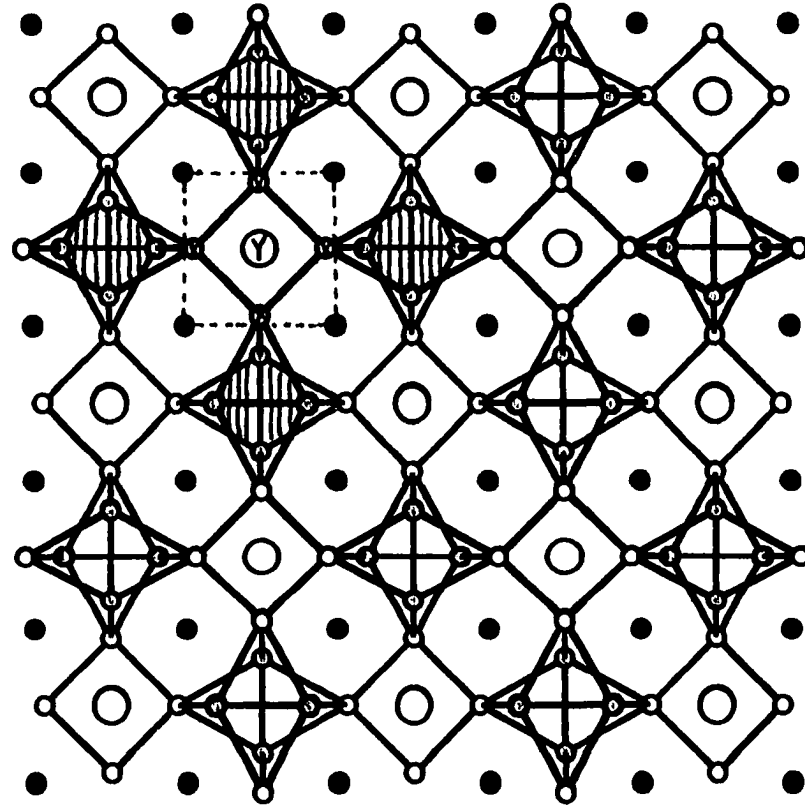
The ' Cu_4Al_8 ' framework in YCu_4Al_8 has the composition $CuAl_2$, and in fact, bears a close resemblance to the $CuAl_2$ structure itself.^[5] One way to view the YCu_4Al_8 structure is a ' $CuAl_2$ - like' structural framework which has been 'interrupted' by the addition of the Y atoms. Figure 3.10 (a) is the $CuAl_2$ structure containing a highlighted region which contains small arrows to designate the atoms that shift slightly in order to open the space in the framework for the Y atoms. A similar area is highlighted in the YCu_4Al_8 network of Figure 3.10 (b).

Extended Hückel Calculations on YCu_4Al_8

The $LnCu_xAl_{12-x}$ compounds form the $ThMn_{12}$ structure between $x = 4$ and 6 ($vec = 2.25 - 2.58$). The ordering of Cu and Al atoms in YCu_4Al_8 was discussed in detail in the previous section, and in YCu_5Al_7 and YCu_6Al_6 , the positions 8f and 8i are fully occupied by copper and aluminum respectively, and 8j is occupied by both copper and aluminum atoms. The calculations of YCu_xAl_{12-x} were broken into two groups; (1) the ordering of copper and aluminum atoms within the ${}^3[Cu_4Al_8]^{3-}$ network, and (2) the investigation of the phase width of YCu_xAl_{12-x} ($0 < x < 12$).



(a)



(b)

Figure 3.10: (a) The CuAl_2 structure with Cu atoms the gray circles, and Al atoms the open circles, is related to (b) YCu_4Al_8 , by the highlighted sections. In YCu_4Al_8 (b), the dark gray circles are the Cu atoms, and the light gray and open circles are the Al1 and Al2 atoms respectively.

The Y - Cu, Y - Al1, and Y - Al2 distances of 3.349 Å, 3.018 Å, and 3.200 Å respectively, are shorter than the Ba - Cu2/Al2 distance of 3.576 Å in BaCu₅Al₈. But to maintain consistency between the two series of calculations, the Y atoms were initially treated as classical cations which donate 3 valence electrons to the metallic framework and no specific orbitals were included in the calculations. This is an appropriate time to point out however, that the electropositive metal atoms should not be ruled out as an important factor contributing to the formation of the different structures. Therefore, in several of the calculations, specific orbitals were included for the Y atoms.

The Ordering of Copper and Aluminum in YCu₄Al₈

The first calculations performed on the YCu₄Al₈ structure considered the all aluminum or all copper networks; ${}^3_{\infty}[\text{Al}_{12}]^{n-}$ and ${}^3_{\infty}[\text{Cu}_{12}]^{n-}$. Using Mulliken populations for the ${}^3_{\infty}[\text{Al}_{12}]^{n-}$ and ${}^3_{\infty}[\text{Cu}_{12}]^{n-}$ frameworks (with various electron counts appropriate for a ${}^3_{\infty}[\text{Cu}_4\text{Al}_8]^{n-}$ network) as guides for the atomic ordering in the ternary compound, the positions with the largest Mulliken populations would be the positions most likely occupied by the atoms with the largest electronegativity.^[53] The first three columns in Table 3.6 contain the Mulliken populations of the 3 positions (8f, 8i, 8j) for each different electron count. There are differences between the Mulliken populations for the 3 sites for the Cu and Al atoms, but the results are not consistent. In the ${}^3_{\infty}[\text{Al}_{12}]^{n-}$ network, each of the three sites has the higher Mulliken population for a different electron count. And in the ${}^3_{\infty}[\text{Cu}_{12}]^{n-}$ framework, the position 8i has the higher Mulliken population at all three electron counts. With the electronegativities of Cu and Al of 1.74 and 1.54 respectively,^[47] the Mulliken populations indicate that Cu atoms should occupy position 8i, which is *not* observed. The second group of Mulliken populations reported in Table 3.6 are those for the same ${}^3_{\infty}[\text{Al}_{12}]^{n-}$ and ${}^3_{\infty}[\text{Cu}_{12}]^{n-}$ frameworks *including* Y atomic orbitals. The results are very similar for both sets of calculations. In Figure 3.11 the Mulliken populations for the three sites (8f, 8i, 8j) are plotted versus various electron counts from 15 to 39 electrons, with and

without Y atomic orbitals included. For the lowest 3 electron counts (15, 18, 22), the arrangement of the atoms based on the Mulliken populations does reflect the observed structure (with Cu on 8f). However, as the electron count increases, the Mulliken populations on positions 8i and 8j are greater than 8f, which is *not* the observed arrangement of atoms.

Without a clear indication of the ordering preference from the Mulliken populations, calculations on YCu_4Al_8 were carried out with different arrangements of the four copper and eight aluminum atoms. Table 3.7 summarizes the results of three calculations in which the four copper atoms occupied each of the 3 (8f, 8i, 8j) positions. The configuration in which the copper atoms occupy the 8i site had the lowest total energy, however, this position is occupied exclusively by Al atoms in the observed structure. In fact, of the three configurations, the observed arrangement of copper and aluminum atoms (Cu:8f and Al:8i, 8j) had the highest total energy.

Table 3.6: The Mulliken populations for the three atomic positions in YCu_4Al_8 for homoatomic calculations on ${}^3[Al_{12}]^{3-}$ and ${}^3[Cu_{12}]^{3-}$ frameworks at various electron counts. For ${}^3[Al_{12}]^{3-}$, the Cu atoms had 1 electron, and the Al atoms had 3. For ${}^3[Cu_{12}]^{3-}$, the Cu atoms had 11 electrons and the Al atoms had 13. The three electron counts considered for each framework correspond to the following three configurations; ${}^3[Cu_{12}]^{3-}$, ${}^3[Cu_4Al_8]^{3-}$, and ${}^3[Al_{12}]^{3-}$.

		<u>Mulliken Populations *</u>					
		Populations without Y			Populations with Y		
electron counts		8f	8i	8j	8f	8i	8j
<u>${}^3[Al_{12}]^{3-}$</u>	$1(12) + 3 = 15$	<u>1.300</u>	1.188	1.267	<u>1.269</u>	1.178	1.241
	$4 + 3(8) + 3 = 31$	2.537	2.562	<u>2.655</u>	2.295	2.369	<u>2.400</u>
	$3(12) + 3 = 39$	3.090	<u>3.413</u>	3.252	2.643	<u>2.871</u>	2.765
<u>${}^3[Cu_{12}]^{3-}$</u>	$11(12) + 3 = 135$	11.172	<u>11.348</u>	11.234	11.087	<u>11.266</u>	11.141
	$11(4) + 13(8) + 3 = 151$	12.440	<u>12.738</u>	12.572	12.192	<u>12.479</u>	12.313
	$13(12) + 3 = 159$	12.966	<u>13.416</u>	13.369	12.665	<u>13.032</u>	12.952

* the underlined population is the highest in each calculation

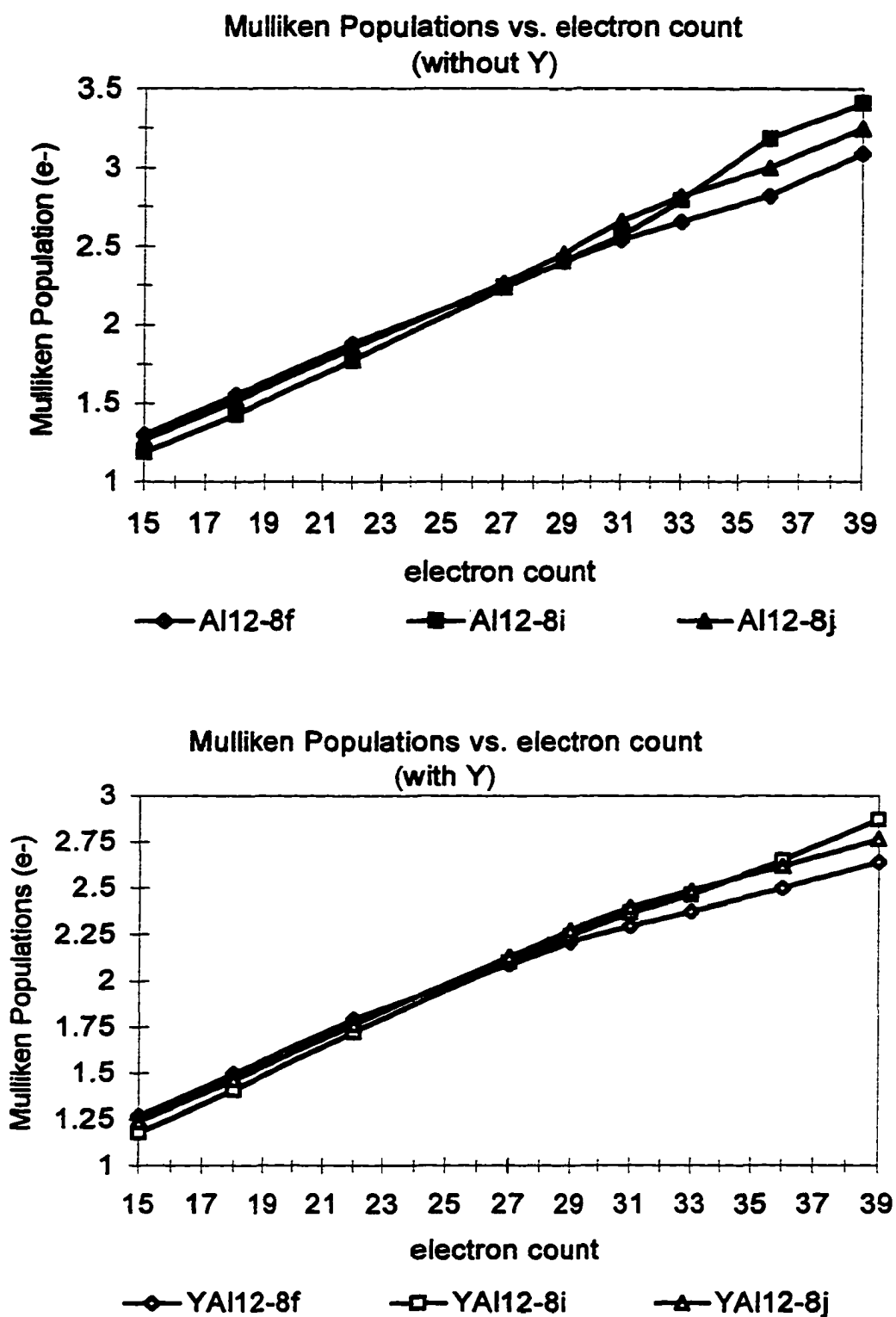


Figure 3.11: The Mulliken populations for the 3 positions in 'YAl₁₂' (8f, 8i, 8j), plotted versus various electron counts, for calculations with and without Y atomic orbitals included.

Table 3.7: The calculated total energies (eV/formula unit) and Fermi energies of the three ${}^3[\text{Cu}_4\text{Al}_8]^{3-}$ structures in which the 4 Cu atoms occupy the each of the 3 positions (8f, 8i, 8j). Each of the three calculations had the same number of Cu and Al atoms, and the same number of electrons (71e⁻).

site with the four Cu atoms	calculated total energy (eV)	calculated Fermi energy (eV)
8f*	-902.164	-6.123
8i	-903.925	-6.513
8j	-902.412	-6.202

* the observed 'coloring' of Cu atoms

The results of these calculations did not give a clear indication of the electronic driving force for the ordering of the copper and aluminum atoms within the framework. However, we decided to reconsider the initial assumption that the rare earth atoms are simply electron donors to the framework, whose orbital interactions with the atoms in the framework could be neglected.

The symmetry of the Y position (2a: 0,0,0) is $4/mmm$ (D_{4h}) and the arrangement of the 8 copper and 12 aluminum atoms around the Y atom in YCu_4Al_8 is shown in Figure 3.12. There are three sets of atoms surrounding Y: 8 Cu (8f) atoms at 3.349 Å, 4 Al1 (8i) atoms at 3.018 Å, and 8 Al2 (8j) atoms at 3.200 Å. We carried out three calculations in which the Y atomic orbitals (s, p and d) were included sequentially. Table 3.8 summarizes the results of including Y orbitals, (a) just s, (b) s and p, and (c) s, p and d orbitals. Listed in Table 3.8 are the Mulliken populations for each atomic orbital on each atom in the primitive unit cell. For the four Al1 (8i) atoms with the short Y - Al1 distance of 3.018 Å, the Mulliken populations of the p_x and p_y orbitals are underlined. The greater Mulliken populations on these orbitals (p_x and p_y) is evidence of a strong interaction between the Y and Al1 atoms. Not only is there not a similar enhancement of any particular orbitals on the Cu or Al2 atoms, but with Cu atoms on the 8i positions, this stabilizing interaction is not observed. The overlap population (type 1: Y - Al) for this bond increases from 0.0341 to

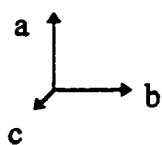
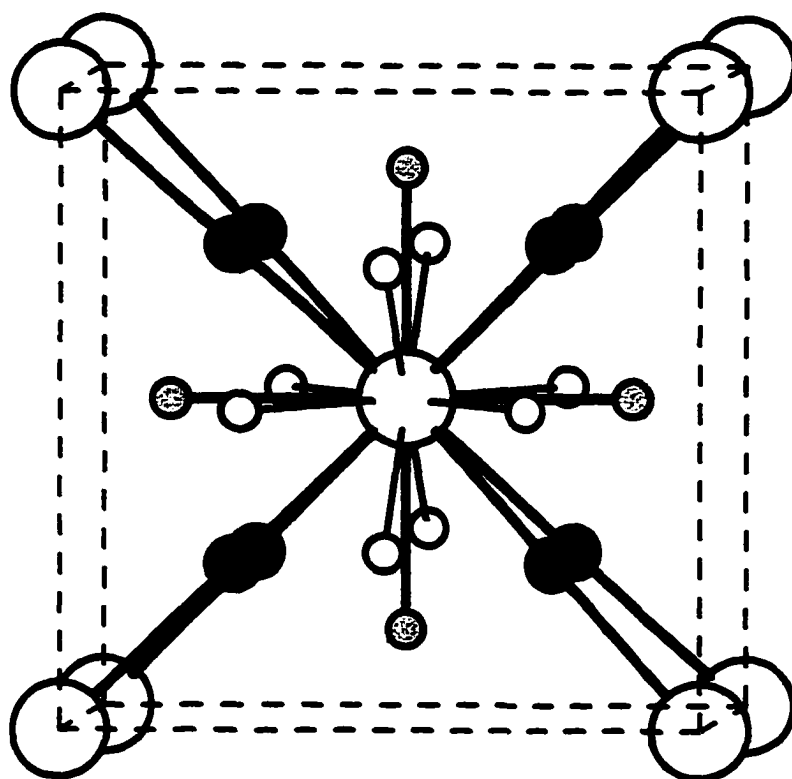


Figure 3.12: The coordination geometry around Y in YCu_4Al_8 . The Y atoms (large open circles) are surrounded by a pseudo-cube of 8 Cu atoms (dark gray circles) at a distance of 3.349 Å, 4 Al1 atoms (light gray circles) with the shortest distance of 3.018 Å, and 8 Al2 atoms (small open circles) at a distance of 3.200 Å.

Table 3.8: Calculation results with Y atomic orbitals included.

(a) Calculation results with the inclusion of the Y s-orbital only.

Number of Electrons: 71.00 Total Energy: -902.8429 eV
 Fermi Energy: -6.1606 eV

Atom	Total	s	x	y	z	x^2-y^2	z^2	xy	xz	yz
Y	0.271	0.271								
8f Cu	12.366	1.080	0.534	0.444	0.414	1.967	1.980	1.990	1.978	1.978
8f Cu	12.536	1.081	0.537	0.603	0.421	1.969	1.980	1.987	1.979	1.978
8f Cu	12.483	1.109	0.524	0.542	0.415	1.967	1.979	1.989	1.979	1.978
8f Cu	12.437	1.087	0.543	0.503	0.410	1.967	1.980	1.991	1.978	1.979
8i Al1	2.567	1.066	<u>0.612</u>	0.478	0.411					
8i Al1	2.567	1.066	<u>0.612</u>	0.478	0.411					
8i Al1	2.562	1.079	0.441	<u>0.629</u>	0.413					
8i Al1	2.562	1.079	0.441	<u>0.629</u>	0.413					
8j Al2	2.673	1.033	0.557	0.496	0.587					
8j Al2	2.673	1.033	0.557	0.496	0.587					
8j Al2	2.661	1.048	0.461	0.562	0.591					
8j Al2	2.661	1.048	0.461	0.562	0.591					

Bond Type	Distance	Overlap Population
1 Al1 Y	3.021 Å	<u>0.0341</u>
2 Cu Y	3.349 Å	0.0043
3 Al2 Y	3.195 Å	0.0115

(b) Calculation results with the inclusion of the Y s and p orbitals.

Number of Electrons: 71.00 Total Energy: -903.5266 eV
 Fermi Energy: -6.1938 eV

Atom	Total	s	x	y	z	x^2-y^2	z^2	xy	xz	yz
Y	0.545	0.274	<u>0.105</u>	<u>0.109</u>	0.057					
8f Cu	12.350	1.096	0.523	0.425	0.416	1.968	1.980	1.987	1.978	1.977
8f Cu	12.475	1.091	0.489	0.577	0.426	1.969	1.980	1.986	1.978	1.978
8f Cu	12.384	1.102	0.482	0.506	0.403	1.967	1.980	1.988	1.978	1.978
8f Cu	12.397	1.096	0.522	0.490	0.396	1.968	1.980	1.989	1.978	1.978
8i Al1	2.571	1.076	<u>0.605</u>	0.476	0.414					
8i Al1	2.571	1.076	<u>0.605</u>	0.476	0.414					

Table 3.8: (continued)

	Al1	2.568	1.086	0.442	<u>0.625</u>	0.415
	Al1	2.568	1.086	0.442	<u>0.625</u>	0.415
	Al2	2.653	1.039	0.541	0.493	0.580
8j	Al2	2.653	1.039	0.541	0.493	0.580
	Al2	2.637	1.053	0.458	0.546	0.581
	Al2	2.637	1.053	0.458	0.546	0.581

Bond Type		Distance	Overlap Population
1	Al1	Y 3.021 Å	<u>0.0698</u>
2	Cu	Y 3.349 Å	0.0005
3	Al2	Y 3.195 Å	0.0202

(c) Calculation results with the inclusion of the Y s, p and d orbitals.

Electron Number: 71.00

Total Energy: -909.1520 eV

Fermi Energy: -6.7683 eV

Atom	Total	s	x	y	z	x^2-y^2	z^2	xy	xz	yz	
	<u>Y</u>	3.128	0.265	<u>0.089</u>	<u>0.087</u>	0.046	<u>0.693</u>	<u>0.663</u>	0.344	0.482	0.459
8f	Cu	11.925	1.052	0.339	0.324	0.328	1.968	1.975	1.986	1.976	1.976
	Cu	11.988	1.031	0.344	0.426	0.304	1.971	1.978	1.983	1.976	1.976
	Cu	12.063	1.031	0.383	0.443	0.322	1.971	1.977	1.983	1.976	1.977
	Cu	12.023	1.031	0.385	0.375	0.349	1.968	1.975	1.985	1.977	1.977
	Al1	2.471	1.071	<u>0.585</u>	0.452	0.363					
8i	Al1	2.471	1.071	<u>0.585</u>	0.452	0.363					
	Al1	2.453	1.079	0.433	<u>0.572</u>	0.369					
	Al1	2.453	1.079	0.433	<u>0.572</u>	0.369					
8j	Al2	2.514	1.031	0.487	0.454	0.543					
	Al2	2.514	1.031	0.487	0.454	0.543					
	Al2	2.503	1.039	0.433	0.488	0.543					
	Al2	2.503	1.039	0.433	0.488	0.543					

Bond Type		Distance	Overlap Population
1	Al1	Y 3.021 Å	<u>0.1902</u>
2	Cu	Y 3.349 Å	0.0469
3	Al2	Y 3.195 Å	0.0754

0.1902 as the p, and d orbitals on Y are added. This increase in overlap is greater than that of the other Y - Cu and Y - Al bonds. These calculations were repeated with the Cu atoms occupying the 8i and 8j positions also, and a comparison of the overlap populations of the three Y - Cu/Al interactions is given in Table 3.9.

In order to further examine the role of the Y atoms in the stabilization of the ordering of copper and aluminum atoms, the three calculation with the copper atoms occupying the 8f, 8i and 8j positions were repeated with the Y atomic orbitals included. The results of these repeated calculations are given in Table 3.10, and like the previous calculations the lowest energy configuration is with the Cu atoms on site 8i.

Table 3.9: The overlap populations for the three Y - Cu/Al bond types for the three orderings of Cu (8f, 8i, 8j).

atomic arrangement	Y- Cu/Al distance (Å)	calculated overlap populations	
Cu 8f	3.349	0.0469	observed geometry
Al 8i	3.018	0.1902	
Al 8j	3.200	0.0754	
Al 8f	3.349	0.0643	
Cu 8i	3.018	0.1370	
Al 8j	3.200	0.0674	
Al 8f	3.349	0.0695	
Al 8i	3.018	0.1613	
Cu 8j	3.200	0.0632	

Table 3.10: The calculated total energies (eV/formula unit) and Fermi energies of the three ${}^3[\text{YCu}_4\text{Al}_8]$ structures in which the 4 Cu atoms occupy the each of the 3 positions (8f, 8i, 8j). Each of the three calculations had the same number of Cu and Al atoms, and the same number of electrons (71e⁻). For the Y charge iterated atomic orbital parameters see Table 3.1.

site with the four Cu atoms	calculated total energy (eV)	calculated Fermi energy (eV)
8f	-909.152	-6.768
8i	-909.988	-6.955
8j	-909.018	-6.742

Conclusions on the Ordering of YCu_4Al_8

The calculation of the total energy is composed of two terms, the site potential (or local configuration) and the pair potential (or nearest neighbor interaction), see (1).^[70]

$$\langle E \rangle \cong \sum q_i \alpha_i + \sum p_{ij} \beta_{ij} \quad (1)$$

Using the Mulliken populations and atomic orbital energies, calculations were performed to separate the total energies into these two parts. The results of these calculations are given in Table 3.11, for calculations using two sets of Cu atomic orbital parameters, as well as with and without Y atomic orbitals included. The first two sections in the table are calculations using the atomic Cu parameters, and the third and fourth sections on the table are calculations using Cu charge iterated parameters. The column of data on the far right in Table 3.11 is the difference between the pair potentials for the calculations with and without yttrium atomic orbitals included. Using the Cu charge iterated parameters, the total energies, site potentials and pair potentials are lower for the observed structure (1c, 1d) than for the Cu atoms on 8i (2c, 2d), which is the site the earlier Mulliken population calculations favored, see Table 3.6. The difference in the pair potentials between the calculations with and without Y is also greater for the observed (1d) structure than for (2d) with the Cu on site 8i. This is encouraging, but we need to continue work on understanding the ordering of Cu and Al in YCu_4Al_8 .

Table 3.11: The calculated total energy separated into the site potentials and pair potentials for different arrangements of Cu and Al for YCu_4Al_8 .

atomic coloring in YCu_4Al_8	total energy (eV)	site potential (eV)	pair potential (eV)	difference in pp with and without Y included
${}^3[\text{Cu}_4\text{Al}_8]^{3-}$ [Cu = (4s)-11.40, (4p) -6.06, (3d) -14.0 eV]				
(1a) Cu (8f)-observed Al (8i) Al (8j)	-902.100	-826.051	-76.049	-
(2a) Al (8f) Cu (8i) Al (8j)	-903.925	-827.425	-76.500	-
(3a) Al (8f) Al (8i) Cu (8j)	-902.412	-827.606	-74.806	-
${}^3[YCu_4Al_8]$ [Y = (4s) -8.45, (4p) -2.98, (3d) -10.94, Cu as above]				
(1b)Cu (8f) Al (8i) Al (8j)	-909.152	-824.993	-84.159	-8.11
(2b) Al (8f) Cu (8i) Al (8j)	-909.988	-825.905	-84.083	-7.58
(3b)Al (8f) Al (8i) Cu (8j)	-909.018	-825.370	-83.648	-8.84

${}^3[\text{Cu}_4\text{Al}_8]^{3-}$ [Cu = (4s)-8.45, (4p) -2.98, (3d) -10.94 eV]				
(1c)Cu (8f) Al (8i) Al (8j)	-753.529	-689.964	-63.565	-
(2c)Al (8f) Cu (8i) Al (8j)	-754.280	-688.866	-65.413	-

Table 3.11 - continued

(3c)Al (8f)	-753.127	-690.062	-63.065	-
Al (8i)				
Cu (8j)				
${}^3_{\infty}[\text{YCu}_4\text{Al}_8]$ [Y = (4s) -8.45, (4p) -2.98, (3d) -10.94, Cu as above]				
(1d) Cu (8f)	-766.063	-690.544	-75.519	-11.95
Al (8i)				
Al (8j)				
(2d) Al (8f)	-764.684	-688.191	-76.493	-11.08
Cu (8i)				
Al (8j)				
(3d) Al (8f)	-764.537	-689.291	-75.245	-12.18
Al (8i)				
Cu (8j)				

Phase Width of $\text{LnCu}_x\text{Al}_{12-x}$: Theoretical Investigation

Since the theoretical investigation of the phase width of $\text{BaCu}_x\text{Al}_{13-x}$ yielded some valuable insight into the observed phase width, a similar series of calculations was carried out on the $\text{LnCu}_x\text{Al}_{12-x}$ compounds. For this series of calculations, as in the $\text{BaCu}_x\text{Al}_{13-x}$ calculations, while LnCu_4Al_8 , LnCu_5Al_7 and LnCu_6Al_6 are known, the other compounds were merely hypothetical isostructural compounds for the purpose of the calculations. In all the calculations a primitive unit cell containing 12 atoms was used with different combinations of copper and aluminum atoms on the three sites to achieve the desired composition and to investigate the differences in energy relating to different arrangements of atoms on particular sites. For these calculations, if the composition allowed, site 1 (8f) was occupied by copper, site 2 (8i) by aluminum, and site 3 (8j) was used for mixing copper and aluminum as the composition dictated. For example, in LnCu_3Al_9 , sites 1 and 3 were all Cu atoms, and site 2 was all Al, but for LnCuAl_{11} , all sites were occupied by Al, except one Cu

atom on site 1. Each calculation considered the precise electron count appropriate for the composition being considered ($\text{LnCu}_4\text{Al}_8 = 31e^-$), as well as one fewer electron per formula unit. Many of the same conclusions derived from the results of the series of $\text{BaCu}_x\text{Al}_{13-x}$ calculations also can be made for this series of calculations. Table 3.12 lists the compositions, Fermi energies, and overlap populations for the phases considered.

Table 3.12: Results for the series of $\text{YCu}_x\text{Al}_{12-x}$ compounds forming the ThMn_{12} structure.

Composition	Fermi Energy (eV)	overlap populations for interactions 1, 2 and 3		
		1[Cu-Cu/Al] (8f)	2[Al-Al] (8i)	[Cu-Al] (wt.avg)
YCu_8Al_4	-7.916	0.0485	0.3718	0.0930
YCu_6Al_6	-7.325	0.0490	0.4154	0.1270
YCu_5Al_7	-6.894	0.0442	0.4331	0.1433
YCu_4Al_8	-6.131	0.0271	0.4373	0.1564
YCu_3Al_9	-5.530	0.0280	0.4712	0.1223
YCuAl_{11}	-4.287	0.0477	0.4972	0.1547

Figure 3.13 shows the DOS curves for the three compounds YCu_8Al_4 , YCu_5Al_7 , and YCuAl_{11} , with the Fermi energies represented with the dashed line. All three DOS curves contain a strong and narrow Cu d-band between -15.0 and -13.0 eV, with a rather dispersed and featureless DOS above this sharp band. The DOS curve for LnCuAl_{11} does contain a few more prominent features between -10.0 and -4.0eV than the other two DOS curves.

Whereas in $\text{BaCu}_x\text{Al}_{13-x}$ there were two general types of interactions (Cu1 central - Cu2/Al surface, and Cu2/Al surface - Cu2/Al surface), in the $\text{LaCu}_x\text{Al}_{12-x}$ calculations, because of the greater complexity of the ThMn_{12} structure, it is not possible to consider interactions which are as general as those in the NaZn_{13} structure. Two of the 3 interactions which are important and representative are (1) the Cu-Cu (or Al) (2.564 Å) interaction along the 'chain' of Cu atoms, and (2) the Al1-Al1 'pair' (2.668 Å). The third interaction is an weighted average overlap population of the other distances in the framework near 2.70Å. Figure 3.14 contains three COOP curves for the three interactions as given in Table 3.12 for

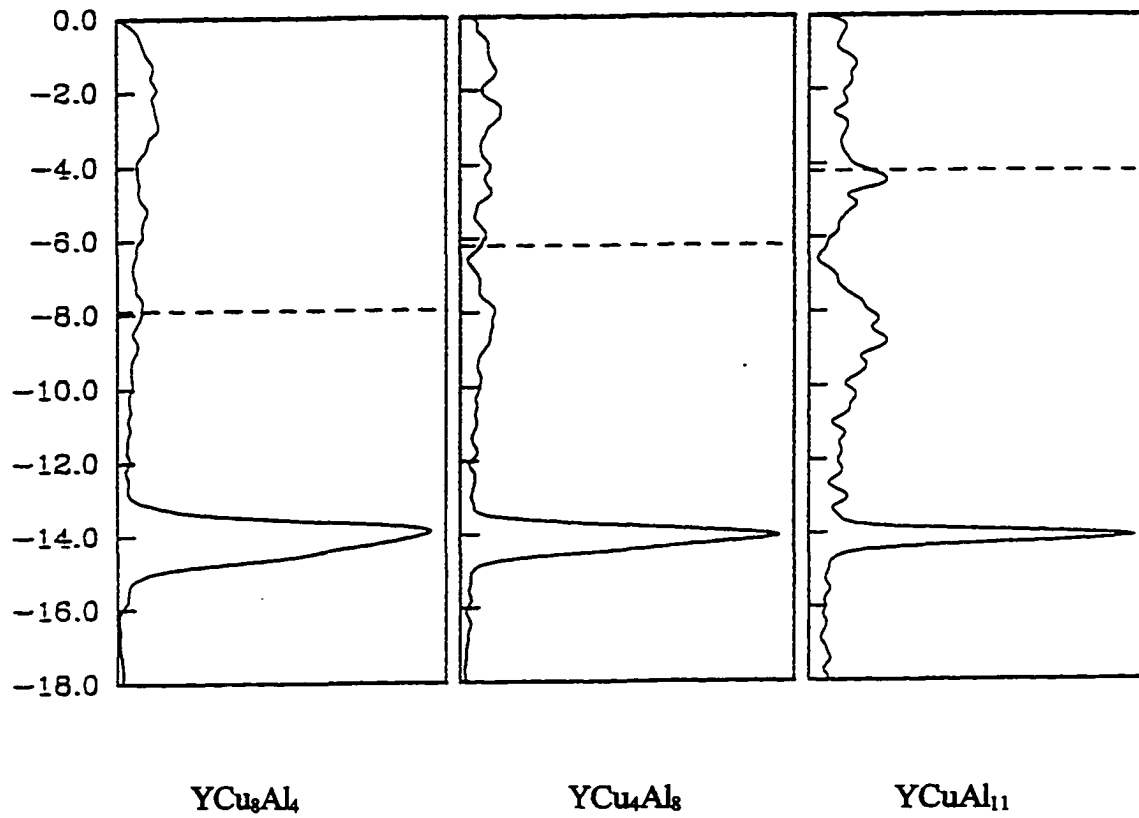


Figure 3.13: The three DOS curves for YCu_8Al_4 , YCu_4Al_8 , and YCuAl_{11} . The Fermi energies (see Table 3.12) are marked with the dotted lines.

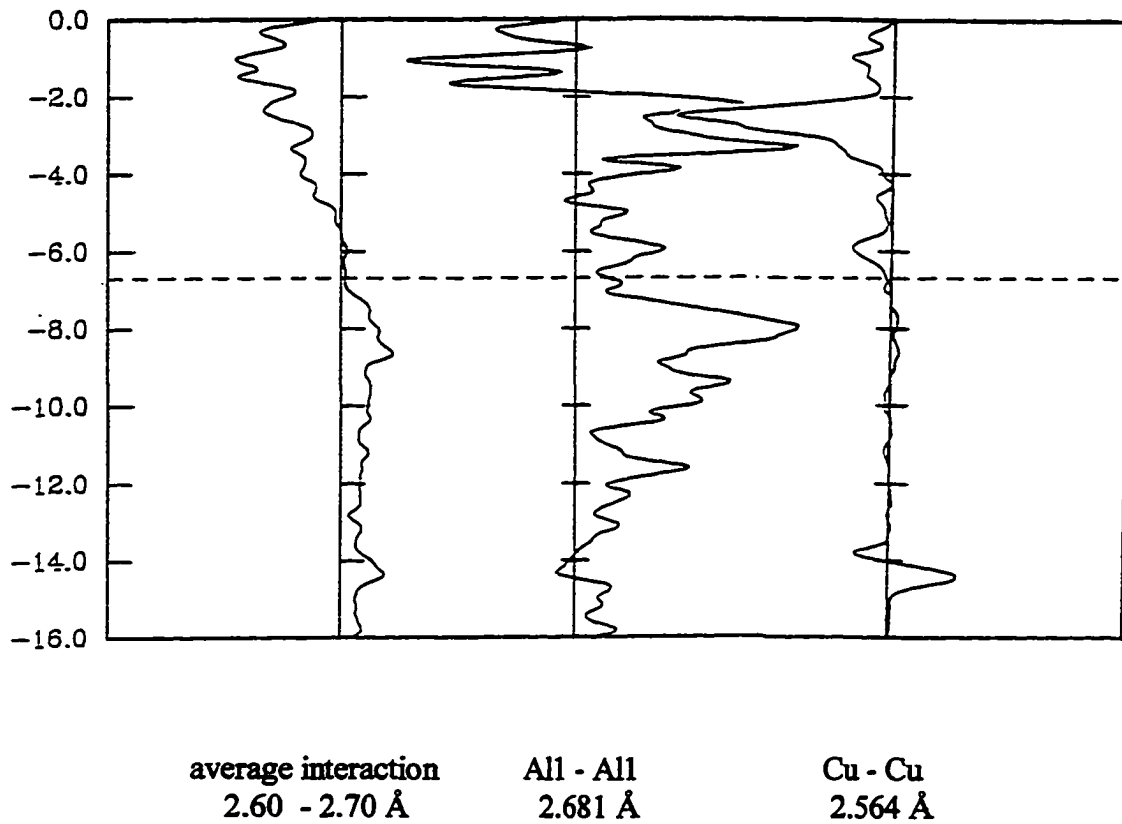


Figure 3.14: The three COOP curves for interactions (1) average framework, 2.60 - 2.70 Å, (2) Al1 - Al1 2.681 Å, and (3) Cu - Cu 2.564 Å, in YCu_5Al_7 . The Fermi energy (-6.69 eV) is marked with the dotted line.

the YCu_5Al_7 composition, with the Fermi energy highlighted with the dashed line at -6.89 eV. Notice that for curves 1 and 3 the Fermi energy crosses at the point where the overlap changes from bonding (+) to antibonding (-), while there are many bonding states left unfilled in curve 2 for the Al - Al dimer-like interaction. In Table 3.12 the maximum in overlap population for interaction 3 occurs for the composition YCu_5Al_7 , (excluding YCuAl_{11}), confirming what the COOP curves demonstrate with the Fermi energy's position at the crossover between bonding and antibonding states. The overlap population for interaction 2 continues to increase due to the filling of the bonding states as the Fermi energy increases. However, in order to maximize the bonding for interaction 2, many antibonding states would be populated for the other interactions in the structure, and this is clearly unfavorable. For the systems which are more copper rich than LnCu_5Al_7 , the Fermi energy crosses at a lower energy, and there are some bonding states which are left empty. Conversely, for the more aluminum rich systems, where the Fermi energy crosses at higher energies, many antibonding states are filled. Similar to what was observed in the $\text{BaCu}_x\text{Al}_{13-x}$ series, the compositions which are observed, have Fermi energies which fall near this crossover, and maximize the bonding in as many interactions as possible.

Calculations on $\text{YCu}_x\text{Al}_{13-x}$ to Investigate the Role of the Cation in NaZn_{13}

In the series of calculations on various ${}^3[\text{Cu}_x\text{Al}_{13-x}]^{-2}$ frameworks, the barium atoms were treated as classical cations donating their 2 electrons, but not contributing any specific orbitals. While we believe this is not an inaccurate representation of the role of the barium atoms, it was important to verify that the conclusions made about the $\text{BaCu}_x\text{Al}_{13-x}$ compounds did not change when atomic orbitals were included for the cations. In the earlier calculations on YCu_4Al_9 , the inclusion of the Y atomic orbitals did yield important information about the ordering of Cu and Al atoms. Since the polyhedron around the Ba atoms is nearly spherical with 24 equivalent distances to the Al/Cu2 atoms (3.576 Å), the Y - framework atom overlaps should be very small. Since comparisons will be made between the NaZn_{13} and ThMn_{12} calculations, we decided to use yttrium as the cation, and treat the

Y cation as donating 2 electrons in the YCu_xAl_{13-x} calculations, and donating 3 in the YCu_xAl_{12-x} ($ThMn_{12}$) calculations. Table 3.13 contains the Mulliken populations for the atoms in a single formula unit of $YCuAl_{12}$, as the Y s orbitals (a) and then s, p, and d orbitals are included (b). As expected there is no enhancement of any orbitals on either the Y or Al atoms as was observed in the case of YCu_4Al_8 . The overlap populations for the Y - Al interaction at 3.576 Å are included in Table 3.13 for both calculations with different orbitals on the Y atoms. These small overlap populations and the lack of Mulliken population enhancement support our conclusions that the roles of the cations in the two structures are different. The Ba atoms, which sit in a highly symmetric, nearly spherical polyhedron in $BaCu_5Al_8$ do not have any stabilizing interactions with specific atoms in the snub cube the way the Y atoms, which sit in a polyhedron of lower symmetry, interact with the Al atoms in YCu_4Al_8 .

Conclusions

The series of calculations on both $BaCu_xAl_{13-x}$ and YCu_yAl_{12-y} systems provided valuable information about trends in Fermi energies, and overlap populations. In both cases, the aluminum-rich phases had higher Fermi energies than the copper-rich phases. The phase widths of both $BaCu_xAl_{13-x}$ ($4 < x < 6$) and YCu_yAl_{12-y} ($4 < y < 6$) can be rationalized by understanding the balance between the Fermi energies and the energy of the crossover between bonding and antibonding states in the COOP curves. The Fermi energies of the observed phases fall at or near the crossover for most (if not all) the interactions within the Cu/Al frameworks of both structures. The calculations suggest a significant difference in the roles of the electropositive metal atoms in the two structures. This difference is one of the factors which drives the formation of either of these phases for the different metals.

Table 3.13: Calculation results of YCu₅Al₈ with Y atomic orbitals included.(a) The calculation results for 'YCu₅Al₈' with only the Y s orbital included.

Number of Electrons: 100.00 Total Energy: -555.565 eV Fermi Energy: -4.142 eV

Atom	Total	s	x	y	z	x ² -y ²	z ²	xy	xz	yz
Y	0.250	0.250								
Cu	13.628	1.083	0.853	0.819	0.978	1.978	1.980	1.979	1.980	1.979
Al	3.019	0.988	0.683	0.584	0.763					
Al	3.030	1.005	0.692	0.611	0.722					
Al	2.984	0.988	0.682	0.591	0.723					
Al	2.996	0.990	0.678	0.593	0.735					
Al	3.013	1.001	0.759	0.688	0.565					
Al	3.037	0.996	0.564	0.778	0.699					
Al	3.012	1.002	0.741	0.680	0.588					
Al	3.066	1.012	0.595	0.740	0.719					
Al	3.009	1.021	0.709	0.690	0.588					
Al	3.058	1.001	0.582	0.761	0.715					
Al	3.008	1.001	0.734	0.688	0.586					

Bond Type	Distance	Overlap Population
Y Al	3.576 Å	<u>0.0062</u>

(b) The calculation results for 'YCu₅Al₈' with the Y s, p and d orbitals included.

Number of Electrons: 100.00 Total Energy: -566.043 eV Fermi Energy: -5.581 eV

Atom	Total	s	x	y	z	x ² -y ²	z ²	xy	xz	yz
Y	5.222	0.222	0.075	0.058	0.053	1.077	0.931	0.947	0.981	0.879
Cu	12.621	0.990	0.529	0.580	0.644	1.976	1.978	1.975	1.974	1.974
Al	2.635	0.979	0.527	0.517	0.612					
Al	2.678	0.995	0.539	0.544	0.601					
Al	2.720	0.981	0.577	0.544	0.618					
Al	2.723	0.982	0.571	0.546	0.624					
Al	2.642	0.980	0.581	0.559	0.521					
Al	2.685	0.989	0.535	0.606	0.554					
Al	2.685	0.983	0.592	0.573	0.536					
Al	2.739	1.004	0.564	0.597	0.575					
Al	2.676	0.998	0.566	0.570	0.542					
Al	2.725	0.994	0.544	0.611	0.576					
Al	2.687	0.983	0.586	0.580	0.537					
Al	2.711	0.992	0.543	0.608	0.568					

Bond Type	Distance	Overlap Population
Y Al	3.576 Å	<u>0.0354</u>

CHAPTER 4

QUATERNARY ALUMINIDES

Introduction

Chapters 2 and 3 contain a detailed discussion of the synthesis and structure of a variety of ternary aluminum-rich phases which form both the NaZn_{13} and ThMn_{12} structure types. Electronic structure calculations addressed the questions of the phase widths of $\text{BaCu}_x\text{Al}_{13-x}$ and $\text{LnCu}_y\text{Al}_{12-y}$, and the ordering of copper and aluminum atoms in YCu_4Al_8 . Besides the alkaline earth ternaries, ACu_6Al_7 ($A = \text{Ba, Sr, Ca}^{[41]}$), both EuCu_6Al_7 and LaCu_6Al_7 adopt the NaZn_{13} structure. However, every other rare earth element, in combination with copper and aluminum such that the Ln to (Cu/Al) ratio is 1:12 (or 1:13) forms the ThMn_{12} structure. The resemblance in both stoichiometry and elemental composition between these two groups of ternary intermetallics forming either of these structures is striking, and yet, as prepared from the elements in the arc welder, no ternary combination has yielded product containing both structure types. In an effort to examine this preference for either the ThMn_{12} or NaZn_{13} structure type, depending on the electropositive metal used, quaternary compounds were made. Similar differences exist in the silver aluminides with $\text{BaAg}_{5.5}\text{Al}_{7.5}$ and $\text{SrAg}_{5.5}\text{Al}_{7.5}$ forming the NaZn_{13} structure, but LnAg_xAl_y compounds (with variable x and y) form other structures. For example, EuAg_5Al_6 forms the BaCd_{11} structure type, and $\text{Ln}_2\text{Ag}_x\text{Al}_{17-x}$ ($\text{Ln} = \text{La} - \text{Lu}$, except Eu and Yb) form either the $\text{Th}_2\text{Ni}_{17}$ or $\text{Th}_2\text{Zn}_{17}$ type depending on the silver: aluminum ratio (see chapter 7).

Synthesis and Results

Using the same experimental techniques described earlier (chapter 2), the synthesis of quaternary phases containing a mixture of electropositive metals was carried out, and Table 4.1 contains a list of the reactants and the products observed by powder X-ray diffraction, and refined lattice parameters if available. The letter before each compound will be used as a reference within the discussion of the results.

Table 4.1: The quaternary reactant compositions and the products observed by powder and single crystal X-ray diffraction.

Reactant Stoichiometry	Pre-Ann. Prod.	Post-Ann. Prod.	Refined Lattice P. (Å)
a) BaSrCu ₁₂ Al ₁₄	BaSrCu ₁₂ Al ₁₄ ($a = 12.073(2)$ Å) * -		
b) BaSrAg ₁₁ Al ₁₅	BaAg _{5.5} Al _{7.5} , SrAg _{5.5} Al _{7.5}	BaSrAg ₁₁ Al ₁₅ * $a = 12.627(1)$	
c) BaYCu ₁₂ Al ₁₄	BaCu _{5.5} Al _{7.5} , YCu ₅ Al ₇	-	
d) BaDyCu ₁₂ Al ₁₄	BaCu ₆ Al ₇ , DyCu ₅ Al ₇	same as pre-annealed	
e) SrGdCu ₁₀ Al ₁₆	SrCu ₆ Al ₇ , GdCu ₄ Al ₈	same as pre-annealed	
f) SrCeCu ₁₂ Al ₁₄	SrCeCu ₁₂ Al ₁₄ *	-	
g) BaEuAg ₁₁ Al ₁₅	BaAg ₆ Al ₇ , EuAg ₅ Al ₆ (BaCd ₁₁)	BaEuAg ₁₁ Al ₁₅ * $a = 12.729(1)$	
h) SrEuAg ₁₂ Al ₁₄	Sr _x Eu _{2-x} Ag ₁₂ Al ₁₄ , EuAg ₅ Al ₆ (trace) -		
i) EuYbAg ₁₀ Al ₁₂	EuYbAg ₁₀ Al ₁₂ * (BaCd ₁₁)	-	
j) BaGdAg ₁₁ Al ₁₅	BaAg ₆ Al ₇ , Gd ₂ Ag ₇ Al ₁₀ (Th ₂ Ni ₁₇)	BaGdAg ₁₁ Al ₁₅ * $a = 12.764(3)$	

* indicates single crystal solution

The results of the reactions (a) BaSrCu₁₂Al₁₄, and (b) BaSrAg₁₁Al₁₅, are not surprising, since all four compounds BaCu₅Al₈, SrCu₆Al₇, BaAg₅Al₆, and SrAg₆Al₇ form the NaZn₁₃ structure. In the quaternary compound BaSrCu₁₂Al₁₄, the barium and strontium atoms occupying the centers of the snub cubes at (8a: 1/4, 1/4, 1/4), are randomly arranged throughout the structure ($a = 12.073(2)$ Å). The powder pattern for the pre-annealed BaSrAg₁₁Al₁₅ product contained two separate patterns indicating that the initial product contained both BaAg₆Al₇ ($a = 12.645(1)$ Å) and SrAg₆Al₇ ($a = 12.594(3)$ Å). Since these two compounds are isostructural, the two patterns are identical, but each line for SrAg_{5.5}Al_{7.5} appears at a fraction of a degree higher than those lines for BaAg_{5.5}Al_{7.5} due to the smaller lattice constant. After annealing the product at 850°C for 10 days, the powder

pattern was consistent with a single phase product ($a = 12.627(1)\text{\AA}$) with Ba and Sr mixed randomly throughout the structure. This was confirmed by the results of two single crystal X-ray solutions whose refined compositions were $\text{BaSrAg}_{12}\text{Al}_{14}$ and $\text{BaSrAg}_{12.4}\text{Al}_{13.6}$. Table 4.2 and 4.3 contain important information about the single crystal solutions for 2 crystals of $\text{BaSrAg}_{12}\text{Al}_{14}$. All of the single crystal collections and refinements reported in this chapter were carried out on a Siemens P4 diffractometer ($\text{Mo K}\alpha_1$) as described in chapter 2.

The next three reactions listed in Table 4.1 (c, d, and e) were all mixtures of one metal which forms the NaZn_{13} structure (i.e. Ba or Sr), and another which forms the ThMn_{12} structure (i.e. Y, Dy or Gd). In all three reactions the products both before and after annealing, were multi-phase. $\text{BaYCu}_{12}\text{Al}_{14}$ (c) as characterized by powder X-ray diffraction, contained a mixture of BaCu_6Al_7 and YCu_5Al_7 , and was not annealed. $\text{BaDyCu}_{12}\text{Al}_{14}$ (d) was also a two phase product containing both BaCu_6Al_7 and DyCu_5Al_7 in the pre-annealed and post-annealed (900°C for 14 days) products. $\text{SrGdCu}_{10}\text{Al}_{16}$ (e) was also a mixture of the two phases SrCu_6Al_7 and GdCu_4Al_8 , both before and after annealing (900°C , 14 days). The annealed products from reactions (d) and (e) were analyzed in a JEOL 6100 Scanning Electron Microscope (SEM) using Energy Dispersive Spectroscopy (EDS) and the presence of all four elements in each sample was confirmed by analysis of multiple areas of the sample.

$\text{SrCeCu}_{12}\text{Al}_{14}$ (f) was expected to yield similar products as the reactions directly preceding it, due to the fact that the ternary $\text{CeCu}_x\text{Al}_{12-x}$ ($4 < x < 6$) compounds have been reported in the ThMn_{12} structure, and SrCu_6Al_7 forms the NaZn_{13} structure. However, a single phase product $\text{SrCeCu}_{12}\text{Al}_{14}$ containing a random mixture of Sr and Ce atoms was characterized forming the NaZn_{13} structure ($a = 11.980 \text{ \AA}$). This result was confirmed by a single crystal X-ray solution of a crystal containing a mixture of Sr and Ce atoms, see Table 4.4 for a summary of relevant crystallographic information. The presence of all four elements was confirmed by EDS in the SEM. The size and valence of these two metal

Table 4.2: The summary of crystallographic information for BaSrAg_{12.4}Al_{13.6}, and BaSrAg₁₂Al₁₄.

Refined Chemical Formula	BaSrAg _{12.4} Al _{13.6}	BaSrAg _{11.97} Al _{14.03}
Space Group	Fm $\bar{3}$ c	Fm $\bar{3}$ c
Unit Cell Dimension	12.705(1) Å	12.689(1) Å
Unit Cell Volume	2050.8 (3) Å ³	2043.1 (3) Å ³
Z	4	4
2 θ_{\max}	50°	50°
Reflections Collected	522	517
Independent Reflections	95	93
Observed Reflections	93 ($F_o \geq 2\sigma(F_o)$)	93
R, wR ($F_o \geq 4.0\sigma(F_o)$)	0.0165, 0.0312	0.0139, 0.0249
R, wR (all data)	0.0165, 0.0312	0.0139, 0.0249
Goof, All Data	1.349	1.222

Table 4.3: The positional coordinates and equivalent isotropic displacement coefficients for BaSrAg_{12.4}Al_{13.6}, and BaSrAg₁₂Al₁₄.

(a) BaSrAg _{12.4} Al _{13.6} .						
Atom	Site	x	y	z	U _{eq}	Site Occ.
Ba	8a	0.25	0.25	0.25	0.0096(5)	0.5
Sr	8a	0.25	0.25	0.25	0.0096(5)	0.5
Ag1	8b	0	0	0	0.0153(11)	0.190(7)
Al1	8b	0	0	0	0.0153(11)	0.810(7)
Ag2	96i	0.1226(1)	0.1808(1)	0.0	0.0139(4)	0.501(5)
Al2	96i	0.1226(1)	0.1808(1)	0.0	0.0139(4)	0.499(5)
(b) BaSrAg ₁₂ Al ₁₄						
Atom	Site	x	y	z	U _{eq}	Site Occ.
Ba	8a	0.25	0.25	0.25	0.0099(4)	0.5
Sr	8a	0.25	0.25	0.25	0.0099(4)	0.5
Ag1	8b	0	0	0	0.0118(11)	0.149(6)
Al1	8b	0	0	0	0.0118(11)	0.851(6)
Ag2	96i	0.1226(1)	0.1807(1)	0.0	0.0133(3)	0.486(4)
Al2	96i	0.1226(1)	0.1807(1)	0.0	0.0133(3)	0.514(4)

cations are two factors which may contribute to this unexpected result. The ionic radius (CN = 12) of Sr^{2+} is 2.151 Å, and Ce^{3+} is 1.846 Å.^[71] Magnetic susceptibility measurements were made on a small sample of $\text{SrCeCu}_8\text{Al}_{18}$, and the material displayed Curie-Weiss paramagnetism with an effective moment of 2.26(1) B.M., which accounts for a nearly 1:1 ratio of Sr:Ce, see Figure 4.1. This size difference (0.30 Å) is much smaller than the differences between Ba^{2+} (2.236 Å) and Y^{3+} (1.773 Å) for reaction (c), and Ba^{2+} and Dy^{3+} (1.775 Å) for reaction (d), of 0.463 Å and 0.461 Å respectively.^[71] $\text{SrGdCu}_{10}\text{Al}_{16}$ (e) formed a combination of the two ternaries SrCu_6Al_7 and GdCu_5Al_7 . It is possible that the similar size difference between Sr and Ce allow for the mixed occupancy of that position within the NaZn_{13} structure.

Table 4.4: The summary of crystallographic information for $\text{SrCeCu}_{7.34}\text{Al}_{18.65}$.

Refined Chemical Formula	$\text{SrCeCu}_{7.34}\text{Al}_{18.65}$					
Space Group	$\text{Fm}\bar{3}\text{c}$					
Unit Cell Dimension	11.938(1) Å					
Unit Cell Volume	1701.4 (2) Å ³					
Z	4					
$2\theta_{\text{max}}$	50°					
Reflections Collected	427					
Independant Reflections	78					
Observed Reflections	69 ($F_o \geq 2\sigma(F_o)$)					
R, wR ($F_o \geq 4.0\sigma(F_o)$)	0.0243, 0.0616					
R, wR (all data)	0.0263, 0.0619					
Goof, All Data	1.180					
Atom	Site	x	y	z	U_{eq}	Site Occ.
Ce	8a	0.25	0.25	0.25	0.0080(9)	0.5
Sr	8a	0.25	0.25	0.25	0.0080(9)	0.5
Cu1	8b	0	0	0	0.0150(2)	0.53(2)
Al1	8b	0	0	0	0.0150(2)	0.47(2)
Cu2	96i	0.1170(1)	0.1769(1)	0.0	0.0139(8)	0.445(11)
Al2	96i	0.1170(1)	0.1769(1)	0.0	0.0139(8)	0.555(11)

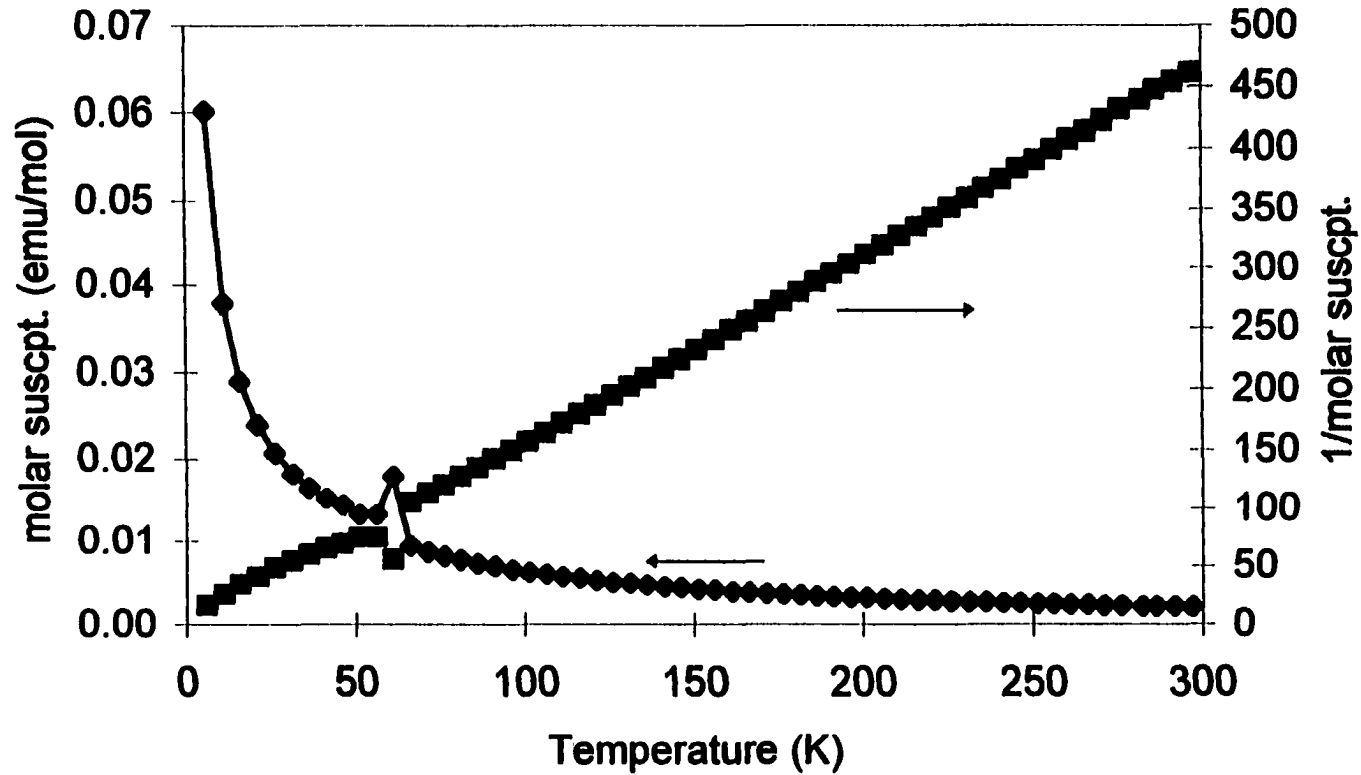


Figure 4.1: The magnetic susceptibility curve for $\text{SrCeCu}_{12}\text{Al}_{14}$, which shows Curie-Weiss paramagnetism, with an effective moment of 2.26(1) Bohr magnetons. The small feature at $\sim 60\text{K}$ is due to the condensation of oxygen on the sample holder, and is not a feature of the magnetic susceptibility of the sample.

The rare earth ternary silver aluminides do not form the ThMn_{12} structure, but form a variety of network structures including the BaCd_{11} , $\text{Th}_2\text{Ni}_{17}$ and $\text{Th}_2\text{Zn}_{17}$ -types. EuAg_5Al_6 and LaAg_5Al_5 form the BaCd_{11} structure,^[35] and a number of ternary silver aluminides ($\text{Ln}_2\text{Ag}_x\text{Al}_{17-x}$) form either the $\text{Th}_2\text{Ni}_{17}$ or $\text{Th}_2\text{Zn}_{17}$ structure depending on the silver : aluminum ratio.^[36]

$\text{BaEuAg}_{11}\text{Al}_{15}$ (g) was initially characterized as a mixture of EuAg_5Al_6 and $\text{BaAg}_{5.5}\text{Al}_{7.5}$. However, after annealing (900°C, 14 days) single phase product was characterized by powder X-ray diffraction, observed in the NaZn_{13} structure with a refined lattice parameter of $a = 12.729(1)$ Å. Based on a single crystal X-ray solution (see Tables 4.5 and 4.6) the refined composition of this product was $\text{BaEuAg}_{14}\text{Al}_{12}$. The magnetic susceptibility of $\text{BaEuAg}_{14}\text{Al}_{12}$ showed Curie-Weiss paramagnetism with $\mu_{\text{eff}} = 6.65(1)$ B.M., which accounts for about 40% of the snub cubes being occupied by Eu atoms (Eu^{+2} , f^7 , $7.94 \mu_B$).^[45] All four elements were detected by EDS in the SEM in various regions of the homogeneous looking sample.

Table 4.5: The summary of crystallographic information for $\text{BaEuAg}_{14}\text{Al}_{12}$.

Refined Chemical Formula	$\text{BaEuAg}_{14.05}\text{Al}_{11.95}$
Space Group	$\text{Fm}\bar{3}\text{c}$
Unit Cell Dimension	12.727(1) Å
Unit Cell Volume	2061.5 (2) Å ³
Z	4
$2\theta_{\text{max}}$	50°
Reflections Collected	523
Independant Reflections	95
Observed Reflections	92 ($F_o \geq 2\sigma(F_o)$)
R, wR ($F_o \geq 4.0 \sigma(F_o)$)	0.0139, 0.0271
R, wR (all data)	0.0141, 0.0271
GooF, All Data	1.145

Table 4.6: The atomic positions, site occupancies and isotropic displacement parameters for $\text{BaEuAg}_{14.05}\text{Al}_{11.95}$.

Atom	Site	x	y	z	U_{eq}	Site Occ.
Ba	8a	0.25	0.25	0.25	0.0111(4)	0.5
Eu	8a	0.25	0.25	0.25	0.0111(4)	0.5
Ag1	8b	0	0	0	0.0129(10)	0.287(7)
Al1	8b	0	0	0	0.0129(10)	0.714(7)
Ag2	96i	0.12215(4)	0.18146(4)	0.0	0.0141(3)	0.561(5)
Al2	96i	0.12215(4)	0.18146(4)	0.0	0.0141(3)	0.439(5)

$\text{SrEuAg}_{12}\text{Al}_{14}$ (h) was a similar combination as $\text{BaEuAg}_{11}\text{Al}_{15}$, except the sizes of Sr^{+2} and Eu^{+2} are very similar, (2.151 Å, and 2.041 Å respectively).^[71] The product contained a trace of EuAg_5Al_6 , but the major phase (approximate composition), $\text{Sr}_x\text{Eu}_{2-x}\text{Ag}_{12}\text{Al}_{14}$, adopts the NaZn_{13} structure.

Since both Eu ($4f^76s^2$) and Yb ($4f^{14}6s^2$) are commonly +2 cations, and often form similar compounds, the quaternary $\text{EuYbAg}_{12}\text{Al}_{10}$ (i) forms single phase product forming the BaCd_{11} structure. From a single crystal X-ray structure refinement the composition of this phase is $\text{EuYbAg}_{11.88}\text{Al}_{10.12}$, and the Yb and Eu are randomly arranged within the structure, (see chapter 7).

In reaction (j) $\text{BaGdAg}_{11}\text{Al}_{15}$ initially formed a mixture of $\text{BaAg}_{5.5}\text{Al}_{7.5}$ and $\text{Gd}_2\text{Ag}_7\text{Al}_{10}$ which forms the $\text{Th}_2\text{Ni}_{17}$ structure. This product was annealed (900°C, 14 days) and characterized as a single phase material with the NaZn_{13} structure, with a refined lattice parameter of $a = 12.763(3)$ Å. The magnetic susceptibility of this product showed Curie-Weiss behavior with a $\mu_{\text{eff}} = 2.40(3)$ B.M., which would account for about 1/6 of the sub cubes occupied by Gd^{+3} (f^7) cations. For a 1Ba:1Gd ratio, a moment of near 7.9 μ_B would be expected.

Conclusions

The investigation of quaternary aluminide systems resulted as expected in products resembling the combination of the ternary systems. In all of the copper aluminum reactions (except $\text{SrCeCu}_{12}\text{Al}_{14}$) in which the two electropositive metals form different ternaries, the quaternary product was a combination of these two phases. Annealing these products did not yield single phase products. However, in the silver aluminum reactions, while the initial products were usually multi-phase, annealing transformed several of the products to a (mixed cation) single phase material. Despite a few single crystal refinements and some EDS, many of these compounds need more accurate compositional analysis, to more carefully determine the phase widths and the extent of cation mixing.

CHAPTER 5

TERNARY RARE EARTH-GOLD-ALUMINIDES FORMING
STRUCTURAL VARIANTS OF BaAl₄

Introduction

We began our investigations of ternary intermetallics with *vec* between 2 and 4, with the barium-copper-aluminum system. As described in chapter 2, the ternary compound, BaCu_xAl_{13-x} (4 < x < 6), forms the NaZn₁₃ structure, in which Ba atoms are surrounded by a $\frac{1}{3}[\text{Cu}(\text{Cu}_y\text{Al}_{12-y})]$ (3 < y < 5) cubic framework of Cu-stuffed icosahedra with randomly arranged copper (ca. 33%) and aluminum (ca. 67%) atoms. As discussed in chapter 3, this compound is an example of a ternary aluminide whose *vec* maximizes the bonding within the $\frac{1}{3}[\text{Cu}_5\text{Al}_8]$ network as observed in its overlap populations. These theoretical results provide justification for attractive Al-Al, Cu-Al, as well as Cu-Cu, interactions in these intermetallics. When the more electronegative Ag and Au are used rather than Cu, we observe some differences in the structural chemistry. As presented in chapter 2, the new ternary silver aluminides AeAg_{5.5}Al_{7.5} (Ae = Ba, Sr) are isostructural with BaCu₅Al₈, but in chapter 7 the rare earth-silver-aluminides (i.e. EuAg₅Al₆, La₂Ag₇Al₁₀) which form several different structure types including BaCd₁₁, Th₂Ni₁₇ and Th₂Zn₁₇ will be presented. With the inclusion of gold into these ternary intermetallics, we observe structural variants of both NaZn₁₃ and BaAl₄. The new ternary gold aluminides, AeAu_{5.5}Al_{6.5} (Ae = Ba, Sr, Eu, La) form a tetragonal variant of the cubic NaZn₁₃ structure and will be introduced in chapter 8. This chapter will present the synthesis, characterization and electronic structure investigation of several new ternary gold aluminides which form structures related to BaAl₄.

While BaAl₄ represents one of the most prolific structure types,^[4,40] isostructural compounds involving main-group metals are restricted to *vec* ≤ 3.5.^[54-55] BaAl₄ is a body-centered tetragonal structure, which crystallizes in the space group *I4/mmm* (No. 139), with 2 atomic positions occupied by aluminum atoms: Al1 4*d* (0, 0.5, 0.25) and Al2 4*e* (0, 0, z). The Al1 (4*d*) atoms are arranged in two-dimensional square nets, which are linked

via pairs of Al2 (4e) atoms which sit above and below the square nets, see Figure 5.1(left). The Al1 atoms are tetrahedrally coordinated by four Al2 atoms, and the Al2 atoms are each surrounded by four Al1 atoms, and one Al2 atom, in a square pyramid. There are several ordered variants of BaAl₄, in which one of these two Al positions is occupied (or partially occupied) by a third type of atom. In ThCr₂Si₂, the transition metals occupy the 4d positions (i.e. the square nets), and the main group atoms occupy the 4e positions (pair linkages). In CaBe₂Ge₂ (*P4/nmm*), the two-dimensional square nets are composed of either all Be or all Ge atoms, and these 'layers' are arranged in an alternating pattern along the *c*-direction. The heteroatomic 'Ge - Be' pairs (4e) which connect the layers are arranged with the Ge atoms connecting to the 'Be₂' layers, and the Be atoms connected to the 'Ge₂' layers. In BaNiSn₃ (*I4mm*), the Sn atoms form the square nets (4d), and the heteroatomic 'Sn-Ni' pairs (4e), align in the same direction throughout the structure. The composition, bonding and electronics of many compounds forming the BaAl₄ structure have been carefully examined,^[54] and though it is not appropriate to include a lengthy discussion here, it is valuable to review a few of the results concerning the electronic structure of BaAl₄, that will apply to the ternary gold compounds.

The BaAl₄ structure is generally observed for compounds with *vec* between 2.75 and 3.5, or alternatively, systems with 11 - 14 valence electrons (i.e. BaAl₄: 2 + 4(3) = 14). In their treatment of BaAl₄, Burdett and Miller^[54a] concluded that 12 of these electrons are involved in multi-center bonding within the ∞ [Al₂Al₂]²⁻ layers, which are connected via two-center, two-electron bonds between Al2 atoms. In BaAl₄ the states near the top of the valence band have antibonding (or π^*) character, and are associated with these Al2 pairs. For systems with fewer than 14 electrons, some of these π^* orbitals would remain unoccupied, and may have stronger (i.e. shorter) bonds between the Al2 atoms. For example, in SrAl₄ (14-electrons) the Al1 - Al2 bond distance is 2.648 Å, and the Al2 - Al2 distance is 2.652 Å, with a *c/a* ratio of 2.510.^[40] In SrCu₂Si₂ (12-electrons), the Al1 - Al2 distance is 2.465 Å, and the Al2 - Al2 distance has shortened to 2.420 Å, with a smaller *c/a* ratio of 2.38.^[40] These considerations of electron count and bonding

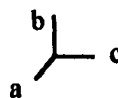
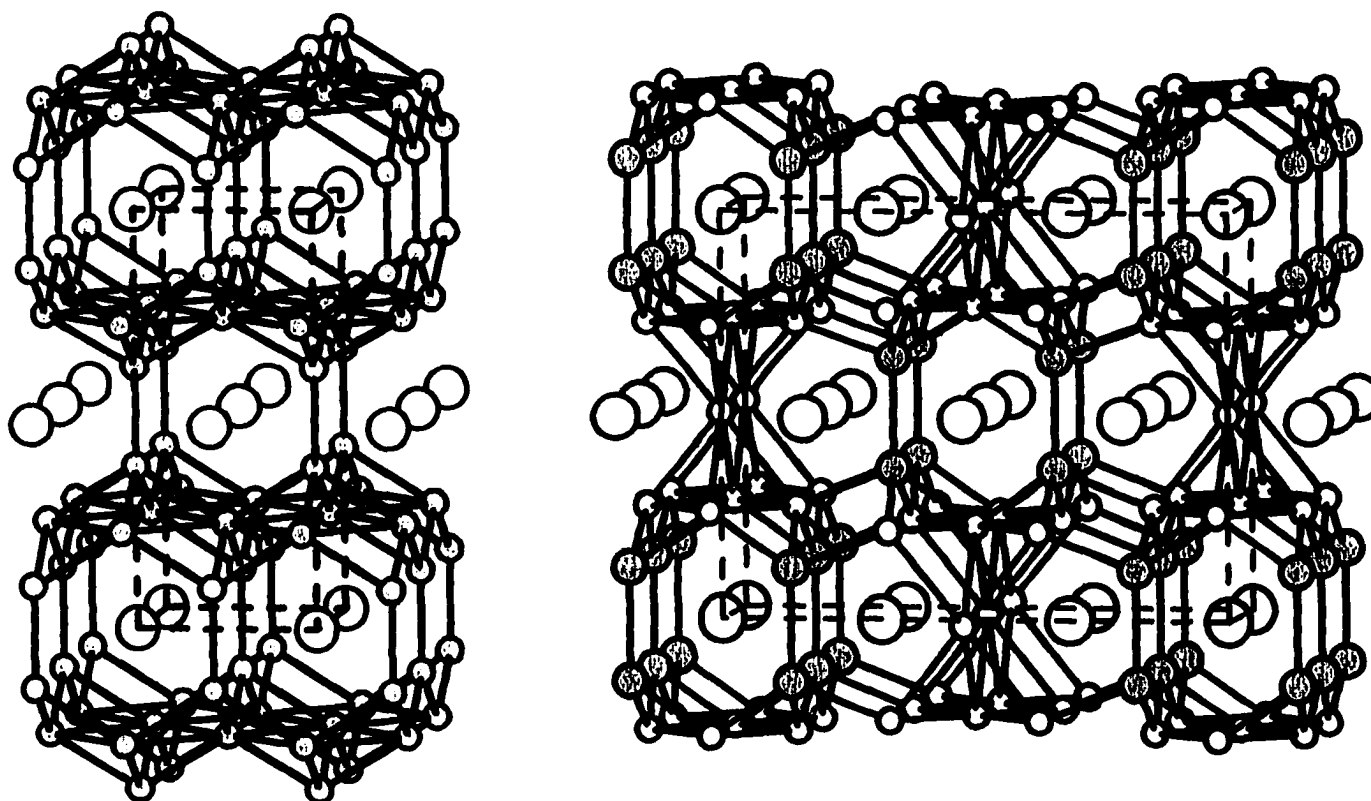


Figure 5.1: Left: The structure of BaAl_4 ; large open circles are Ba, and small gray circles are Al.
 Right: The structure of $\text{Dy}_3\text{Au}_2\text{Al}_9$, ($\alpha\text{-La}_3\text{Al}_{11}$); the large open circles are Dy, the small open circles are nearly exclusively Al, and the large gray circles are occupied 48% Au : 52% Al.

will be useful in the following discussions about the new ternary gold compounds, and their electronic structures.

The rare earths (except Eu) do not form binary aluminides with composition LnAl_4 in the BaAl_4 structure type ($vec = 3.75$, 15-electrons): rather, they form $\text{Ln}_3\text{Al}_{11}$.^[56] The low temperature $\alpha\text{-Ln}_3\text{Al}_{11}$ ($\text{Ln} = \text{La, Ce, Pr, Nd}$) is a body-centered orthorhombic structure which undergoes a phase transition (above 976 °C for $\text{La}_3\text{Al}_{11}$) to the tetragonal BaAl_4 structure type with ordered vacancies, $\beta\text{-Ln}_3\text{Al}_{11}$ ($\text{Ln}\square_{0.33}\text{Al}_{3.67}$, $vec = 3.5$). The structure of $\alpha\text{-Ln}_3\text{Al}_{11}$ is also closely related to BaAl_4 as shown in Figure 5.1(a) and (b). In $\alpha\text{-La}_3\text{Al}_{11}$, the unit cell is three times the size of BaAl_4 , and one of the ‘pairs’ from the BaAl_4 framework has been condensed to a single Al atom, making the composition $\text{La}_3\text{Al}_{11}$, not ‘ $\text{La}_3\text{Al}_{12}$ ’. With the condensation of a ‘pair’ to a single atom the two-dimensional sheets shift to form one-dimensional ribbons of squares extended in the a -direction. While in BaAl_4 there is a single type of polyhedron surrounding the Ba atoms, in $\alpha\text{-La}_3\text{Al}_{11}$ there are two polyhedra for the La atoms, see Figure 5.5. The reason these rare earth elements form $\text{Ln}_3\text{Al}_{11}$ rather than LnAl_4 is probably a combination of several factors including cation size and electron count.

In previous investigations of ternary rare earth-gold-aluminum systems, Hulliger et al. have reported $\text{LnAu}_x\text{Al}_{4-x}$ ($x = 1\text{--}1.5$, $\text{Ln} = \text{La--Tb}$) with $vec = 3.0\text{--}3.25$, which form the BaAl_4 structure, if Au and Al are disordered, but form the BaNiSn_3 -type if the Al atoms are ordered.^[57a] $\text{LnAu}_x\text{Al}_{4-x}$ ($x = 1.5\text{--}2$, $\text{Ln} = \text{La--Tb}$) with $vec = 2.75\text{--}3.0$ are reported to form the CaBe_2Ge_2 structure type.^[57b] Hulliger comments that “while the samples with La, Ce, Pr and Nd were fairly pure, those with the heavier Ln elements contained increasing amounts of foreign phases”, and “the samples with $\text{Ln} = \text{Dy}$ were very impure”.^[57b] Several rare-earth-gold-gallides have been reported in variants of BaAl_4 also; $\text{LnAu}_x\text{Ga}_{4-x}$ ($\text{Ln} = \text{La, Ce, Pr, Nd, Sm}$, $0.3 < x < 1.3$) form a ternary BaAl_4 -type, and $\text{LnAu}_{1.5}\text{Ga}_{2.5}$ ($\text{Ln} = \text{La, Ce, Pr, Nd, Sm}$) form the CaBe_2Ge_2 -type.^[58] I have observed several rare earth-gold-aluminides (e.g. $\text{EuAu}_{0.75}\text{Al}_{3.25}$, $vec = 3.125$), forming the BaAl_4 structure type, with no ordering of the Au and Al atoms, as well as the formation of

several new ternary gold-aluminides, $\text{Ln}_3\text{Au}_2\text{Al}_9$ ($\text{Ln} = \text{Sm, Gd, Tb, Dy, Yb}$), which form the $\alpha\text{-La}_3\text{Al}_{11}$ structure type.

$\text{Ln}_3\text{Au}_2\text{Al}_9$ ($\text{Ln} = \text{Sm, Gd, Tb, Dy, Yb}$) - New Ternaries Forming the $\alpha\text{-La}_3\text{Al}_{11}$ Structure

Synthesis and Characterization

The new ternary compounds $\text{Ln}_3\text{Au}_2\text{Al}_9$ ($\text{Ln} = \text{Sm, Gd, Tb, Dy, Yb}$) were prepared from the elements in an Ar-filled arc melting furnace, with a zirconium getter for further atmosphere purification, using the same techniques described in chapter 2. The elements, Sm, Gd, Tb, Dy, Ho, Yb, Y (Materials Preparation Center, Ames Lab, 99.0%), Au wire (Aesar 99.95%), and Al foil, were cut into stoichiometric amounts in an Ar-filled glovebox using foil to wrap the metals into a small ball to be transferred to the arc melting chamber. The reaction products were shiny silver and homogeneous in appearance, and the arc-melted buttons were easily broken with a mortar and pestle and ground into dark gray or black powders. Table 5.1 gives the reactant composition and the products identified by powder X-ray diffraction. The $\text{Dy}_3\text{Au}_2\text{Al}_9$ product was wrapped in Nb foil and sealed in an evacuated fused silica tube for annealing (850 °C, 14 days). These new compounds crystallize in a ternary derivative of the $\alpha\text{-La}_3\text{Al}_{11}$ -type.

Table 5.1: $\text{Ln}_3\text{Au}_2\text{Al}_9$ ($\text{Ln} = \text{Sm, Gd, Tb, Dy, Ho, Yb, Y}$) reactions and products identified by X-ray diffraction. For those reactions in which multiple phases were observed in the powder patterns, the major product is indicated with a (*).

reactant composition	reaction products	X-ray characterization
$\text{Sm}_3\text{Au}_2\text{Al}_9$	$\text{Sm}_3\text{Au}_2\text{Al}_9$ * + ' SmAu_xAl_y '	powder
$\text{Gd}_3\text{Au}_2\text{Al}_9$	$\text{Gd}_3\text{Au}_2\text{Al}_9$ * + ' GdAu_xAl_y '	powder
$\text{Tb}_3\text{Au}_2\text{Al}_9$	$\text{Tb}_3\text{Au}_2\text{Al}_9$	powder
$\text{Dy}_3\text{Au}_2\text{Al}_9$	$\text{Dy}_3\text{Au}_2\text{Al}_9$	powder, single crystal
$\text{Ho}_3\text{Au}_2\text{Al}_9$	' AuAl_2 ' + ?	powder
$\text{Yb}_3\text{Au}_2\text{Al}_9$	$\text{Yb}_3\text{Au}_2\text{Al}_9$	powder
$\text{Y}_3\text{Au}_2\text{Al}_9$	' AuAl_2 ' + ' YAu_xAl_y '	powder

Powder X-ray structure analysis was carried out on all the products, using an Enraf-Nonius Guinier camera (Cu $K\alpha_1$ with Si standard), and for $Dy_3Au_2Al_9$, single crystal analysis was carried out on a Siemens (Mo $K\alpha_1$) diffractometer. By powder X-ray diffraction $Dy_3Au_2Al_9$, $Tb_3Au_2Al_9$, and $Yb_3Au_2Al_9$, were single phase products, and using measured lines from the powder pattern lattice parameters were refined. The refined lattice parameters for these ternary gold compounds are listed in Table 5.2, and decrease according to the decreasing size of the rare earth atoms from Sm to Yb.

Table 5.2: The refined lattice parameters from powder X-ray data.

Compound	a (Å)	b (Å)	c (Å)
$Sm_3Au_2Al_9$	4.305 (4)	10.064 (3)	12.733 (2)
$Gd_3Au_2Al_9$	4.275 (3)	9.978 (4)	12.602 (8)
$Tb_3Au_2Al_9$	4.276 (3)	9.970 (5)	12.583 (8)
$Dy_3Au_2Al_9$	4.265 (1)	9.952 (2)	12.563 (4)
$Yb_3Au_2Al_9$	4.251 (3)	9.952 (5)	12.522 (9)

$Sm_3Au_2Al_9$, $Gd_3Au_2Al_9$ were the major phases identified in the reaction products, but a cubic Laves phase was also identified in the powder pattern. $SmAl_2$ and $GdAl_2$ are both cubic Laves phases, and the lines in the product powder patterns match those of the binary aluminides well. However, the theoretical X-ray powder patterns of $LnAu_xAl_{2-x}$ (where $0 < x < 1$), differ only slightly from the theoretical patterns of the binary aluminides, making it difficult to assess the composition of the Laves phase without a single crystal refinement. While there are no $LnAu_xAl_{2-x}$ cubic Laves phases reported in *Pearson's Handbook of Crystallographic Data for Intermetallic Phases*, several $LnAg_xAl_{2-x}$ phases are known.

Dy₃Au₂Al₉: Structure Solution

A crystal fragment of Dy₃Au₂Al₉ taken from the annealed product was loaded in air into a glass capillary, for single crystal X-ray analysis. Peaks located from a rotation photo were used to obtain a unit cell whose orientation matrix was refined using a group of 48 reflections in the 2θ range 10° to 30°. A data set of 899 reflections, containing 295 unique reflections, as well as absorption correction reflections, was collected on a Siemens P4 diffractometer at 298 ± 1 K. Lorentz and polarization corrections were applied to the data set. A semi-empirical absorption correction was applied based on a series of azimuthal reflections collected. The structure was solved using direct methods with refinement calculations performed on a Digital Equipment Micro Vax 3100 computer using SHELXTL-PLUS^[43] programs as described in chapter 2. Table 5.3 summarizes the important structure solution information and Table 5.4 contains positional and displacement parameters for the Dy₃Au₂Al₉ structure.

Physical Measurements

Several crystallites of Dy₃Au₂Al₉ were analyzed with energy-dispersive spectroscopy in a Jeol 6100 scanning electron microscope, which indicated that Dy, Au and Al were the only elements present in the sample.

Small pieces from the buttons of Dy₃Au₂Al₉ (annealed, 0.0392 g), Gd₃Au₂Al₉ (0.0328g), and Tb₃Au₂Al₉ (0.0254g) were glued inside straws for magnetic susceptibility measurements from 6 K to 300 K at a field strength of 3 Tesla, see Figures 5.2, 5.3 and 5.4. For multiple magnetic atoms per formula unit the calculated effective moment is determined by equation (1).

$$\mu_{\text{eff}} = g [n(J)(J+1)]^{1/2} \quad (\text{where } n \text{ is the \# mag. atoms/formula unit}) \quad (1)$$

Magnetic susceptibility measurements on Dy₃Au₂Al₉ showed Curie-Weiss paramagnetism with an effective moment of 18.54(4) μ_B (for T >100 K), corresponding to three noninteracting Dy⁺³ (f⁹), or 10.70μ_B per Dy⁺³ atom. By equation (1), the magnetic moment for three noninteracting Dy⁺³ atoms is 18.43 μ_B. Gd₃Au₂Al₉ also showed

paramagnetic behavior with an effective moment of 12.82(1) μ_B (for $T > 150K$), corresponding to three noninteracting Gd^{+3} (f^7), or 7.40 μ_B per Gd^{+3} atom. $Tb_3Au_2Al_9$ also showed Curie-Weiss paramagnetism with an effective moment of 15.71(1) μ_B (for $T > 100K$), which is slightly higher than the moment expected for three noninteracting Tb^{+3} (f^8) of 14.70 μ_B , or 8.50 μ_B per Tb^{+3} atom.

Table 5.3: A summary of the single crystal refinement of $Dy_3Au_2Al_9$.

Refined Composition	$Dy_3Au_{2.08}Al_{8.92}$
Space Group	<i>Immm</i> (no. 71)
Unit Cell Dimensions	$a = 4.262(1) \text{ \AA}$ $b = 9.941(2) \text{ \AA}$ $c = 12.552(4) \text{ \AA}$
Unit Cell Volume	$531.8(2) \text{ \AA}^3$
Z	2
Density (calc.)	7.106 Mg/m^3
Crystal habit : shape	silver : irregular
Absorption Coefficient	50.079
Radiation	Mo $K\alpha$ ($\lambda = 0.71073 \text{ \AA}$)
Temperature (K)	298(1)
$2\theta_{\text{max}}$	50°
Scan Range (ω)	0.85°
Scan Speeds	Variable; 3.0 to $20.0^\circ/\text{min}$. in ω
Index Ranges	$-5 \leq h \leq 5, -11 \leq k \leq 11, -14 \leq l \leq 14$
Reflections Collected	588
Independent Reflections	295 ($R_{\text{int}} = 0.0272$)
Observed Reflections	253 ($F_o \geq 2.0\sigma(F_o)$)
Weighting Scheme	$w = 1/[s^2(F_o^2) + (0.0331P)^2 + 0.0P]$ *
Parameters Refined	33
R Indices [$F_o \geq 2.0\sigma(F_o)$]	$R = 0.0253$ $wR = 0.0589$
R Indices (all data)	$R = 0.0329$ $wR = 0.0617$
Goof (all data)	1.008
Data-to-Parameter Ratio	7.7:1
Largest Difference Peak	1.487 e/\AA^3
Largest Difference Hole	-1.272 e/\AA^3

$$* P = (F_o^2 + 2F_c^2) / 3$$

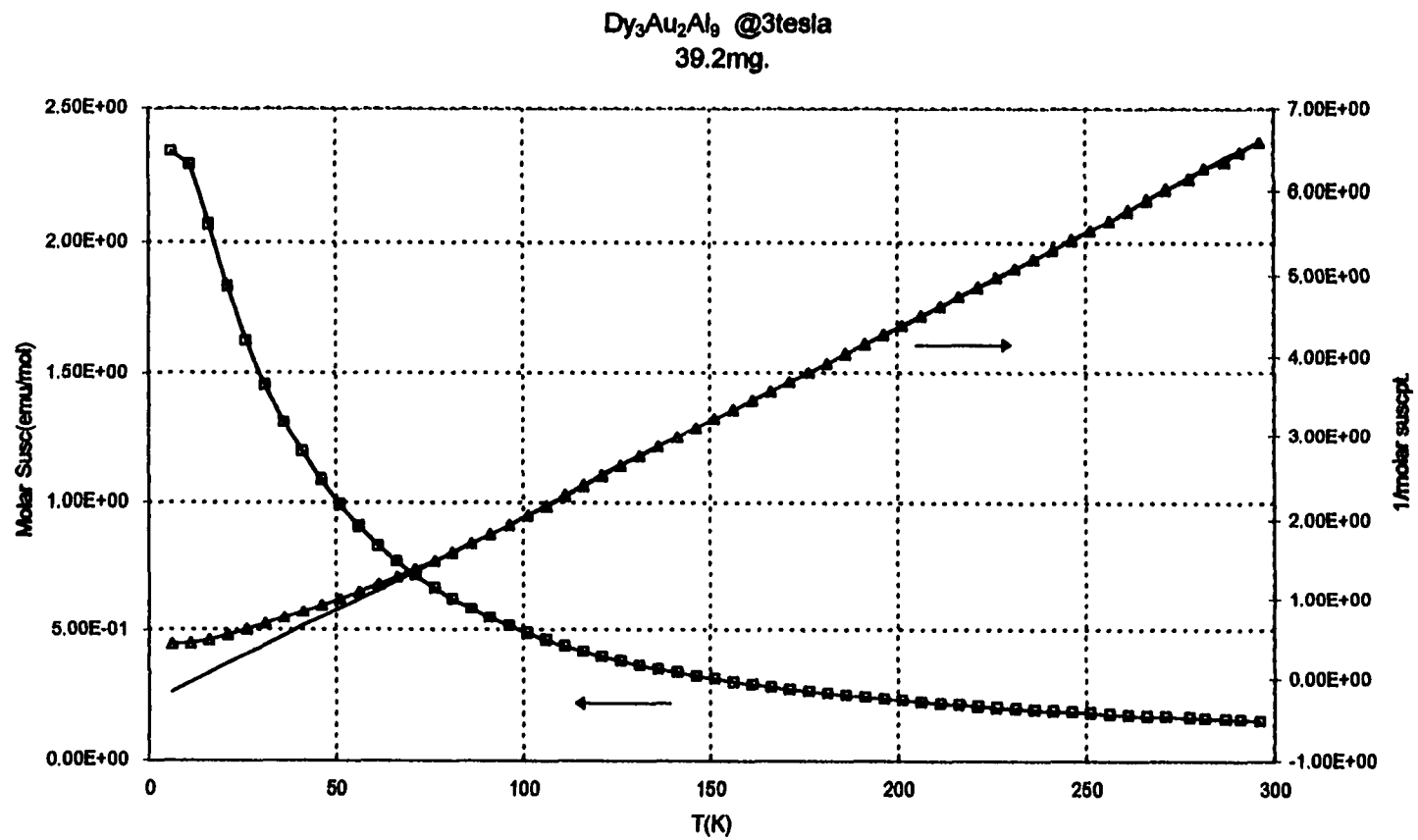


Figure 5.2: The magnetic susceptibility data for $Dy_3Au_2Al_9$.

Nordell $Gd_3Au_2Al_9$ @3tesla
32.8mg

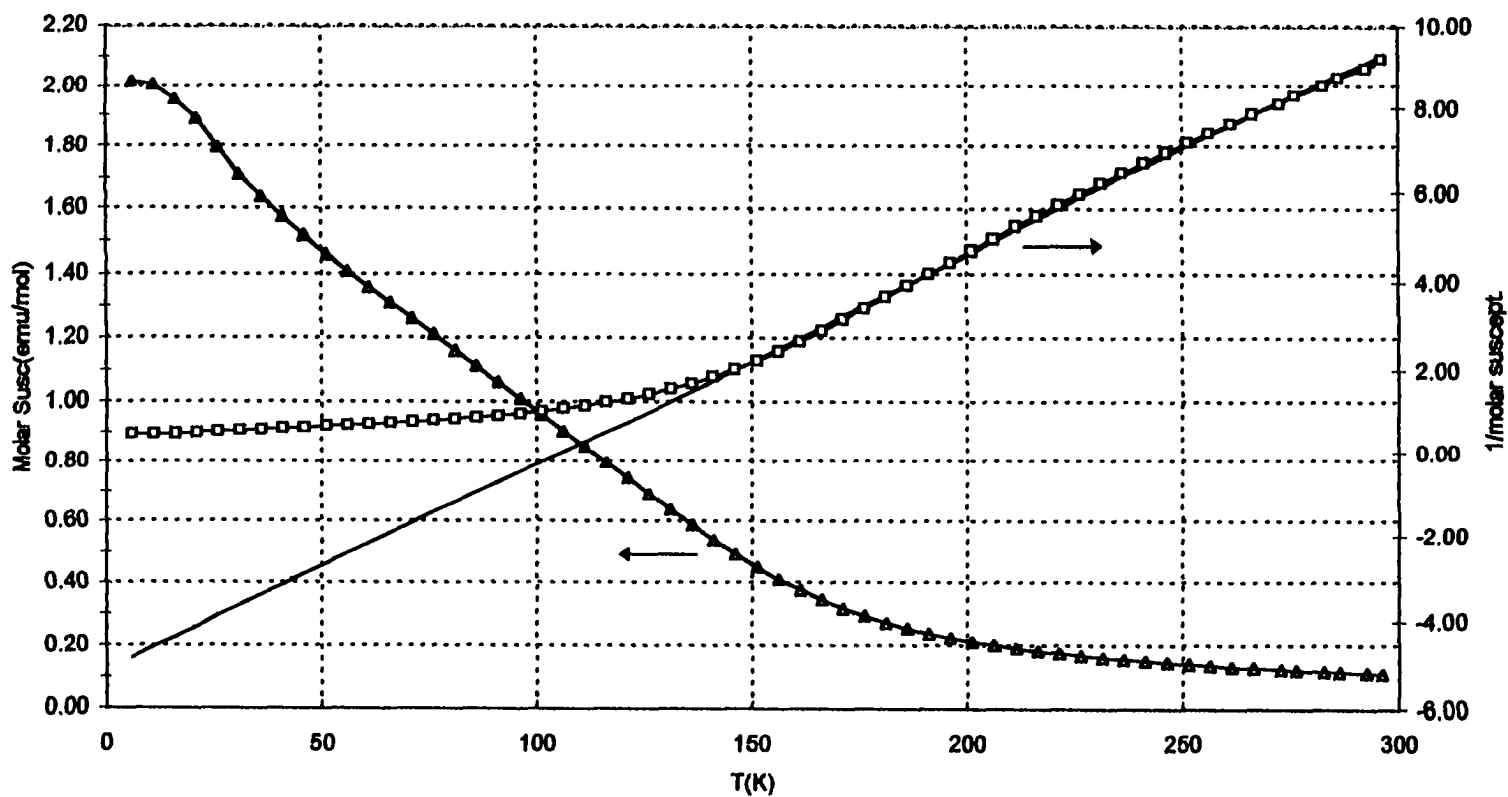


Figure 5.3 : The magnetic susceptibility curve for $Gd_3Au_2Al_9$.

Nordell Tb₃Au₂Al₉ @3tesla
25.4mg

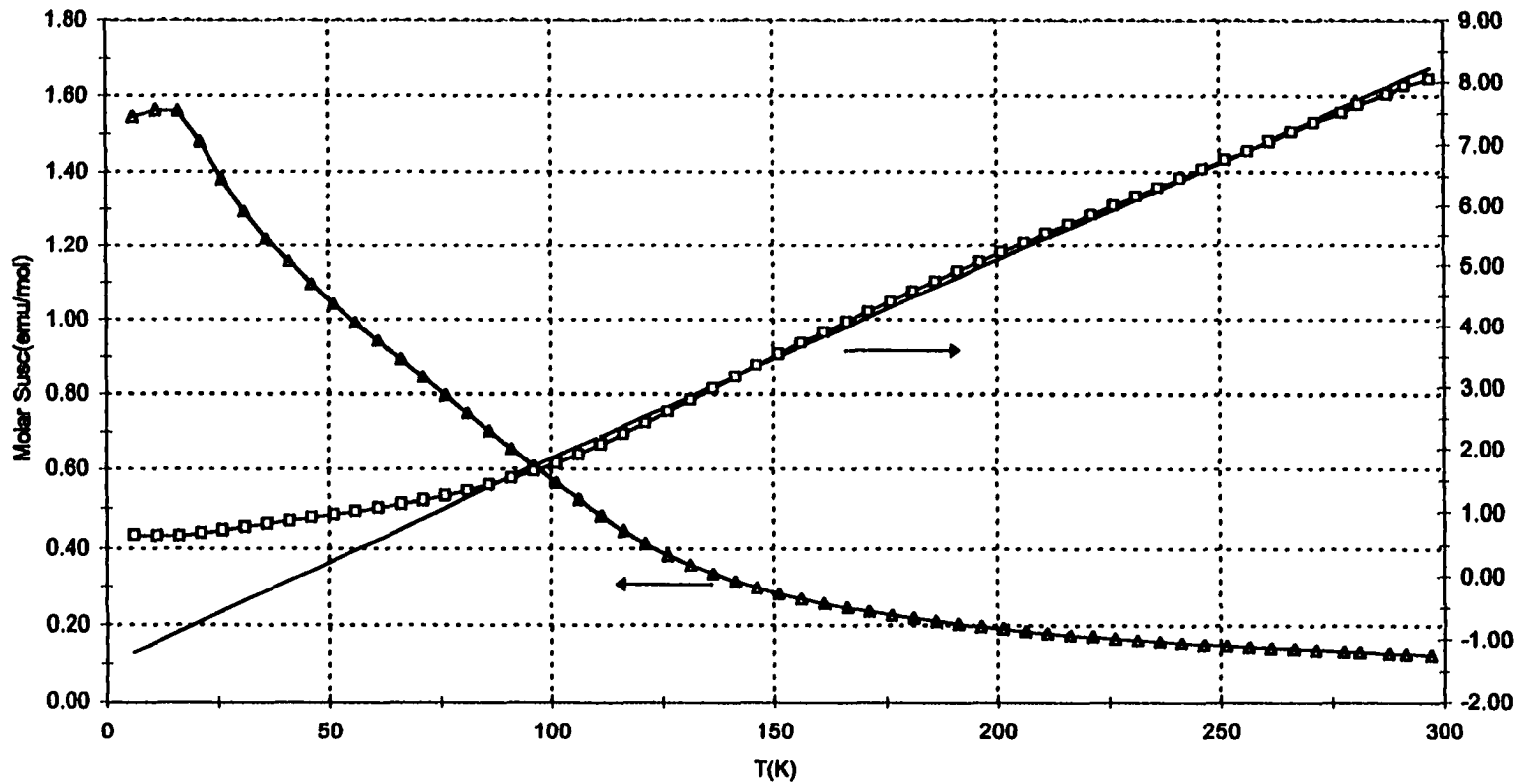


Figure 5.4: The magnetic susceptibility measurement for Tb₃Au₂Al₉.

Table 5.4: A summary of structural information for Dy₃Au₂Al₉.

Refined Composition		Dy ₃ Au _{2.08} Al _{8.92}				
Space Group		<i>Immm</i> (no. 71)				
Unit Cell Dimensions *		<i>a</i> = 4.265(1) Å				
		<i>b</i> = 9.952(2) Å				
		<i>c</i> = 12.563(4) Å				
Atom	Wyckoff	x	y	z	occ.	U _{eq}
Dy1	2 <i>a</i>	0	0	0	1.0	0.0080(4)
Dy2	4 <i>i</i>	0	0	0.3155(1)	1.0	0.0081(3)
Au1	8 <i>n</i>	0	0.3608(1)	0.3401(1)	0.484(3)	0.0092(5)
Al1	8 <i>n</i>	0	0.3927(2)	0.3462(8)	0.516(3)	0.0092(5)
Au2	4 <i>h</i>	0	0.2137(4)	0.5	0.068(4)	0.0097(14)
Al2	4 <i>h</i>	0	0.2137(4)	0.5	0.932(4)	0.0097(14)
Al3	8 <i>l</i>	0	0.2716(4)	0.1477(3)	1.0	0.0099(9)
Al4	2 <i>d</i>	0	0.5	0	1.0	0.013(2)

* Lattice parameters as refined from powder X-ray data.

Dy₃Au₂Al₉ - Structure Description

Note: Multiple crystals of Dy₃Au₂Al₉ were analyzed by single crystal X-ray diffraction techniques, and the following structure description and electronic structure discussion will be in reference to this compound. The other Ln₃Au₂Al₉ phases (Ln = Sm, Gd, Tb, Yb) are considered isostructural based on the powder X-ray analysis, but their structures and compositions have not been confirmed by single crystal analysis.

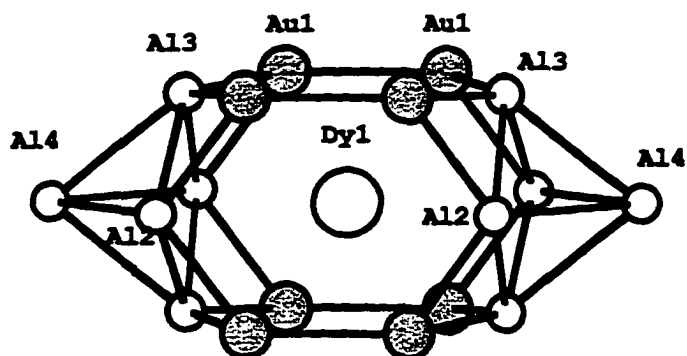
Dy₃Au₂Al₉ forms the α -La₃Al₁₁ structure type whose body-centered orthorhombic unit cell contains 2 formula units or 28 atoms, and is closely related to BaAl₄ (see Figure 5.1(right)). In BaAl₄, sheets of square pyramids are linked together along the *c*-direction by direct connections between apex atoms, which results in the formation of 18-vertex polyhedra surrounding the Ba atoms. As mentioned earlier, calculations suggest these linkages to be two-center, two-electron bonds.^[54a] In α -Ln₃Al₁₁, the unit cell is three times as large, and two of the apex-apex connections have been condensed to single atoms (Al4), which have square prismatic coordination, and account for the deficiency in Al

making the composition $\text{Dy}_3\text{Au}_2\text{Al}_9$ and not “ $\text{Dy}_3\text{Au}_2\text{Al}_{10}$ ”. This difference from BaAl_4 also leads to the disruption of the square net of Al atoms (the bases of the square pyramids) into ribbons along the a axis. There are two types of polyhedra surrounding the Dy atoms: (1) an elongated rhombic dodecahedron composed of 18 Al and Au atoms, Figure 5.5 (a), surrounds the Dy1 atoms on the corners and body center of the cell; and (2) an irregular polyhedron composed of 16 Al and Au atoms, Figure 5.5 (b), encapsulates each Dy2 atom. The large gray atoms in Figure 5.5 (labeled Au1), which is an averaged position of the Au1 and Al1 parameters (see Table 5.4), form a cube around the Dy1 atom and are occupied by 48.4(3)% Au and 51.6(3)% Al. The one-dimensional ribbons of squares which extend in the a -direction (position 4h, labeled Al2 in Figure 5.5), contain a small fraction of gold atoms (6.8(4)%).

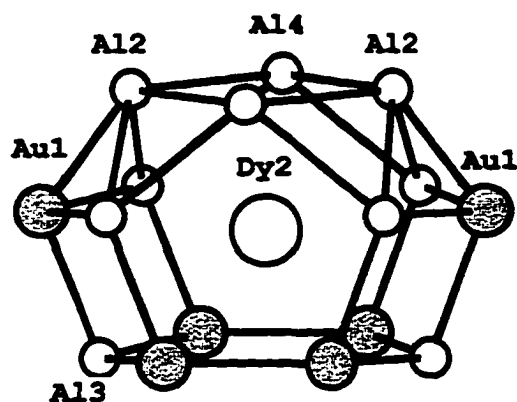
Electronic Structure Calculations on $\text{Ln}_3\text{Au}_2\text{Al}_9$

Extended Hückel calculations^[48] were performed on $\text{Ln}_3\text{Au}_2\text{Al}_9$ to examine the electronic structure of this compound and to help understand the mixing of Au and Al within the structure. Valence atomic orbitals of Y were selected to mimic Dy without its localized 4f orbitals, since the ionic radius of Y^{3+} (1.773 Å) is similar to Dy^{3+} (1.775 Å).^[71] Usually we can treat these elements as classical cations, Ln^{3+} , but with the shortest Dy–Al distance of 3.067(7) Å and the shortest Dy–Au distance of 3.204(1) Å, we included them in the calculation. Table 5.5 contains the atomic parameters used in the calculations for Y, Au and Al.^[27,52]

As an initial investigation of the electronic structure of the aluminum-rich framework, we considered the homoatomic $^3[\text{Al}_{11}]^{2-}$ framework from $\alpha\text{-La}_3\text{Al}_{11}$ with an electron count of 38, which is appropriate for $\text{Ln}_3\text{Au}_2\text{Al}_9$. Mulliken populations were calculated for each atomic position: these are 3.676 (8n), 3.374 (4h), 3.266 (8l), and 3.512 (2d). For 42 electrons per formula unit, the electron count appropriate for $\text{La}_3\text{Al}_{11}$, the Mulliken populations are, 3.900 (8n), 3.653 (4h), 3.810 (8l), and 3.853 (2d). The position



(a) The 18-vertex elongated rhombic dodecahedron around Dy1 with Au1 atoms shown but not Al1. Dy1 distances to the framework atoms are: Dy1–Au1 3.238(1) Å, Dy1–Al2 3.555(2) Å, Dy1–Al3 3.275(2) Å, and Dy1–Al4 4.971(3) Å. Other bond distances within the framework: Au1–Au1 2.767(2)Å, Al1–Al1 2.13(2)Å, Au1–Al1 2.452(1)Å, Au1–Al3 2.509(2)Å, Au1–Al2 2.484(2)Å, Al1–Al2 2.625(1)Å, Al4–Al3 2.931(4)Å, Al4–Al2 3.009(3)Å. Bond distance Dy1–Al1, not shown 3.067(7)Å.



(b) The 16-vertex polyhedron around Dy2, with Au1, but not Al1 atoms shown. Distances are: Dy2–Al1 3.130(9) Å, Dy2–Au1 3.204(1) Å, Dy2–Au2/Al2 3.143(3)Å, Dy2–Al3 3.148(3) Å, and Dy2–Al4 3.1474(9) Å.

Figure 5.5: The polyhedra surrounding the (a) Dy1 and (b) Dy2 atoms.

with the largest population at both electron counts is the 8n position. Using Mulliken populations for the ${}^3[\text{Al}_{11}]^{2-}$ framework as a guide for the atomic ordering in the ternary compound, the positions with the largest Mulliken populations would be the positions most likely occupied by the atoms with the largest electronegativity.^[53] The Pauling electronegativity of gold is 2.4, and aluminum is 1.5.^[47] In the ternary compound $\text{Dy}_3\text{Au}_2\text{Al}_9$, this 8n position is occupied by 48.4(3)% Au and 51.6(3)% Al.

Table 5.5: The atomic orbital parameters used for the extended Hückel calculations.^[27]

Element	Atomic Orbital	H_{ii} (eV)	ζ_1	C_1	ζ_2	C_2
Al	3s	-12.30	1.37			
	3p	-6.50	1.36			
Au	6s	-10.92	2.60			
	6p	-5.55	2.58			
	5d	-15.07	6.16	0.6444	2.79	0.5357
Y ^[52]	5s	-6.78	1.74			
	5p	-4.28	1.70			
	4d	-6.50	1.56	0.8316	3.55	0.3041

Since the X-ray diffraction experiment indicated no special ordering of Au and Al atoms on the 8n position, calculations were performed on model structures in which the Au and Al atoms were arranged with only homoatomic (Au–Au and Al–Al) or only heteroatomic (Au–Al) contacts. The partial density of states (DOS) curve for the ${}^3[\text{Au}_2\text{Al}_9]^{9-}$ framework in $\text{Ln}_3\text{Au}_2\text{Al}_9$ and the crystal orbital overlap population (COOP) curve for the Au1–Al1 contacts are shown in Figure 5.6. The Fermi energy lies in an area of nonzero DOS, and falls in the region of the crossover from bonding to antibonding levels in the Au1–Al1 COOP curve indicating a near optimization of the bonding at this *vec*. The total energy for the structure with just heteroatomic contacts is 0.5 eV per

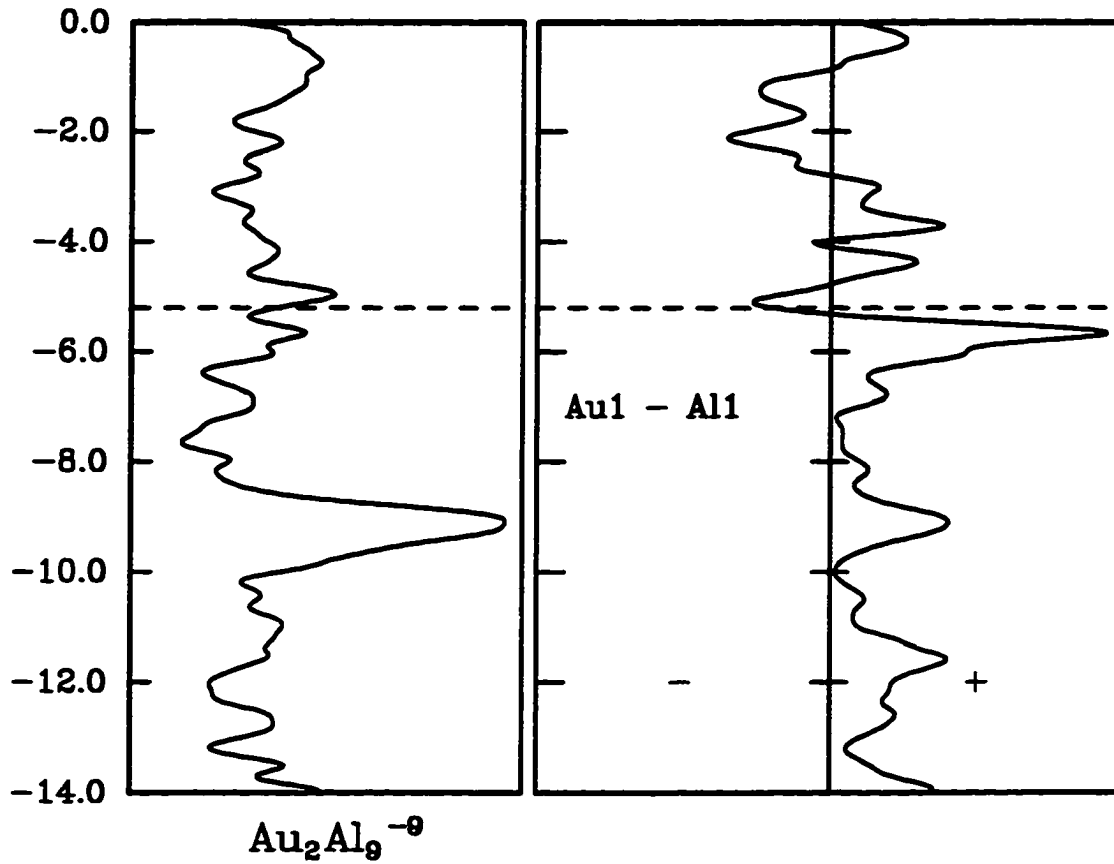


Figure 5.6: Left: (a) The partial DOS curve for the ${}^3[\text{Au}_2\text{Al}_9]^{-9}$ framework of $\text{Y}_3\text{Au}_2\text{Al}_9$. Right: (b) The crystal orbital overlap population curve for the Au1-Al1 interaction, showing the nearly optimal filling of bonding orbitals (+), and leaving unfilled the antibonding orbitals (-). The Fermi energy is -5.21 eV, and is marked with a dotted line.

formula unit lower than that of the structure with homoatomic contacts.^[59] Having two such bonding contacts per formula unit, with only heteroatomic Au–Al contacts places an upper limit of two gold atoms per formula unit. These results indicate there may be a range in composition between $x = 0$ and 2, for $\text{Ln}_3\text{Au}_x\text{Al}_{11-x}$.

EuAu_{0.75}Al_{3.75} - A Disordered Ternary Derivative of BaAl₄

Synthesis and Structure Solution

The synthesis of this europium-gold-aluminide was carried out in an arc welding furnace from the elements, with the reactant composition EuAuAl_5 . Based on powder X-ray diffraction the product was a mixture of Al and a 'BaAl₄' - like phase (but not EuAl_4), and some weak lines which could not be assigned. A crystal from the reaction product was loaded onto a fiber in air with epoxy. Peaks located from a rotation photo were used to obtain a unit cell whose orientation matrix was refined using a group of 34 reflections in the 2θ range 13° to 30° . A data set of 262 reflections, containing 77 unique reflections, as well as absorption correction reflections, was collected on a Siemens P4 diffractometer at 298 ± 1 K. Lorentz and polarization corrections were applied to the data set. A semi-empirical absorption correction was applied based on a series of azimuthal reflections collected. The structure was solved using direct methods with refinement calculations performed on a Digital Equipment Micro Vax 3100 computer using SHELXTL-PLUS^[43] programs as described in chapter 2. Table 5.6 summarizes the important structure solution information and Table 5.7 contains positional parameters, site occupancies and displacement parameters for the $\text{EuAu}_{0.75}\text{Al}_{3.25}$ structure.

Structure Description

The structure of $\text{EuAu}_{0.75}\text{Al}_{3.25}$ is a ternary variant of BaAl_4 in which Au₂ and Al₂ atoms occupy the positions which connect the two-dimensional square nets of Al₁₁ atoms, see Figure 5.7. This arrangement of Au₂ and Al₂ atoms in $\text{EuAu}_{0.75}\text{Al}_{3.25}$ is similar to the Au and Al distribution in $\text{Dy}_3\text{Au}_2\text{Al}_9$. The structure solution indicated no ordering

Table 5.6: A summary of the structure refinement for $\text{EuAu}_{0.75}\text{Al}_{3.25}$.

Refined Composition	$\text{EuAu}_{0.78}\text{Al}_{3.22}$
Space Group	$I4/mmm$ (no. 139)
Unit Cell Dimensions	$a = 4.318(1) \text{ \AA}$ $c = 11.165(2) \text{ \AA}$
Unit Cell Volume	$208.17(8) \text{ \AA}^3$
Z	2
Density (calc.)	6.261 Mg/m^3
Crystal habit : shape	silver : irregular
Absorption Coefficient	50.079
Radiation	Mo $K\alpha$ ($\lambda = 0.71073 \text{ \AA}$)
Temperature (K)	298(1)
$2\theta_{\text{max}}$	50°
Scan Range (ω)	0.85°
Scan Speeds	Variable; 3.0 to $20.0^\circ/\text{min.}$ in ω
Index Ranges	$-5 \leq h \leq 5, -5 \leq k \leq 5, -13 \leq l \leq 13$
Reflections Collected	262
Independent Reflections	77 ($R_{\text{int}} = 0.1109$)
Observed Reflections	64 ($F_o \geq 2.0\sigma(F_o)$)
Parameters Refined	14
R Indices [$F_o \geq 2.0\sigma(F_o)$]	$R = 0.0277$ $wR = 0.0612$
R Indices (all data)	$R = 0.0367$ $wR = 0.0647$
Goof (all data)	1.187
Data-to-Parameter Ratio	4.5:1
Largest Difference Peak	1.460 e/\AA^3
Largest Difference Hole	-1.546 e/\AA^3

Table 5.7: Positional Parameters and Occupancies for $\text{EuAu}_{0.75}\text{Al}_{3.25}$

Refined Composition: $\text{EuAu}_{0.78}\text{Al}_{3.22}$						
$a = 4.318(1) \text{ \AA}$						
$c = 11.165(2) \text{ \AA}$						
Space Group $I4/mmm$ (No. 139)						
Atom	Wyckoff	x	y	z	occ.	U_{eq}
Eu	2a	0	0	0	1.0	0.015(1)
Al1	4d	-0.5	0	0.25	1.0	0.014(2)
Al2	4e	0	0	0.3967(28)	0.610(9)	0.013(2)
Au2	4e	0	0	0.3764(4)	0.390(9)	0.013(2)

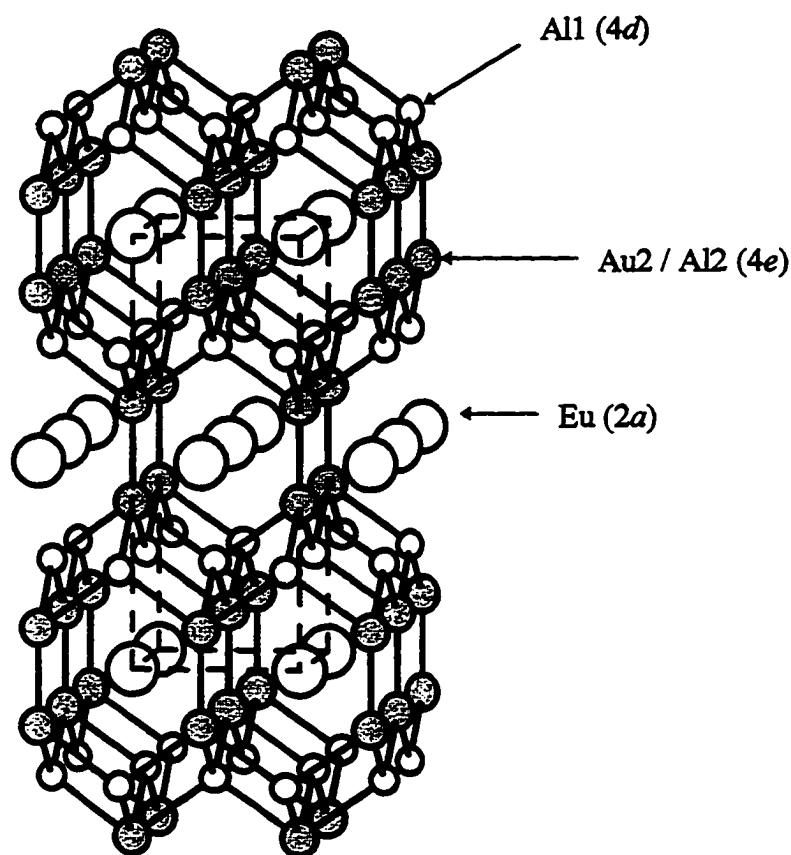


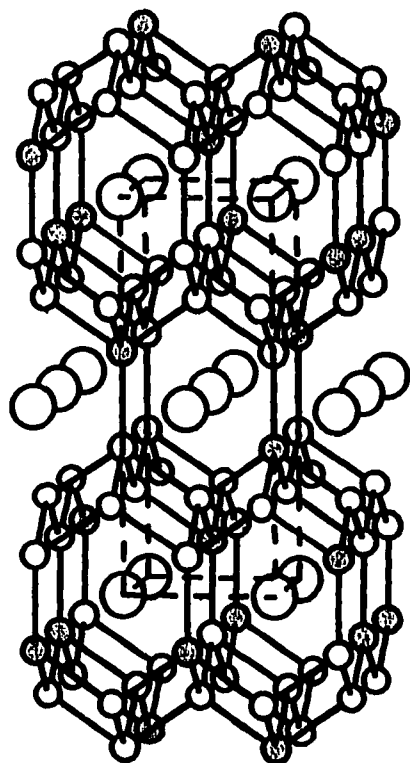
Figure 5.7: The structure of $\text{EuAu}_{0.75}\text{Al}_{3.25}$, with Eu atoms (large open circles) surrounded by 18 vertex polyhedra composed of 8 Al1 (4d) atoms (small open circles), and 10 Au2/Al2 (4e) atoms (gray circles). The average position of the Au2 and Al2 atoms is shown in the figure at (0,0,0.3865). The distances within the structure are; Au2-Al2= 2.53(3)Å, Au2-Au2= 2.759(8)Å, Al2-Al2= 2.31(6), Au2-Al1= 2.580(2)Å, Al2-Al1= 2.71(2). The Eu - Au2/Al2(avg) distances are 3.305(2) Å and 4.315(1)Å, and the distance between Eu and Al1 is 3.5288(5)Å.

of the Au₂ and Al₂ atoms, and an attempt to refine the data in the space group *I4mm* (BaNiSn₃ structure type) was unsuccessful. It is possible that long term annealing of the sample may allow for the ordering of the Au₂ and Al₂ atoms. Figure 5.8 contains three possible ‘colorings’ of a BaAl₄ network with Au and Al atoms, and the theoretical powder patterns for three possible ternary structures are given in Figure 5.9. Figure 5.9 (a) is the pattern for the refined structure EuAuAl₃ (*I4/mmm*), with no ordering of the Au - Al ‘pairs’. Figure 5.9 (b) is the pattern for the ordered EuAuAl₃ (BaNiSn₃ *I4mm*), which differs only slightly from the pattern for the observed structure (a). Figure 5.9 (c) is the pattern for EuAu₂Al₂ forming the CaBe₂Ge₂ structure (*P4/nmm*), which differs significantly from the other two patterns.

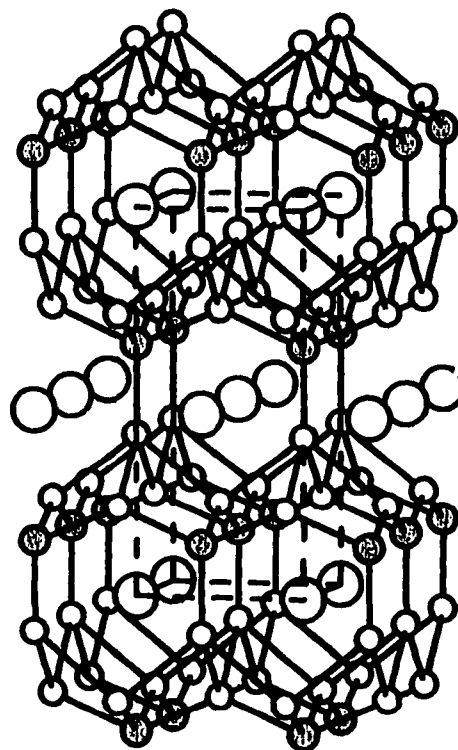
Electronic Structure Calculations on EuAuAl₃

The electronic structure of EuAuAl₃ was investigated using extended Hückel calculations. The Eu atoms were treated as classical electron donating cations, due to the long Eu - Al₁ (3.5287 Å) and Eu - Au₂/Al₂ (3.3056 Å, and 4.3158 Å) average distances, and therefore no orbitals of Eu were included. Similar to the electronic structure calculations of Dy₃Au₂Al₉, the first calculation on an all aluminum framework (${}^3[\text{Al}_4]^{n-}$), was used to indicate which positions the more electronegative Au atoms would be most likely to occupy based on the Mulliken populations. For an electron count appropriate for EuAu_{0.75}Al_{3.25} (12.5 electrons / formula unit), the two sites Al₂ (4e), and Al₁ (4d) had Mulliken populations of 3.419 (Al₂) and 2.831 (Al₁), and for an electron count appropriate for EuAuAl₃, (12 electrons / formula unit), the populations were 3.243 (Al₂) and 2.757 (Al₁). Since gold is the more electronegative of the two elements (Au: 2.4 and Al: 1.5),^[47,53] the gold atoms preferentially occupy the sites with the greater Mulliken population, Al₂. The structure refinement of EuAu_{0.75}Al_{3.25} indicated a mixture of 61(1)% aluminum and 39(1)% gold on the 4e position.

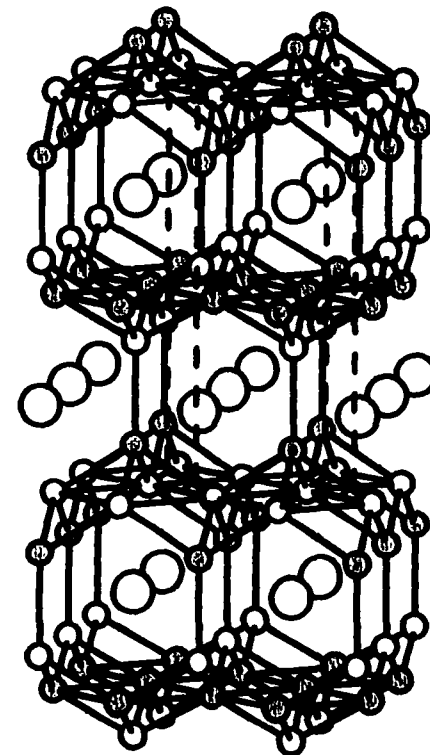
In the same manner that we examined the preference for homoatomic (Au - Au, Al - Al) or heteroatomic (Al - Au) contacts in Dy₃Au₂Al₉, we considered them in the EuAuAl₃ compound as well. In Table 5.7 the total energies for three different gold-



EuAuAl₃ - BaAl₄
I4/mmm



EuAuAl₃ - BaNiSn₃
I4mm



EuAu₂Al₂ - CaBe₂Ge₂
P4/nmm

Figure 5.8: Three 'colorings' of a BaAl₄ framework. The first coloring (left) is the refined EuAuAl₃ structure with disordered Au - Al 'pairs'. The middle coloring is EuAuAl₃ forming the ordered BaNiSn₃ structure, with all the Au - Al 'pairs' aligned in the c direction. The third coloring (right), is EuAu₂Al₂, adopting the CaBe₂Ge₂ structure type. The small open circles are the Al atoms, the gray circles are the Au atoms, and the large open circles are the Eu atoms.

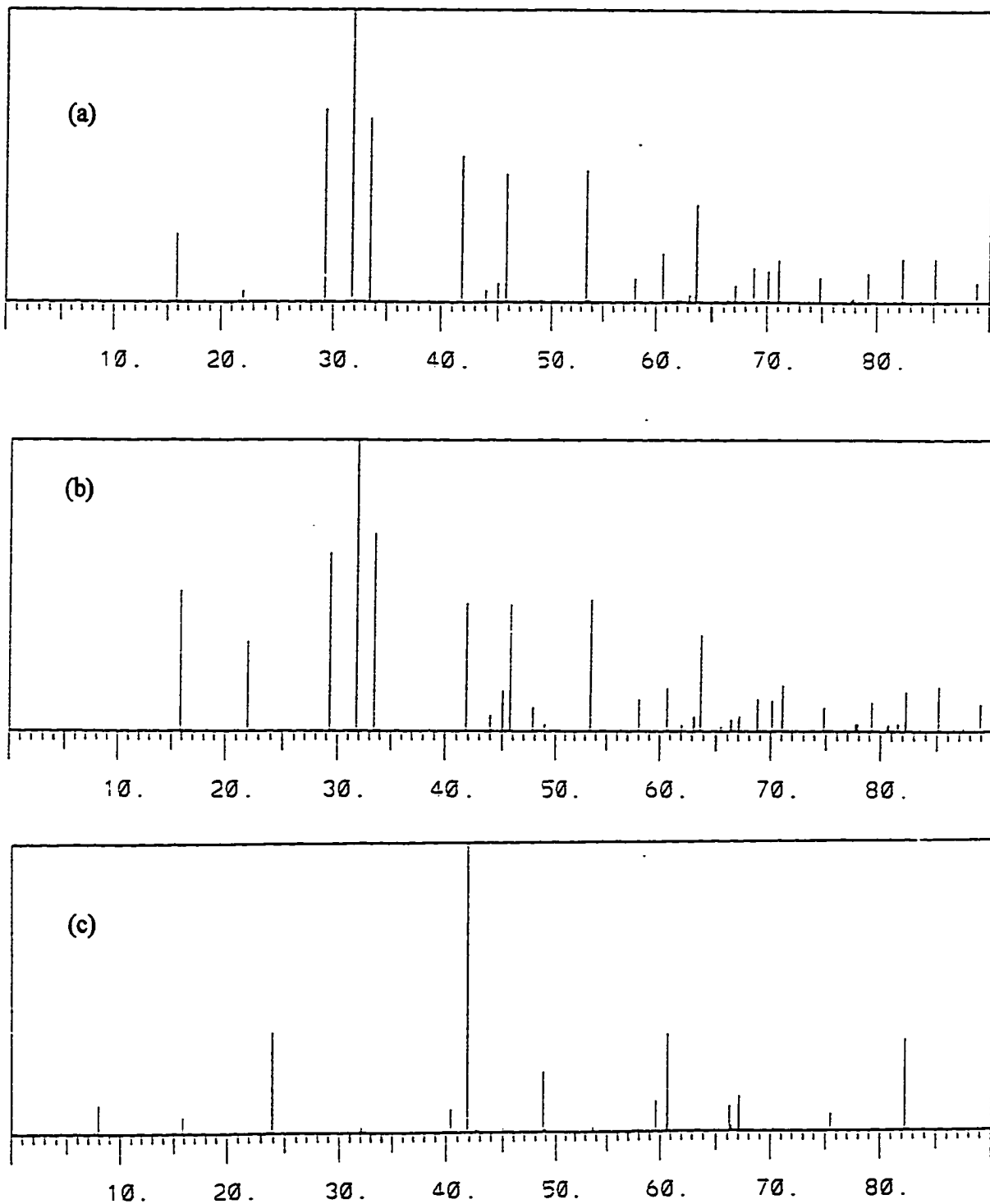


Figure 5.9 (a) The generated powder pattern for EuAuAl_3 as refined in $I4/mmm$. (b) The pattern of ordered EuAuAl_3 , forming the BaNiSn_3 ($I4mm$) structure. (c) The pattern of EuAu_2Al_2 forming the CaBe_2Ge_2 structure ($P4/nmm$).

aluminum arrangements are listed, including the overlap populations for the different interactions. There is an energetic preference for heteroatomic Au -Al contacts in EuAuAl_3 , just as there was in $\text{Dy}_3\text{Au}_2\text{Al}_9$. The structures with heteroatomic contacts (calculations 2 and 3) have lower calculated total energies than the structure with homoatomic contacts (calculation 1) by 0.21 eV / formula unit. The complete unit cell contains 2 formula units, which means that within a unit cell the heteroatomic (Au - Al) contacts can be ordered, such that they are aligned in the same direction (BaNiSn_3 : $I4mm$), or such that they alternate. In the case of $\text{EuAu}_{0.75}\text{Al}_{3.25}$, no evidence for the ordering was observed, and the calculated total energies are very similar, with the ordered structure (calc. 3) favored by 0.0036 eV versus the disordered structure (calc. 2).

Table 5.7: The results of extended Hückel calculations on EuAuAl_3 , in which the Au and Al atoms are arranged such that there are either homoatomic (Au - Au, Al - Al) or heteroatomic (Au - Al) contacts.

type of contacts on (4e)	total energy (46 e) (eV / formula unit)	overlap populations
1. homoatomic (Au - Au, Al - Al)	-284.9482	Au-Au 0.7746 Al - Al 0.4015
2. heteroatomic (Au - Al alternating*)	-285.1541	Au - Al 0.5912
3. heteroatomic (Au - Al ordered**)	-285.1577	Au - Al 0.5926

* alternating: the Au - Al contacts are arranged in an alternating pattern along *c*.

** ordered: all the Au - Al contacts are arranged in the same direction along *c*.

Figure 5.10 contains the DOS curve for the disordered EuAuAl_3 structure, and the COOP curve for the Au2 - Al2 heteroatomic contact (4e) at 2.533 Å, with two Fermi energies marked ($44 e^-$ (Eu^{+2}) and $46 e^-$ (Eu^{+3})). In the DOS curve there is a narrow band between -16.0 and -14.0 eV corresponding to the Au d-orbitals, and a gap in the DOS above the Fermi energy between -5.0 and -4.0 eV (refer to Table 5.5). As observed in the calculations of $\text{Dy}_3\text{Au}_2\text{Al}_9$, the Fermi energy falls at the crossover between bonding and antibonding levels for the Au2 - Al2 (4e) contact with an average distance of 2.533 Å.

The compounds LaAuAl_3 and SmAuAl_3 have been synthesized, and characterized by powder X-ray diffraction. The refined lattice parameters of LaAuAl_3 are: $a = 4.355(1)$ Å, $c = 10.887(1)$ Å. From the powder patterns, these phases appear to be isostructural with EuAuAl_3 . However, single crystal solutions need to confirm the composition and distribution of Au and Al within these compounds.

Conclusions

These ternary phases demonstrate the delicate balance between the factors which influence the composition and observed structure for a particular compound. The two factors which appear to be most influential in these ternary gold-aluminides are size and electron count. The LnAl_4 compounds (except EuAl_4) do not form the BaAl_4 structure type because their vec of 3.75 is too high. Instead, they form α - $\text{Ln}_3\text{Al}_{11}$, at low temperatures ($\text{Ln} = \text{La, Ce, Pr, Nd}$), and β - $\text{Ln}_3\text{Al}_{11}$ at high temperatures, ($\text{Ln} \square_{0.33}\text{Al}_{3.67}$, $vec = 3.5$) which is the tetragonal BaAl_4 structure type with ordered vacancies. The inclusion of gold into these compounds results in the lowering of the vec , from 3.75 (LnAl_4), to 3.25 (LnAuAl_3). I have observed the larger (La, Eu, Sm) rare-earth atoms in a disordered BaAl_4 structure type, and Hulliger et al. have reported $\text{LnAu}_x\text{Al}_{4-x}$ ($x = 1-1.5$, $\text{Ln} = \text{La-Tb}$) with $vec = 3.0-3.25$, and $\text{LnAu}_x\text{Al}_{4-x}$ ($x = 1.5-2$, $\text{Ln} = \text{La-Tb}$) with $vec = 2.75-3.0$, which form the BaAl_4 , BaNiSn_3 , and CaBe_2Ge_2 structure types.

Upon moving to the smaller rare-earth atoms ($\text{Gd} - \text{Yb}$), in combination with gold and aluminum, while the electron count is appropriate (i.e. $vec < 3.5$) for the formation of the BaAl_4 structure, the α - $\text{La}_3\text{Al}_{11}$ structure is observed. This structural change is

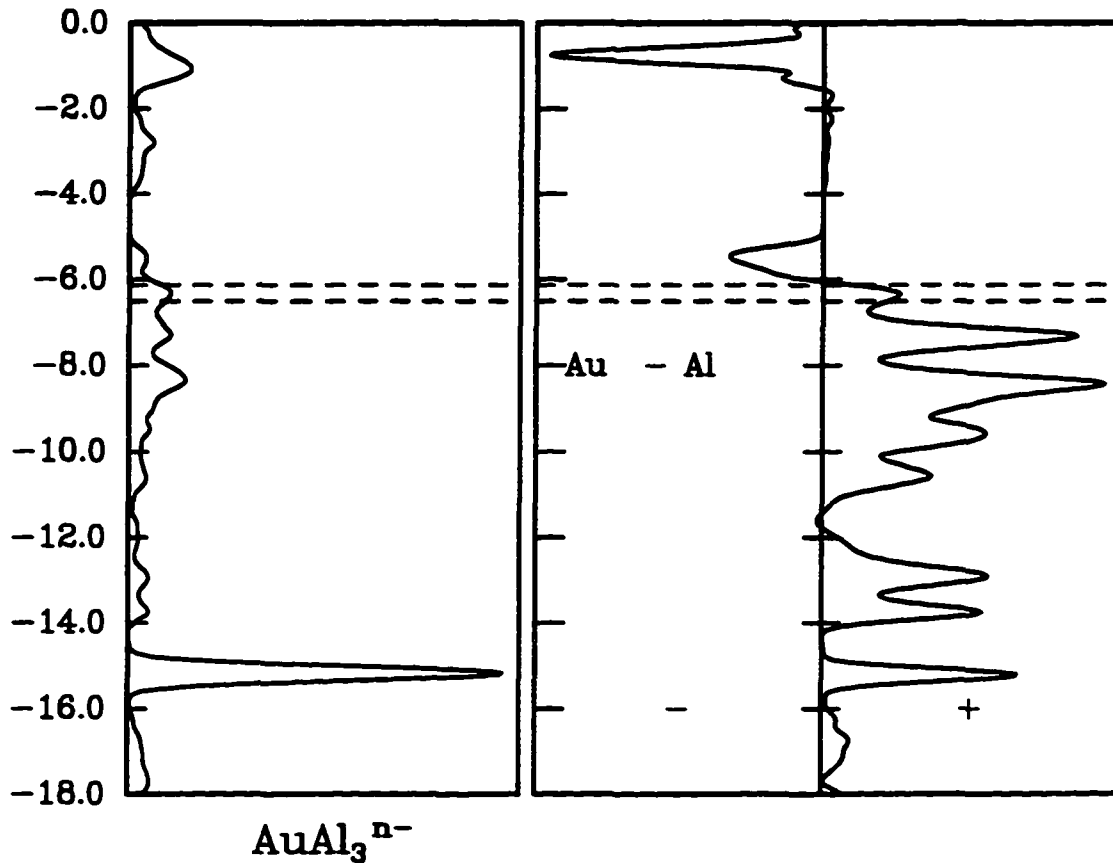


Figure 5.10: Left: (a) The DOS curve for the $[\text{AuAl}_3]^{n-}$ framework of EuAuAl_3 , with the Fermi energies of -6.51 eV ($44e^- \text{Eu}^{+2}$) and -6.13 eV ($46e^- \text{Eu}^{+3}$) marked by the dotted lines. Right: (b) The crystal orbital overlap population curve for the Au - Al interaction, showing the nearly optimal filling of bonding orbitals (+), and leaving unfilled the antibonding orbitals (-).

presumably driven by the preference of the smaller rare-earth atoms for the smaller cages in the $\text{Dy}_3\text{Au}_2\text{Al}_9$ structure.

In both groups of ternary gold aluminides forming structural variants of BaAl_4 and $\alpha - \text{La}_3\text{Al}_{11}$, electronic structure calculations indicate the preference for gold atoms to occupy the short contacts between the layers, and the preference for heteroatomic Au - Al contacts. Further synthesis and electronic structure calculations could further explore these conclusions about the importance of rare-earth atom size, and *vec*.

CHAPTER 6

STRUCTURE SORTING BY *VEC* USING SECOND MOMENT SCALING

Introduction

The Hückel (H) and extended Hückel (eH) tight-binding methods have been applied very successfully to many questions involving electronic structure and orbital interactions within molecules and extended solids.^[48-51] Due to the simplicity of the one-electron Hückel method, it has been applied to a remarkably wide range of systems, with an even more remarkable success and utility. However, because these calculations explicitly ignore electron-electron repulsion, their application has been seriously limited. In particular, one must be careful when using the calculated Hückel energies to compare the relative stabilities of compounds with different structures, because these calculations have an inherent bias favoring structures with more highly coordinated atoms. Because no repulsion energy is considered in the calculation of the total energy, the structure in which the atoms are more highly coordinated will naturally have a lower energy. For example, while at room temperature, graphite is more thermodynamically stable than diamond by 1.9 kJ/mol, a tight-binding calculation of the total energies of diamond (coordination number (CN) = 4, C-C distance = 1.545 Å) and graphite (CN = 3, C-C distance = 1.415 Å) results in diamond being favored by 1eV / atom (1eV = 96.5 kJ / mol).^[60]

However, if the coordination numbers and bond distances of the molecules (or extended structures) to be compared are equal, then the differences in the H energies can be used as reliable predictive tools. This is because the repulsive energy for structures with equivalent bond distances and coordination numbers is the same, allowing the differences in the H energies to more accurately reflect the differences in stability. For example, in the AB₂ systems (where both A and B are main group atoms), H calculations do correctly account for bent or linear molecular geometries.^[61-62] This is a very important result for two reasons, (1) it suggests that repulsive energy is a function of nearest neighbor interactions (i.e. first

coordination sphere), and (2) if the repulsive energies of structures with different coordination numbers and bond distances could be made equivalent, then the calculated H energies would be comparable.^[61] It has been shown that the repulsive energy for different structures can be equalized by scaling the second moments of different structures to a fixed value. For a complete discussion of the theory and development of second moment scaling see references [63-65].

The second moment (μ_2) is defined as,

$$\mu_2 = \sum_{i=1}^N E_i^2 \quad (1)$$

where N is the number of molecular orbitals and E_i is the energy of the *i*th orbital.^[63] Qualitatively, the second moment is a description of the first coordination sphere of the atoms in a structure, and the size of the second moment is a measure of the 'coordination strength' of the atoms. Diamond has a larger second moment than graphite because the atoms in the diamond structure are more highly coordinated than the atoms in graphite. By scaling the second moments of compounds with different structures (like diamond and graphite), the bias of the Hückel calculations can be eliminated since the 'coordination strengths' of the two structures are equalized. The second moments of compounds having different structures are scaled to an intermediate value. After scaling, the Hückel energies of these adjusted structures can be calculated and compared.

In this series of calculations, the Hückel energies are calculated for electron counts from 0 to 8 (s and p) or from 0 to 18 (s, p and d) and are compared as a function of *vec*. Using this method, various structures can be sorted (or separated) into ranges of *vec* for which any particular structure is favored. Second moment scaling has been successfully applied to many groups of structures, including elemental structures,^[66] the Hume-Rothery phases,^[67] and main group intermetallics,^[61] with excellent agreement between calculated and observed results. In fact, second moment scaling calculations were able to separate 7 different Hume-Rothery phases into narrow ranges of *vec* between 1 and 2 which were nearly identical to the ranges for the observed compounds.^[67]

As detailed in the previous chapters, the majority of my synthetic efforts has focused on making new ternary compounds with *vec* between 2 and 4, coupled with the investigation of the electronic structures of these compounds, all in an effort to understand certain aspects of their formation and stability. Among the multitude of factors whose delicate balance results in the observation of a particular structure type for any one compound, the *vec* is undoubtedly an important contributor. With the successful separation of the Hume-Rothery phases using second moment scaling, we decided to use second moment scaling to try to separate intermetallics with *vec* between 1 and 4. The structure-types included in this series of second moment scaling calculations will be discussed in the next section of this chapter.

Structure Types Chosen for Second Moment Scaling

The structure types included in this series of second moment scaling (*sms*) calculations are: NaZn_{13} , ThMn_{12} , BaCd_{11} , BaNi_2Al_9 , MoAl_{12} , and K_4Si_{23} , (see Table 6.1). With the exception of MoAl_{12} , I have observed all of these structure types in the synthesis of ternary aluminides, and the majority of these aluminum-rich compounds have *vec* between 2 and 4. MoAl_{12} was included because the structure contains Mo-centered, interconnected Al_{12} icosahedra, and is similar to the NaZn_{13} structure. Table 6.1 includes a variety of ternary aluminides which form each of the structure types, and the *vec* for each of these compounds. Many of these examples are new ternary compounds which I have made and characterized. However, *Pearson's Handbook of Crystallographic Data for Intermetallic Phases* ^[40] includes many more examples of compounds which form each of these structure types, and ranges of *vec* for each structure type were compiled from the *vec*'s of all of the observed and reported compounds. Figures 6.1- 6.6 are representations of the six structures with the lattice parameters used in the *sms* calculations.

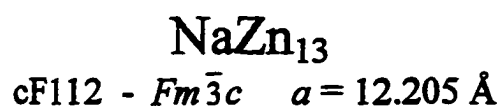
The *vec* is calculated by adding the number of valence electrons per atom in the formula unit, and dividing by the total number of atoms. These ternary aluminides, like the

Table 6.1: The structures included in the second moment scaling calculations, and the ranges of *vec* for observed compounds. ^[40]

Structure Type	number of ternaries	range of <i>vec</i> (s & p)	number of binaries	range of <i>vec</i> (s & p)	examples of aluminide phases	<i>vec</i> (s & p)
NaZn ₁₃	15	2.21-2.38	36	2.08-2.23	BaCu ₅ Al ₈ *	2.38
					SrCu ₆ Al ₇ *	2.23
					BaAg _{5.5} Al _{7.5} *	2.30
ThMn ₁₂	42	0.9-1.55	14	1.5-2.08	LnCu ₄ Al ₈ ‡	2.58
	13	2.58	8	2.25	LnCu ₅ Al ₇ *	2.41
	9	2.25			LnCu ₆ Al ₆	2.25
BaNi ₂ Al ₉	7	2.27-2.636	0		SrNi ₂ Al ₉	2.64
					BaFe ₂ Al ₉	2.27
					EuCo ₂ Al ₉ *	2.45
BaCd ₁₁	4	2.10-2.27	10	2.18-2.27	EuAg ₅ Al ₆ *	2.27
	10	0.2-1.2			LaAg ₅ Al ₆ *	2.36
					EuYbAg ₁₂ Al ₁₄ *	2.27
MoAl ₁₂	0		6	2.66-2.75	WAl ₁₂	2.66
					MnAl ₁₂	2.75
K ₄ Si ₂₃	25	3.5-4.2	4	4.17	Ba ₄ Cu ₃ Ge ₂₀	3.96
					Ba ₄ Ag ₃ Al ₁₀ Si ₁₀ *	3.52
					K ₈ Al ₂₃ Si ₂₃	3.67

* indicates the compounds I have observed and characterized

‡ Ln = Ce, Pr, Nd, Sm, Gd, Tb, Dy, Ho, Er, Tm, Lu, Y



2 atomic positions

(8b) 0, 0, 0

(96i) 0, y, z ($y = 0.117, z = 0.175$)

BaCu₅Al₈ SrAg_{5.5}Al_{7.5}
 EuCu_{6.5}Al_{6.5} LaCu₆Al₇

$vec = 2.2 - 2.4$

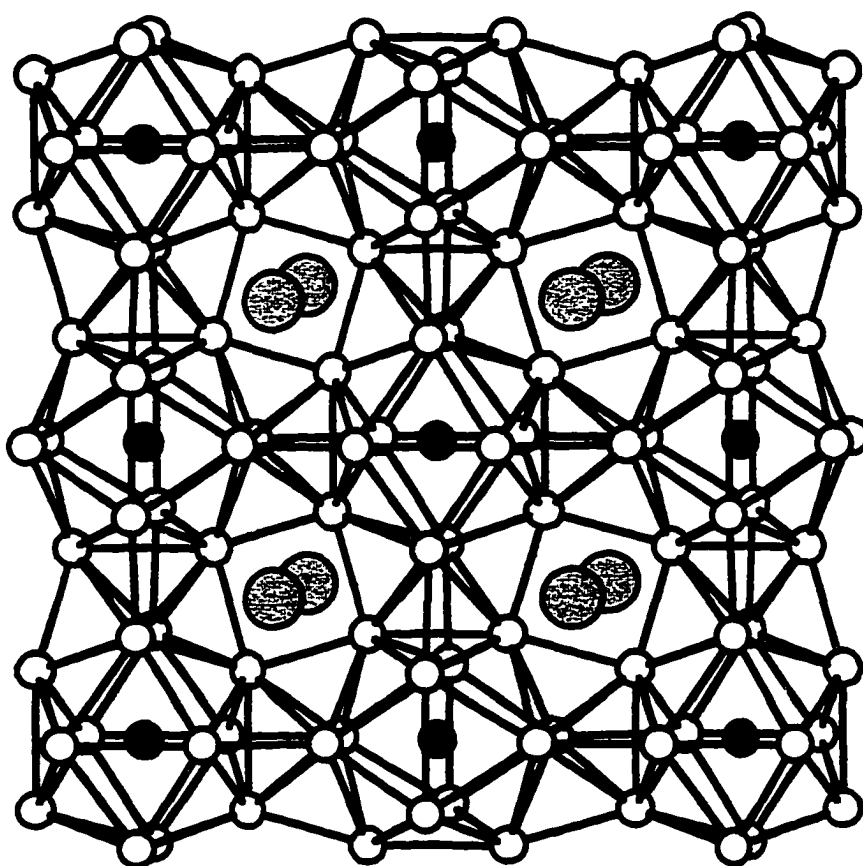


Figure 6.1: The NaZn₁₃ structure, observed for BaCu₅Al₈ and other ternary aluminides. The structure contains a framework of interconnected centered-icosahedra, which form 24-vertex snub cubes around the Na atoms.

ThMn₁₂

tI26 - I4/mmm $a = 8.705 \text{ \AA}$, $c = 5.128 \text{ \AA}$

3 atomic positions

(8f) 0.25, 0.25, 0.25,

(8i) x , 0, 0 ($x = 0.346$)

(8j) x , 0.5, 0 ($x = 0.281$)

LnCu_4Al_8 LnCu_5Al_7 LnCu_6Al_6

Ln = (Y, Ce - Lu)

$vec = 2.1 - 2.6$

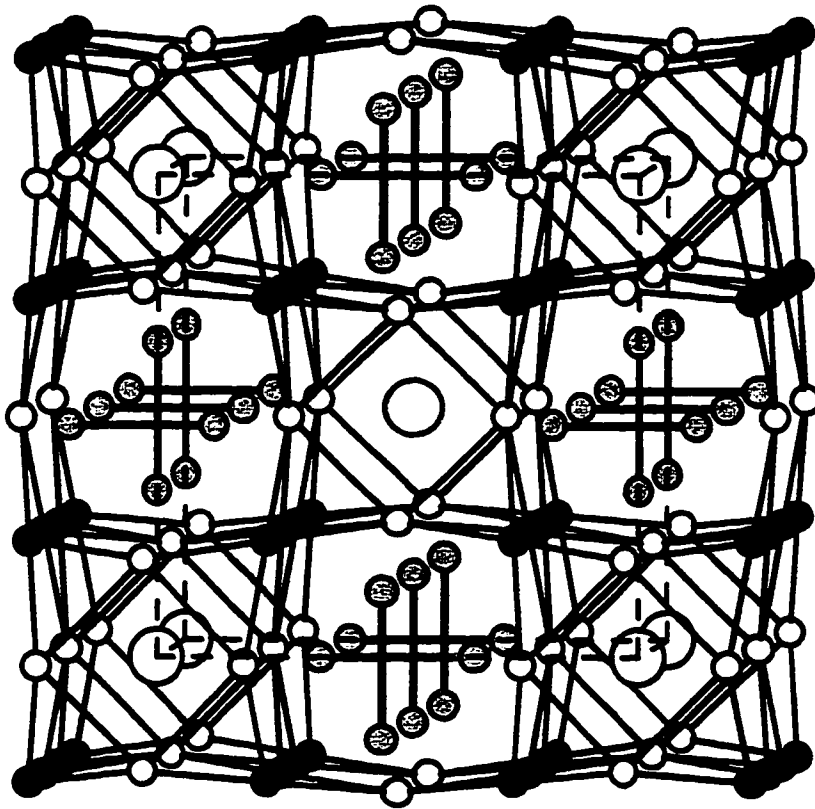


Figure 6.2: The body centered tetragonal ThMn₁₂ structure, observed for many rare earth copper aluminides, LnCu_xAl_{12-x} ($4 < x < 6$).

BaNi₂Al₉

hP12 - P6/mmm $a = 7.93 \text{ \AA}$, $c = 3.96 \text{ \AA}$

3 atomic positions

(2c) 0.333, 0.666, 0

(3f) 0.5, 0, 0

(6m) $x, 2x, 0.5$ ($x = 0.213$)

SrCo₂Al₉ EuFe₂Al₉ BaFe₂Al₉

vec range = 2.3 - 2.65

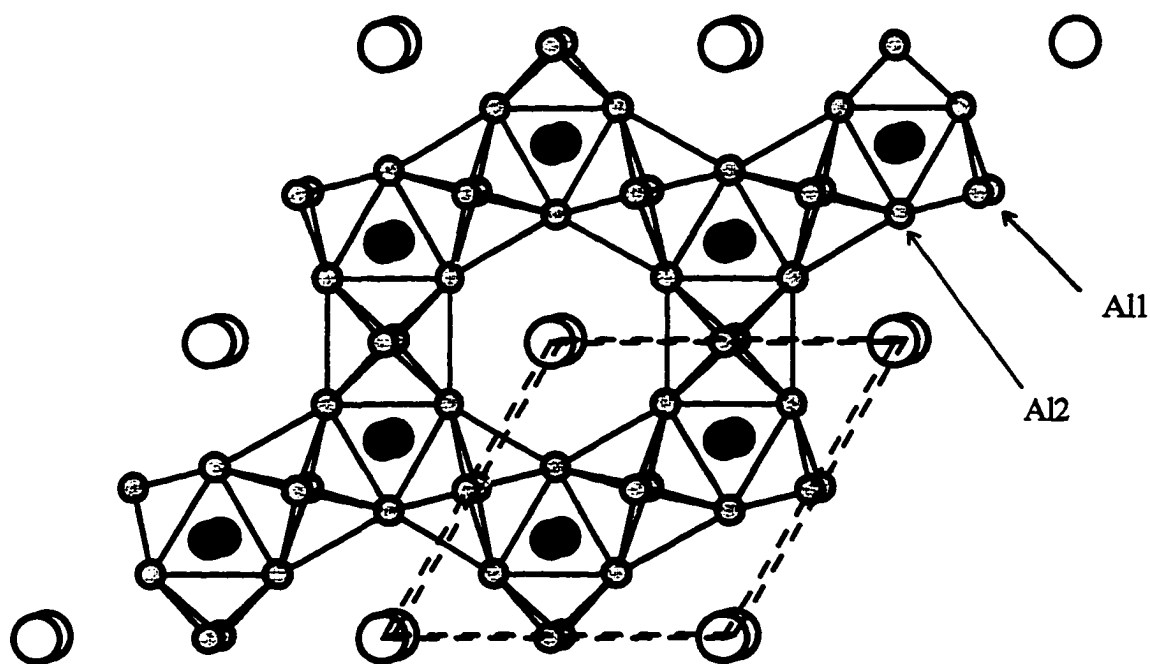


Figure 6.3: The BaNi₂Al₉ structure (hP12, P6/mmm): the large open circles are Ba atoms, the smaller dark gray atoms are Ni, and the small light gray atoms are Al. The Ba atoms occupy large hexagonal channels along the c-direction. The Ni atoms are coordinated by 9 Al atoms in a tri-capped trigonal prism, with 6 Ni - Al distances of 2.5792 Å, and 3 Ni - Al distances of 2.2892 Å. There are two atomic positions occupied by Al atoms. Al1 atoms are coordinated by 2 Ni atoms with distances 2.2892 Å, and 6 Al atoms with distances of 2.8476 Å. Al2 is coordinated by 2 Ni atoms at distances of 2.5792 Å, and 6 Al atoms at 2.8476 Å and 2.8627 Å.

BaCd₁₁tI48 - I₄/amd $a = 11.055\text{\AA}$, $c = 7.116\text{\AA}$

3 atomic positions

(8d) 0, 0, 0.5

(4a) 0, 0.25, 0.635

(32i) x, y, z ($x = 0.123, y = 0.205, z = 0.308$)EuAg₅Al₆ LaAg₆Al₅EuYbAg₁₂Al₁₀

vec range = 2.1 - 2.3

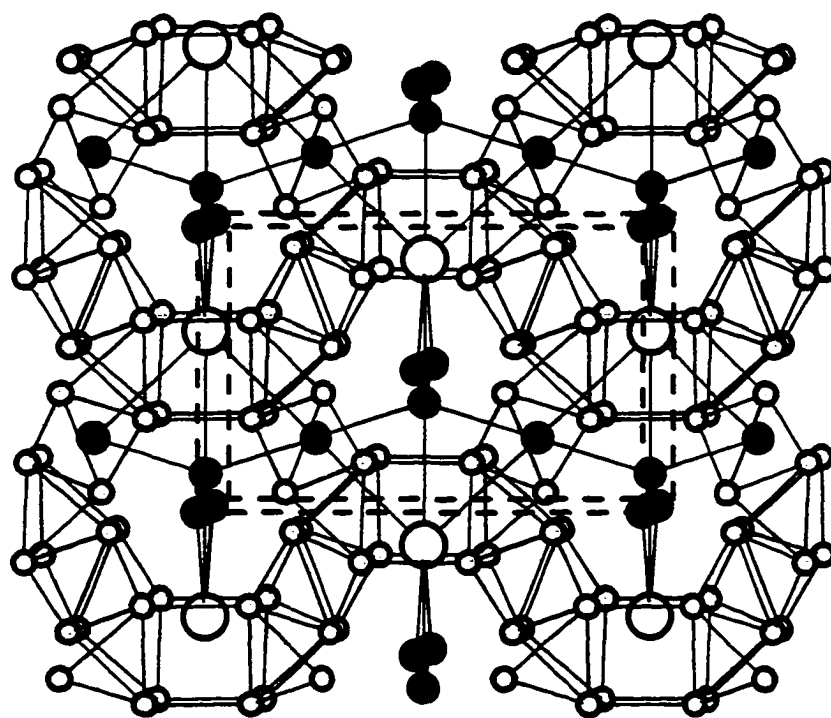


Figure 6.4: The structure of BaCd₁₁ (tI48, I₄/amd): the large open circles are Ba atoms, and the darker and lighter gray circles are the Cd atoms. For the compound EuAg₅Al₆, the light gray circles are the Al and Ag atoms which form a network of tetrahedra which surround the Eu and Al/Ag atoms. Each Al atom is coordinated by 5 other Al atoms at distances between 2.660 Å and 2.802 Å.

MoAl₁₂

cI26 - $Im\bar{3}$ $a = 7.582 \text{ \AA}$

1 atomic position
(24g) $0, y, z$ ($y = 0.1854, z = 0.3083$)

MnAl₁₂ WAl₁₂ ReAl₁₂

vec range = 2.66 - 2.75

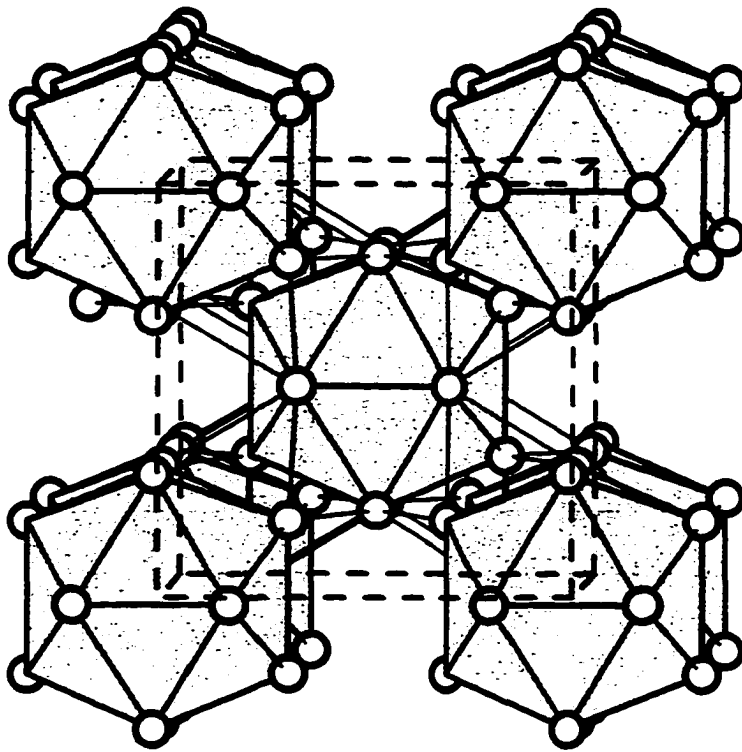


Figure 6.5: The structure of MoAl₁₂ (cI26, $Im\bar{3}$): Mo atoms (not shown) center each Al₁₂ (small white atoms) icosahedron. The distance between the Mo atom and the 12 Al atoms is 2.726 Å, and the distances between Al atoms are 2.78 - 2.88 Å.



cP54 - $Pm\bar{3}n$ $a = 10.30 \text{ \AA}$

3 atomic positions

(6c) 0.25, 0, 0.5

(16i) x, x, x , ($x=0.185$)

(24k) 0, y, z , ($y=0.306, z=0.118$)

$\text{Ba}_4\text{Cu}_3\text{Ge}_{20}$ $\text{Ba}_4\text{Ag}_3\text{Al}_{10}\text{Si}_{10}$ $\text{K}_8\text{Al}_{23}\text{Si}_{23}$

$\text{Na}_8\text{Ga}_{23}\text{Sn}_{23}$ $\text{K}_8\text{Sn}_{23}\text{In}_{23}$ $\text{K}_4\text{Ga}_7\text{Si}_{16}$

vec range = 3.5 - 4.2

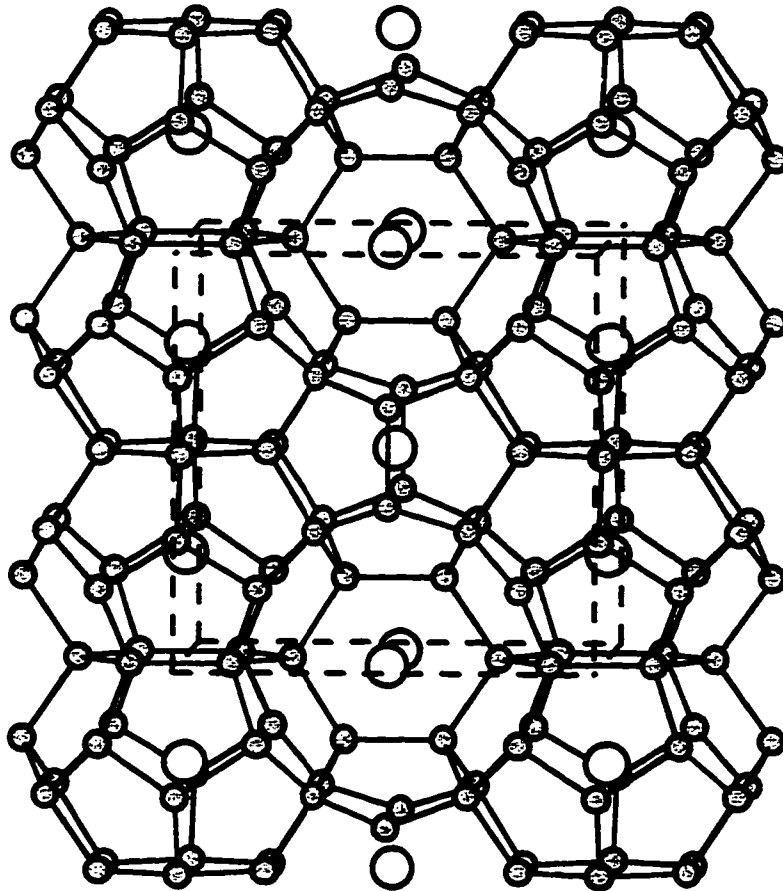


Figure 6.6: The structure of K_4Si_{23} (cP54, $Pm\bar{3}n$): the large open circles are K, and the small gray circles are Si. Each Si (gray) atom is tetrahedrally coordinated by other Si atoms with distances between 2.413 - 2.488 \AA . The K atoms occupy 24-vertex, and 20-vertex polyhedra.

majority of the Hume-Rothery and Zintl phases, are compounds with s and p metals for which a *vec* between 0 and 8 is appropriate. This includes the late transition metals (i.e. Ni, Cu, Zn) for which the d-orbitals are treated as filled 'core' orbitals. Using this counting scheme, Ni has 0 valence electrons (ve), Cu has 1 ve, Zn has 2 ve, Al has 3 ve, and so on. In these compounds however, as in the eH calculations in previous chapters, the electropositive metal atoms donate their valence electrons to the framework, but are not included in the total number of atoms. For example, the *vec* of BaCu₅Al₈ is: $(2 + 5 + 24)/13 = 2.38$.

Besides those structures listed in Table 6.1, several other structure types were considered for the *sms*. These were CaCu₅ and two CaCu₅ structural derivatives, Th₂Ni₁₇ and Th₂Zn₁₇. The synthesis of ternary aluminides in these structure types will be discussed in chapter 7, but the comparison of these structures using *sms* is included here.

In chapter 5, several new ternary gold aluminides which form derivatives of the BaAl₄ structure were introduced. We believe the *vec* plays a very important role in the formation of the BaAl₄ and α -La₃Al₁₁ structure types for the rare earth-gold-aluminide compounds. The *sms* of these two structures will be presented and discussed in this chapter.

Finally, in chapter 3 the structural and compositional relationship between LnCu₄Al₈ (ThMn₁₂) and CuAl₂ was introduced. If the Ln atoms are considered classical cations (Ln⁺³), then the *vec*/network atom for the ${}^3[\text{Cu}_4\text{Al}_8]^{2-}$ framework of LnCu₄Al₈ (*vec* = 2.58) is greater than the *vec* for CuAl₂ (*vec* = 2.33). If these two structures are compared using *sms*, one would expect to see the LnCu₄Al₈ structure type favored at higher *vec* than CuAl₂. Similarly, the Hume-Rothery phase Cu₅Zn₈ has structural features reminiscent of BaCu₅Al₈ (NaZn₁₃). And if these two structures are scaled, the BaCu₅Al₈ (*vec* = 2.38) should be more stable at a higher *vec* than the Cu₅Zn₈ (*vec* = 1.61). These scaling results will be included at the end of this chapter.

Practical Considerations of the Second Moment Scaling Calculations

The introduction to this chapter presented the motivation for scaling structures and it is clearly important to understand how these calculations are actually performed. Second moment scaling calculations are performed on homoatomic structures, (i.e. a single atom type located on every atomic position). The second moment for each structure is calculated, then scaled to a fixed intermediate value, and then the Hückel energies are recalculated using the 'scaled' structures. Two of the most important considerations in the *sms* calculations are: (1) the choice of atomic orbital parameters (2) the extent to which a structure can be scaled and still yield meaningful results.

The first of these considerations is made complex by the variety of elements which are involved in the binary and ternary compounds adopting these structure types. In particular, it is difficult to model ternary compounds (like BaCu_5Al_8) containing a network of at least two kinds of atoms with only a single set of atomic orbital parameters. For example, consider the two compounds BaCu_5Al_8 and LnCu_4Al_8 , forming the NaZn_{13} and ThMn_{12} structures respectively. In BaCu_5Al_8 (NaZn_{13}), the network of interconnected stuffed icosahedra is "colored" by a random arrangement of copper and aluminum atoms, which may conceivably be modeled with a single type of atom whose atomic parameters lie between those for Al and Cu. In LnCu_4Al_8 (ThMn_{12}) however, the network of copper and aluminum atoms is ordered, making the selection of a single set of atomic parameters for the network more difficult.

In previous calculations which scaled the elemental structures from Cu ($vec = 1$) through Se ($vec = 6$), germanium atomic orbital parameters were chosen since they lie midway between the parameters for the end points of the series (Cu and Se).^[66] Using germanium atomic orbital parameters for each of the structure types, the *sms* results correlated nicely with the observed structural preferences. While this is not *proof* that using germanium parameters was the best choice, it does seem that their selection is reasonable. Germanium parameters were also used in the *sms* calculations of the Hume-Rothery phases. Due to their mid-range atomic orbital energies and sizes, germanium parameters were used

as a starting point for the *sms* calculations on the structures listed in Table 6.1. The effects of the calculation results upon changing the atomic orbital parameters to those of Ga, and also from the addition of a low lying 'd-orbital core' will be discussed briefly later. Table 6.2 lists the atomic orbital energies and orbital exponents for those elements used in this series of calculations.

Table 6.2: The atomic orbital parameters used for the second moment scaling calculations.^[27]

Element	Atomic Orbital	H_{ii} (eV)	ζ_i
Ge	4s	-16.00	2.16
	4p	-9.00	1.85
Ga	4s	-14.58	1.77
	4p	-6.75	1.55
Al	3s	-12.30	1.37
	3p	-6.50	1.36

The second consideration of practical importance in the *sms* calculations is the actual scaling itself. The premise of scaling the second moments of structures to a fixed value is to eliminate the bias the H and eH calculations have for structures with atoms with higher coordination numbers. The process of scaling the second moments involves actually compressing or expanding the various structures (slightly) in order to increase or decrease the 'coordination strengths' of the atoms in the structures. Technically this is accomplished by increasing or decreasing the unit cell volumes, thereby lengthening or shortening distances within the structures, which corresponds to increasing or decreasing the second moment. In reference to the earlier example involving graphite and diamond, graphite (CN = 3, 1.415 Å) would be compressed and diamond (CN = 4, 1.544 Å) would be expanded in order to scale the two structures to a second moment value midway between the two. The expansion or compression of the structures occurs isotropically, (i.e. maintaining the c/a ratio for a

tetragonal structure), and while the distances between atoms are changed slightly, the bond angles remain unchanged. For this reason, it is unreasonable to scale structures with widely varying second moments, due to the large changes in bond distances and unit cell volumes that would result. As a general rule, for comparisons of scaled structures to be valid, the structures should be scaled by no more than 10 - 15 % of their respective second moments. For example, it would be unrealistic for two structures with second moments of 100 and 200, to be compared using *sms* calculations, because the scaling (to 150) is well outside the 10 - 15 % guideline. However, the scaling of two structures with second moments of 200 and 210, (scaled to 205) would result in a modification of only 2.5% of their second moments.

Second Moment Scaling of Aluminum-Rich Compounds Using Ge Parameters

Table 6.3 contains a list of the calculated second moments and the scaled second moments of each of the structures in Table 6.1, calculated using Ge parameters (see Table 6.2). For example, using the lattice parameters and atomic positions for BaCu_5Al_8 (NaZn_{13}), "Ge₁₂" was calculated for all electron counts between 0 and 8. Due to the wide range of calculated second moments, all six of these structures could not be scaled to a single second moment (and be within the 15% scaling guideline), so the structures were split into two groups. The fact that the second moments of the NaZn_{13} and ThMn_{12} structures were so similar indicated that it would be appropriate to scale these structures to the midway value of 369.0, which means a compression of 1.5% for NaZn_{13} and an expansion of 1.5% for ThMn_{12} . The second moments of MoAl_{12} , BaCd_{11} , K_4Si_{23} and BaNi_2Al_9 were all scaled to 287.0, even though the second moment for BaNi_2Al_9 is rather different from the second moments of the other three.

Results

The total energies of the scaled structures are calculated via the Hückel method, and the energies are compared as a function of *vec* per atom. Figure 6.7 is a plot of the results from the scaling of NaZn_{13} and ThMn_{12} to a second moment value of 369.0. The difference

Table 6.3: Calculated and scaled second moments for the structures in Table 6.1, using Ge parameters ($4s = -16.0$ eV (2.16), $4p = -9.0$ eV (1.85)).

Structure	Calc. Second Moment	Scaled Second Moment
NaZn ₁₃	364.03	369.0
ThMn ₁₂	376.98	369.0
BaNi ₂ Al ₉	337.91	287.0
BaCd ₁₁	295.62	287.0
K ₄ Si ₂₃	295.49	287.0
MoAl ₁₂	280.11	287.0

in energy between the two structures is plotted versus vec per network atom, with the NaZn₁₃ energy values as the reference at $\Delta E = 0$. The curves can be interpreted as follows: for any particular vec , the curve which is higher (i.e. ΔE is most positive) has the lower total energy, and is therefore predicted to be the more stable structure. That means the ThMn₁₂ structure (dotted curve in Figure 6.7), is favored for vec 's above 0.75, although the difference in energy between the two structures is small in the region of vec 2.0 - 2.6.

In the second series of *sms* calculations, MoAl₁₂, BaCd₁₁, K₄Si₂₃ and BaNi₂Al₉ were scaled to 287.0, and their relative energies are plotted in Figure 6.8. BaNi₂Al₉ was chosen as the reference for this series, and as before the curve which has the most positive ΔE at any particular vec is the most stable structure type. From vec 0 to 1.6 the BaNi₂Al₉ structure has the lowest total energy, and as the vec increases, this calculation predicts that for vec between 1.6 - 2.55, the BaCd₁₁ structure is the most stable, and from 2.55 - 2.8 the MoAl₁₂ structure is favored, and above vec 2.8, K₄Si₂₃ is strongly favored. The separation of the BaCd₁₁, MoAl₁₂ and K₄Si₂₃ structures agrees with the ranges of vec for the observed compounds, as given in Table 6.1, and shown in Figure 6.8 by the heavier black lines above the curves.

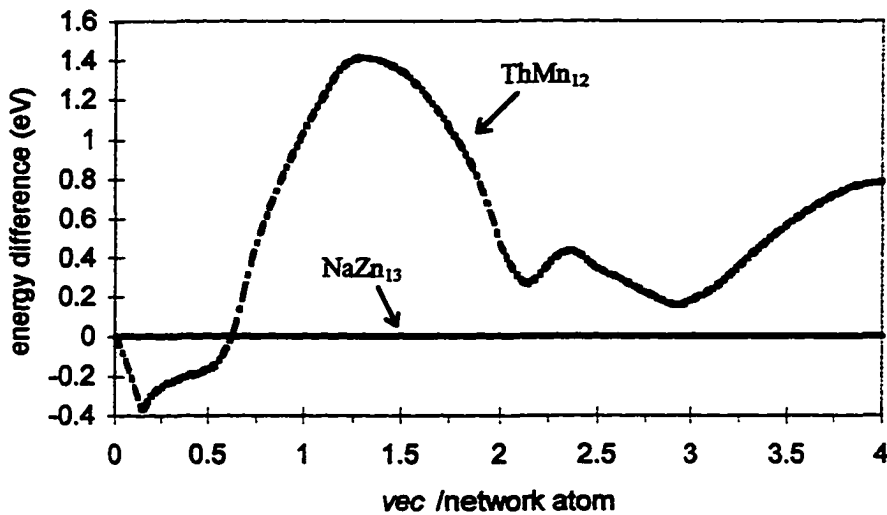


Figure 6.7: The energy difference between NaZn_{13} and ThMn_{12} scaled to 375, using Ge parameters. The solid line is the calculated energy for the NaZn_{13} structure which is set at zero, and the dotted curve is the energy difference between the ThMn_{12} structure and the NaZn_{13} structure. The ThMn_{12} structure is predicted stable for vec above 0.6.

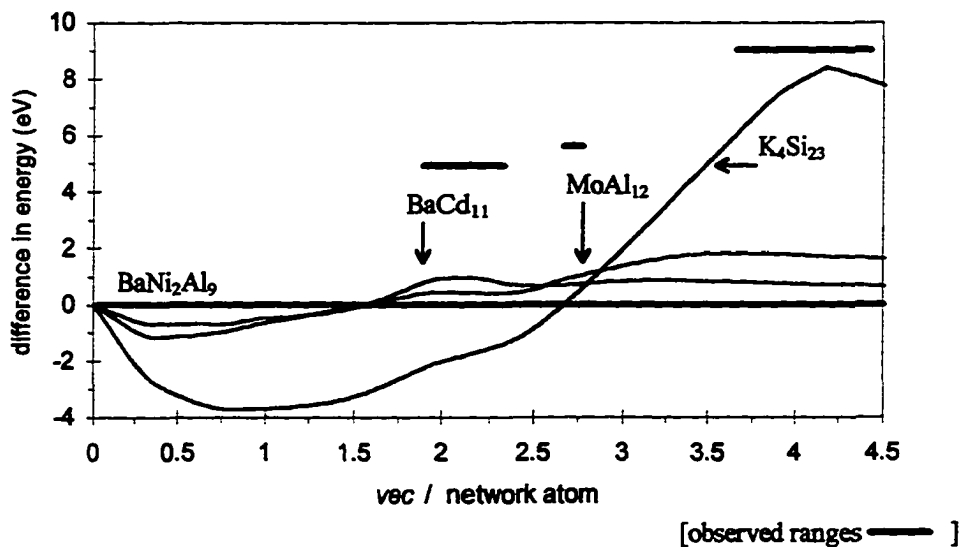


Figure 6.8: The energy differences between MoAl_{12} , BaCd_{11} , BaNi_2Al_9 and K_4Si_{23} scaled to 287, using Ge parameters. BaNi_2Al_9 is predicted most stable for vec 0 – 1.5, BaCd_{11} is predicted stable for vec 1.6 – 2.55, MoAl_{12} is favored from vec 2.55 – 2.8, and K_4Si_{23} is predicted stable for vec above 2.8. There is good agreement with the observed vec ranges (as marked by the lines above the structure types) for all the structure types except BaNi_2Al_9 .

Second Moment Scaling Calculations Using Ga Parameters

Figures 6.7 and 6.8 are the separations of structures based on *vec* for homoatomic calculations performed with Ge parameters (see Table 6.2). As mentioned previously, the choice of parameters is an important factor in the *sms* calculations, and the selection of appropriate parameters is especially difficult in this series, because the compositions of the observed phases are quite varied. Two of the structures, MoAl_{12} and BaNi_2Al_9 are true aluminide phases, and are not observed for any other main group element as the majority component, but there are only three aluminum-rich compounds known for the BaCd_{11} structure. With this in mind, the *sms* calculations were repeated with a variety of atomic orbital parameters to examine the sensitivity of the results to changes in orbital energies and orbital exponents. Table 6.4 contains the calculated and scaled second moments with Ga parameters. Figures 6.9 and 6.10 plot the results of the *sms* calculations with the energy differences between the structures as a function of *vec*.

Table 6.4: Calculated and scaled second moments for the same groups of structures using Ga atomic orbital parameters. ($4s = -14.58$ eV (1.77), $4p = -6.75$ eV (1.55))

Structure	Second Moment	Scaled Second Moment
NaZn_{13}	532.23	539.1
ThMn_{12}	547.38	539.1
BaCd_{11}	437.30	401.0
K_4Si_{23}	365.80	401.0
MoAl_{12}	426.09	401.0
BaNi_2Al_9	486.44	401.0

The *sms* results are similar with the Ge and Ga atomic orbital parameters, but there are some differences. With Ge parameters, the ThMn_{12} structure is predicted to be the stable structure type for the *vec* range of the observed structures (2.0 - 2.6), however, with the Ga parameters, the energy differences between the ThMn_{12} and NaZn_{13} structures in the

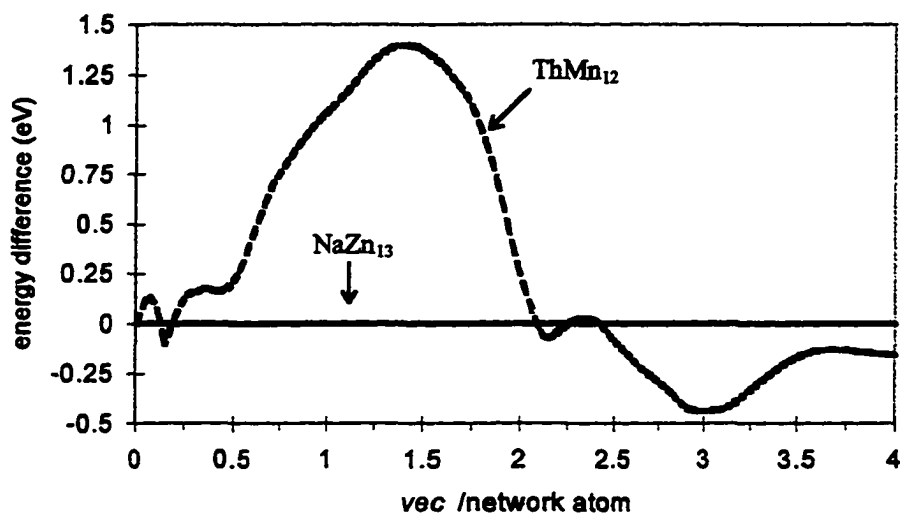


Figure 6.9: The energy difference between $NaZn_{13}$ and $ThMn_{12}$ plotted as a function of vec , scaled to 539, using Ga parameters. The energy $NaZn_{13}$ is set at zero and the dotted curve is the energy difference between $ThMn_{12}$ and $NaZn_{13}$.

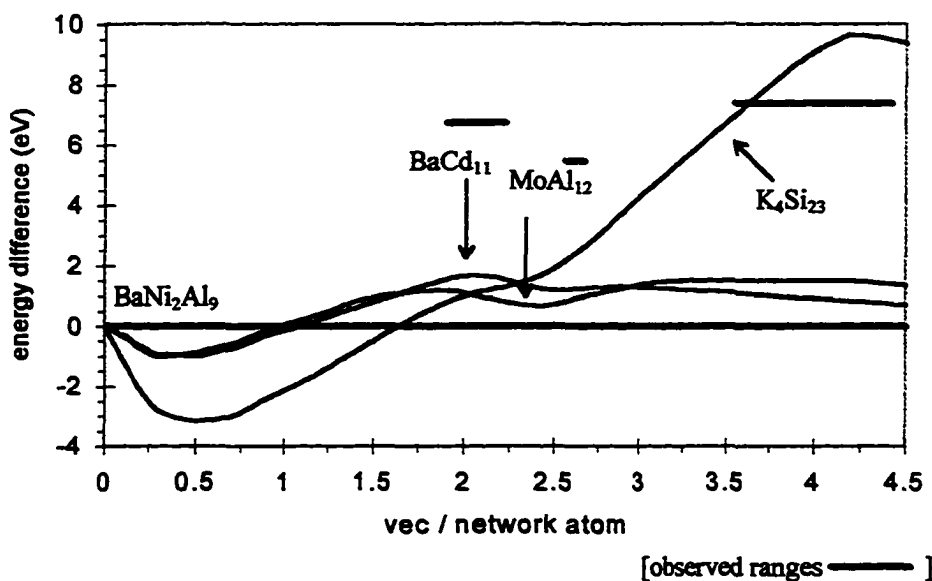


Figure 6.10: The differences in energy between $MoAl_{12}$, $BaNi_2Al_9$, K_4Si_{23} , and $BaCd_{11}$, scaled to 401, using Ga parameters. The agreement between the observed ranges of vec for known compounds and predicted ranges of stability is pretty good for $BaCd_{11}$ and K_4Si_{23} , as shown by the straight lines above the curves. However, the separation of all four of the structure types using Ga parameters is not as successful as with the Ge parameters (Figure 6.8).

critical region of vec from 2.0 to 2.5 are very small. The results of this calculation are not surprising, based on what we already know about these two systems of ternary aluminides from synthesis and eH calculations. In the second moment scaling calculations the ThMn_{12} structure is predicted to be stable throughout the majority of the vec range 1-3, but there is a small section between vec 2.05 and 2.125 for which the NaZn_{13} structure is favored, and again above $vec = 2.55$. Within the error of the calculations (± 0.04 eV), there is no difference between the two structures for the vec ranges 2.0 - 2.5, and in fact, both structures are observed within that region, refer to Table 6.1. As discussed in chapter 3, there are other factors besides the vec which contribute to the formation of either the ThMn_{12} or the NaZn_{13} structures, and the role of the electropositive metal atoms was discussed at length. It was discovered that the orbital overlaps between the Ln atoms and the framework atoms in LnCu_4Al_8 (ThMn_{12}) was significant in determining the ordering of the Cu and Al atoms. Clearly this effect is not considered in these calculations, because the electropositive metal atoms are not included.

The scaling results of the four structures, MoAl_{12} , BaCd_{11} , K_4Si_{23} and BaNi_2Al_9 in Figure 6.8 and 6.10 are similar, but the separation of the structures with Ge parameters is better. Using Ge parameters and scaling the structures to 287, the separation of MoAl_{12} , BaCd_{11} and K_4Si_{23} was in excellent agreement with the observed ranges of vec .

Second Moment Scaling of Two CaCu_5 Derivatives: $\text{Th}_2\text{Ni}_{17}$ and $\text{Th}_2\text{Zn}_{17}$

The hexagonal phase CaCu_5 has four structural derivatives: ThMn_{12} , $\text{Th}_2\text{Ni}_{17}$, $\text{Th}_2\text{Zn}_{17}$, and $\text{Pu}_3\text{Zn}_{22}$. $\text{Th}_2\text{Ni}_{17}$ and $\text{Th}_2\text{Zn}_{17}$ are very closely related structure types which will be discussed in detail in chapter 7. Many ternary trielide phases have been reported forming one of these two structures, particularly in the rare earth-silver-aluminide systems $\text{Ln}_2\text{Ag}_x\text{Al}_{17-x}$ ($\text{Ln} = \text{La} \dots \text{Yb}$). The general (although not exclusive) trend in the literature reports, as well as in my synthetic observations of compounds which adopt these two structures, is that the silver-rich compounds (where $x \geq 9$) form the $\text{Th}_2\text{Zn}_{17}$ structure, and the aluminum-rich compounds (where $x \leq 8$) adopt the $\text{Th}_2\text{Ni}_{17}$ structure, see Table 6.5.

From this point of view, the change in structure is related to the change in composition. From a slightly different point of view however, this structural change could be based on the change of *vec*, with the silver-rich compounds, forming the Th₂Zn₁₇ structure having a lower *vec* (s and p) than the aluminum-rich compounds forming the Th₂Ni₁₇ structure. Second moment scaling calculations could be very effective at investigating the differences in energies between the two structures at different *vec*(s).

Table 6.5: Literature reports of ternary aluminides forming either the Th₂Ni₁₇ or Th₂Zn₁₇ structure. For the s and p counting, Ag is s¹, and Al is s²p¹. For the s, p, and d counting, Ag is d¹⁰s¹, Al is s²p¹, (or more reasonably, add 10 to the s and p counting).

Composition	Structure	<i>vec</i> / network atom		Reference
		(s and p)	(s, p and d)	
La _{1.8} Ag _{6.5} Al _{10.5}	Th ₂ Ni ₁₇	2.55	6.38	36
Ce _{1.8} Ag _{6.5} Al _{10.5}	Th ₂ Ni ₁₇	2.55	6.38	36
Pr _{1.8} Ag _{6.5} Al _{10.5}	Th ₂ Ni ₁₇	2.55	6.38	36
Yb _{1.8} Ag ₇ Al ₁₀	Th ₂ Ni ₁₇	2.50	6.61	36
La ₂ Ag ₄ Al ₁₃	Th ₂ Ni ₁₇	2.88	5.24	ch 7
La ₂ Ag _{9.6} Al _{7.3}	Th ₂ Zn ₁₇	2.21	7.91	36
Ce ₂ Ag _{8.8} Al _{8.2}	Th ₂ Zn ₁₇	2.32	7.49	36
Pr ₂ Ag ₁₀ Al ₇	Th ₂ Zn ₁₇	2.18	8.05	36
Yb ₂ Ag ₉ Al ₈	Th ₂ Zn ₁₇	2.29	7.58	36

The second moments of each structure were calculated using (a) Ge s and p parameters, and (b) Ge s and p, with a 'd-orbital core' at -30.0 eV, and are reported in Table 6.6, with the values to which the second moments were scaled. The results of both scaling calculations are shown in Figures 6.11 and 6.12. For the scaling with s and p orbitals only, (Figure 6.11) the *sms* separation of the structure types based on their *vec* is exactly the reverse of the observed separation, for the ternary aluminides. The Th₂Ni₁₇ structure is predicted stable for *vec* < 1.4, and the Th₂Zn₁₇ structure is favored for *vec* > 1.5, (see Table 6.5). While these ranges in *vec* do not correspond to the observed ranges for the silver

aluminides, they do correspond to the parent compounds themselves; CaCu_5 , $\text{Th}_2\text{Ni}_{17}$ and $\text{Th}_2\text{Zn}_{17}$. If Ni is counted as s^0 , Cu as s^1 , and Zn as s^2 , then the predicted ranges are correct, including the small *vec* range between 1.4 and 1.5 in which the CaCu_5 (*vec* = 1.4) is the most stable structure.

Table 6.6: The calculated second moments for $\text{Th}_2\text{Ni}_{17}$, $\text{Th}_2\text{Zn}_{17}$ and CaCu_5 , using (a) s and p Ge atomic orbital parameters, and (b) adding a d-orbital core at -30.0eV.

Structure Type	second moment	scaled second moment
(a) s and p Ge parameters (4s = -16.0 (2.16), 4p = -9.0 (1.85))		
CaCu_5	371.94	359.75
$\text{Th}_2\text{Ni}_{17}$	392.03	359.75
$\text{Th}_2\text{Zn}_{17}$	327.50	359.75
(b) Ge 4s and 4p , with d-orbitals at -30.0eV		
CaCu_5	665.62	665.0
$\text{Th}_2\text{Ni}_{17}$	675.04	665.0
$\text{Th}_2\text{Zn}_{17}$	646.21	665.0

While the failure to separate the ternary aluminides correctly is discouraging, there are several contributing factors which make the scaling of these structures difficult. As discussed earlier, the choice of atomic parameters can be difficult for these ternary phases, and in this case that is especially true. Aluminum has high lying unfilled d-orbitals, and the silver atoms have low lying filled d-orbitals. It is very difficult to model the mixing of Al and Ag atoms within a structure using a single set of 'pseudo-element' atomic parameters. Having noted this difficulty, we repeated the scaling with the inclusion of a low lying d- core at -30.0eV, see Figure 6.12.

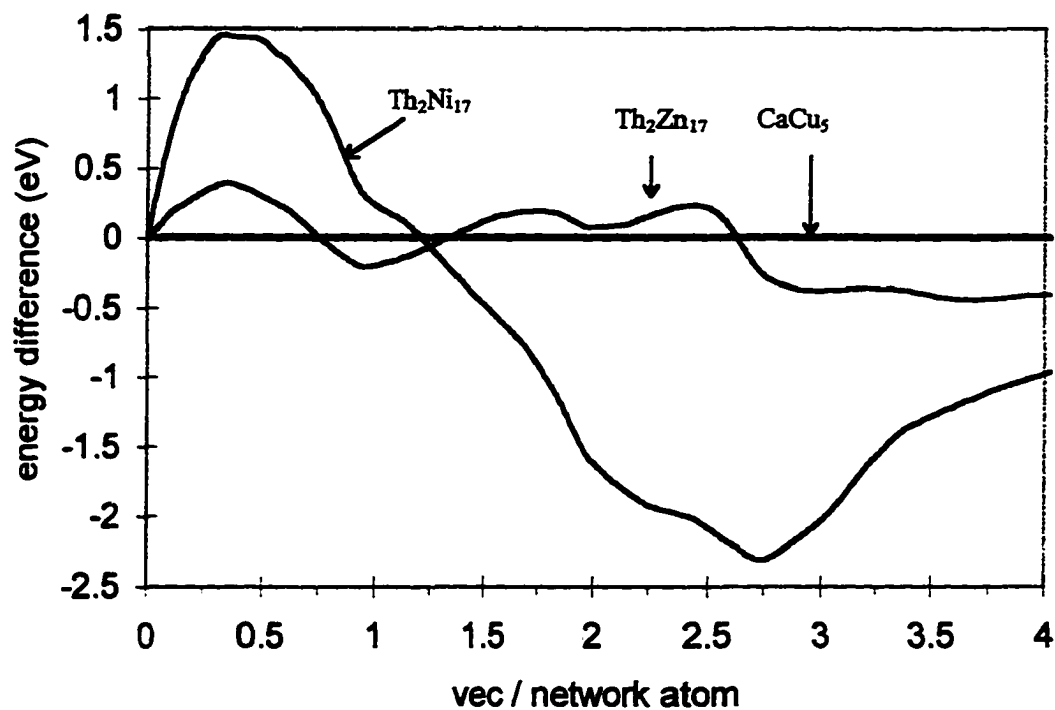


Figure 6.11: The results of the scaling of $\text{Th}_2\text{Zn}_{17}$, $\text{Th}_2\text{Ni}_{17}$ and CaCu_5 with Ge s and p parameters. The $\text{Th}_2\text{Ni}_{17}$ structure is predicted to be stable from vec 0 - 1.2, and the $\text{Th}_2\text{Zn}_{17}$ structure is favored from vec 1.3 - 2.6, with CaCu_5 stable for a small portion of vec between 1.2 and 1.3, and above vec 2.6.

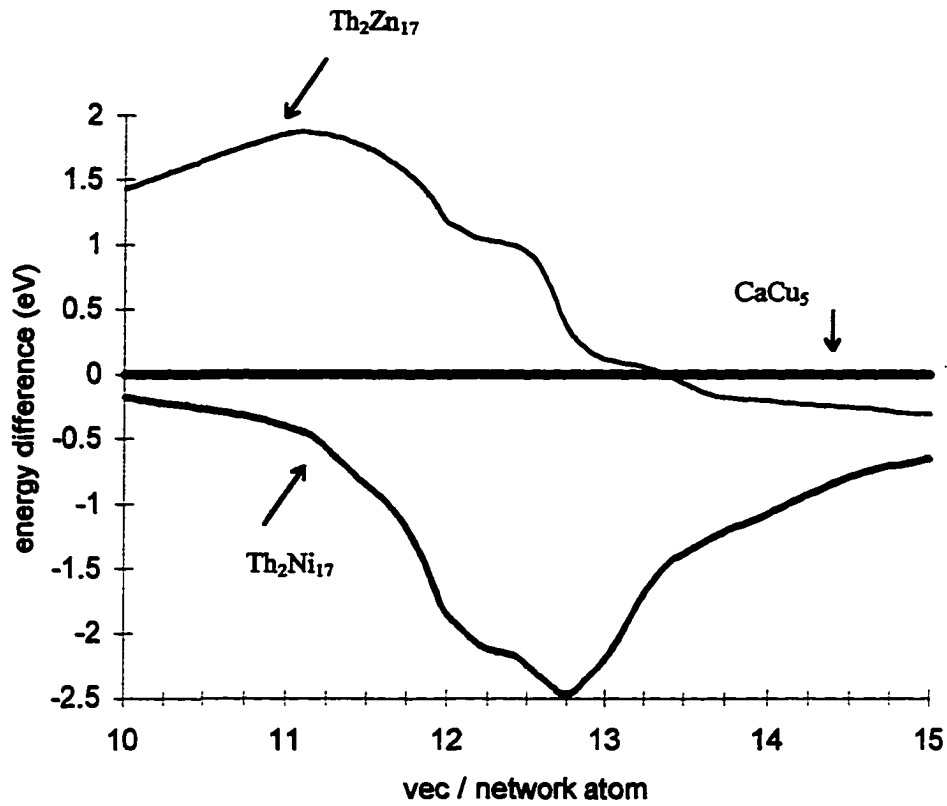


Figure 6.12: The scaling of CaCu_5 , $\text{Th}_2\text{Ni}_{17}$ and $\text{Th}_2\text{Zn}_{17}$ with the inclusion of a d - orbital core at -30.0 eV. The scaling predicts the $\text{Th}_2\text{Zn}_{17}$ structure to be favored between *vec* 10 and 13.4, and the CaCu_5 structure is favored between *vec* 13.4 and 15, but the $\text{Th}_2\text{Ni}_{17}$ structure is never predicted stable between *vec* 10 and 15.

There is a distinct crossing of the two curves for $\text{Th}_2\text{Zn}_{17}$ and CaCu_5 near vec 13.5, but now the $\text{Th}_2\text{Ni}_{17}$ structure is not favored for any vec . With the inclusion of a low lying d-core, the electron counting needs to be reconsidered. It is not reasonable to count electrons as Ag: $d^{10}s^1$, and Al s^2p^1 , which results in partially filled d-orbitals (i.e. $vec < 10$), see Table 6.5. Rather, the Al atoms should be counted as ' $d^{10}s^2p^1$ '. This counting results in the same vec ranges as the s and p counting, with the addition of the filled d-core (i.e. vec from 10 - 18). The $\text{Th}_2\text{Zn}_{17}$ structure is the more stable structure at vec between 10 and 12.75, but the $\text{Th}_2\text{Ni}_{17}$ structure is not the favored structure anywhere between vec 10 and 18. For a further discussion of some ternary aluminide compounds which adopt these two structures, see chapter 7.

BaAl₄ vs. α - La₃Al₁₁

The synthesis, characterization and electronic structures of several new ternary gold aluminides which adopt variants of the BaAl₄ structure were introduced in chapter 5, and the importance of the vec as a factor in the formation of these structures was discussed. Compounds involving main-group metals forming the BaAl₄ structure are restricted to $vec \leq 3.5$. It was proposed that one of the reasons the LnAl₄ (except EuAl₄) compounds do not form the BaAl₄ structure is their vec is too high (LaAl₄ = 3.75). The α - La₃Al₁₁ structure is a derivative of BaAl₄ in which a 'pair' of Al atoms has been condensed to a single atomic position allowing for the composition La₃Al₁₁ ($vec = 3.82$) and not 'La₃Al₁₂'. A structural phase transition takes place at high temperatures, and the β -La₃Al₁₁ structure forms the BaAl₄ structure with an ordered vacancy (La□_{0.33}Al_{3.67}, $vec = 3.5$).^[56-57] Second moment scaling calculations were carried out to examine the possible separation of these two structures into ranges of vec for which their formation is favored. Using Ge parameters, the second moments for the two structures were 235.3 for α - La₃Al₁₁ and 229.7 for BaAl₄, and they were scaled to 232.0, (see Figure 6.13). In this *sms* calculation, the α - La₃Al₁₁ structure is the more stable structure for compounds with vec between 1.1 and 3.4, with BaAl₄ the favored structure above vec 3.4. Using Al parameters (see Table 6.2), the calculated second

moments were 223.07 for α - $\text{La}_3\text{Al}_{11}$ and 226.6 for BaAl_4 , and the structures were scaled to 226.0, (see Figure 6.14). The scaling calculations with the Al parameters again predicted the α - $\text{La}_3\text{Al}_{11}$ structure more stable for $vec > 1.25$.

CuAl_2 vs. LnCu_4Al_8 and Cu_5Zn_8 vs. BaCu_5Al_8

The two binary compounds CuAl_2 and Cu_5Zn_8 have similar compositions and structural features as the two ternary aluminides LnCu_4Al_8 and BaCu_5Al_8 respectively. The copper aluminum network in LnCu_4Al_8 has the same composition as CuAl_2 , and their structural relationship was described in chapter 3. If the Ln atoms are treated as classical cations, and donate their electrons to the Cu/Al network, the vec (per network atom) is greater for LnCu_4Al_8 than for CuAl_2 . These two structures were scaled using Ga parameters and the results are plotted in Figure 6.15. The CuAl_2 structure is stable for low vec (< 0.75) and the LnCu_4Al_8 structure is stable at higher vec . Likewise, the Cu_5Zn_8 and BaCu_5Al_8 structures were scaled using Ga parameters, and Figure 6.16 contains the results. Again, the Cu_5Zn_8 structure is stable at low vec (< 1.45), the two structures have very similar energies between vec 1.45 and 1.75, and above vec 1.75 the BaCu_5Al_8 structure is stable. In both cases, the ternary aluminides in which the framework vec has been increased by the donation of the Ba and Ln valence electrons, are favored at higher vec than the two binary phases.

Conclusions

The second moment scaling calculations were a useful addition to the electronic structure investigations of these aluminum-rich phases. The separation of the structure types based on vec was successful in some cases, and disappointing in others, but this is not surprising. The Hume-Rothery electron phases are a unique group of compounds for which the vec is one of, if not *the* determining factor in the formation of those structures. Clearly the vec is one of many factors which influence the formation of these ternary aluminides, but

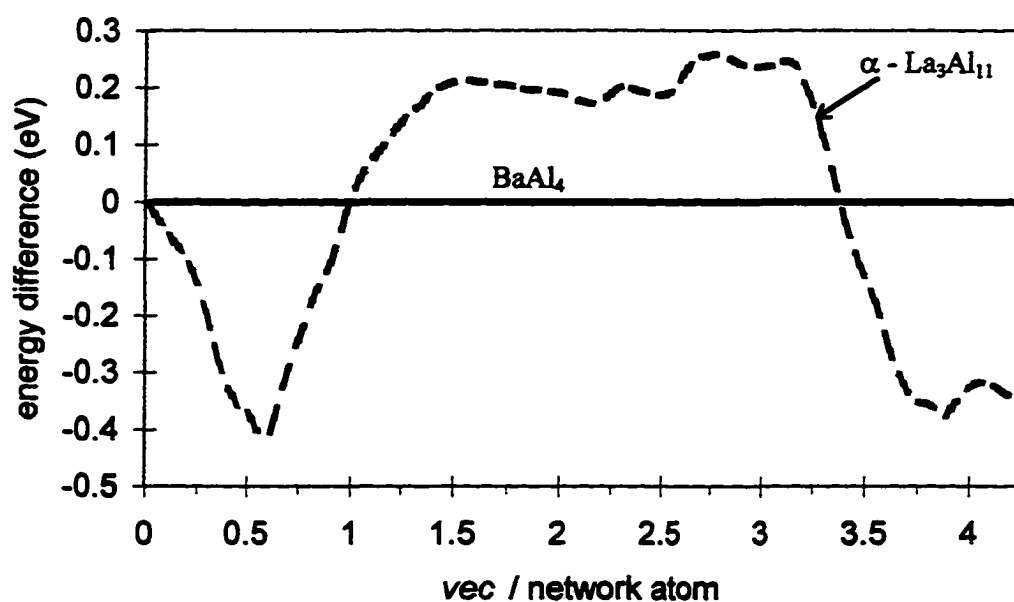


Figure 6.13: The results of second moment scaling of $BaAl_4$ and $\alpha-La_3Al_{11}$ with Ge parameters. The $\alpha-La_3Al_{11}$ is predicted to be stable from vec 1.0 - 3.4.

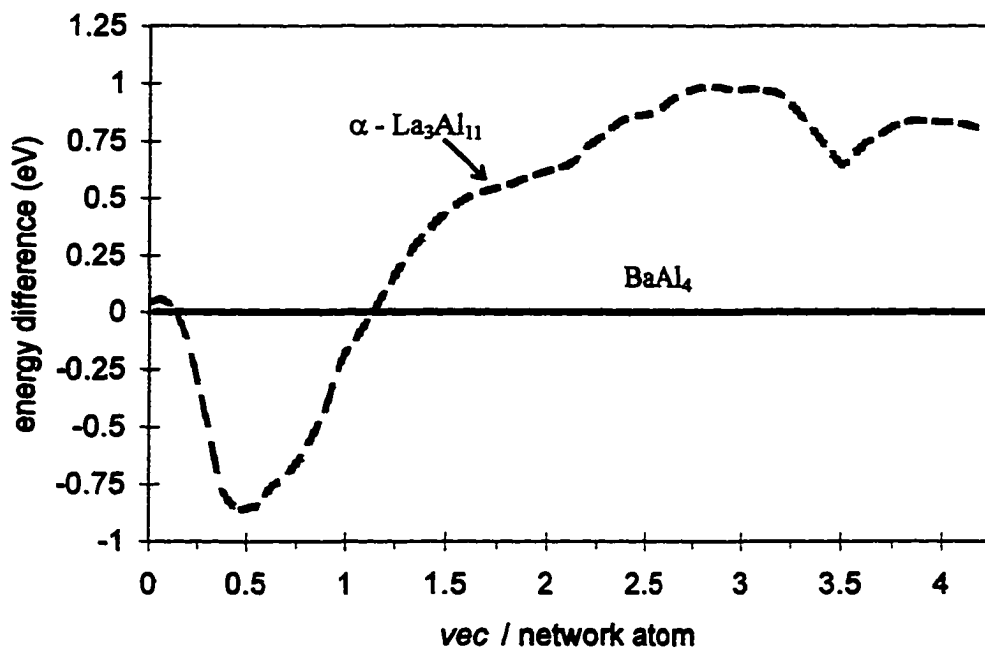


Figure 6.14: The results of scaling $BaAl_4$ and $\alpha-La_3Al_{11}$ with Al parameters. The calculation results predict $\alpha-La_3Al_{11}$ structure to be stable for $vec > 1.2$.

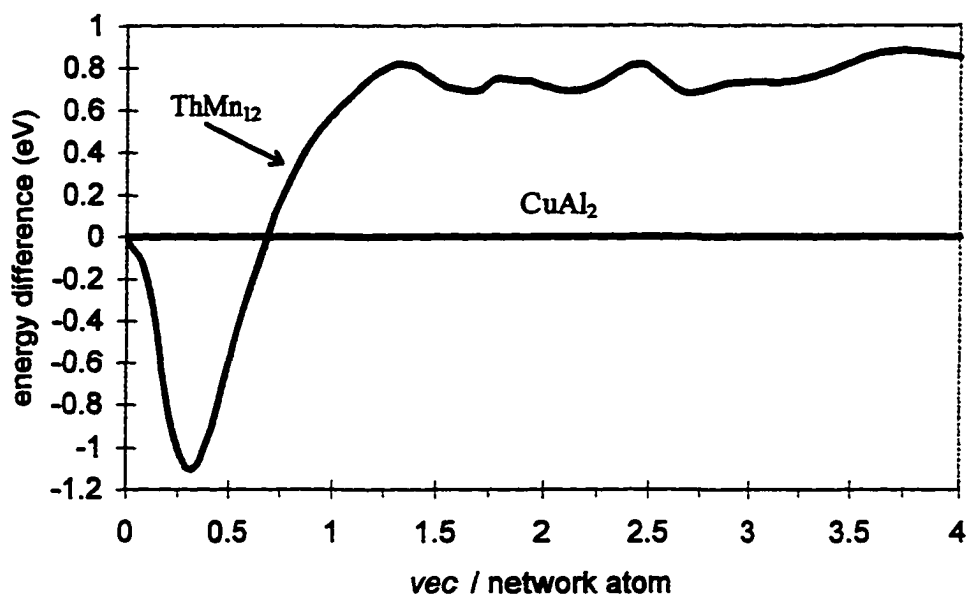


Figure 6.15: The scaling of $ThMn_{12}$ ($LnCu_4Al_8$) and $CuAl_2$ using Ga parameters. The scaling confirms that the $LnCu_4Al_8$ (or ${}^3[Cu_4Al_8]^{3-}$), is predicted to be more stable at higher vec than $CuAl_2$.

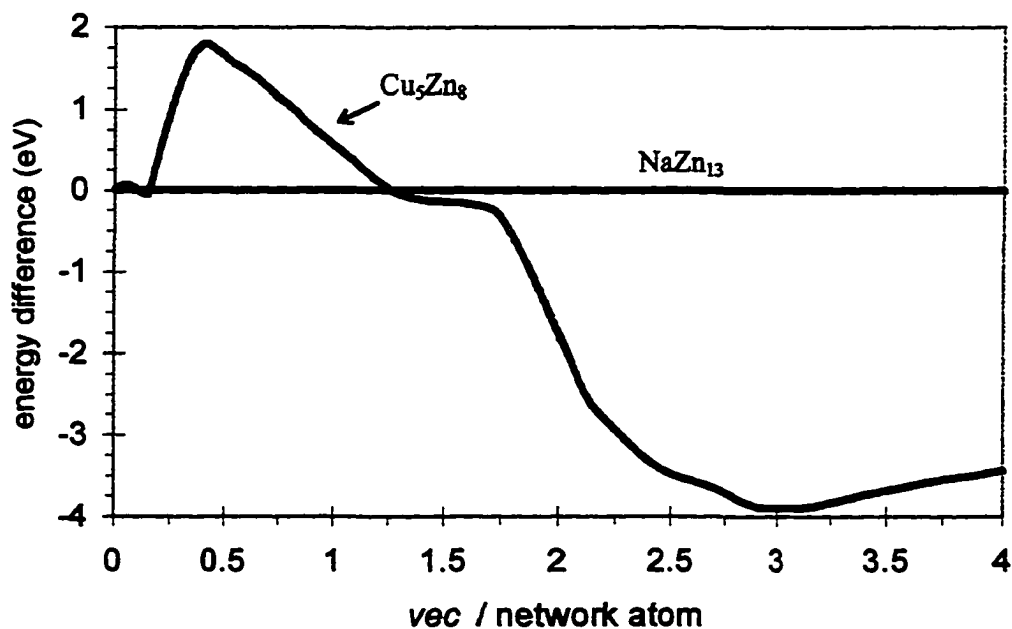


Figure 6.16: The scaling of $NaZn_{13}$ ($BaCu_5Al_8$) and Cu_5Zn_8 using Ga parameters. Like the $CuAl_2$ / $LnCu_4Al_8$ calculation, the $BaCu_5Al_8$ is predicted to be favored at higher vec than Cu_5Zn_8 .

it may not always be the determining factor. If that is the case, then second moment scaling calculations alone cannot provide the 'answers' to the questions of structural preferences.

Using second moment scaling in combination with the extended Hückel calculations, as well as creative synthesis and thorough characterization is probably the most effective way to approach these complex systems.

CHAPTER 7

THE SYNTHESIS AND STRUCTURE OF TERNARY
ALUMINIDES FORMING THE
BaCd₁₁, ErZn₅, Th₂Ni₁₇ AND Th₂Zn₁₇ STRUCTURES

EuAg₅Al₆ – BaCd₁₁ Structure type*Synthesis*

The new ternary aluminide EuAg₅Al₆ was synthesized from the elements in an arc melting furnace, using the same synthetic techniques described in chapter 2. The products of reaction (1) contained the new ternary, EuAg₅Al₆ and aluminum. Several irregular silvery crystals from the product of reaction (1) were loaded for single crystal X-ray analysis. From the refined composition of one of these single crystals, reaction (2) was carried out, and yielded single phase EuAg₅Al₆.



A large piece of the arc melted button of reaction (2) was analyzed with energy dispersive spectroscopy in a JEOL 6100 scanning electron microscope, which indicated that Eu, Ag, and Al were the only elements present in the sample.

Structure Solution

A crystal fragment from reaction (1) was mounted on a glass fiber with epoxy in air for single crystal X-ray analysis. A unit cell was indexed from a collection of peaks located from a rotation photograph, whose orientation matrix was refined using a group of 30 reflections between $12^\circ < 2\theta < 25^\circ$. A data set of 920 reflections, containing 354 unique reflections, as well as absorption correction reflections was collected on a Siemens P4

diffractometer at 298 ± 2 K. Lorentz and polarization corrections were applied to the data as well as a semi-empirical absorption correction based on the collected azimuthal scans. The structure was solved by direct methods and refinement calculations were performed on a Digital Equipment Micro VAX 3100 computer using the SHELXTL-PLUS programs.^[43] Table 7.1 contains a summary of the structure solution and refinement calculations, and the positional parameters, site occupancies and isotropic displacement parameters are listed in Table 7.2.

Table 7.1: Structure determination summary for a crystal of EuAg_5Al_6 chosen from the product of reaction (1).

Refined Chemical Formula	$\text{EuAg}_{4.67}\text{Al}_{6.33}$
Space Group	$I4_1/amd$
Unit Cell Dimensions	$a = 11.047(2) \text{ \AA}$ $c = 7.167(1) \text{ \AA}$
Unit Cell Volume	$874.6 (3) \text{ \AA}^3$
Z	4
Density (calc.)	6.278 Mg/m^3
Absorption Coefficient	17.877 mm^{-1}
Radiation	$\text{MoK}\alpha (\lambda = 0.71073 \text{ \AA})$
Temperature (K)	298(2)
2 θ Range	3.0 to 60.0 °
Scan Range (ω)	0.75 °
Scan Speed	Variable: 3.0 to 20.0 °/min. in ω
Index Ranges	$-1 \leq h \leq 15, -1 \leq k \leq 15, -1 \leq l \leq 10$
Reflections Collected	920
Independent Reflections	354 ($R_{\text{int}} = 0.0798, R_{\sigma} = 0.0628$)
Observed Reflections	324 ($F_o \geq 2\sigma(F_o)$)
Weighting Scheme	$w = 1/[s^2(F_o^2) + (0.0253P)^2 + 39.8079P]$ *
Parameters Refined	19
R Indices ($F_o \geq 4.0 \sigma(F_o)$)	$R = 0.0361, wR = 0.0910$
R Indices (all data)	$R = 0.0396, wR = 0.0932$
GooF, All Data	1.086
Data : Parameter Ratio	18.6 : 1
Largest Difference Peak	2.038 e/\AA^3
Largest Difference Hole	-2.168 e/\AA^3

* $P = (F_o^2 + 2F_c^2)/3$

Table 7.2: The positional parameters, site occupancies and isotropic thermal parameters for $\text{EuAg}_{4.67}\text{Al}_{6.33}$.

Atom	Wyck.	(sym)	x	y	z	Occ.	Ueq
Eu	4b	($\bar{4}m2$)	0.0	0.25	0.325	1.0	0.0093(3)
Ag	4a	($\bar{4}m2$)	0.0	0.75	0.125	0.796(15)	0.0136(7)
Al	4a	($\bar{4}m2$)	0.0	0.75	0.125	0.204(15)	0.0136(7)
Ag1	8c	(.2/m.)	0.0	0.0	0.0	0.472(9)	0.0132(6)
Al1	8c	(.2/m.)	0.0	0.0	0.0	0.528(9)	0.0132(6)
Ag2	32i	(1)	0.2058(1)	0.3703(1)	0.0764(1)	0.367(6)	0.0121(4)
Al2	32i	(1)	0.2058(1)	0.3703(1)	0.0764(1)	0.633(6)	0.0121(4)

Another single crystal collection and structure refinement was carried out on a crystal chosen from the single phase product of reaction (2). An abbreviated summary of the results of this structure refinement are given in Tables 7.3 and 7.4.

Structure Description

EuAg_5Al_6 adopts the body-centered tetragonal BaCd_{11} structure, with the aluminum and silver atoms mixing throughout the network on each of the three atomic positions; 4a, 8c, and 32i. As refined for the second crystal, some of the distances are listed in Table 7.5. The Eu atoms are surrounded by 22-vertex polyhedra composed of Al and Ag atoms, the Ag1/Al1 atoms sit in 12-vertex polyhedra, the Ag/Al atoms in 14-vertex polyhedra, and the Ag2/Al2 atoms are surrounded by irregular polyhedra of 10 atoms. A section of the structure is shown in Figure 7.1 (a), and the polyhedron around the Eu atoms is shown in Figure 7.1 (b). The network of Ag2/Al2 atoms is shown in Figure 7.1 (c).

Table 7.3: The summary of the solution and refinement of a single crystal of EuAg_5Al_6 chosen from reaction (2).

Refined Chemical Formula	$\text{EuAg}_{5.175}\text{Al}_{5.825}$
Space Group	$I4_1/amd$
Unit Cell Dimensions	$a = 11.055(2) \text{ \AA}$ $c = 7.116(1) \text{ \AA}$
Unit Cell Volume	$867.28(3) \text{ \AA}^3$
Z	4
2 θ Range	3.0 to 60.0 °
Index Ranges	$-1 \leq h \leq 15, -1 \leq k \leq 15, -1 \leq l \leq 10$
Reflections Collected	906
Independent Reflections	349 ($R_{int} = 0.0356, R_{\sigma} = 0.0383$)
Observed Reflections	294 ($F_o \geq 2\sigma(F_o)$)
R Indices ($F_o \geq 4.0 \sigma(F_o)$)	$R = 0.0206, wR = 0.0383$
R Indices (all data)	$R = 0.0326, wR = 0.0406$
GooF, All Data	1.014
Data : Parameter Ratio	10.26 : 1
Largest Difference Peak	0.876 e/\AA^3
Largest Difference Hole	-0.839 e/\AA^3

Table 7.4: The positional parameters and site occupancies and isotropic displacement parameters for $\text{EuAg}_{5.175}\text{Al}_{5.825}$.

Atom	Wyck. (sym)	x	y	z	Occ.	Ueq
Eu	4b ($\bar{4}m2$)	0.0	0.25	0.325	1.0	0.0093(2)
Ag	4a ($\bar{4}m2$)	0.5	0.75	0.125	0.875(6)	0.0138(3)
Al	4a ($\bar{4}m2$)	0.5	0.75	0.125	0.125(6)	0.0138(3)
Ag1	8c ($.2/m.$)	0.0	0.0	0.0	0.475(6)	0.0091(11)
Al1	8c ($.2/m.$)	0.0	0.0	0.0	0.525(6)	0.036(9)
Ag2	32i (1)	0.1740(1)	0.3802(1)	0.0441(1)	0.417(3)	0.0122(13)
Al2	32i (1)	0.1740(1)	0.3802(1)	0.0441(1)	0.583(3)	0.015(4)

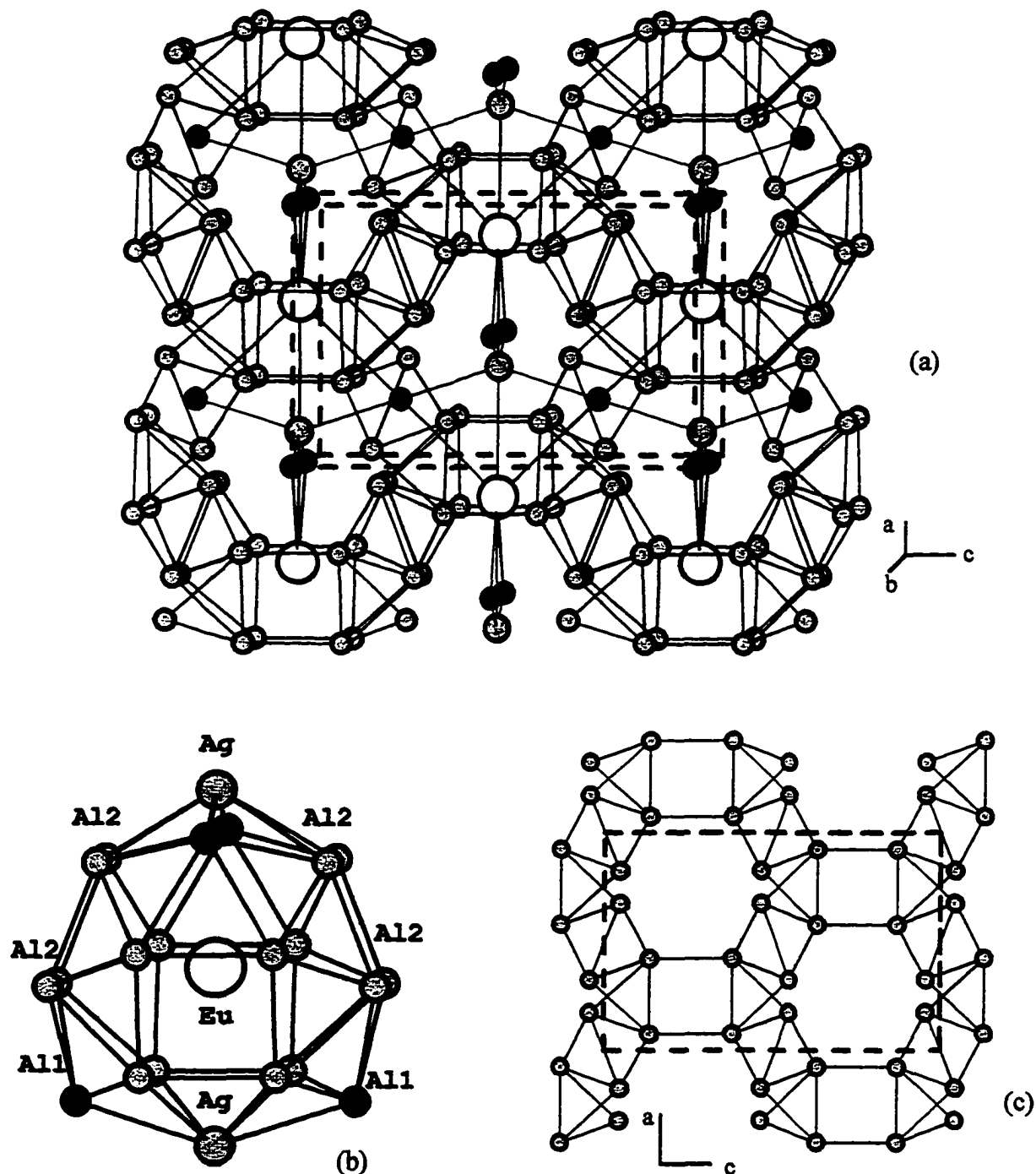


Figure 7.1(a) The extended network of EuAg_5Al_6 . The large open circles are the Eu atoms, the large gray circles are Ag/Al atoms, the dark gray circles are Ag1/Al1, and the small gray circles are Ag2/Al2 atoms. (b) The 22-vertex polyhedron surrounding the Eu atoms. (c) The Ag2/Al2 network of edge-sharing tetrahedra.

Several ternary compounds have been reported forming the BaCd₁₁ structure including: LaAg₆Al₅,^[35] Pr₂Cu₁₅Al₇, DyGa₄Cu₇, and SmGa₄Cu₇.^[40] In several reactions involving La, Ag and Al, I have observed LaAg_xAl_{11-x} in the products, and have collected and solved single crystal data, with a refined composition of LaAg_{6.7}Al_{4.3}.

Reaction (3) was carried out during the investigations of quaternary phases as reported in chapter 4. EuYbAg₁₀Al₁₂ adopts the BaCd₁₁ structure, with Eu and Yb atoms mixed throughout the structure. A small crystal from the products of reaction (3) was analyzed with single crystal X-ray diffraction, with a refined composition of EuYbAg_{11.8}Al_{10.2}.



Table 7.5: Distances within EuAg₅Al₆, as refined in the second crystal structure.

atom (1)	atom (2)	distance Å	# of interactions
Eu	Ag1/Al1	3.8412(4)	4
	Ag/Al	3.5580(5)	2
	Ag2/Al2	3.3860(7)	8
	Ag2/Al2	3.5270(3)	8
Ag/Al	Ag1/Al1	2.9034(5)	4
	Ag2/Al2	2.9969(7)	8
Ag1/Al1	Ag2/Al2	2.7153(7)	4
	Ag2/Al2	2.7467(8)	4
Ag2/Al2	Ag2/Al2	2.6494(14)	1
	Ag2Al2	2.6619(13)	1
	Ag2/Al2	2.6467(8)	1
	Ag2/Al2	2.7896(8)	2

Gd₃Ag₁₀Al₅ – ErZn₅ Structure

Synthesis and Physical Measurements

The new ternary compound Gd₃Ag₁₀Al₅ was prepared from the elements in an arc melting furnace, using the techniques described in chapter 2. The new ternary was observed in the annealed products of reaction (1).



The initial products of reaction (1) after arc welding were a combination of a ternary silver aluminide in the Th₂Ni₁₇ structure, and a phase which has the α - La₃Al₁₁ structure. Gd₃Al₁₁ has not been reported, but there are reports of ternary aluminides and gallides forming this structure type including several new phases Ln₃Au₂Al₉ (Ln = Sm, Gd, Tb, Dy, Yb) reported in chapter 5, and Ln₃Cu₄Ga₇ (Ln = Dy, Ho, Er, Tm, Yb, Lu).^[40] It is possible that this product is a new silver containing ternary aluminide adopting the α -La₃Al₁₁ structure, but this was not confirmed by any single crystal measurements. The product button was wrapped in Nb foil for annealing in a fused silica jacket at 850°C for 2 weeks. After annealing the silvery product button was intact, however, there were also some golden crystallites on the Nb foil. Both the product button and the golden crystallites were identified as the new ternary phase Gd₃Ag₁₀Al₅. The powder pattern of the crystallites which were taken off the foil, and some of the small powder that fell off the foil (see SEM photos) included NbAl₃.

A piece of foil with golden crystallites on it was analyzed by EDS in a JEOL scanning electron microscope. Gd, Ag and Al were the only elements identified in the crystallites, and small NbAl₃ crystals were observed on the foil. Three SEM pictures are included in Figure 7.2: (a) is a picture of the golden crystallites on the Nb foil, and (b) and (c) are pictures of the smaller NbAl₃ crystals on the Nb foil, at different magnifications.

A small piece (21 mg) of Gd₃Ag₁₀Al₅ was glued inside a plastic straw for a magnetic susceptibility measurement which was performed using a SQUID magnetometer, from 6 -



- (a): An SEM image of three crystallites of annealed $Gd_3Ag_{10}Al_5$ on a small piece of Nb foil. The magnification of this image is $\times 230$, so the approximate size of the crystallites is 100-200 μm . The EDS analysis of these crystallites indicated Gd, Ag and Al were the only elements present.



- (b): An SEM image of the edge of a $Gd_3Ag_{10}Al_5$ crystallite (upper left) and the small square shaped $NbAl_3$ crystallites on the Nb foil. The magnification of this image is $\times 850$, so the size of the square crystals of $NbAl_3$ is $< 10 \mu m$.

Figure 7.2: Three SEM images of some $Gd_3Ag_{10}Al_5$ and $NbAl_3$ crystallites.



- (c) An SEM image of the NbAl_3 crystallites on the Nb foil of the annealed reaction $\text{Gd}_3\text{Ag}_{10}\text{Al}_5$. The magnification of this image is $\times 2,300$, so the crystallites are $< 10\mu\text{m}$ in size.

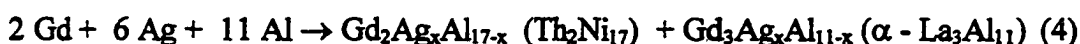
Figure 7.2: continued

300K at a field strength of 3 Tesla. After a diamagnetic core correction was applied, $\text{Gd}_3\text{Ag}_{10}\text{Al}_5$ was paramagnetic with an effective moment of 14.63(2) Bohr magnetons ($T > 80\text{K}$), slightly higher than the moment calculated for 3 non-interacting Gd^{3+} (f^7), or $8.44 \mu\text{B}$ for each Gd^{3+} atom, see Figure 7.3. The calculated moment for 3 non-interacting Gd^{3+} per formula unit is $13.5 \mu\text{B}$ (see ch5, equation (1)).

Structure Solution

A small golden crystal was loaded in a capillary for single crystal analysis, using the same procedure as described earlier for EuAg_5Al_6 . The results of the structure solution are reported in Table 7.6, with the positional parameters, site occupancies, and isotropic displacement parameters listed in Table 7.7. A second single crystal data set was collected and solved with a refined composition of $\text{Gd}_3\text{Ag}_{10}\text{Al}_{5.1}$, and the nearly identical fractional occupancies of silver and aluminum.

The lattice parameters for $\text{Gd}_3\text{Ag}_{10}\text{Al}_5$ were refined from the measured lines of the powder X-ray pattern, and are $a = 9.232(2) \text{ \AA}$, $c = 9.456(3) \text{ \AA}$. Reactions (2) - (4), were all carried out in the arc melting furnace, and the products have been characterized by powder X-ray diffraction.



Structure Description

$\text{Gd}_3\text{Ag}_{10}\text{Al}_5$ forms a ternary variant of the primitive hexagonal ErZn_5 structure, ^[68] as shown in Figure 7.4 (a), with a single 17 atom ‘cluster-like’ unit shown in Figure 7.4 (b). The atoms labeled Ag1, Al2 and Al3 in Figure 7.4 (b) are all sites occupied by both Ag and Al, but are labeled with the atom type whose occupancy on that site is the greatest (refer to Table 7.6). There is disorder of the Ag atoms (Ag4 - Ag7) along the c-axis between (0,0,0,

Gd₃Ag₁₀Al₅ @3tesla
21.2mg.

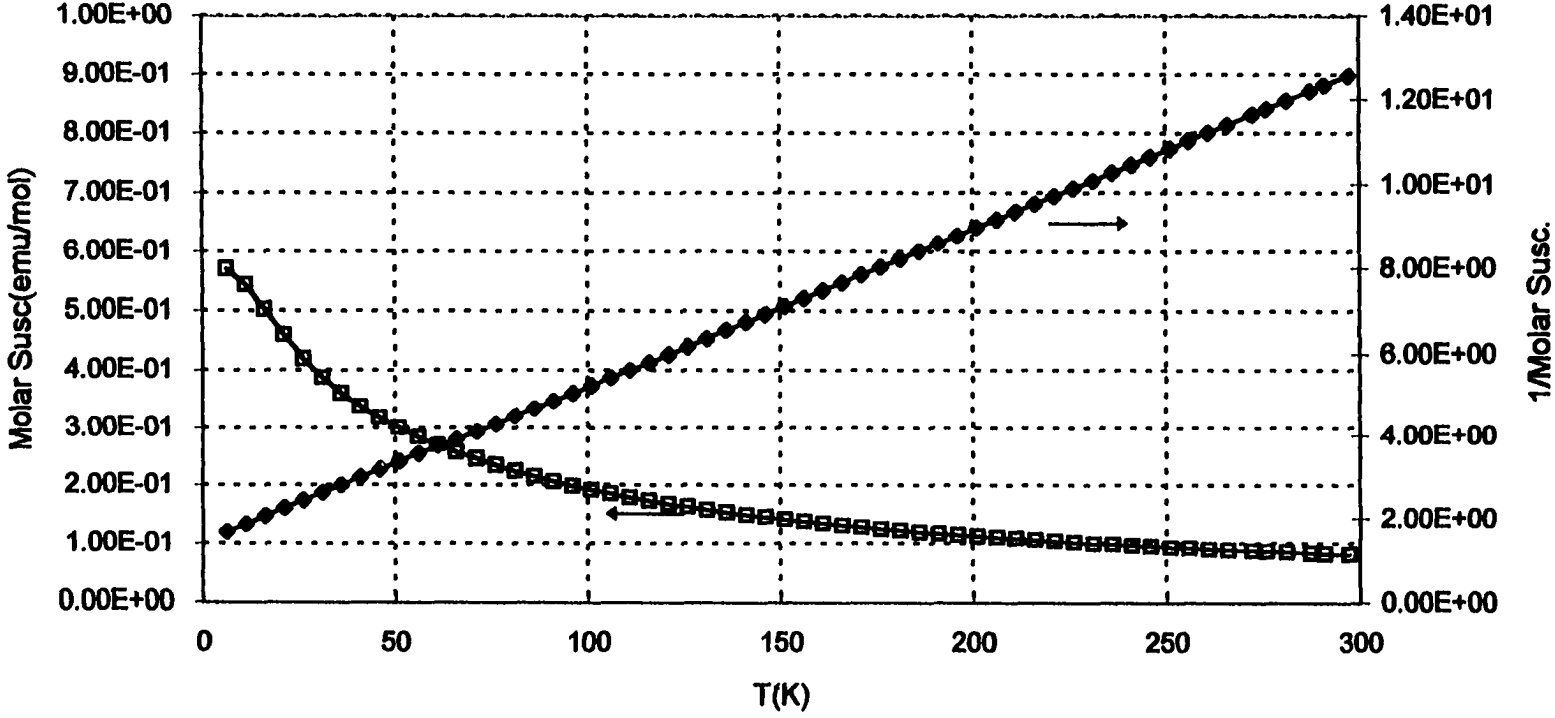


Figure 7.3: The magnetic susceptibility data for Gd₃Ag₁₀Al₅.

Table 7.6: Structure determination summary for a crystal of $\text{Gd}_3\text{Ag}_{10}\text{Al}_5$ chosen from the product of reaction (1).

Refined Chemical Formula	$\text{Gd}_3\text{Ag}_{10.15}\text{Al}_5$
Space Group	$P6_3/mmc$
Unit Cell Dimensions	$a = 9.223 (1) \text{ \AA}$ $c = 9.446 (2) \text{ \AA}$
Unit Cell Volume	$695.9 (2) \text{ \AA}^3$
Z	2
Density (calc.)	8.139 Mg/m^3
Absorption Coefficient	29.210 mm^{-1}
Radiation	$\text{MoK}\alpha (\lambda = 0.71073 \text{ \AA})$
Temperature (K)	298(2)
2θ Range	5.0 to 50.0°
Scan Range (ω)	0.75°
Scan Speed	Variable: 3.0 to $20.0^\circ/\text{min.}$ in ω
Index Ranges	$-1 \leq h \leq 10, -10 \leq k \leq 1, -1 \leq l \leq 11$
Reflections Collected	1748
Independent Reflections	261 ($R_{\text{int}} = 0.0570, R_\sigma = 0.0298$)
Observed Reflections	246 ($F_o \geq 2\sigma(F_o)$)
Weighting Scheme	$w = 1/[s^2(F_o^2) + (0.00P)^2 + 6.4928P]$ *
Extinction Coefficient	$0.00146(14)$
Parameters Refined	40
R Indices ($F_o \geq 4.0 \sigma(F_o)$)	$R = 0.0184, wR = 0.0405$
R Indices (all data)	$R = 0.0203, wR = 0.0411$
GooF, All Data	1.204
Data : Parameter Ratio	6.15 : 1
Largest Difference Peak	0.916 e/\AA^3
Largest Difference Hole	-0.774 e/\AA^3

$$* P = (F_o^2 + 2F_c^2)/3$$

Table 7.7: The positional parameters, site occupancies and isotropic displacement parameters for $\text{Gd}_3\text{Ag}_{10.15}\text{Al}_5$.

Atom	Wyck.	(sym)	x	y	z	Occ.	U _{eq}
Gd	6h	(mm2)	0.3903(1)	0.1952(5)	0.25	1.0	0.0075(2)
Ag	12k	(.m.)	0.1586(1)	0.3174(1)	0.0886(1)	1.0	0.0120(2)
Ag1	4f	(3m.)	0.33333	0.66667	-0.0083(3)	0.552(8)	0.0086(7)
Al1	4f	(3m.)	0.33333	0.66667	-0.0083(3)	0.448(8)	0.0086(7)
Ag2	6h	(mm2)	0.1340(2)	0.5670(1)	0.25	0.436(7)	0.0094(6)
Al2	6h	(mm2)	0.1340(2)	0.5670(1)	0.25	0.564(7)	0.0094(6)
Ag3	6g	(.2/m.)	0.0	0.5	0.0	0.198(8)	0.011(1)
Al3	6g	(.2/m.)	0.0	0.5	0.0	0.802(8)	0.011(1)
Ag4	2b	(6m2)	0.0	0.0	0.25	0.43(2)	0.010(2)
Ag5	12i	(.2/m.)	0.0	0.0	0.313(2)	0.208(12)	0.017(3)
Ag6	2a	(3m)	0.0	0.0	0.0	0.116(11)	0.011(6)
Ag7	12i	(.2/m.)	0.0	0.0	0.088(2)	0.079(7)	0.005(6)

and 0,0,0.313), but only the 0,0,1/4 position is shown in the figures. The Gd atoms are surrounded by 15 Ag and Al atoms in irregular polyhedra, and the shortest Gd - Gd distance is 3.8233 Å, see Figure 7.4 (c). The structure is built of 17 atom 'cluster-like' units which are linked together by the Ag4 (and Ag5 - Ag7) atoms along the *c*-direction (0,0,*z*). The 17 atom 'cluster-like' units are three face-sharing 8-vertex parallelepipeds which are each centered by a Ag2 (44%)/Al2 (56%) atom, which together form a triangle with distances from Ag2/Al2 - Ag2/Al2 of 2.758(3) Å. The Ag1/Al1 atoms sit above and below this triangle of Ag2/Al2 atoms. The Ag atoms form trigonal prisms around the atoms along (0,0,*z*), and it is through these atoms (Ag4 - Ag7) that the cluster units are linked. Figure 7.4 (a) shows a single 'layer' of these clusters and the triangles of Gd atoms which pack between these clusters in the *c*-direction. Table 7.8 lists the bond distances within the structure.

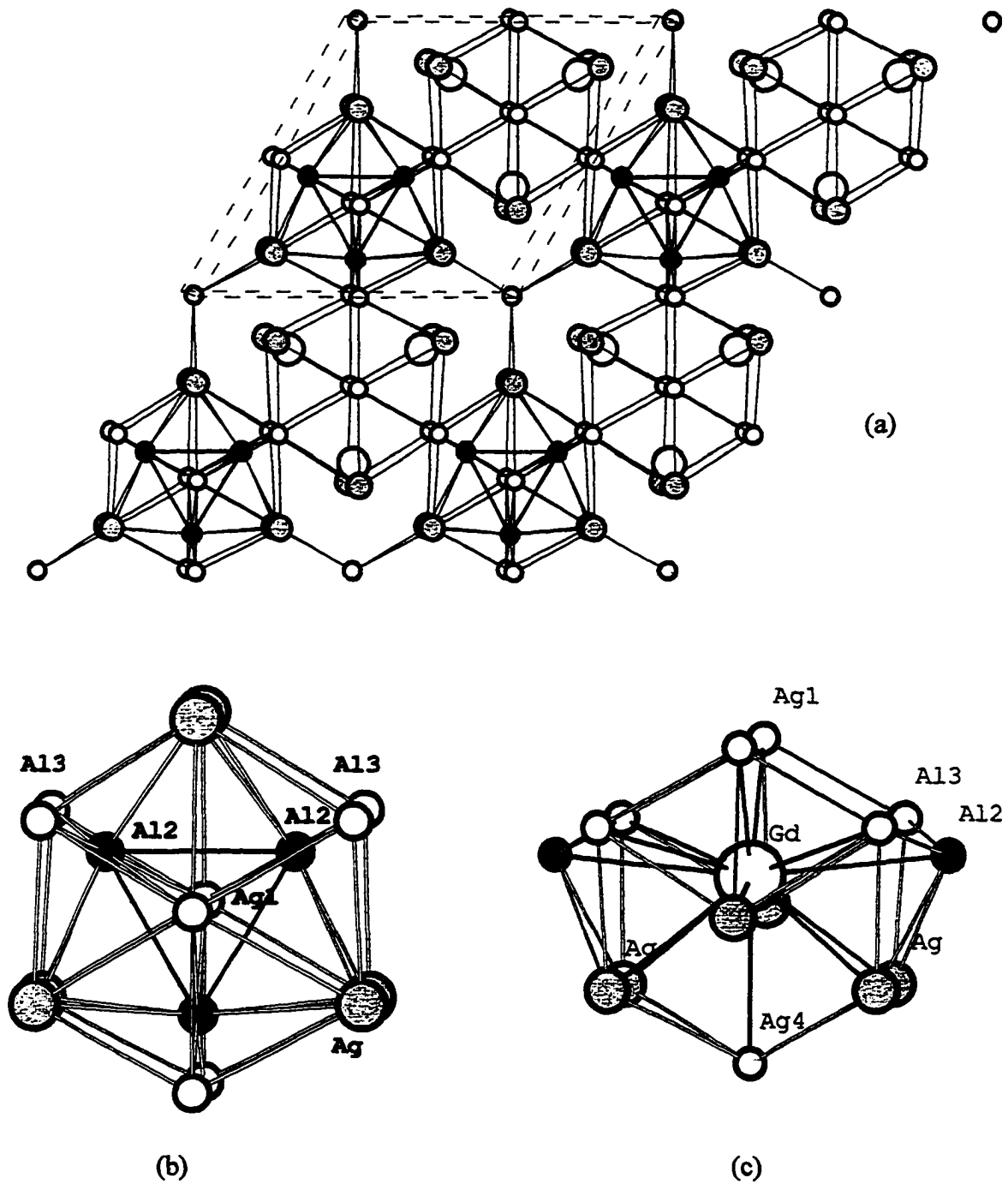


Figure 7.4: (a) The extended network of $Gd_3Ag_{10}Al_5$. (b) The 17 atom 'cluster-like' unit with 3 face-sharing 8 vertex polyhedra around Ag_2/Al_2 atoms (small dark gray circles). (c) The 15 nearest neighbors surrounding the Gd atoms (large open circle).

The disorder along the c-axis results in the fractional occupation of four sites (Ag4 - Ag7 in Table 7.7). The refinement of these positions was most successful as Ag atoms, and attempts at refining with Al or O atoms were unsuccessful. Although these positions are not well resolved, two other crystals structure solutions do show similar refinements of the same positions along the (0,0,1) direction.

Table 7.8 : Selected distances in $Gd_3Ag_{10}Al_5$.

Atom(1)	Atom (2)	distance (Å)	number
Gd	Ag	3.205(1)	6
	Ag1/Al1	3.176(2)	2
	Ag2/Al2	3.250(1)	2
	Ag3/Al3	3.414(2)	4
	Ag4	3.117(1)	1
Ag	Ag	3.035(1)	2
	Ag	3.051(1)	1
	Ag1/Al1	2.936(1)	1
	Ag2/Al2	2.864(1)	2
	Ag3/Al3	2.854(1)	2
	Ag4	2.958(1)	1
	Ag	2.936(1)	3
Ag1/Al1	Ag2/Al2	2.913(2)	3
	Ag3/Al3	2.664(1)	3
	Ag	2.758(3)	2
Ag2/Al2	Ag3/Al3	2.593(1)	2
	Ag	2.958(1)	6

$Ln_2Ag_xAl_{17-x}$ - Th_2Ni_{17} vs. Th_2Zn_{17}

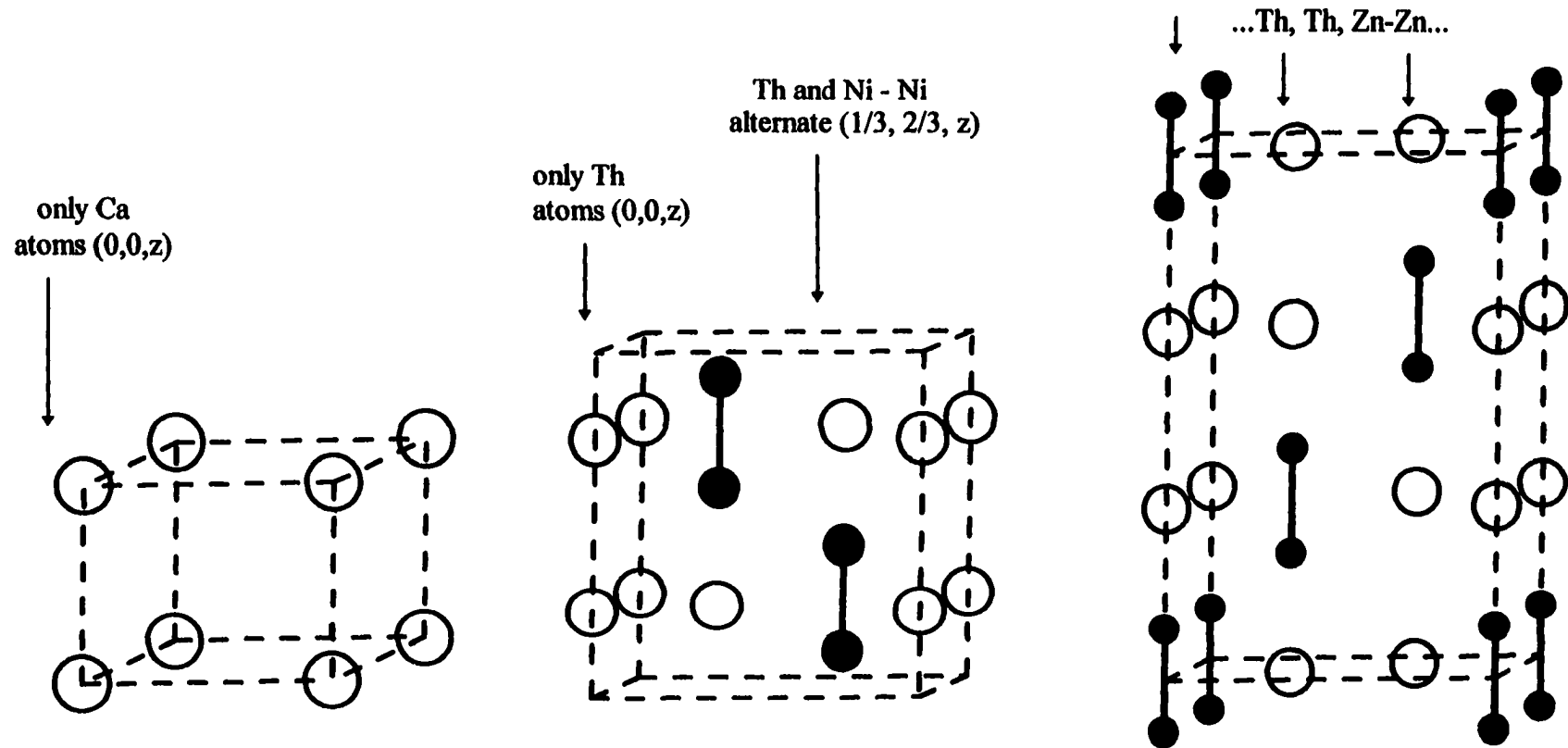
Structure Description

Th_2Ni_{17} and Th_2Zn_{17} are structural derivatives of $CaCu_5$, in which one fifth of the Ca atoms are replaced by pairs of transition metal atoms.^[4, 69] Th_2Ni_{17} is a hexagonal structure which crystallizes in the space group $P6_3/mmc$ ($Z = 2$), with a unit cell volume six times as large as that of $CaCu_5$. Th_2Zn_{17} is a rhombohedral structure, ($Z = 3, R\bar{3}m$) with a unit cell volume nine times that of $CaCu_5$. Figure 7.5 contains the arrangement of Ca atoms in $CaCu_5$.

(a), and the arrangement of Th atoms and Ni - Ni (or Zn - Zn) 'pairs' in $\text{Th}_2\text{Ni}_{17}$ (b) and $\text{Th}_2\text{Zn}_{17}$ (c). In CaCu_5 (a) the Ca atoms are located at (0,0,0) and equivalent positions. In $\text{Th}_2\text{Ni}_{17}$, the Th atoms arrange themselves along the c-axis at (0,0,1/4 and 0,0,3/4), but along (1/3, 2/3, z), Th atoms and Ni-Ni 'pairs' alternate, see Figure 7.5 (b). In $\text{Th}_2\text{Zn}_{17}$, see Figure 7.5 (c), the Th atoms and Zn-Zn 'pairs' are arranged in a ...Th, Th, Zn-Zn... pattern along the (0,0,z) and (1/3, 2/3, z) directions. Figures 7.6 (a) - (c) are pictures of the three structures, including the kagomé networks of Cu, Ni and Zn atoms, with the unit cells highlighted. Figures 7.7 and 7.8 further demonstrate the arrangements of Th atoms and M - M 'pairs' in the 'columns' formed by the nets of Ni and Zn atoms in both $\text{Th}_2\text{Zn}_{17}$ and $\text{Th}_2\text{Ni}_{17}$.

A variety of ternary aluminide phases has been reported in both of these structure types. In *Pearson's Handbook of Crystallographic Data for Intermetallic Phases*, there are 16 aluminum-containing compounds reported in the $\text{Th}_2\text{Ni}_{17}$ structure, and 38 for $\text{Th}_2\text{Zn}_{17}$ structure.^[40] The majority of these phases have been characterized by powder X-ray diffraction, but several of them have been characterized by single crystal X-ray analysis, and some examples are listed Table 7.9.

From the single crystal solutions reported for $\text{La}_{1.8}\text{Ag}_{6.5}\text{Al}_{10.5}$ ($\text{Th}_2\text{Ni}_{17}$) and $\text{La}_2\text{Ag}_{9.6}\text{Al}_{7.3}$ ($\text{Th}_2\text{Zn}_{17}$), theoretical powder X-ray patterns were generated, see Figures 7.9 (a) and (b). The theoretical patterns are similar, however, there are some differences in line positions and in the intensities of several coincidental lines. Despite these differences, it is possible that a powder pattern including the lines of one of these phases could be misidentified, especially if the product contained multiple phases. Without careful powder or single crystal X-ray analysis, it is possible that some of the reported compounds may have been characterized incorrectly, and their reported compositions are only approximate. Having made note of this, the single crystal reports do suggest that the aluminum-rich ternary compounds form the $\text{Th}_2\text{Ni}_{17}$ structure, and the silver-rich compounds form the $\text{Th}_2\text{Zn}_{17}$ structure. To our knowledge however, there has not been a systematic synthetic effort to explore the compositional dependence on the formation of either of these phases.



(a)
 CaCu_5 (Ca shown) hP6
 $P6/mmm$
 $\text{Ca} (1a) \rightarrow 0, 0, 0$

(b)
 $\text{Th}_2\text{Ni}_{17}$ - (Th and Ni - Ni pairs) hP38
 $P6_3/mmc$
 $\text{Th}1 (2b) \rightarrow 0, 0, 1/4$; $\text{Th}2 (2d) \rightarrow 1/3, 2/3, 3/4$
 $\text{Ni}1 (4f) \rightarrow 1/3, 2/3, 0.110$

(c)
 $\text{Th}_2\text{Zn}_{17}$ - (Th and Zn - Zn pairs) hR19
 $R\bar{3}m$
 $\text{Th}1 (6c) \rightarrow 0, 0, 1/3$
 $\text{Zn}1 (6c) \rightarrow 0, 0, 0.097$

Figure 7.5: (a) The Ca atoms in CaCu_5 . (b) The arrangement of Th and Ni-Ni 'pairs' in $\text{Th}_2\text{Ni}_{17}$. Along the direction (0,0,z) there are only Th atoms, and in the (1/3, 2/3, z) direction, Th atoms and Ni-Ni 'pairs' alternate. (c) The arrangement of Th and Zn-Zn 'pairs' in $\text{Th}_2\text{Zn}_{17}$, is alternating ...Th, Th, Zn-Zn... along (0,0,z) and (1/3, 2/3 z).

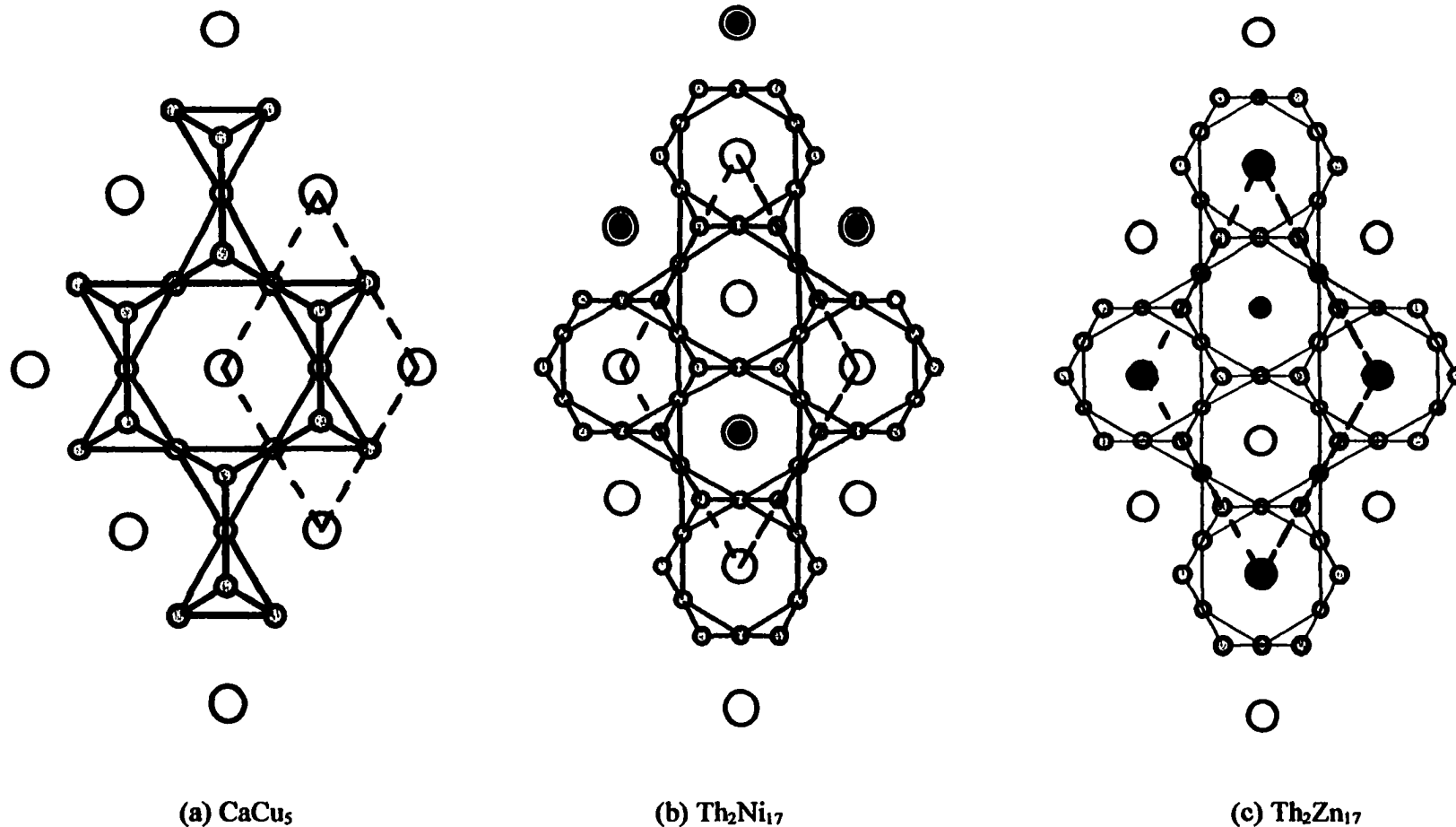


Figure 7.6: In each picture the unit cell is highlighted by the dashed line. The gray circles in each structure are the Cu, Ni and Zn respectively, the large open circles are the Ca and Th atoms, and the Ni-Ni and Zn-Zn ‘pairs’ in (b) and (c) are the black circles. (a) The CaCu_5 structure showing the Ca atoms and the Cu network. (b) The $\text{Th}_2\text{Ni}_{17}$ structure with only Th atoms in the channels running along $(0,0,z)$ and Th atoms and Ni-Ni ‘pairs’ alternating along $(1/3, 2/3, z)$. (c) The $\text{Th}_2\text{Zn}_{17}$ structure with all ‘channels’ occupied by both Th atoms and Zn-Zn ‘pairs’.

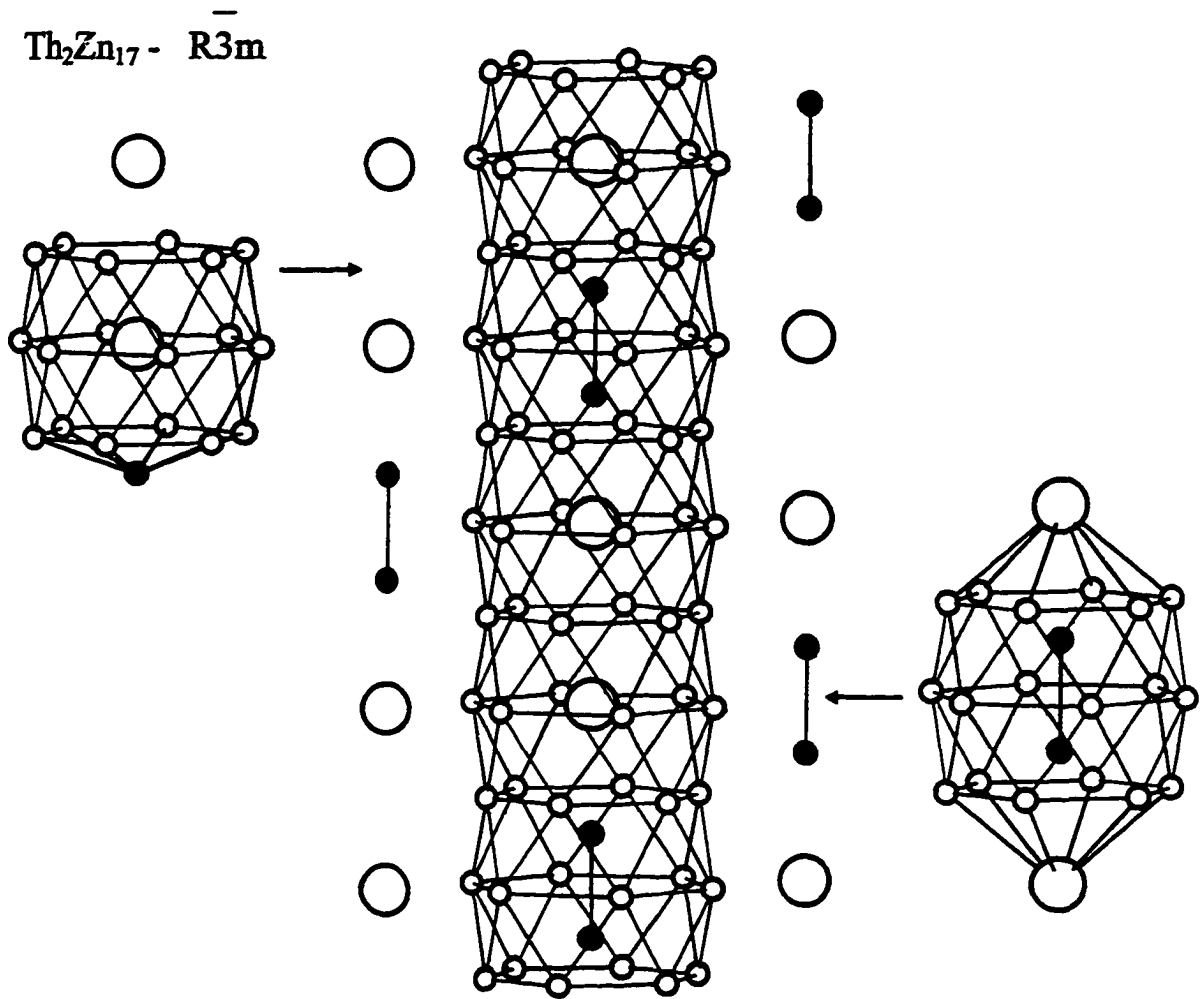


Figure 7.7: The two 20 vertex polyhedra around the Zn-Zn pairs and the Th atoms in $\overline{\text{Th}_2\text{Zn}_{17}}$. The large open circles are Th, the smaller gray circles are the Zn - Zn pairs, and the small open circles are the Zn atoms of the kagomé nets.

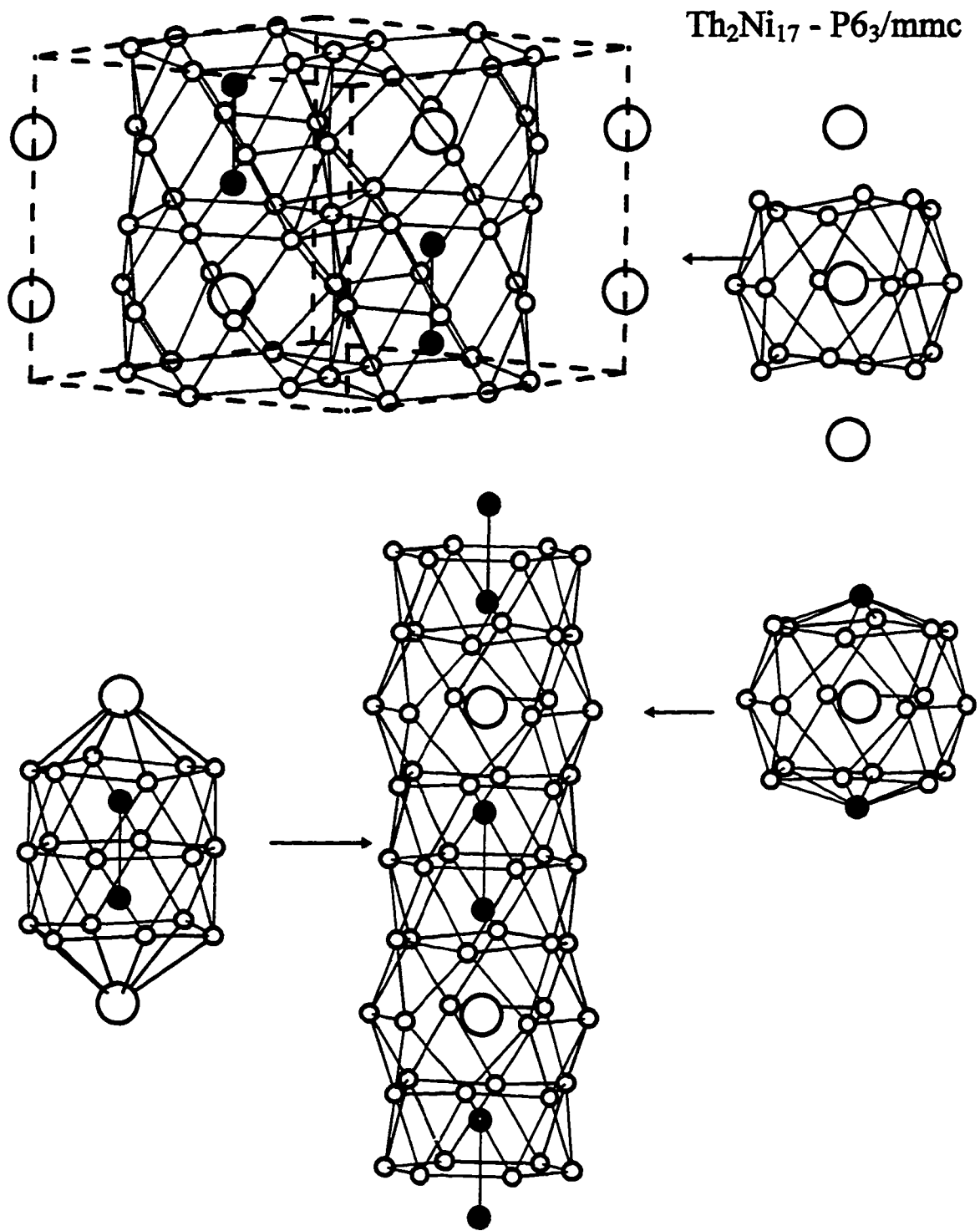


Figure 7.8: The three 20 vertex polyhedra that surround the 2 Th atoms and Ni-Ni 'pairs'.

Since these phases were similar in composition to the other aluminum-rich compounds under consideration with *vec* between 2 and 4, a systematic synthetic approach was carried out for the $\text{La}_2\text{Ag}_x\text{Al}_{17-x}$ series.

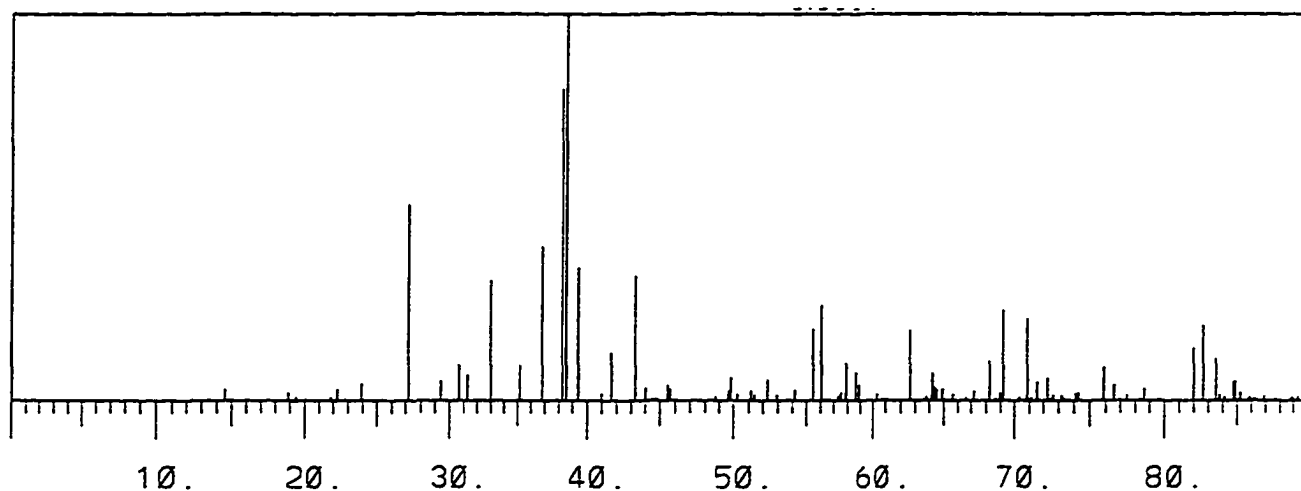
Synthesis and Characterization

The synthesis of the series of $\text{La}_2\text{Ag}_x\text{Al}_{17-x}$ compounds was carried out from stoichiometric combinations of the elements in an arc melting furnace, as described in chapter 2. The reactant compositions and the products identified by powder X-ray diffraction are given in Table 7.10. In many of the products, multiple phases were observed in the powder patterns, in which cases the major phases are underlined. Since the compositions of the product phases are difficult to assess, particularly in the presence of multiple phases, the general compounds $\text{Th}_2\text{Ni}_{17}$ and $\text{Th}_2\text{Zn}_{17}$ are listed in cases where only the structure type could be identified. For many compositions, reactions were carried out multiple times, however, if the results were identical, only one is reported.

Table 7.9: Ternary aluminides forming either the $\text{Th}_2\text{Ni}_{17}$ or $\text{Th}_2\text{Zn}_{17}$ structure having been characterized with single crystal X-ray analysis.

<u>Composition</u>	<u>Structure</u>	<u><i>vec</i> (s and p)</u>	<u>Reference</u>
$\text{La}_{1.8}\text{Ag}_{6.5}\text{Al}_{10.5}$	$\text{Th}_2\text{Ni}_{17}$	2.55	36
$\text{Ce}_{1.8}\text{Ag}_{6.5}\text{Al}_{10.5}$	$\text{Th}_2\text{Ni}_{17}$	2.55	36
$\text{Pr}_{1.8}\text{Ag}_{6.5}\text{Al}_{10.5}$	$\text{Th}_2\text{Ni}_{17}$	2.55	36
$\text{Yb}_{1.8}\text{Ag}_7\text{Al}_{10}$	$\text{Th}_2\text{Ni}_{17}$	2.49	36
$\text{La}_2\text{Ag}_{9.6}\text{Al}_{7.3}$	$\text{Th}_2\text{Zn}_{17}$	2.21	36
$\text{Ce}_2\text{Ag}_{8.8}\text{Al}_{8.2}$	$\text{Th}_2\text{Zn}_{17}$	2.31	36
$\text{Pr}_2\text{Ag}_{10}\text{Al}_7$	$\text{Th}_2\text{Zn}_{17}$	2.17	36
$\text{Yb}_2\text{Ag}_9\text{Al}_8$	$\text{Th}_2\text{Zn}_{17}$	2.29	36

(a) $\text{La}_{1.8}\text{Ag}_{6.5}\text{Al}_{10.5}$ ($\text{Th}_2\text{Ni}_{17}$)
 $P6_3/mmc$ $a = 9.404 \text{ \AA}$ $c = 9.153 \text{ \AA}$



(b) $\text{La}_2\text{Ag}_{9.7}\text{Al}_{7.3}$ ($\text{Th}_2\text{Zn}_{17}$)
 $R\bar{3}m$ $a = 9.451 \text{ \AA}$ $c = 13.726 \text{ \AA}$

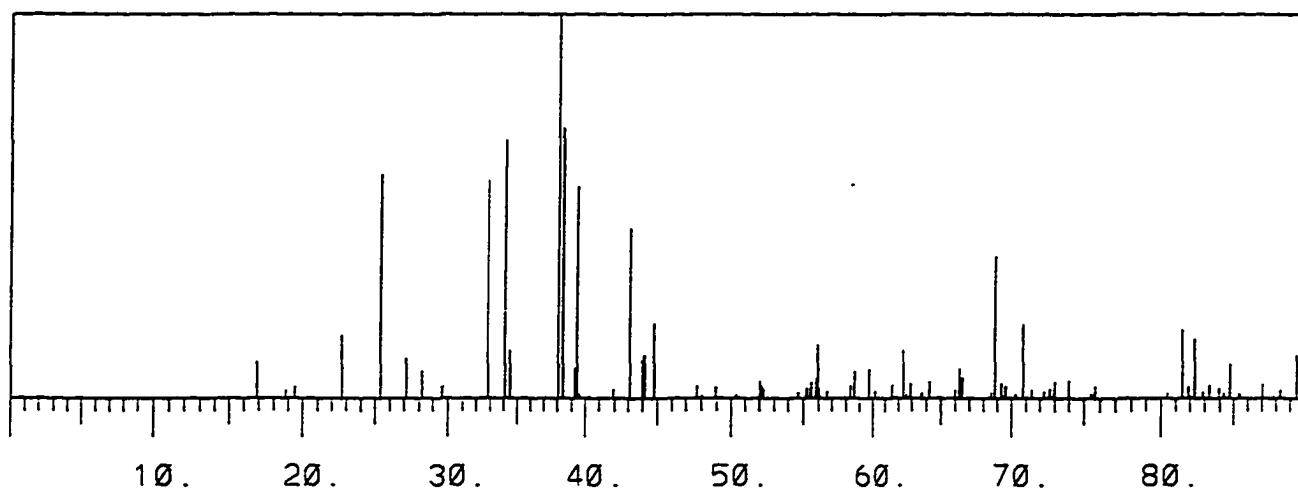


Figure 7.9 (a): The theoretical X-ray powder pattern generated from the single crystal solution of $\text{La}_{1.8}\text{Ag}_{6.5}\text{Al}_{10.5}$ from reference [36]. This compound adopts the $\text{Th}_2\text{Ni}_{17}$ structure type. (b) The theoretical X-ray powder pattern generated from the single crystal solution of $\text{La}_2\text{Ag}_{9.7}\text{Al}_{7.3}$ from reference [36]. This compound adopts the $\text{Th}_2\text{Zn}_{17}$ structure type.

Table 7.10: The reactant composition and crystalline products identified by powder X-ray diffraction. The underlined phases represent the major products based on intensities of the diffracted patterns.

<u>Reactant Composition</u>	<u>Products (as identified by powder X-ray diffraction)</u>
La ₂ Ag ₄ Al ₁₃	<u>Th₂Ni₁₇</u> + 'BaAl ₄ ' type
La ₂ Ag ₅ Al ₁₂	<u>Th₂Ni₁₇</u> + 'BaAl ₄ ' type
La ₂ Ag ₅ Al ₁₂	La ₂ Ag ₅ Al ₁₂ (Th ₂ Ni ₁₇) → (annealed) same
La ₂ Ag ₇ Al ₁₀	<u>Th₂Ni₁₇</u> + Th ₂ Zn ₁₇
La _{1.8} Ag ₈ Al ₉	<u>Th₂Ni₁₇</u> + LaAg ₆ Al ₅ (BaCd ₁₁) →(annealed) same
La ₂ Ag _{8.5} Al _{8.5}	<u>Th₂Zn₁₇</u> + LaAg ₆ Al ₅ (BaCd ₁₁)
La ₂ Ag ₉ Al ₈	Th ₂ Ni ₁₇ → (annealed) Th ₂ Zn ₁₇
La ₂ Ag ₁₀ Al ₇	La ₂ Ag ₁₀ Al ₇ (Th ₂ Zn ₁₇)*
La ₂ Ag ₁₁ Al ₆	<u>Th₂Zn₁₇</u> + Th ₂ Ni ₁₇ *

(*) pattern includes several weak unidentified lines

Results

The results of this series of reactions agrees with the general observation that silver - rich systems form the Th₂Zn₁₇ structure, and aluminum-rich systems adopt the Th₂Ni₁₇ structure, but it is far from definitive. Many of these reaction products were annealed in an attempt to improve the crystallinity of the products for single crystal X-ray analysis. In all but one case, the crystals were poor quality, they were weakly diffracting and had broad, noisy reflection profiles. A crystal of suitable quality was discovered from the products of reaction (5), and a data set was collected on a Siemens P4 diffractometer.



Tables 7.11 and 7.12 summarize the results of the single crystal refinement. La₂Ag₇Al₁₀ forms a variation of the Th₂Ni₁₇ structure. In Th₂Ni₁₇, (see figure 7.8), the 'channels' along

(0,0,1) are occupied exclusively by cations, but $\text{La}_2\text{Ag}_7\text{Al}_{10}$ is a 'filled' variant of $\text{Th}_2\text{Ni}_{17}$ in which all three 'channels' are occupied to some extent by both La atoms and dimers. The refinement was not straightforward, and is not of sufficient quality to be considered adequate, but unfortunately, despite many attempts, another suitable crystal was not found. However, the theoretical powder pattern generated from this refinement matches the powder pattern of the product from reaction (5) very well.

Table 7.11: The structure determination summary for $\text{La}_{1.90}\text{Ag}_{7.34}\text{Al}_{9.6}$.

Refined Chemical Formula	$\text{La}_{1.90}\text{Ag}_{7.34}\text{Al}_{9.6}$
Space Group	$P6_3/mmc$
Unit Cell Dimensions	$a = 9.394(1) \text{ \AA}$ $c = 9.416(2) \text{ \AA}$
Unit Cell Volume	$699.0(2) \text{ \AA}^3$
Z	2
Density (calc.)	6.250 Mg/m^3
Absorption Coefficient	16.303 mm^{-1}
Radiation	$\text{MoK}\alpha$ ($\lambda = 0.71073 \text{ \AA}$)
Temperature (K)	298(2)
2 θ Range	3.0 to 50.0 °
Scan Range (ω)	0.85 °
Scan Speed	Variable: 3.0 to 30.0 °/min. in ω
Index Ranges	$-1 \leq h \leq 10, -11 \leq k \leq 1, -1 \leq l \leq 10$
Reflections Collected	1184
Independent Reflections	267 ($R_{\text{int}} = 0.0477, R_{\sigma} = 0.0302$)
Observed Reflections	195 ($F_o \geq 2\sigma(F_o)$)
Weighting Scheme	$w = 1/[s^2(F_o^2) + (0.0496P)^2 + 15.212P]$ *
Parameters Refined	40
R Indices ($F_o \geq 4.0 \sigma(F_o)$)	$R = 0.0385, wR = 0.1027$
R Indices (all data)	$R = 0.0585, wR = 0.1129$
GooF, All Data	1.189
Data : Parameter Ratio	6.68 : 1
Largest Difference Peak	1.181 e/\AA^3
Largest Difference Hole	-1.013 e/\AA^3

* $P = (F_o^2 + 2F_c^2)/3$

Table 7.12: The positional parameters, site occupancies and isotropic thermal parameters for $\text{La}_{1.92}\text{Ag}_{7.16}\text{Al}_{10.44}$.

Atom	Wyck.	(sym)	x	y	z	Occ.	Ueq
La	2d	($\bar{6}m$ 2)	0.6666	0.3333	0.25	0.982(9)	0.0090(9)
La	2c	($\bar{6}m$ 2)	0.6666	0.3333	0.75	0.13	0.029(5)
La	2b	($\bar{6}m$ 2)	0.0	0.0	0.25	0.79(1)	0.009(1)
Ag	4f	(3m)	0.6666	0.33333	-0.1026(4)	0.45(2)	0.0128(13)
Al	4f	(3m)	0.6666	0.33333	-0.1026(4)	0.42(2)	0.0128(13)
Ag1	12k	(.m.)	0.3277(3)	0.1638(1)	0.0194(3)	0.416(10)	0.0124(9)
Al1	12k	(.m.)	0.3277(3)	0.1638(1)	0.0194(3)	0.584(10)	0.0124(9)
Ag2	12j	(m...)	0.3347(6)	0.3755(5)	0.25	0.47(1)	0.0128(11)
Al2	12j	(m...)	0.306(2)	0.320(2)	0.25	0.53(1)	0.0128(11)
Al3	6g	(.2/m.)	0.5	0.0	0.0	0.70(1)	0.0129(14)
Ag3	6g	(.2/m.)	0.5	0.0	0.0	0.30(1)	0.0129(14)
Ag4	4e	(3m)	0.0	0.0	0.106(4)	0.077(9)	0.019(10)
Ag5	4f	(3m)	0.6666	0.33333	0.10(1)	0.02(1)	0.000(3)

Conclusions

With the challenges presented by both the powder and single crystal X-ray diffraction, it is clear that more careful examination of these structures and compounds is necessary. However, with the general observation that the formation of one of the two structures is related to composition, and therefore to the *vec*, the structures were evaluated using both the extended Hückel and second moment scaling calculations. The results of the second moment scaling calculations were presented in chapter 6, and were somewhat disappointing for the separation of the structures using s and p orbitals only. The inclusion of a low lying d-orbital core did affect the *vec* separation of the three structures, however,

this presents an additional challenge in the case of the ternary aluminides. How does a single set of atomic orbitals (including a d-core) effectively model compounds of silver and aluminum? There is not an appropriate pseudo-element, whose parameters would be a realistic mixture of those of silver and aluminum.

Given the wide range of rare earth-silver-aluminides for which these structures are observed, the thorough investigation of these compounds, their structures, and their physical properties could be a complex, but rich area of further study.

CHAPTER 8

AAu₆Al₆ AND APd₄Al₉ (A = Ba, Sr, Eu, La)
TETRAGONAL VARIANTS OF BaCu₅Al₈

Introduction

AM_xAl_{13-x} compounds where A = Ba and Sr, M = Cu and Ag, and 4 < x < 6, form the NaZn₁₃ structure with the copper and aluminum atoms mixed throughout the structure. As discussed at the end of chapter 2, significant synthetic effort was invested in investigating the substitutional derivatives of these parent aluminides (see Table 2.5 or Appendix A). Many transition metals were included such as Fe, Co, Ni, and other main group elements were included such as Si, Sn, and Ge in addition to, or in place of the trielide element. The majority of these reactions resulted in the observation of compounds with structures other than BaCu₅Al₈. In the reactions including the heavier transition metals Pd and Au however, two new structure types were observed, both tetragonal variants of BaCu₅Al₈. APd₄Al₉ (A = Ba, Sr, Eu) form a body-centered tetragonal variant of BaCu₅Al₈, and AAu₆Al₆ (A = Ba, Sr, La, Eu) form a primitive tetragonal variant.

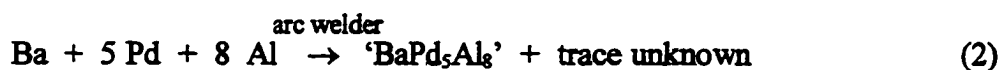
APd₄Al₉ (A = Ba, Sr, Eu)*Synthesis and Structure Solution*

The preliminary indication of this structural derivative was clear in the powder pattern of the products from reaction (1). The initial reaction from the elements in the arc melting furnace, was an attempt to make the Pd derivative of BaNi₂Al₉.



The product was silvery, metallic looking and ground into a black powder for X-ray analysis. The powder pattern of the product contained a very similar pattern of lines as BaCu₅Al₈, but many of the most intense lines were split, and there were some additional lines. This was the first indication that the product contained a compound with a similar

structure as BaCu_5Al_8 , but of lower symmetry. With the initial indication of a Ba - Pd - Al compound similar to BaCu_5Al_8 , reaction (2) was carried out.

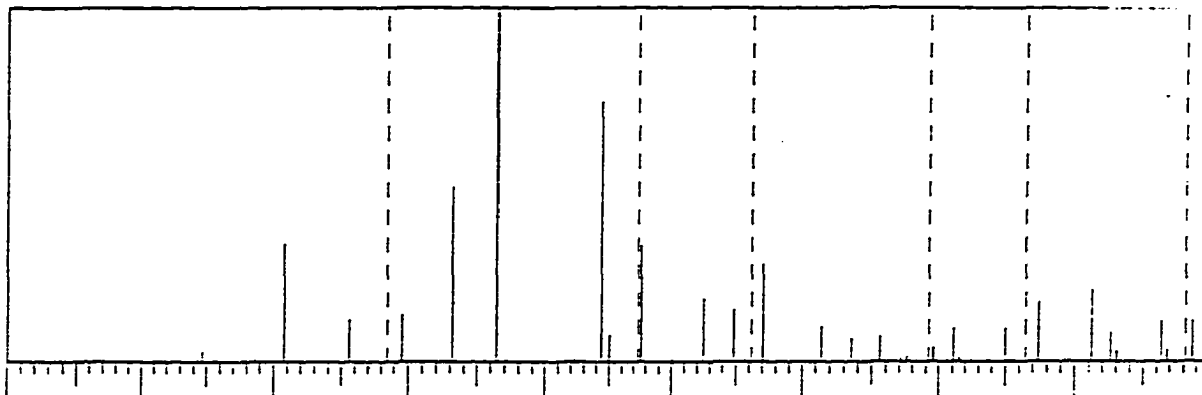


The product was analyzed using EDS in the SEM, and all three elements were identified in the sample. Several crystallites of this product were loaded into a capillary for single crystal X-ray analysis. It was very difficult to find a suitable crystal for single crystal X-ray data collection, because the samples were weakly diffracting and the peaks were generally broad and noisy.

When an acceptable crystal was located, single crystal data were collected on a Siemens P4 diffractometer at 298 ± 2 K (Mo $K\alpha_1$). Peaks located from a rotation photo were used to obtain a unit cell whose orientation matrix was refined using a group of 50 reflections in the 2θ range 10° to 30° . A data set of 896 reflections, containing 472 unique reflections, as well as absorption correction reflections was collected on a Siemens P4 diffractometer at 298(2) K. Lorentz and polarization corrections were applied to the data sets as well as a semi-empirical absorption correction based on collected azimuthal scans. The structure was solved by direct methods and refinement calculations were performed on a Digital Equipment Micro VAX 3100 computer using the SHELXTL-PLUS programs.^[43] Table 8.1 and 8.2 summarize the structure refinement and unit cell contents. The structure refinement was carried out in several space groups, and the centrosymmetric $I4/mcm$ was the best choice.

The structure refinement is poor, but it is good enough to generate a theoretical powder pattern which is an excellent match to the observed lines in the powder X-ray diffraction pattern of this phase. For comparison, the theoretical powder patterns for BaCu_5Al_8 and BaPd_4Al_9 are shown in Figure 8.1. The refined lattice parameters for BaPd_4Al_9 from measured powder data are $a = 8.741(4)$ Å, and $c = 12.538(1)$ Å.

(a) BaCu_6Al_7 : $a = 12.084 \text{ \AA}$ $Fm\bar{3}c$



(b) BaPd_4Al_9 : $a = 8.731 \text{ \AA}$ $c = 12.494 \text{ \AA}$ $I4/mcm$

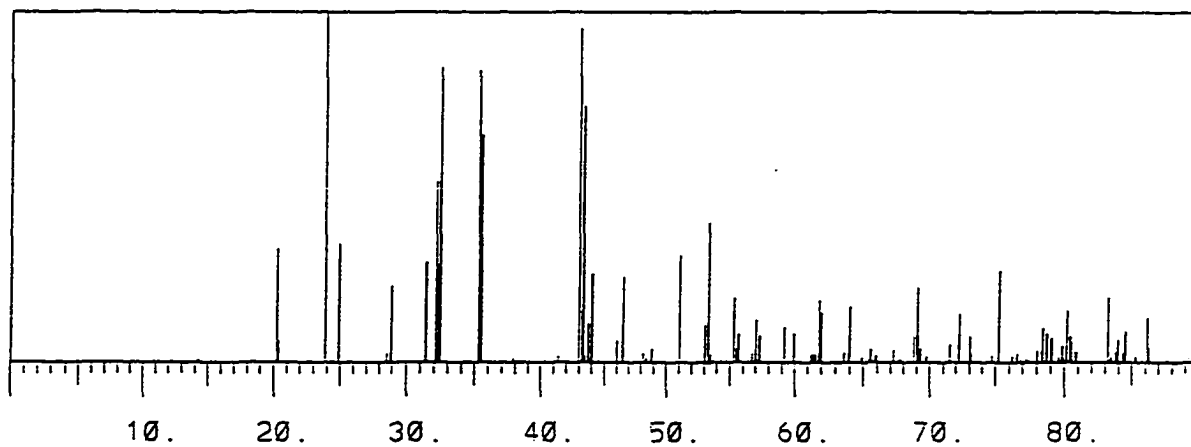


Figure 8.1: The theoretical powder patterns generated from the single crystal refinements of (a) BaCu_6Al_7 ($Fm\bar{3}c$), and (b) BaPd_4Al_9 ($I4/mcm$).

Table 8.1: The structure refinement summary for BaPd₄Al₉.

Refined Composition	BaPd _{3.49} Al _{9.51}
Space Group	<i>I4/mcm</i> (No. 140)
Unit Cell Dimensions	$a = 8.731(1) \text{ \AA}$ $c = 12.494(2) \text{ \AA}$
Unit Cell Volume	$952.4(2) \text{ \AA}^3$
Z	4
Density (calc.)	5.724 Mg/m^3
Crystal habit : shape	silver : irregular
Absorption Coefficient	11.362
Radiation	Mo K α ($\lambda = 0.71073 \text{ \AA}$)
Temperature (K)	298(1)
$2\theta_{\text{max}}$	50°
Scan Range (ω)	0.85°
Scan Speeds	Variable; 3.0 to $20.0^\circ/\text{min}$. in ω
Index Ranges	$-10 \leq h \leq 10$, $-10 \leq k \leq 10$, $-14 \leq l \leq 14$
Reflections Collected	896
Independent Reflections	250 ($R_{\text{int}} = 0.090$)
Observed Reflections	195 ($F_o \geq 2.0\sigma(F_o)$)
Weighting Scheme	$w = 1/[s^2(F_o^2) + (0.0005P)^2 + 300.0P]$ *
Parameters Refined	24
R Indices [$F_o \geq 2.0\sigma(F_o)$]	$R = 0.075$ $wR = 0.1844$
R Indices (all data)	$R = 0.098$ $wR = 0.1933$
Goof (all data)	1.53
Largest Difference Peak	2.41 e/\AA^3
Largest Difference Hole	-3.23 e/\AA^3

$$* P = (F_o^2 + 2F_c^2) / 3$$

Table 8.2: The positional parameters, occupancies, and isotropic displacement parameters for BaPd₄Al₉.

Refined Composition	BaPd _{3.49} Al _{9.51}					
Space Group	<i>I4/mcm</i> (no. 140)					
Unit Cell Dimensions	<i>a</i> = 8.731(1) Å					
	<i>c</i> = 12.494(2) Å					
Atom	Wyckoff	x	y	z	occ.	U _{eq}
Ba	4 <i>a</i>	0	0	0.25	1.0	0.014(2)
Al	4 <i>d</i>	0.5	0	0.5	1.0	0.021(6)
Pd1	16 <i>l</i>	0.1692(3)	-0.3308(3)	0.3849(3)	0.83(3)	0.015(1)
Al1	16 <i>l</i>	0.1692(3)	-0.3308(3)	0.3849(3)	0.17(3)	0.015(1)
Pd2	16 <i>l</i>	0.129(1)	-0.371(1)	0.183(1)	0.05(2)	0.024(5)
Al2	16 <i>l</i>	0.129(1)	-0.371(1)	0.183(1)	0.95(2)	0.024(5)
Al3	16 <i>k</i>	0.703(1)	0.565(1)	0.5	1.0	0.013(3)

Structure Description

BaPd₄Al₉ is a tetragonal derivative of BaCu₅Al₈ and has a very similar arrangement of atoms. There are centered icosahedral units, and 24-vertex polyhedra around the Ba atoms. Figure 8.2 shows a slice of the structure with the shaded icosahedral units highlighted. Included in Figure 8.2 is an Al-centered, 12-vertex, icosahedron and the 24-vertex polyhedron centered by Ba. The large open circles are the Ba atoms, the smaller open circles are the Pd atoms, and the small dark gray atoms are the Al. (For those positions with mixed Pd and Al, the atom is identified with the majority atom.) Positions 4*d* (Al) and 4*a* (Ba) are the centers of the icosahedra and snub cubes, with symmetries (*m.mmm*) and (422) respectively. Neither of these atoms has equivalent bond distances to the atoms in the two polyhedra, as in BaCu₅Al₈.

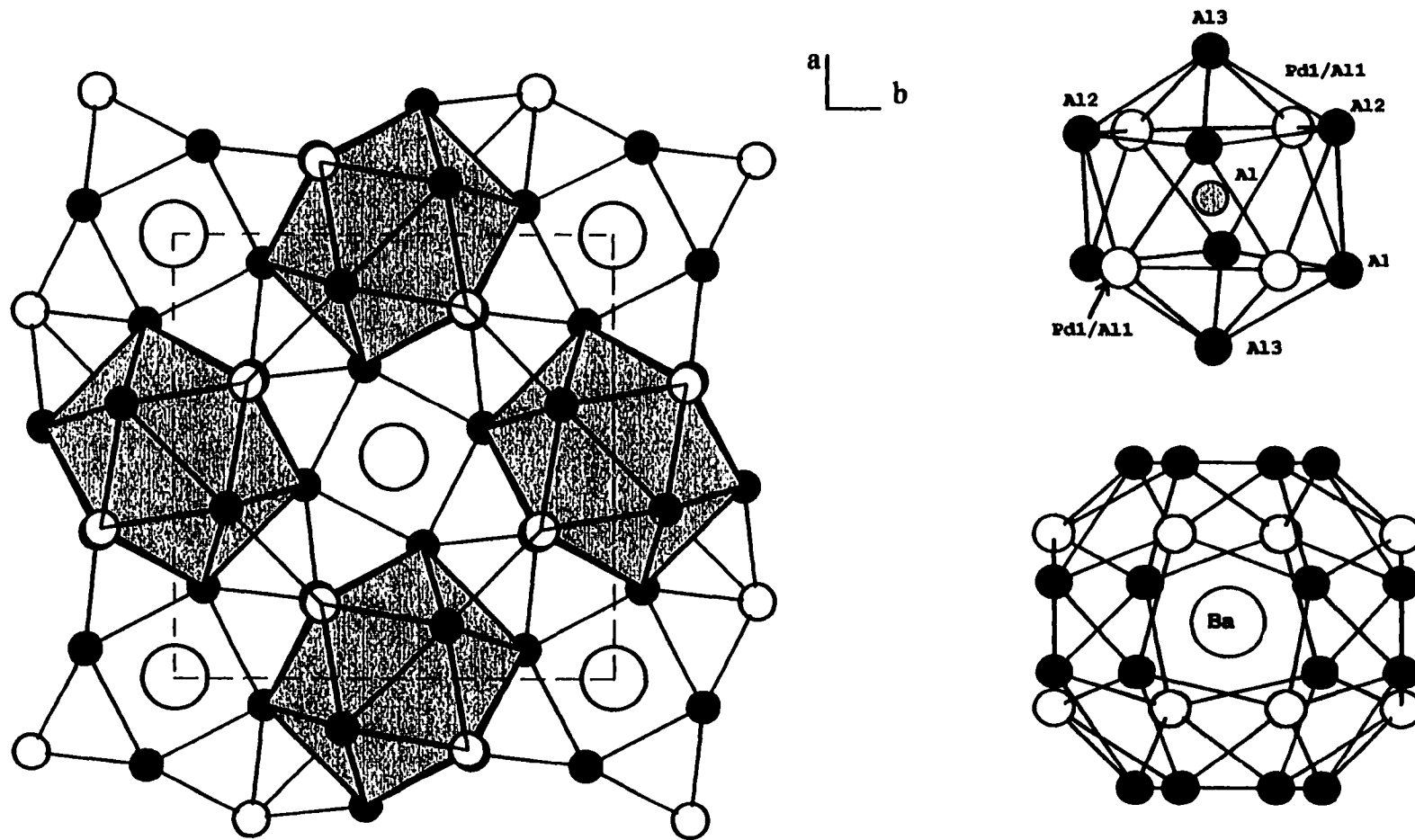
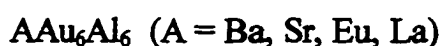


Figure 8.2: The structure of BaPd_4Al_9 , which is a tetragonal variant of BaCu_5Al_8 . The large open circles are the Ba atoms, the smaller open circles are Pd1/Al1 atoms, the light gray atoms are Al, and the dark gray circles are the Pd2/Al2 and Al3 atoms.

Reactions (3) and (4) were also carried out in the arc melting furnace and the powder patterns of the products are very similar to the theoretical pattern generated from the single crystal solution of BaPd_4Al_9 . These new products have been confirmed by multiple reactions yielding the same phases, which persist upon annealing.



These new compounds APd_4Al_9 ($A = \text{Ba}, \text{Sr}, \text{Eu}$) represent the first derivative structures of the NaZn_{13} type observed. In order to further explore and confirm the structure of these new ternaries, a more complete and well behaved structure solution must be obtained.



Synthesis and Structure Solution

To complete the series of ternary compounds BaM_5Al_8 with $M = \text{copper}, \text{silver}$ and gold , reaction (5) was carried out from the elements in the arc melting furnace.



As in the case of the Pd reaction, the powder pattern resembled, but contained many more lines than the pattern of BaCu_5Al_8 . Again, it was very difficult to isolate suitable single crystals because the products were very weakly diffracting. After trying many crystals, an acceptable crystal from reaction (6) was identified, and an orientation matrix was refined based on 82 reflection from $12^\circ < 2\theta < 26^\circ$. A data set of 1190 reflections was collected at 298(2) K on a Siemens P4 diffractometer ($\text{Mo}, \text{K}\alpha_1$). Lorentz and polarization corrections

were applied to the data sets as well as a semi-empirical absorption correction based on collected azimuthal scans. The structure was solved by direct methods and refinement calculations were performed using the SHELXTL-PLUS programs.^[43] Table 8.3 and 8.4 summarize the structure refinement and unit cell contents.

Table 8.3: The structure refinement summary for SrAu_{5.96}Al_{6.34}.

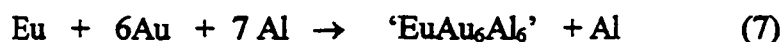
Refined Composition	SrAu _{5.96} Al ₆
Space Group	<i>P4/nbm</i> (no. 125)
Unit Cell Dimensions	$a = 8.720(1) \text{ \AA}$ $c = 12.470(2) \text{ \AA}$
Unit Cell Volume	$948.2(2) \text{ \AA}^3$
Z	4
Density (calc.)	10.042 Mg/m ³
Crystal habit : shape	silver : irregular
Absorption Coefficient	98.03
Radiation	Mo K α ($\lambda = 0.71073 \text{ \AA}$)
Temperature (K)	298(1)
$2\theta_{\text{max}}$	50°
Scan Range (ω)	0.85°
Scan Speeds	Variable; 3.0 to 20.0°/min. in ω
Index Ranges	$-1 \leq h \leq 10, -1 \leq k \leq 10,$ $-1 \leq l \leq 14$
Reflections Collected	1190
Independent Reflections	469 ($R_{\text{int}} = 0.0891$)
Observed Reflections	341 ($F_o \geq 2.0\sigma(F_o)$)
Weighting Scheme	$w = 1/[s^2(F_o^2) + (0.0424P)^2 + 0.0]$ *
Parameters Refined	43
R Indices [$F_o \geq 2.0\sigma(F_o)$]	R = 0.064 wR = 0.1250
R Indices (all data)	R = 0.098 wR = 0.1383
Goof (all data)	1.356
Data-to-Parameter Ratio	10.9:1
Largest Difference Peak	5.71 e/ \AA^3
Largest Difference Hole	-3.69 e/ \AA^3

* $P = (F_o^2 + 2F_c^2) / 3$

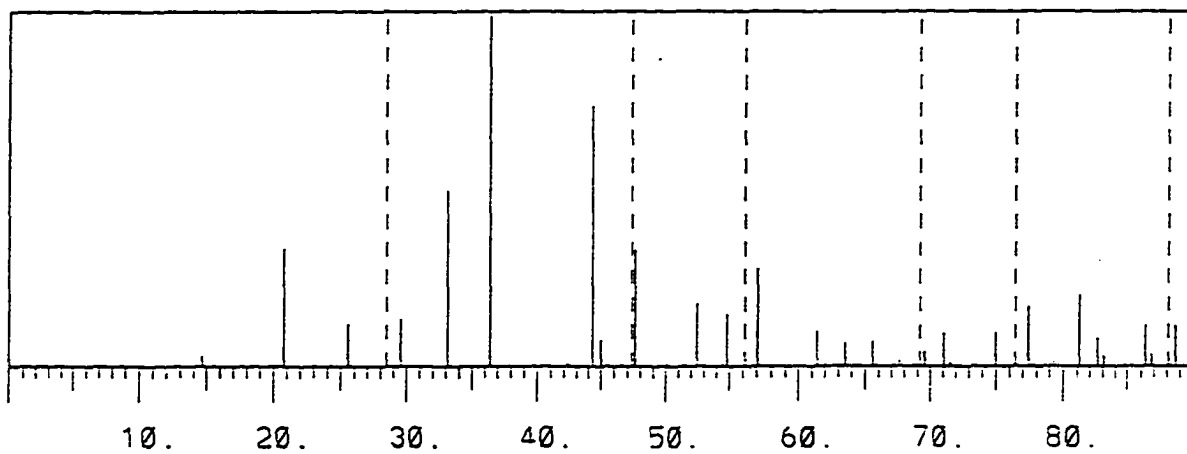
Table 8.4: The positional parameters, occupancies, and isotropic displacement parameters for SrAu_{5.96}Al_{6.34}.

Refined Composition		SrAu _{5.96} Al _{6.34}				
Space Group		<i>P4/nbm</i> (no. 125)				
Unit Cell Dimensions		<i>a</i> = 8.720(1) Å				
		<i>c</i> = 12.470(2) Å				
Atom	Wyckoff	x	y	z	occ.	U _{eq}
Sr	2 <i>a</i>	0.25	0.25	0.0	1.0	0.010(3)
Sr	2 <i>b</i>	0.25	0.25	0.5	1.0	0.006(2)
Au	8 <i>m</i>	0.9210(2)	0.0790(2)	0.3765(2)	1.0	0.0195(8)
Au1	8 <i>m</i>	0.1182(2)	-0.1182(2)	0.0708(2)	0.91(3)	0.0235(9)
Al1	8 <i>m</i>	0.1182(2)	-0.1182(2)	0.0708(2)	0.09(3)	0.0235(9)
Au2	16 <i>n</i>	0.1901(3)	0.0552(3)	0.2469(2)	0.50(2)	0.0121(9)
Al2	16 <i>n</i>	0.1901(3)	0.0552(3)	0.2469(2)	0.50(2)	0.0121(9)
Au3	8 <i>m</i>	0.8688(10)	0.1312(10)	0.5755(9)	0.095(12)	0.033(4)
Al3	8 <i>m</i>	0.8688(10)	0.1312(10)	0.5755(9)	0.905(12)	0.033(4)
Al4	8 <i>m</i>	0.9123(16)	0.0877(16)	0.1357(13)	1.0	0.022(4)
Al5	4 <i>h</i>	0.75	0.25	0.2431(40)	0.33	0.00(1)

Figure 8.3 is a comparison of the powder patterns generated from the single crystal refinements of BaCu₆Al₇ and SrAu₆Al₆ respectively. The pattern for SrAu₆Al₆ is much more complex than that of BaCu₆Al₇, as is expected with the lowering of the symmetry. The structure of SrAu₆Al₆ is shown in Figure 8.4 with the 'empty' icosahedron. This same powder pattern has been observed in the products of reactions (7) and (8) also.



(a) BaCu_6Al_7 : $a = 12.084 \text{ \AA}$ $Fm\bar{3}c$



(b) $\text{SrAu}_{5.5}\text{Al}_{6.5}$: $a = 8.720 \text{ \AA}$ $c = 12.460 \text{ \AA}$ $P4/nbm$

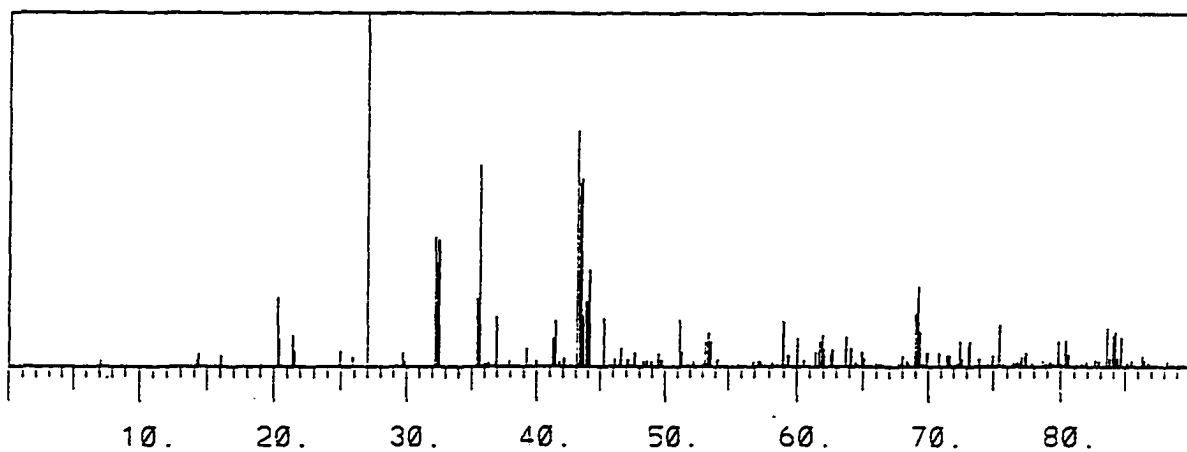


Figure 8.3: The theoretical powder patterns generated from the single crystal refinements of (a) BaCu_6Al_7 ($Fm\bar{3}c$), and (b) $\text{SrAu}_{5.5}\text{Al}_{6.5}$ ($P4/nbm$).

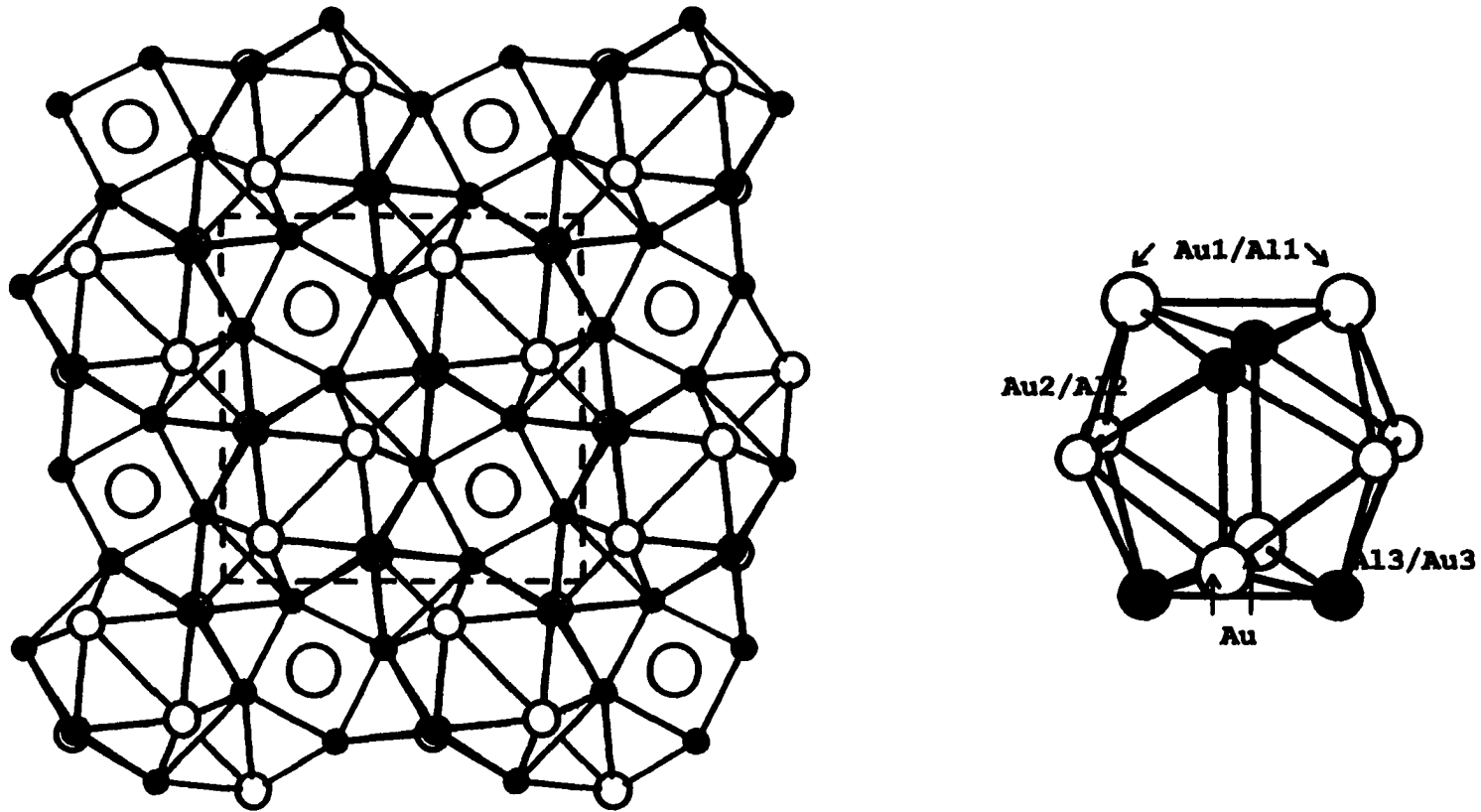


Figure 8.4: The structure of SrAu_{5.5}Al_{6.5} (P4/nbm), a tetragonal variant of BaCu₅Al₆. The large open circles are Sr, the smaller open circles are positions occupied by mostly (or all) Au atoms, and the smaller gray circles are Al atoms, (refer to Table 8.4).

Conclusions

These new compounds, while not completely structurally characterized yet, are an exciting addition to the BaCu_5Al_8 family. These Pd containing aluminides represent new connections to quasicrystalline materials. Many of the well characterized quasicrystalline compounds, such as $\text{Al}_{70}\text{Pd}_{21.5}\text{Mn}_{8.5}$, contain frameworks of similar Al:Pd ratios as this new ternary BaPd_4Al_9 .^[28] With further study of BaPd_4Al_9 , whose structure contains polyhedral resembling icosahedra, this compound may provide new insights into the formation, composition and structure of quasicrystalline materials.

AAu_6Al_6 (A = Sr, Ba, Eu, La) may provide a connection between the ThMn_{12} and the NaZn_{13} structures. If the 12-vertex polyhedra in SrAu_6Al_6 are in fact empty, then the composition of the network is the same as the LnCu_6Al_6 compounds forming the ThMn_{12} structure, but with a structure that resembles BaCu_5Al_8 .

GENERAL CONCLUSIONS

It was mentioned in chapter 1 that intermetallic compounds offer chemists 'complex structural challenges such as fractional and mixed site occupancies, site preferences, vacancy ordering and structural phase transitions.' Many of the ternary aluminide systems I have investigated presented these very challenges. The networks of interconnected polyhedra in BaCu_5Al_8 (NaZn_{13}), the two new tetragonal BaPd_4Al_9 and SrAu_6Al_6 derivatives, EuAg_5Al_6 , $\text{Dy}_3\text{Au}_2\text{Al}_9$ and $\text{Gd}_3\text{Ag}_{10}\text{Al}_5$ all contain positions of mixed occupancies. The rare earth gold aluminides involved interesting questions about site preferences, and vacancy ordering within the Au - Al frameworks. The rare earth silver aluminide phases adopting either the $\text{Th}_2\text{Ni}_{17}$ or $\text{Th}_2\text{Zn}_{17}$ structures were a complex study of structure versus composition (or *vec*). In all of these compounds, whether they contained ordered or disordered intermetallic networks, the 'coloring' question was an important one. In many cases, long term annealing of crystalline samples and multiple structure refinements were necessary to complete a thorough structure solution. Electronic structure calculations in addition to careful crystallography, were necessary to understand the arrangements of atoms within the various structures.

From the beginning, we have examined the structures, phase widths, compositions and properties of aluminum-rich intermetallics in an effort to understand materials with *vec* between the Hume-Rothery and Zintl phases. Furthermore, our interests included establishing whether these compounds and their structures could be rationalized by a set of valence or 'counting' rules. This, as we expected, has proven very difficult. Throughout this research, I have come to appreciate features of these compounds which resemble both the Hume-Rothery and Zintl phases. Like the Hume-Rothery phases, many of these aluminum-rich phases form densely packed structures associated with narrow ranges of *vec*. For example, the phase width of $\text{BaCu}_x\text{Al}_{13-x}$ ($4 < x < 6$) is fairly narrow, and the ${}^3_{\infty}[\text{Cu}_5\text{Al}_8]^{2-}$ framework is electron precise (or nearly so), having the proper electron count to fill the bonding levels in the COOP curves, but leave the antibonding levels empty.

However, in some ways these aluminides also resemble Zintl phases. Like the Zintl phases, the electropositive metal atoms donate their electrons to the intermetallic framework and in most cases do not play a significant role in the structure and bonding of the anionic network. We are continuing to investigate the role of the electropositive metal atoms in some of these structures, because there are some early indications that these cations are not always 'innocent' components of the structure. Particularly in the case of the copper aluminides forming either the NaZn_{13} or ThMn_{12} structure, we believe the cation does have an important role in the ordering of the ${}^3_{\infty}[\text{Cu}_4\text{Al}_8]^{3-}$ network in YCu_4Al_8 .

Using second moment scaling calculations to investigate the hypothesis that these ternary aluminides can be separated into narrow ranges of *vec* within which their formation is favored, was disappointing for some compounds, and encouraging for others. A significant difficulty in the second moment scaling calculations is the selection of a single set of atomic orbital parameters with which to model phases with widely varying elemental components, such as Al, Ga, Pd, Ag, Au and Ba. If and when the *sms* calculations have the capability of scaling and comparing heteroatomic systems, then they may be able to better assess the ranges of *vec* for which these ternary compounds are stable.

APPENDIX A: REACTION COMPOSITION AND PRODUCT IDENTIFICATION

Reaction Stoichiometry	Heating Method	Reaction Products (by powder x-ray diffraction) <small>*single crystal collection and solution</small>
BaCu ₅ Al ₈	furnace(1150C) & arc welder	BaCu ₅ Al ₈ *
BaCu ₁₃	arc welder	BaCu ₁₃
BaCu ₉ Al ₄	arc welder	BaCu ₆ Al ₇ + Cu ?
BaCu ₆ Al ₇	furnace (1150C) & arc welder	BaCu ₆ Al ₇
BaCu ₄ Al ₉	arc welder	BaCu ₄ Al ₉
BaCu ₃ Al ₁₀	arc welder	BaCu ₅ Al ₈ + CuAl ₂ + Al
BaCuAl ₁₂	furnace (1100C) & arc welder	BaAl ₄ + Al + BaCu ₅ Al ₈ trace
BaAl ₁₃	arc welder	BaAl ₄ + Al
BaZn ₅ Al ₈	furnace (1000C)	BaZn ₅ Al ₈ + Al + trace BaAl ₄
BaZn ₅ Al ₈	arc welder	BaAl ₄ + Al + Zn
BaAg ₅ Al ₈	furnace (1120C) & arc welder	BaAg ₅ Al ₈ * + trace Al + trace BaAl ₄
BaAg _{5.5} Al _{7.5}	arc welder	BaAg _{5.5} Al _{7.5} * (a = 12.675 Å)
BaAg ₃ Al ₁₀	arc welder	BaAg ₅ Al ₈ + Al
BaAg _{5.5} Al _{7.5}	arc welder	BaAg _{5.5} Al _{7.5} *
BaCu ₅ Ga ₈	furnace (600C, 950C)	BaCu ₅ Ga ₈ + Ga + CuGa ₂
BaCu ₅ In ₈	furnace (600C, 950C)	BaCu ₅ In ₈ + In
BaAg ₇ Ga ₆	furnace (1000C)	BaAg _x Ga _{13-x} + BaGa ₄
BaAg ₆ In ₇	furnace (1000C)	BaAg _x In _{13-x} + In
BaAu ₅ Al ₈	arc welder (annealed 750C)	SrAu ₆ Al ₆ + ?
BaNi ₅ Al ₈	furnace (1075C)	BaNi ₂ Al ₉ + Ni
BaNi ₄ Al ₉	arc welder	Ni ₂ Al ₃ + ?
BaCo ₅ Al ₈	furnace (1100C)	BaCo ₂ Al ₉ + CoAl ₂
BaCoAl ₁₂	arc welder	BaCo ₂ Al ₉ + Al + trace BaAl ₄
BaPd ₅ Al ₈	arc welder	BaPd ₄ Al ₉ * + Al + unknown (weak)
BaRu ₂ Al ₉	arc welder	BaAl ₄ + Ru ₄ Al ₁₃
BaCu ₅ Sn ₈	furnace (600C, 950C) arc welder	BaCuSn ₂ + Sn
SrCu ₅ Al ₈	furnace and arc welder	SrCu ₆ Al ₇ * + CuAl ₂
SrCu ₆ Al ₇	arc welder	SrCu ₆ Al ₇ *

SrCu ₇ Al ₆	arc welder	SrCu ₇ Al ₆
SrAg ₅ Al ₈	arc welder	SrAg ₆ Al ₇ + Al
SrAg _{5.5} Al _{7.5}	arc welder	SrAg _{5.5} Al _{7.5} (a = 12.6051Å)
SrAu ₆ Al ₇	arc welder (annealed 750C)	SrAu ₆ Al ₆ *
SrPd ₅ Al ₈	arc welder	SrPd ₄ Al ₉ + unknown
EuCu ₆ Al ₇	arc welder	EuCu ₆ Al ₇ * + CuAl ₂
EuAg ₅ Al ₈	arc welder	EuAg ₅ Al ₆ * (BaCd ₁₁ structure type)
EuAg ₅ Al ₆	arc welder	EuAg ₅ Al ₆ (BaCd ₁₁ structure type)
EuAu ₅ Al ₆	arc welder (annealed 750C)	EuAu ₆ Al ₆
EuNi ₅ Al ₆	arc welder	Laves phase Cu ₂ Mg type
EuPd ₅ Al ₆	arc welder	EuPd ₄ Al ₉ + unknown (weak)
EuCu ₅ Al ₇ Sn	arc welder	EuCu ₆ Al ₇ + Sn
EuFe ₂ Al ₉	arc welder	EuFe ₂ Al ₉ (BaNi ₂ Al ₉) + tr. unknown
EuCo ₂ Al ₉	arc welder	EuCo ₂ Al ₉ (BaNi ₂ Al ₉) + tr. unknown
EuNi ₂ Al ₉	arc welder	EuNiAl ₃ * + ?
EuNi ₅ Al ₈	arc welding (annealed 850C)	(Ni ₂ Al ₃) very sharp and single phase!
LaCu ₅ Al ₈	furnace	LaCu ₆ Al ₇ * + LaAl ₄
LaCu ₆ Al ₇	arc welder	LaCu ₆ Al ₇ *
LaAg _{5.5} Al _{7.5}	arc welder	La-Ag-Al [Th ₂ Ni ₁₇]*
	annealed	LaAg _{6.33} Al _{4.66} * (BaCd ₁₁)
LaAg ₅ Al ₆	arc welder	La-Ag-Al [Th ₂ Ni ₁₇]
LaAu ₅ Al ₇	arc welder (annealed 750C)	LaAu ₆ Al ₆
LaCo ₂ Al ₉	arc welder	mixture of NaZn ₁₃ and BaNi ₂ Al ₉
LaFe ₂ Al ₉	arc welder	mixture of NaZn ₁₃ and BaNi ₂ Al ₉
YCu ₆ Al ₇	arc welder	ThMn ₁₂ *
CeCu ₅ Al ₈	arc welder	ThMn ₁₂ + Al + weak unknown
GdCu ₅ Al ₈	arc welder	ThMn ₁₂ + trace Al
HoCu ₅ Al ₈	arc welder	ThMn ₁₂ *
HoCu ₆ Al ₇	arc welder	ThMn ₁₂
YbCu ₅ Al ₈	arc welder	ThMn ₁₂ brd. lines + weak unknown

TbCu ₅ Al ₈	arc welder	ThMn ₁₂
SmCu ₅ Al ₈	arc welder	ThMn ₁₂
DyCu ₅ Al ₈	arc welder	ThMn ₁₂
YbAg ₅ Al ₈	arc welder	Yb-Ag-Al, (Th ₂ Ni ₁₇ , La-Ag-Al)
CeAg ₅ Al ₈	arc welder	Ce-Ag-Al, (Th ₂ Ni ₁₇ , La-Ag-Al)
HoAu ₅ Al ₇	arc welder	?

Sm ₃ Au ₂ Al ₉	arc welder	Sm ₃ Au ₂ Al ₉ * + 'SmAu _x Al _y '
Gd ₃ Au ₂ Al ₉	arc welder	Gd ₃ Au ₂ Al ₉ * + 'GdAu _x Al _y '
Tb ₃ Au ₂ Al ₉	arc welder	Tb ₃ Au ₂ Al ₉
Dy ₃ Au ₂ Al ₉	arc welder (annealing 850C)	Dy ₃ Au ₂ Al ₉
Ho ₃ Au ₂ Al ₉	arc welder	'AuAl ₂ ' + ?
Yb ₃ Au ₂ Al ₉	arc welder	Yb ₃ Au ₂ Al ₉
Y ₃ Au ₂ Al ₉	arc welder	'AuAl ₂ ' + 'YAu _x Al _y '

La ₂ Ag ₄ Al ₁₃	arc welder	<u>Th₂Ni₁₇</u> + 'BaAl ₄ ' type
La ₂ Ag ₅ Al ₁₂	arc welder	<u>Th₂Ni₁₇</u> + 'BaAl ₄ ' type
La ₂ Ag ₅ Al ₁₂	arc welder	La ₂ Ag ₅ Al ₁₂ (Th ₂ Ni ₁₇)
La ₂ Ag ₇ Al ₁₀	arc welder	<u>Th₂Ni₁₇</u> + Th ₂ Zn ₁₇
La _{1.8} Ag ₈ Al ₉	arc welder	<u>Th₂Ni₁₇</u> + LaAg ₆ Al ₅ (BaCd ₁₁)
La ₂ Ag _{8.5} Al _{8.5}	arc welder	<u>Th₂Zn₁₇</u> + LaAg ₆ Al ₅ (BaCd ₁₁)
La ₂ Ag ₉ Al ₈	arc welder	Th ₂ Ni ₁₇ → (annealed) Th ₂ Zn ₁₇
La ₂ Ag ₁₀ Al ₇	arc welder	La ₂ Ag ₁₀ Al ₇ (Th ₂ Zn ₁₇)*
La ₂ Ag ₁₁ Al ₆	arc welder	<u>Th₂Zn₁₇</u> + Th ₂ Ni ₁₇ *

Quaternary Reactions

(BaSr) ₁ Cu ₆ Al ₇	arc welder	(BaSr) ₁ Cu ₆ Al ₇ *
(BaSr) ₁ Ag _{5.5} Al _{7.5}	arc welder annealing (900C)	BaAg _{5.5} Al _{7.5} + SrAg _{5.5} Al _{7.5} (BaSr) ₁ Ag _{5.5} Al _{7.5}
(BaY) ₁ Cu ₆ Al ₇	arc welder	BaCu _{5.5} Al _{7.5} + YCu ₅ Al ₇
(BaDy) ₁ Cu ₆ Al ₇	arc welder annealing (900C)	BaCu _{5.5} Al _{7.5} + DyCu ₅ Al ₇ DyCu ₅ Al ₇ + BaCu _{5.5} Al _{7.5} fuzzier

$(\text{BaGd})_1\text{Ag}_{5.5}\text{Al}_{7.5}$	arc welder annealing (900C)	$\text{BaAg}_{5.5}\text{Al}_{7.5} + \text{Gd-Ag-Al (Th}_2\text{Ni}_{17})$ $(\text{BaGd})_1\text{Ag}_{5.5}\text{Al}_{7.5} \quad a = 12.779(6) \text{ \AA}$
$(\text{BaEu})_1\text{Ag}_{5.5}\text{Al}_{7.5}$	arc welder annealing (900C)	$\text{BaAg}_{5.5}\text{Al}_{7.5} + \text{EuAg}_5\text{Al}_6 (\text{BaCd}_{11})$ $(\text{BaEu})_1\text{Ag}_{5.5}\text{Al}_{7.5} \quad a = 12.753(4) \text{ \AA}$
$(\text{SrCe})_1\text{Cu}_6\text{Al}_7$ $(\text{SrGd})_1\text{Cu}_5\text{Al}_8$	arc welder arc welder annealing (900C)	$(\text{SrCe})_1\text{Cu}_6\text{Al}_7 \quad *$ $\text{SrCu}_6\text{Al}_7 + \text{GdCu}_5\text{Al}_7$ $\text{SrCu}_6\text{Al}_7 + \text{GdCu}_5\text{Al}_7 \quad \text{sharper}$
$(\text{SrEu})\text{Ag}_{5.5}\text{Al}_{7.5}$ $(\text{EuYb})_1\text{Ag}_5\text{Al}_6$	arc welder arc welder	$\text{SrEuAg}_{11}\text{Al}_{15} + \text{traceEuAg}_5\text{Al}_6$ $(\text{EuYb})_1\text{Ag}_5\text{Al}_6 (\text{BaCd}_{11})$
$\text{Eu}(\text{CuAg})_5\text{Al}_8$	arc welder	broadened NaZn_{13}

APPENDIX B: SUMMARY OF SINGLE CRYSTAL REFINEMENTS ON VARIOUS TERNARY ALUMINIDES

Refined Composition	a (Å)	# uniq /obsvd* reflections	$2\theta_{\max}$ (degrees)	R, wR ($F_o \geq 4\sigma(F_o)$)	filename [dir]	reaction nb# : p#	Structure Type
Compounds 1-24 all form the NaZn_{13} structure, in space group $Fm\bar{3}c$ (no. 226).							
1. $\text{BaCu}_{5.27}\text{Al}_{7.73}$	12.205 (4)	117 / 115	60.0	0.0186, 0.0452	[u5]bacual1	1:49, 75-77	
2. $\text{BaCu}_{5.66}\text{Al}_{7.33}$	12.134 (1)	128 / 110	60.0	0.0290, 0.0710	[u5]knbcas1	3:111, 4:18 (xtal 55)	
3. $\text{BaCu}_{6.1}\text{Al}_{6.9}$	12.061 (1)	55 / 45	50.0	0.0143, 0.0300	[u5]cr90l	4:9, xtal 51	
4. $\text{BaCu}_{5.41}\text{Al}_{7.60}$	12.167 (1)	63 / 59	45.0	0.0181, 0.0264	[u5]str577s	4:89, 105, 5:5	
5. $\text{BaCu}_{5.48}\text{Al}_{7.52}$	12.169 (1)	63 / 59	45.0	0.0237, 0.0493	[u5]str578s	"	
6. $\text{BaCu}_{5.52}\text{Al}_{7.48}$	12.168 (1)	63 / 59	45.0	0.0162, 0.0288	[u5]str580s	"	
7. $\text{BaCu}_{6.09}\text{Al}_{6.91}$	12.084 (1)	82 / 82	50.0	0.0219, 0.0542	[u6.bacual]655raw		
8. $\text{BaCu}_{5.42}\text{Al}_{7.58}$	12.154	130/130	60.0	0.0437 0.0975	[u5.bacualo] cent		
9. $\text{SrCu}_{6.17}\text{Al}_{6.83}$	11.980 (1)	125 / 111	60.0	0.0315, 0.0674	[u5]kn10cent	1:113, 124	
10. $\text{SrCu}_{6.0}\text{Al}_{7.0}$	11.980 (1)	110 / 96	60.0	0.0442, 0.0927	[u5]kn11c	2:3, 19	
11. $\text{LaCu}_{5.9}\text{Al}_{7.1}$	11.965 (1)	125 / 113	60.0	0.0170, 0.0398	[u5]lcacent	1:115, 2:3, 96	
12. $\text{LaCu}_{6.07}\text{Al}_{6.93}$	11.913 (1)	61 / 59	45.0	0.0163, 0.0329	[u5]str590l	5:11, 3:128 (syn)	
13. $\text{LaCu}_{6.12}\text{Al}_{6.88}$	11.916 (1)	61 / 59	45.0	0.0236, 0.0563	[u5]str591m	"	
14. $\text{LaCu}_{6.11}\text{Al}_{6.89}$	11.915 (1)	78 / 73	50.0	0.0223, 0.0420	[u5]str592t	"	

Refined Composition	a (Å)	# uniq /obsvd* reflections	2θ _{max} (degrees)	R, wR (F _o ≥ 4σ (F _o))	filename [dir]	reaction nb# : p#	Structure Type
15. EuCu _{6.4} Al _{6.6}	11.928 (1)	124 / 117	60.0	0.0218, 0.0554	[u5]kn12a	2:37	
16. EuCu _{6.13} Al _{6.87}	11.936 (1)	61 / 59	45.0	0.0204, 0.0436	[u5]ecas2	5:9	
17. EuCu _{5.95} Al _{7.05}	11.940 (1)	61 / 59	45.0	0.0165, 0.0353	[u5]eucualsn	5:9	
18. BaAg _{3.0} Al _{10.0}	12.100 (1)	127 / 115	60.0	0.0305, 0.0596	[u5]baagal2c		
19. BaAg _{5.8} Al _{7.2}	12.665 (1)	93 / 88	50.0	0.0433, 0.0813	[u5]kn16c		
20. BaAg _{5.53} Al _{7.47}	12.677 (1)	93 / 89	50.0	0.0222, 0.0501	[u6]str599	5:18	
21. SrCeCu _{7.34} Al _{18.65}	11.938 (1)	78/69	50.0	0.0243 0.0616	[u6.cesrcual]str601		
22. BaSrAg _{12.4} Al _{13.6}	12.705(1)	95/93	50.0	0.0165 0.0312	[u6.basragal]str608		
23. BaSrAg ₁₂ Al ₁₄	12.689(1)	93/93	50.0	0.0139 0.0249	[u6.basragal]str608a		
24. BaEuAg ₁₄ Al ₁₂	12.727(1)	95/92	50.0	0.0139 0.0271	[u6.baeuagal]str609		
25. BaPd _{3.49} Al _{9.51}	a = 8.731 (1) c = 12.494 (2)	250 / 195	50.0	0.075, 0.187	[u6.bapdal]i4mcm		BaPd ₄ Al ₉
26. SrAu _{5.96} Al _{6.34}	a = 8.729 (1) c = 12.470 (2)	469 / 341	50.0	0.0643, 0.1250	[u6.sraual]str636		SrAu ₆ Al ₆
27. CuAl ₂	a = 6.063 (1) c = 4.869 (1)	102 / 93	65.0	0.0266, 0.0624	[u6.cual2]cual2		CuAl ₂

Refined Composition	a (Å)	# uniq /obsvd* reflections	2θ _{max} (degrees)	R, wR (F _o ≥ 4σ (F _o))	filename [dir]	reaction nb# : p#	Structure Type
28. YCu _{5.66} Al _{6.33}	a = 8.666 (I4/mmm) c = 5.096	119/112	50.0	0.0261 0.0626	[u5.hocual]str594l		ThMn ₁₂
29. YCu _{5.64} Al _{6.36}	a = 8.664 (I4/mmm) c = 5.098	119/101	50.0	0.0309 0.0688	[u5.hocual]str593t		ThMn ₁₂
30. HoCu _{4.7} Al _{7.3}	a = 8.708 (I4/mmm) c = 5.128	190/170	60.0	0.0307 0.0663	[u5.hocual]cent		ThMn ₁₂
31. EuAg _{4.67} Al _{6.33}	a = 11.047 (I4 ₁ /amd) c = 7.167	354/324	60.0	0.0361 0.0910	[u5.euagal]euagal		BaCd ₁₁
32. EuAg _{5.18} Al _{5.82}	a = 11.055 (I4 ₁ /amd) c = 7.116	349/294	60.0	0.0206 0.0383	[u5.euagal]euagal2		BaCd ₁₁
33. LaAg _{6.37} Al _{4.63}	a = 11.006 (I4 ₁ /amd) c = 7.071	214/202	50.0	0.0271 0.0532	[u6.laagal]str604		BaCd ₁₁
34. LaAg _{4.3} Al _{6.7}	a = 11.066 (I4 ₁ /amd) c = 7.106	218/157	50.0	0.0438 0.0784	[u6.laagal]str600b		BaCd ₁₁
35. EuYbAg _{11.88} Al _{10.12}	a = 11.053 (I4 ₁ /amd) c = 7.107	218/172	50.0	0.0322 0.0588	[u6.euybagal]str607		BaCd ₁₁
36. La _{1.90} Ag _{7.34} Al _{9.6}	a = 9.394(1) (P6 ₃ /mmc) c = 9.146 (2)	267 / 195	50.0	0.0385 0.01027	[u6.laagal]str600		Th ₂ Ni ₁₇
37. EuNiAl ₃	a = 4.268 (I4/mmm) c = 11.381	74/73	50.0	0.0149 0.0314	[u6.eunial]str605		BaAl ₄
38. EuNiAl ₃	a = 4.267 (I4/mmm) c = 11.382	74/74	50.0	0.0304 0.0642	[u6.eunial]str606		BaAl ₄

Refined Composition	a (Å)	# uniq /obsvd* reflections	2θ _{max} (degrees)	R, wR (F _o ≥ 4σ (F _o))	filename [dir]	reaction nb# : p#	Structure Type
39. Ta ₄ Co _{2.5} Al _{5.5}	a = 4.976 (P6 ₃ /mmc) c = 8.091	119/107	60.00	0.0183 0.0338	[u5.tacual]knta		MgZn ₂
40. Dy ₃ Au _{2.2} Al _{8.8}	a = 4.261 (Immm) b = 9.953 c = 12.526	295/226	50.0	0.0363 0.0769	[u6.dyaua]str617		La ₃ Al ₁₁
41. Dy ₃ Au _{2.1} Al _{8.9}	a = 4.262 (Immm) b = 9.941 c = 12.552	295/253	50.0	0.0253 0.0589	[u6.dyaua]str638c		La ₃ Al ₁₁
42. EuAu _{0.75} Al _{3.25}	a = 4.318 (I4/mmm) c = 11.165	77/64	50.0	0.0277 0.0612	[u6.euaua]str633		BaAl ₄
43. Gd ₆ Ag _{20.85} Al _{6.75}	a = 9.223 (P6 ₃ /mmc) c = 9.446	261/221	50.0	0.0268 0.0436	[u6.tbaga]str619		ErZn ₅
44. Gd ₆ Ag _{20.8} Al _{6.7}	a = 9.224 (P6 ₃ /mmc) c = 9.442	261/?	50.00	0.0233 0.0471	[u6.tbaga]str621		ErZn ₅
45. Gd ₆ Ag _{19.83} Al _{11.74}	a = 9.223 (P6 ₃ /mmc) c = 9.444	261/?	50.00	0.0187 0.0418	[u6.tbaga]str632		ErZn ₅

* observed means (F_o ≥ 2σ (F_o))

**APPENDIX C: REFINED LATTICE PARAMETERS FROM
X-RAY POWDER DATA**

Compound	Lattice parameter(s) Å	pow pat #	nb# - P#	single crystal data filename
BaCu _{5.3} Al _{7.7}	a = 12.205(4)		1-49	bacual1
BaCu _{5.5} Al _{7.5}	a = 12.180(3)	0371A	4-89,105	3- str577
BaCu ₆ Al ₇	a = 12.102(4)	0344	5-	str655
SrCu ₆ Al ₇	a = 11.975(1)	0161b	1-113,124	kn10cent
EuCu _{6.5} Al _{6.5}	a = 11.977(1)			kn12a,ecas2
LaCu ₆ Al ₇	a = 11.952(4)			lcacent
BaCu ₆ Ga ₇ *	a = 12.026(2)			
BaCu ₆ In ₇ *	a = 12.739(4)	0246	4 -69	
BaAg _{5.8} Al _{7.2}	a = 12.666(3)			kn16c, str599
SrAg _{5.5} Al _{7.5}	a = 12.605(6)	0299b		
BaAg _{5.5} Ga _{7.5} *	a = 12.757(3)	0302a		
BaAg _{5.5} In _{7.5} *	a = 13.442(3)			
post-an(BaSr)Ag _{5.5} Al _{7.5}	a = 12.627(1)	0396c	5-	str608, str608a
pre-an 'Ba-Ag-Al'	a = 12.645(1)	0396b	5-	
pre-an 'Sr-Ag-Al'	a = 12.594(3)	0396b	5-	
(BaSr)Cu ₆ Al ₇	a = 12.074(2)	0313	5-	
pst-an(BaEu)Ag _{5.5} Al _{7.5}	a = 12.730(1)	0306b	5-25	str609
pst-an(BaGd)Ag _{5.5} Al _{7.5}	a = 12.764(3)	0308b	5-2	
CuAl ₂	a = 6.066(2) c = 4.877(3)	0368c	5-	cual2
Sm ₃ Au ₂ Al ₉	a = 4.305(4) b = 10.064(3) c = 12.733(2)	0356c	5-	
Gd ₃ Au ₂ Al ₉	a = 4.275(1) b = 9.978(1) c = 12.602(1)	0356b	5-	

$\text{Tb}_3\text{Au}_2\text{Al}_9$	a = 4.276(3) b = 9.970(5) c = 12.583(8)	0368a	5-	
$\text{Dy}_3\text{Au}_2\text{Al}_9$	a = 4.267(1) b = 9.974(2) c = 12.573(4)	0333a	5-	str617 str638c
$\text{Yb}_3\text{Au}_2\text{Al}_9$	a = 4.251(3) b = 9.952(5) c = 12.522(9)	0366a	5-	
LaAuAl_3	a = 4.355(1) c = 10.887(1)	0367c	5-	
BaPd_4Al_9	a = 8.741(4) c = 12.538(1)	0269A	4-106	
$\text{Gd}_3\text{Ag}_{10}\text{Al}_5$	a = 9.232(2) c = 9.456(3)			

APPENDIX D: ELECTRONIC STRUCTURE, SUPERCONDUCTIVITY, AND SUBSTITUTION PATTERNS IN Tl_5Te_3

Karen J. Nordell and Gordon J. Miller*

Department of Chemistry
Iowa State University
Ames, Iowa 50011 USA

This paper is dedicated to Prof. Dr. Dr. h.c. Hans Georg von Schnering on
the occasion of his 65th birthday.

ABSTRACT

Tl_5Te_3 adopts a common intermetallic structure type (Cr_5B_3), and shows a superconducting transition at 3 K. Based on the structure of Tl_5Te_3 , twenty percent of the thallium atoms show crystal chemical behavior consistent with Tl^{+2} , according to the formulation $\text{Tl}^{+2}(\text{Tl}^+)_4(\text{Te}^{2-})_3$. These Tl^{+2} atoms are susceptible to disproportionation into Tl^{+3} and Tl^{+1} . In order to explore this aspect of the electronic structure of Tl_5Te_3 and to investigate potential mechanisms for superconductivity, semi-empirical electronic calculations were carried out on this compound. Recent experiments illustrate that Sn, as well as Bi, Pb, and Cu, can substitute for one-fifth of the thallium atoms to give SnTl_4Te_3 . Both thallium sites are substituted by Sn according to the formula $(\text{Sn}_{0.8}\text{Tl}_{0.2})(\text{Sn}_{0.20}\text{Tl}_{3.80})\text{Te}_3$. Energy density of states and crystal orbital overlap population curves for observed and hypothetical substitution patterns are examined to assess the electronic stability of these phases and to account for the observed arrangement.

Keywords: superconductivity, tellurides, intermetallics, electronic structure

Submitted: February 2, 1996

Accepted: Journal of Alloys and Compounds

Two important problems involving the electronic structure of matter are the so-called “coloring problem”, and the identification of electronic instabilities. The first addresses how two or more different elements may arrange themselves in a given structure, as found, for example, in As_4S_4 or S_4N_4 as well as the B-C arrangement in tetragonal borocarbides MB_2C_2 ($\text{M} = \text{Ca}, \text{La} \dots$)[1a]. As_4S_4 and S_4N_4 , Figure 1a, adopt the same cage structure with the sulfur atoms respectively occupying the two- and three-coordinate sites (shaded) in these molecules. For these 44 electron molecules, the two-coordinate sites are preferred for the atom in the pair with the greater Pauling electronegativity (χ). Since $\chi(\text{As}) < \chi(\text{S}) < \chi(\text{N})$, we can account for the site preference in As_4S_4 and S_4N_4 . In MB_2C_2 , two arrangements have been theoretically examined, see Figure 1b. Calculations suggest the alternate 48^2 network (left) to be preferred, although crystallographic analysis realizes the borocarbide net on the right. Unlike molecules, quasi-infinite solids offer fractional occupancies of sites, as in $\text{BaCu}(\text{Cu}_{1/3}\text{Al}_{2/3})_{12}$ [1b] which can make any theoretical analysis of this coloring problem quite complicated. The second problem, instabilities in the electronic structure, involves features of a spectrum that suggest a phase transition will take place. This transition may be structural, i.e. displacive, or electronic, as to a superconducting or charge density wave state. We have shown how energy band theory and the Landau theory of second-order phase transitions provide a complete analysis of the tetragonal-monoclinic distortion of CaAl_4 [2]. In this article, we shall examine a system that offers both problems for study.

Tl_5Te_3 , In_5Bi_3 , and the substitutional derivatives $\text{M}'\text{Tl}_4\text{Te}_3$ and $\text{M}''\text{In}_4\text{Bi}_3$ ($\text{M}' = \text{Cu}, \text{Sn}, \text{Ag}$ and $\text{M}'' = \text{Sn}, \text{Pb}, \text{Ga}$) are all superconductors with critical temperatures ranging from 2.2 - 7.0 K [3]. With the recent explosion in research on high- T_c

superconductors to understand their electronic structures and postulate the mechanism(s) of superconductivity, even these low- T_c compounds evoke interest. Some of the recent work done by chemists has focused on the coupling of structural and electronic instabilities in materials which undergo the superconducting phase transition [4]. This work examines the electronic structure and bonding of the family of compounds MTl_4Te_3 in an effort to elucidate the nature of the superconducting phase change at low temperatures.

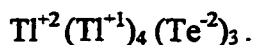
Tl_5Te_3 , In_5Bi_3 , and Tl_5Se_3 are three compounds from the Cr_5B_3 family of intermetallic phases with several important differences from the majority of examples. Among the M_5X_3 systems forming the Cr_5B_3 structure listed in Pearson's Handbook [5], M is an alkaline earth or rare earth metal and X is a group 13 or 14 element in about 70% of the binaries. Recent work by Corbett et al. [6], however, indicates that many of these phases are really ternary hydrides. Tl_5Te_3 , In_5Bi_3 , and Tl_5Se_3 have M components from group 13, and X from group 15 or 16, making both M and X post transition elements. There are also some structural features of these three compounds that are different from many of the remaining Cr_5B_3 compounds. The Cr_5B_3 structure is body-centered tetragonal ($I4/mcm$), and most examples have c/a ratios near 1.90, but the c/a ratios of Tl_5Te_3 and In_5Bi_3 are 1.41 and 1.48, respectively. Also, the minority component (X) often forms dimers in addition to isolated atoms, but Te, Se, and Bi in these three exceptional examples do not.

The Tl_5Te_3 structure contains four crystallographic sites: Tl(A) atoms, Wyckoff site 4c ($4/m (C_{4h})$ point symmetry); Tl(B) atoms, site 16l ($m (C_s)$); Te(C) atoms, site 4a ($422(D_4)$); and Te(D) atoms, site 8h ($m.2m(C_{2v})$). In Table 1 the first coordination spheres around Tl(A) and Ca(A) (in Ca_5Si_3) [7] are compared. In Ca_5Si_3 each Ca(A) is surrounded

by a distorted octahedron of Si atoms with 4 short contacts in the waist (the *ab* plane) and two longer distances to the axial Si(C) atoms, whereas in Tl_5Te_3 the coordination of Tl(A) shows four long equatorial Tl(A)-Te(D) and 2 shorter axial Tl(A)-Te(C) bonds. In fact, these octahedra share vertices to form a three-dimensional ${}^3_{\infty}[\text{TlTe}_{6/2}]$ net. However if we consider just the shortest bond distances in each octahedron, the 4 short interactions in Ca_5Si_3 form a ${}^2_{\infty}[\text{CaSi}_{4/2}]$ layer in the *ab* plane, while the two short axial bonds in Tl_5Te_3 form ${}^1_{\infty}[\text{TlTe}_{2/2}]$ chains parallel to the *c*- direction. It is precisely this structural feature of Tl_5Te_3 that we highlight in this investigation.

With a $\text{Tl-Te}_{\text{ax}} : \text{Tl-Te}_{\text{eq}}$ distance ratio of 0.937, the structure of Tl_5Te_3 can also be described as $[\text{TlTe}_{6/2}]\text{Tl}_4$. The $[\text{TlTe}_{6/2}]$ substructure is an ReO_3 -like, three-dimensional network of vertex-sharing, Tl(A)-centered, slightly compressed octahedra, shown in Figure 2a. The remaining Tl atoms, Tl(B), form square antiprisms around the Te(C) atoms and tetragonally compressed cubes around the Tl(A) sites as shown in Figure 2b. Furthermore, the shortest Te-Te distance (4.01 Å) is greater than twice the van der Waals radius of Te (2.0 Å), making each tellurium isolated from other tellurium atoms, and formally Te^{-2} according to the Zintl-Klemm [8] concept. The shortest Tl-Te bond distance is 3.147 Å between Tl(A) and Te(C) sites, and the next shortest bond distance is 3.159 Å between Tl(B) and Te(D) sites. Each Tl(A) atom is surrounded by 6 Te atoms, and the distance to the nearest Tl(B) atoms is 3.954 Å, which implies weak metal-metal interaction. Each Tl(B) atom has one short bond to a Te atom (3.159 Å), while the remaining distances to Te are longer (3.390 Å, 2x; 3.600 Å, 2x), and the

Tl(B) - Tl(B) separations are 3.458 Å and 3.496 Å. These bond distances and coordination environments around each atom suggest the ionic formulation



Besides the crystallographic evidence for two kinds of Tl atoms in the structure, further support for the assignment of formal charges comes from a Mulliken population analysis carried out on the two Tl sites (A and B) in the structure. The Mulliken population of Tl(A) is 2.126 (i.e. $\text{Tl}^{+0.874}$), and the four other Tl(B) atoms have a population of 2.429 ($\text{Tl}^{+0.571}$). Thus, the more oxidized Tl(A) site was assigned formally Tl^{+2} and the less oxidized Tl^{+1} . To confirm our assignment of formal charges in Tl_5Te_3 , Mulliken population analyses were carried out on several compounds which contain Tl^{+1} and Tl^{+3} . These included TlS, TlSe and Tl_2Te_3 [5]. In these three structures, Tl^{+1} and Tl^{+3} had average Mulliken populations of 2.422 and 1.578 respectively, which are consistent with our assignments of the Tl^{+1} (2.429) and Tl^{+2} (2.126) in Tl_5Te_3 . Recall that a Mulliken population analysis divides the “bond charge” equally between the two components, which generally overestimates the electron density at the “cation”.

Electronic Structure of Tl_5Te_3

We begin with a description of the electronic structure of Tl_5Te_3 , as evaluated using the Extended Hückel method within the tight-binding approximation. Details of the calculations are described in the Appendix. The total DOS curve for Tl_5Te_3 (the Fermi energy is indicated by the dotted line at -7.45 eV) is shown in Figure 3a. There is no gap, i.e. $N(E_F) \neq 0$, observed at or near the Fermi energy, which is consistent with the metallic

behavior of Tl_5Te_3 above its superconducting critical temperature (3.3 K) [3]. The fairly narrow band between -16.0 and -14.0 eV may be assigned to the Te 5p orbitals, which remain close to the energy of the atomic orbitals themselves (Te 5p = -14.80 eV). The region between -12.0 and -6.0 eV are states associated with the Tl atoms (both Tl(A) and Tl(B)) in the structure whose 6s and 6p atomic orbital energies are -11.80 eV and -5.80 eV respectively. The shaded regions of the total DOS curve correspond to states associated with the Tl(A) and Te(C) atomic orbitals and are widely dispersed throughout the curve. States associated with the Tl(A) atoms contribute to the majority of the DOS near the Fermi energy. The DOS region between -12.0 and -5.0 eV is expanded in Figure 4, with the Tl(A) (left), and Tl(B) (right) atomic contributions shaded. The states associated with the Tl(A) atoms lie higher in energy than the Tl(B) states (many are above the Fermi level), which supports the idea that the Tl(B) atoms are more reduced (Tl^{+1}) than the Tl(A) atoms (Tl^{+2}).

The COOP curve for the Tl(A)-Te(C) interaction along the chain is shown in Figure 3b. At the Fermi energy -7.45eV (33 valence electrons/formula unit), some levels with antibonding character are filled. The Tl(A)-Te(C) overlap population of 0.20, compared with the Tl(A) - Te(D) overlap population of 0.07 is another indication of the strength of the Tl(A)-Te(C) interactions. As further evidence of the tendency for the tetragonal compression of these "TlTe₆" octahedra within Tl_5Te_3 , the overlap populations for the Tl(A) - Te(C) and Tl(A) - Te(D) interactions were calculated using a hypothetical structure in which the two bond distances are equal at 3.361Å. The overlap population for the Tl(A) - Te(C) interaction was 0.14, and 0.08 for the Tl(A) - Te(D) interaction, confirming that even

when the bond lengths are set equal in the calculation, there is still a tendency for the octahedra to be compressed based on the differences in overlap populations.

The complete structure of Tl_5Te_3 can be described as an overlapping combination [9] of two partial structural frameworks, (1) the Tl(A)-centered, Te octahedra forming a ${}^3_{\infty}[\text{TlTe}_{6/2}]$ partial structure, reminiscent of ReO_3 , and (2) a ${}^3_{\infty}[\text{Tl}_4\text{Te}_3]$ partial structure, involving just the Tl(B) atoms. The DOS curves for the two individual frameworks are shown in Figure 5 (left and middle), and if these two curves are superimposed, the resulting plot is very similar to the total DOS for Tl_5Te_3 (right). This effect on the Tl orbital contribution to the total DOS indicates that both Tl(A) - Tl(B) through-space interactions (overlap population of -0.02) and Tl(A) - Te - Tl(B) through-bond interactions are very weak. Since much of this electronic structure investigation will focus on the pseudo-one-dimensional chains ${}^1_{\infty}[\text{}^2_{\infty}(\text{TlTe}_{4/2})\text{Te}_{2/2}]$, the fact that this partial structure is not strongly influenced by the surrounding Tl(B) atoms is an important observation.

Superconductivity in Tl_5Te_3

Band Structure: To further investigate the electronic structure of Tl_5Te_3 with respect to potential electronic instabilities, its band structure along high symmetry directions in reciprocal space in the space group $I4/mcm$ was calculated. The body-centered tetragonal Brillouin zone is shown in Figure 6 (top), and the band structure for the directions $\Gamma \rightarrow \text{M} \rightarrow \Gamma \rightarrow \text{X} \rightarrow \text{P} \rightarrow \text{N} \rightarrow \Gamma$ is shown in Figure 6 (bottom). Since the Fermi level intersects bands along directions both parallel and perpendicular to c^* , the electrical conductivity is three-dimensional. An interesting section of the band structure is along $\text{X} \rightarrow \text{P} \rightarrow \text{N}$, where the calculated Fermi level intersects bands close to a degeneracy at point P. This band

degeneracy persists with very little dispersion (± 0.2 eV) as we move across the face of the Brillouin zone from $P \rightarrow N$, and breaks upon moving from $N \rightarrow \Gamma$. While Tl_5Te_3 is strictly not a one-dimensional system, the band structure from $X \rightarrow P$ represents the section of the Brillouin zone parallel to the $Tl(A)$ - $Te(C)$ chains of interest, and has characteristics reminiscent of a Peierls instability. The Peierls distortion is a well-known phenomenon in one-dimensional systems when there is a half-filled band. In the case of a classic Peierls distortion, the chain distorts into dimers to break the degeneracy at the Fermi energy, which lowers the energy of the filled band and creates a gap between the highest filled band and the lowest unfilled band. In Tl_5Te_3 , states near the Fermi level are coupled by the wave vector $c^*/2$, (states along the $P - N$ line have $k_z = \pm c^*/4$) and in the next section we investigate potential distortions consistent with this wavevector.

Another interesting section of the band structure is the area surrounding Γ where a hole pocket is observed as the highest occupied band rises above the Fermi energy. A corresponding electron pocket is observed near N , where the lowest unoccupied band dips below the Fermi energy. It is unclear whether a Peierls-like distortion in Tl_5Te_3 would lead to a more energetically favorable structure: none is observed at 293 K [3], but point P (where the Fermi energy crosses very near a band degeneracy) is a point of electronic instability in the structure.

Frozen Phonon Calculations: According to the band structure, a structural distortion with the wavevector $q = 1/2 c^*$ can couple states on the Fermi surface, since the Fermi

level intersects bands along the P - N line; \mathbf{q} is a Fermi surface nesting vector [10]. Another important aspect of the electronic structure of Tl_5Te_3 is the assignment of Tl(A) as Tl^{+2} , because of the possible disproportionation of Tl^{+2} into Tl^{+1} and Tl^{+3} , (gas phase value of $\Delta H_{\text{disp}} = -4.92 \text{ eV}$) which may drive a structural distortion or be involved with the mechanism of superconductivity, or both. The electronic instability of the Tl^{+2} could manifest itself in a charge density wave, or the long range pairing of electrons, which according to BCS theory leads to superconductivity. Simon [4] has presented the idea that charge disproportionation in systems similar to Tl_5Te_3 could be an electron-pairing mechanism. Tight-binding calculations cannot provide reliable quantitative information of dynamic processes like vibrational modes in solids (phonons) or charge density waves. Nevertheless, static models, i.e. “frozen phonon” calculations can be used within the framework of perturbation theory to probe structural instabilities associated with electronic instabilities in the DOS.

In order to explore the nature of potential structural distortions driven by both a disproportionation of Tl^{+2} and the Fermi surface nesting vector $\mathbf{q} = 1/2 \mathbf{c}^*$, Extended Hückel calculations were performed on four hypothetical structural models which are all derived from the $I4/mcm$ Tl_5Te_3 structure. These four structures involve different shifts of the Te(C) atom(s) along the Tl(A)-Te(C) “chains” parallel to the c -direction, (see Figure 7). We have included displacements which break the body-centering symmetry in order to consider the possibility of detectable coupling between the chains. The space groups of the four hypothetical structures are subgroups of $I4/mcm$ [11]. Included in Figure 7 are the designations $t2$ or $k2$, with t and k meaning *translationengleich* (lattice-equivalent) and

klassengleich (class-equivalent) respectively. The number associated with either t or k , in this case 2, means that $I4/mcm$ has twice the number of symmetry elements as the four subgroups $I4/m$, $I4cm$, $P4/mbm$, $P4/ncc$. In each of the four models represented in Figure 7, the two chains of octahedra demonstrate the relationship between the Tl(A) - Te(C) “chains” running along the unit cell edges and through the unit cell center, in the c -direction. $I4/m$ and $P4/mbm$ structures are based on symmetric, but opposite shifts of each Te(C) atom which results in the alternation of tetragonally compressed and elongated octahedra around the Tl(A) atoms. In both $I4/m$ and $P4/mbm$ the distortion gives two inequivalent Tl(A) sites according to the disproportionation of Tl^{+2} . $I4cm$ and $P4/ncc$ models are structures resulting from a shift of each Te(C) atom in the same direction. This shift creates one long, and one short axial Tl(A) - Te(C) interaction, resulting in Tl(A) -Te(C) “chains” of unsymmetrically compressed octahedra, but not exactly square pyramids: all Tl(A) sites remain equivalent. In all four distorted structures, the original unit cell lattice parameters and origin are retained. In the calculations, the Te(C) z -coordinate was altered from $z = 0.25$ to between $z = 0.23$ and 0.27 to simulate a change in Tl(A)-Te(C) bond length from 3.147 \AA to between 2.895 \AA and 3.399 \AA .

Table 2 compares the differences in total energies and Fermi energies between the undistorted $I4/mcm$ structure and the four distorted structures ($I4/m$, $I4cm$, $P4/mbm$, $P4/ncc$), as well as the second derivative d^2E/du^2 , where u is the shift in the Tl(A) - Te(C) bond distance. These results are plotted in Figure 8 as d^2E/du^2 vs. u (\AA) for the four distortions. If the potential were indeed harmonic, the second derivative (d^2E/du^2), should be

independent of u , and would correspond to a Tl - Te stretching force constant. But, there is certainly a weak anharmonic term which contributes to the softening of this mode.

The total DOS curves for the distorted structures retaining a body-centered lattice ($I4/m$ and $I4cm$) were similar to the undistorted Tl_5Te_3 curves, shown in Figure 9. The $I4/m$ and $I4cm$ DOS curves look nearly identical to the $I4/mcm$ curve. Since the DOS for structures where the only difference is the retention or loss of the body-centering symmetry (i.e. $I4/m$ and $P4/mbm$) are very similar, this coupling between neighboring “chains” running in the c -direction is negligible. Based on the results of these calculations there is no indication that any one of these distorted structures is preferred electronically over the undistorted structure. The total energies per formula unit drop slightly for the distortions that mimic disproportionation effects, i.e. $2Tl^{+2} \rightarrow Tl^{+3} + Tl^{+1}$. On the other hand, the undistorted structure has the lowest Fermi energy. Shifts in the Fermi level arise from changes in the coordination at the Tl(B) sites (the majority Tl component). Therefore, while the total energy reveals a slight preference for either distorted structure, the energy changes associated with the states near the Fermi level counteract this.

Lattice Energy Calculations: Although the band structure seems to support the idea of an electronic instability driving a structural distortion, the results of our Extended Hückel calculations do not unequivocally reveal a more stable structure than the $I4/mcm$ structure. To investigate effects from other forces, changes in lattice energies were also calculated as a function of the distortion of the Te(C) position to the $P4/mbm$ and $I4/m$ structures, using the following summation of relevant energy terms [12]

$$U_{\text{LAT}} = U_{\text{MAD}} + U_{\text{BM}} + U_{\text{VDW}}$$

U_{LAT} is the total lattice energy (U_{LAT} is the enthalpy change for the process $\text{Ti}_5\text{Te}_3 (\text{s}) \rightarrow \text{Ti}^{+2}_{(\text{g})} + 4\text{Ti}^{+1}_{(\text{g})} + 3\text{Te}^{-2}_{(\text{g})}$), U_{MAD} is the Madelung term (long range, net attractive ionic interaction), U_{BM} is the Born-Mayer term (short range, repulsive interaction), and U_{VDW} is the van der Waals term. Further details of the calculations are given in the Appendix. The results for the $P4/mbm$ structure (see Figure 10), are plotted as changes in energy (ΔU) with respect to the displacement of the Te(C) atom, z (Te(C)), where

$\Delta U(z = 0.25) = 0.0 \text{ eV}$; (the curves for the $I4/m$ structure are very similar). Upon changing z (Te(C)), the Madelung and the van der Waals terms both sum positively to yield an increase in lattice energy (lower potential energy), but the Born-Mayer repulsion term is sharply negative. These two forces are competitive in this case, with the Born-Mayer term exerting the greater influence. Thus these distortions are unfavorable. Based on these results, structural distortions driven by electronic instabilities may be strongly resisted by near-neighbor short range repulsions. The electronic instability in the band structure, therefore, manifests itself in a superconducting transition. Formation of Cooper pairs, which involves electrons near the Fermi level, can arise by coupling of occupied and unoccupied states via the wave vector $\mathbf{q} = \mathbf{c}^*/2$.

SnTe₄Te₃ Calculations

Recently, several ternary phases with the composition MTl_4Te_3 ($M = \text{Sn, Pb, Mo, and Cu}$) [13] have been reported. In the cases of $M = \text{Cu}$ or Mo , however, the formulation MTl_4Te_3 is misleading for two reasons: (1) the actual compositions as refined by X-ray data

are $\text{Cu}_{0.7}\text{Tl}_{4.3}\text{Te}_3$ and $\text{Mo}_{0.6}\text{Tl}_{4.4}\text{Te}_3$; [13a] and (2) the Cu and Mo statistically occupy both the Tl(A) and Tl(B) sites as defined in Tl_5Te_3 . In the case of SnTl_4Te_3 , Sn^{+2} is expected to substitute on the Tl(A) site, but crystallographic evidence reveals a small amount of Sn mixing on the Tl(B) site, according to the formulation $(\text{Sn}_{0.8}\text{Tl}_{0.2})(\text{Tl}_{3.8}\text{Sn}_{0.2})\text{Te}_3$ [13b].

The refined unit cell parameters and c/a ratios of Tl_5Te_3 and SnTl_4Te_3 are as follows: Tl_5Te_3 , $a=8.930\text{\AA}$, $c=12.589\text{\AA}$, $c/a=1.41$; and SnTl_4Te_3 , $a=8.819\text{\AA}$, $c=13.013\text{\AA}$, $c/a=1.47$. This shortening of the a -axis and lengthening of the c -axis as Sn replaces Tl changes the coordination of the Sn atom in the Tl(A) position slightly. The two axial bonds (3.253\AA) are still shorter than the four equatorial bonds (3.300\AA), $d_{ax}/d_{eq}=0.986$, but the difference is not as pronounced as in Tl_5Te_3 ($d_{ax}/d_{eq}=0.936$).

In SnTl_4Te_3 , Sn^{+2} (unlike Tl^{+2} in Tl_5Te_3) would lead to a closed subshell configuration (s^2p^0) for each of the elements in the compound, and we may at first expect semiconducting behavior. The total DOS curve for SnTl_4Te_3 with Sn completely occupying the 4c site is shown in Figure 11, and the calculated Fermi energy falls in the gap between -6.0 and -7.0 eV. However, SnTl_4Te_3 is a superconductor below 3.3K, and a metal above 3.3K. These experimental observations coupled with the crystallography present a challenge to the understanding of the chemistry of the Sn substituted Tl_5Te_3 system. In particular, what controls the substitution pattern of Sn onto the crystallographically inequivalent Tl positions? Three approaches to investigating the SnTl_4Te_3 composition and site occupations were considered: (1) possible vacancies in the Sn occupation of the Tl(A) site making the composition $\text{Sn}_{1-x}\text{Tl}_4\text{Te}_3$, (2) sub-stoichiometric substitution

of Sn on the Tl(A) site: $(\text{Sn}_{1-x}\text{Tl}_x)\text{Tl}_4\text{Te}_3$, and (3) Sn occupation of both Tl(A) and Tl(B) sites such that the composition $\text{Sn}_{1.0}\text{Tl}_4\text{Te}_3$ is still appropriate.

For the first scenario, a series of calculations in which the Sn occupation of the Tl(A) position was varied from 0.25 to 1.0, (compositions ranging from $\text{Sn}_{0.25}\text{Tl}_4\text{Te}_3$ to SnTl_4Te_3) was carried out. The fully occupied model, $\text{Sn}_{1.0}\text{Tl}_4\text{Te}_3$, is strikingly unfavorable with respect to $\text{Sn}_{0.75}\text{Tl}_4\text{Te}_3$ (the structure with 25% vacancies at the Tl(A) position) and Sn : $\Delta E = -1.24\text{eV}$. Analysis of the overlap population for the Sn - Te(C) bonds parallel to the *c*-axis, shows a significant increase in these values from $\text{Sn}_{1.0}\text{Tl}_4\text{Te}_3$ to $\text{Sn}_{0.75}\text{Tl}_4\text{Te}_3$ as σ - antibonding crystal orbitals are depleted of electrons. Furthermore, $\text{Sn}_{0.75}\text{Tl}_4\text{Te}_3$ is energetically favored against disproportionation to both $\text{Sn}_{1.0}\text{Tl}_4\text{Te}_3 + \text{Sn}_{0.50}\text{Tl}_4\text{Te}_3$ (by 0.26eV), and $\text{Sn}_{1.0}\text{Tl}_4\text{Te}_3 + \text{Sn}_{0.0}\text{Tl}_4\text{Te}_3$ (by 1.28eV). However, the $\text{Sn}_x\text{Tl}_4\text{Te}_3$ system gains energy by lowering *x*. Therefore, we conclude that the strong Sn - Te(C) σ - antibonding orbital interactions provide the energetic driving force against $\text{Sn}_{1.0}\text{Tl}_4\text{Te}_3$. Although our results provide no conclusive support for a specific vacancy concentration, we do find that Sn enters the structure as Sn^{-2} , and not Sn^{+4} . Therefore, we examined two other models of Sn and Tl distribution.

Extended Hückel calculations relating to the second possibility, i.e., partial Sn substitution on the Tl(A) position, were performed on systems $(\text{Sn}_{1-x}\text{Tl}_x)\text{Tl}_4\text{Te}_3$, where *x* = 0.0, 0.25, 0.5, 0.75, and 1.0. The two endpoints, where *x* = 0.0 and 1.0, represent either complete Sn or complete Tl occupation of the Tl(A) site, whose DOS curves are plotted in Figures 11 and 3a respectively. Based upon the position of the respective Fermi levels, the two materials would be predicted to have very different physical properties. If *x* = 1.0, the

material is Tl_5Te_3 , and the Fermi energy falls near the top of the large band from -12.0 to -6.0 eV, in good agreement with the observed metallic and superconducting properties. But, if $x = 0$, all the Tl(A) sites are occupied with Sn, and the Fermi energy falls in a gap. This would imply semiconducting behavior which is incongruous with the observation that SnTl_4Te_3 is metallic and shows a low temperature superconducting transition. In the three cases where $x = 0.25, 0.5$ and 0.75 and both Sn and Tl atoms occupy the Tl(A) position, the Fermi energy (-7.4 ± 0.1 eV in all three cases) drops into the band between -12.0 and -7.0 eV, and states near the Fermi level have metal (Sn and Tl) character. This is good evidence that upon mixing of even a small amount of Tl and Sn on the Tl(A) position, the calculated Fermi energy is in much better agreement with the observed physical properties.

As an extension of the ideas presented just above, it may be that even with the mixing of Sn and Tl on the Tl(A) site, the overall stoichiometry may remain $\text{Sn}_1\text{Tl}_4\text{Te}_3$ by allowing for some Sn mixing on the Tl(B) position also. Our third approach involves a careful look at the bonding and electronic differences between Sn completely substituting on the Tl(A) site, or partially occupying both Tl(A) and Tl(B) sites in the structure, i.e., $(\text{Sn}_{1-x}\text{Tl}_x)(\text{Tl}_{4-x}\text{Sn}_x)\text{Te}_3$, $0 \leq x \leq 1$. One way to evaluate the difference in site preferences within these models is to evaluate site potentials using Madelung calculations [14]. In both structures, SnTl_4Te_3 and Tl_5Te_3 , the Tl(A) site has a larger site potential than the Tl(B) site, which supports our assignment of the formal oxidation states as Tl(A)^{+2} and Tl(B)^{+1} . Therefore we would expect all the Sn to substitute as Sn^{+2} on the Tl(A) sites, using a purely ionic model.

Extended Hückel calculations were carried out on different arrangements of the Sn and Tl atoms from SnTl_4Te_3 to $\text{Tl}(\text{Tl}_{3.0}\text{Sn}_{1.0})\text{Te}_3$. In each calculation, the complete 32 atom unit cell was used, and the electron count and number of k-points remained the same. A rigid band model for the mixing of Sn from the Tl(A) sites onto the Tl(B) sites would be appropriate only if the features of the DOS curve remained the same for each Sn configuration. We find, however, that it is not appropriate for this series of calculations based on the significant changes in the DOS curves as the Sn substitution pattern changes. The most notable change in the DOS curves is the disappearance of the gap between -6.0 and -7.0 eV. The results of the calculations are summarized in Table 3 and Figure 12, showing the DOS curves with Fermi energies for three cases: (a) SnTl_4Te_3 ; (b) $(\text{Sn}_{0.75}\text{Tl}_{0.25})(\text{Tl}_{3.75}\text{Sn}_{0.25})\text{Te}_3$; and (c) $(\text{Sn}_{0.50}\text{Tl}_{0.50})(\text{Tl}_{3.5}\text{Sn}_{0.5})\text{Te}_3$. There are several noteworthy trends in the computational results. First, as the ratio of Sn on the Tl(A) site to Sn on the Tl(B) site decreases, the total energies and Fermi energies decrease, indicating a stabilization of the structure upon the substitution of Sn onto the Tl(B) site(s). Second, the energy gap at the Fermi energy in the DOS for $\text{Sn}_{1.0}\text{Tl}_4\text{Te}_3$ (Figure 12a) disappears as the Sn concentration on the Tl(B) site relative to the Tl(A) site increases as in $(\text{Sn}_{0.75}\text{Tl}_{0.25})(\text{Tl}_{3.75}\text{Sn}_{0.25})\text{Te}_3$ (Figure 12b), and $(\text{Sn}_{0.50}\text{Tl}_{0.50})(\text{Tl}_{3.5}\text{Sn}_{0.5})\text{Te}_3$ (Figure 12c).

To understand why this occurs, recall that the Sn 5p atomic orbitals (-8.32 eV) lie lower in energy than the Tl 6p atomic orbitals (-5.80 eV). Also the two shortest M - Te interactions in the structure are 3.148 Å (M(B) - Te(D)), and 3.253 Å (M(A) - Te(C)). In $\text{Sn}_{1.0}\text{Tl}_4\text{Te}_3$ the states just above the Fermi energy are associated with the Tl(B) atoms, and the states just below the Fermi level are mostly Sn(A) character.

When Sn(A) atoms move to the Tl(B) positions the energy of the Sn - Te antibonding states just above the Fermi energy is lowered due to the lower Sn 5p orbital energy. Conversely, when Tl(B) atoms move onto the Sn(A) sites the Tl - Te antibonding states just below the Fermi level are pushed up in energy. These Tl(A) states contribute to a new peak near -7.0eV, which appears in the DOS curves in Figures 12b and 12c but was not present in Figure 12a. Figure 13 highlights these features of the DOS curve of $(\text{Sn}_{0.5}\text{Tl}_{0.5})(\text{Tl}_{3.5}\text{Sn}_{0.5})\text{Te}_3$ due to the states associated with the Tl and Sn atoms that switch places. In Figure 13a the states with Tl(A) character are shaded in the peak at -7.0 eV, which is not observed in the DOS curve for $\text{Sn}_{1.0}\text{Tl}_4\text{Te}_3$ (Figure 12a). In Figure 13b Sn(B) states are shaded just above the Fermi energy.

Figure 14 contains two plots of the Madelung energy (top) and the Extended Hückel total energy (bottom) vs. the Sn composition on the Tl(A) position. The slopes of the two curves clearly oppose each other, and the magnitude of the slope of the Madelung curve is greater than that of the total energy curve. The negative slope of the Madelung curve indicates that it is unfavorable to move Sn from the Tl(A) site to the Tl(B) site, while the positive slope of the total energy curve means just the opposite, i.e. the total energy decreases as Sn is moved from the Tl(A) to the Tl(B) positions. Although the two trends oppose each other, the greater slope of the Madelung curve indicates that the destabilizing effect of the Madelung term has a greater effect than the stabilizing effect on the total energy. The intersection of these two curves (near 50%) may provide an estimate of the optimal Sn distribution between Tl(A) and Tl(B) sites. The dotted curves which lie below each of the bold curves demonstrate the lowering of energy that is accompanied by the

inclusion of a configurational entropy term. The calculation of the Helmholtz free energy from the following expression, $A = U - TS$ (where $S = k \ln \Omega$, and $k = 8.617 \times 10^{-5}$ eV/K, with Ω being the number of possible configurations), includes a temperature dependent entropy term, which results in a lowering of both the total energy and Madelung energy as Sn atoms are moved from the Tl(A) sites to the Tl(B) sites. The two curves are for $T = 1000\text{K}$, and effect a shift on the intersection point of the total energy and Madelung energy from near 50% to 60% Sn on the Tl(A) site.

Conclusions

Although the results of the calculated band structure of Tl_5Te_3 show an electronic instability at the Fermi level due to orbitals assigned to the Tl(A)-Te(C) chains, lattice energy calculations reveal there are strong short range repulsive forces which resist the shift of atomic positions. This frustration between pairwise interactions and states near the Fermi level may be directly related to the observation of a superconducting transition at low temperature, rather than a displacive structural distortion.

In the calculations involving the ternary system $\text{Sn}_x\text{Tl}_{5-x}\text{Te}_3$, our results support the idea that Sn and Tl occupy both the Tl(A) and Tl(B) positions in this structure. This atomic arrangement leads to an electronic structure which is in agreement with the observed physical properties. The driving force for the simultaneous mixing results from a competition between classical ionic forces and quantum mechanical orbital overlap.

Acknowledgments

This research was funded by the donors of the Petroleum Research Fund as administered by the American Chemical Society, and a GAANN Fellowship awarded to Karen Nordell.

Appendix

Extended Hückel calculations

The electronic structure of Tl_5Te_3 is evaluated within the tight-binding, LCAO approximation using the extended Hückel method [15]. The structural parameters for each of the two structures, i.e., lattice and positional parameters, were taken from the literature [3]. Density of states (DOS) and crystal orbital overlap population (COOP) curves were generated by summing over a set of 150 k-points in the irreducible Brillouin zone. The atomic orbital parameters [16] used for Tl, Sn and Te are given in Table 4. Quasi-relativistic effects were considered for both heavy main group elements, consequently the s-orbitals were slightly contracted while the p-orbitals were slightly expanded.

Lattice energy calculations

The lattice energy U_{LAT} can be expressed (approximately) as:

$$U_{\text{LAT}} \approx U_{\text{MAD}} + U_{\text{BM}} + U_{\text{VDW}}.$$

For a detailed explanation of each term see reference [14].

References:

1. (a) J.K. Burdett, E. Canadell and T. Hughbanks, *J. Am. Chem. Soc.*, *108* (1986) 3971; J. Bauer and O. Bars, *Acta Cryst.*, *B36* (1980) 1540.
(b) K.J. Nordell and G.J. Miller, *Croat. Chim. Acta*, in press.
2. G.J. Miller, F. Li and H.F. Franzen, *J. Am. Chem. Soc.*, *115* (1993), 3739.
3. (a) I. Schewe, P. Böttcher and H.G. v. Schnering, *Z. Kristallogr.* *188* (1989) 287. (and references therein)
(b) A. Judoakis and C.R. Kannerwurf, *J. Appl. Phys.* *39* (1968) 3003.
(c) R. Wang, B.C. Giessen and N.J. Grant, *Z. Kristallog.* *129* (1969) 244. R. Kubiak, *Z. Anorg. Allg. Chem.* *431* (1977) 261. J.V. Hutcherson, R.L. Guay and J.S. Herold, *J. Less-Common Met.* *11* (1966) 296.
(d) R. Marsh, *J. of Solid State Chem.*, *92* (1991) 594.
4. A. Simon, *Angew. Chem. Int. Ed. Engl.* *26* (1987) No. 6, 579.
5. P. Villars and L.D. Calvert, *Pearson's Handbook of Crystallographic Data for Intermetallic Phases*, Vol. 2, 1989.
6. J. Corbett and A. Leon-Escamilla, personal communications, 1995.
7. G. Bruzzone and F. Merlo, *J. Less-Common Met.* *60* (1978) 59. B. Eisenmann and H. Schäfer, *Z. Naturforsch.*, *29b* (1974) 460.
8. H. Schäfer, *Ann. Rev. Mater. Sci.*, *15*, 1 (1985). N.N. Greenwood and A. Earnshaw, *The Chemistry of the Elements*, Pergamon Press (1990) 225.
9. Note: The two frameworks are described as an overlapping combination, not two interpenetrating networks. 'Interpenetrating networks' means the two frameworks are distinct and independent, while an 'overlapping combination' of networks implies that some component belongs to both nets.
10. E. Canadell and M-H Wangbo, *Chemical Reviews*, *91* (1991) 965.
11. H. Bärnighausen, *Match*, *9* (1980) 139. T. Hahn ed. *International Tables for Crystallography*, Vol A. Space Group Symmetry, 1989.
12. See Appendix and references therein

13. (a) S. Bradtmöller and P. Böttcher, *Z. Kristallogr.* 209 (1994) 75.
(b) S. Bradtmöller and P. Böttcher, *Z. Anorg. Allg. Chem.*, 619 (1993) 1155.
P. Böttcher, personal communications, 1995.

14. G.J. Miller and J. Lin, *J. of Solid State Chem.*, 113, (1994), 296. (and references therein); S.C. Bevan and D.F.C. Morris, *J. Chem. Soc.* (1960) 516.
L. Pauling, *Proc. R. Soc. London Ser. A*, 114 (1927) 191. S.S. Jaswasl and T.P. Sharma, *J. Phys. Chem. Solids*, 34 (1973) 509. J.R. Tessman, A.H. Kahn and W. Shockley, *Phys. Rev.* 92 (1953) 890; J.E. Mayer, *J. Chem. Phys.*, 1 (1933) 270.
J.M. Ziman, *Principles of the Theory of Solids*, Cambridge University Press, London, 1964, p.39.

15. R. Hoffmann and W.N. Lipscomb, *J. Chem Phys.* 36 (1962) 2179, 3489. R. Hoffmann, *J. Chem. Phys.*, 39 (1963) 1397. J.H. Ammeter, H.B. Bürgi, J.C. Thilbeault and R. Hoffmann, *J. Amer. Chem. Soc.* 100 (1978) 3686. M.H. Wangbo, R. Hoffmann and R.B. Woodward, *Prog. Roy. Soc. A366* (1979) 23.

16. E. Clementi and C. Roetti, *At. Data Nucl. Data Tbls.* 14 (1974) 177.

Table 1: Structure Comparison of Tl_5Te_3 with Ca_5Si_3

	Tl_5Te_3	Ca_5Si_3
a Å	8.930(2)	7.64(2)
c Å	12.589(4)	14.62(2)
c/a	1.41	1.91
M(A) - X(C) Å	3.147 (x2)	3.66 (x2)
M(A) - X(D) Å	3.361 (x4)	3.09 (x4)

Table 2: A comparison of relevant energies between undistorted Tl_5Te_3 and the four distorted structures.

Space Group	Second Derivative (d^2E/du^2)	Relative Energy/ FU (eV)	Fermi Energy (eV)
$I4/mcm$	0.00	0.00	-7.45
$I4/m$	-5.03	-0.08	-7.08
$I4cm$	-0.24	-0.01	-7.30
$P4/mbm$	-5.09	-0.08	-7.11
$P4/ncc$	-0.87	-0.01	-7.33

Table 3: A comparison of Fermi energies for the calculations on SnTl_4Te_3 in which Sn was mixed on both Tl(A) and Tl(B) sites.

<u>Stoichiometry</u>	<u>Mixing on Tl (A) site</u>	<u>Fermi Energy (eV)</u>
SnTl_4Te_3	$\text{Sn}_{1.0}$	-6.51
SnTl_4Te_3	$\text{Sn}_{0.75}\text{Tl}_{0.25}$	-6.73
SnTl_4Te_3	$\text{Sn}_{0.50}\text{Tl}_{0.50}$	-6.84
SnTl_4Te_3	$\text{Sn}_{0.25}\text{Tl}_{0.75}$	-6.98
$\text{Sn}_{0.75}\text{Tl}_{4.25}\text{Te}_3$	$\text{Sn}_{0.75}\text{Tl}_{0.25}$	-7.38
Tl_5Te_3	$\text{Tl}_{1.0}$	-7.45

Table 4: Atomic Orbital Parameters [16]

<u>Element</u>	<u>Atomic Orbital</u>	<u>$H_{ij}(\text{eV})$</u>	<u>ζ_i</u>
Tl	6s	-11.60	2.52
	6p	-5.80	1.77
Te	5s	-20.80	2.51
	5p	-14.80	2.16
Sn	5s	-16.16	2.21
	5p	-8.32	1.82

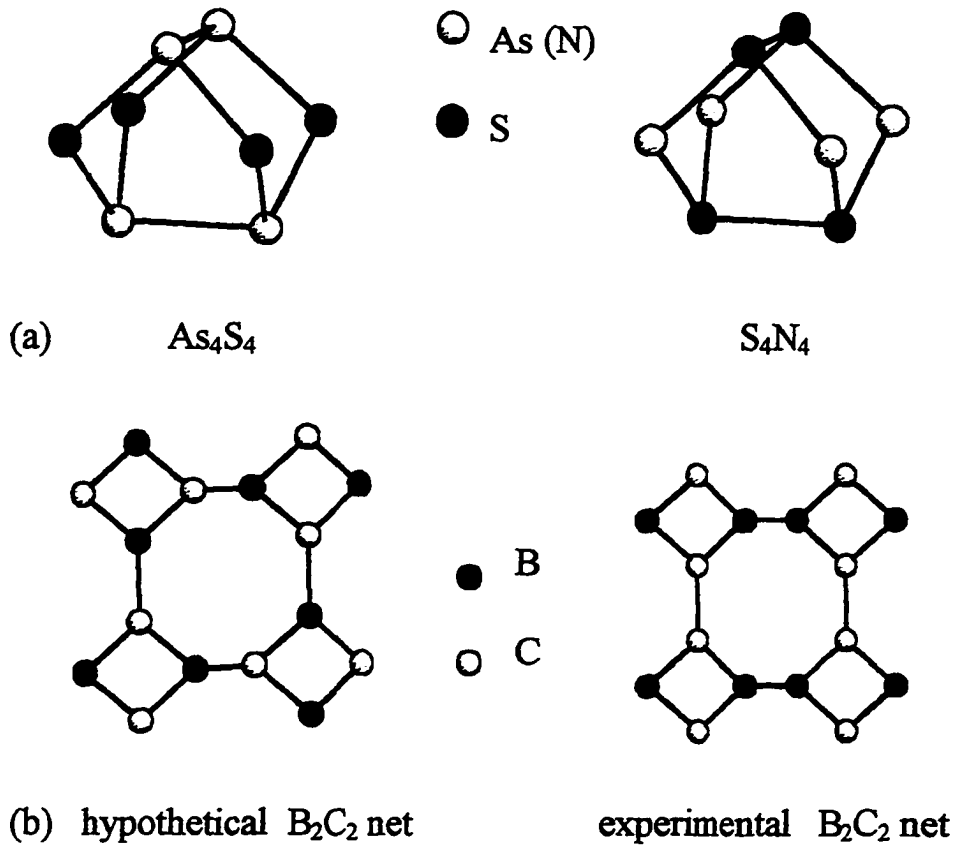


Figure 1a: As_4S_4 vs. S_4N_4 where the more electronegative atom occupies the two-coordinate position. S atoms are shaded in both molecules.

1b: Two coloring possibilities for the B_2C_2 net in MB_2C_2 systems. M atoms are not pictured.

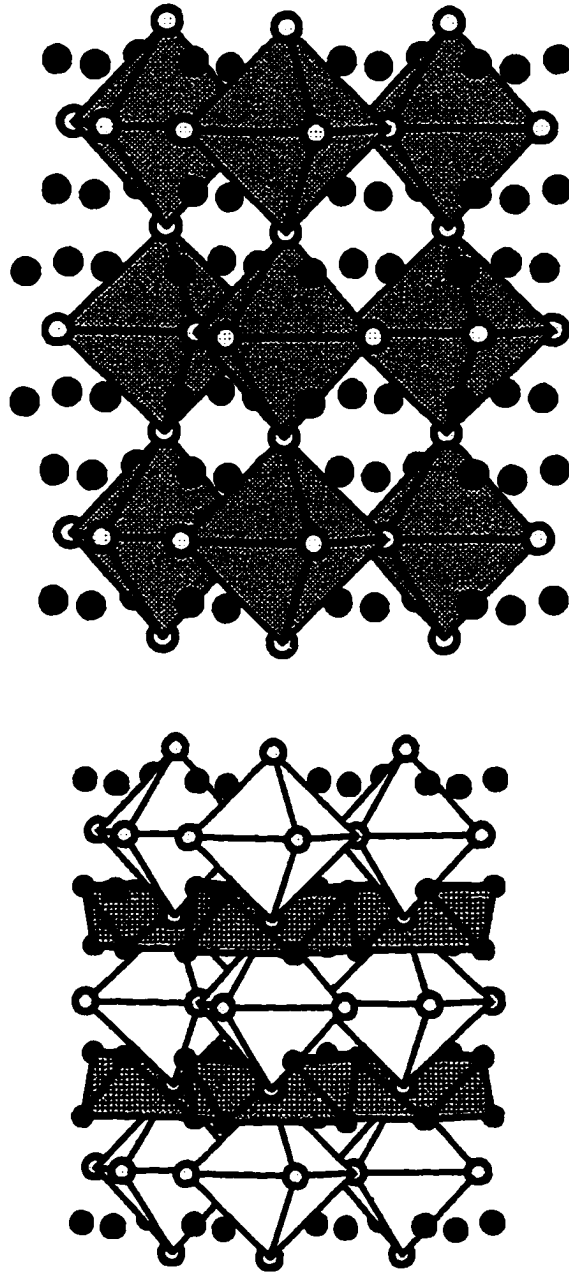


Figure 2a: Structure of Tl_5Te_3 with Tl(A)-centered, Te octahedra highlighted. Tl(B) atoms are dark atoms, and Te atoms are light atoms.

2b: Tl_5Te_3 with Tl(B) square antiprisms highlighted with shaded polyhedra.

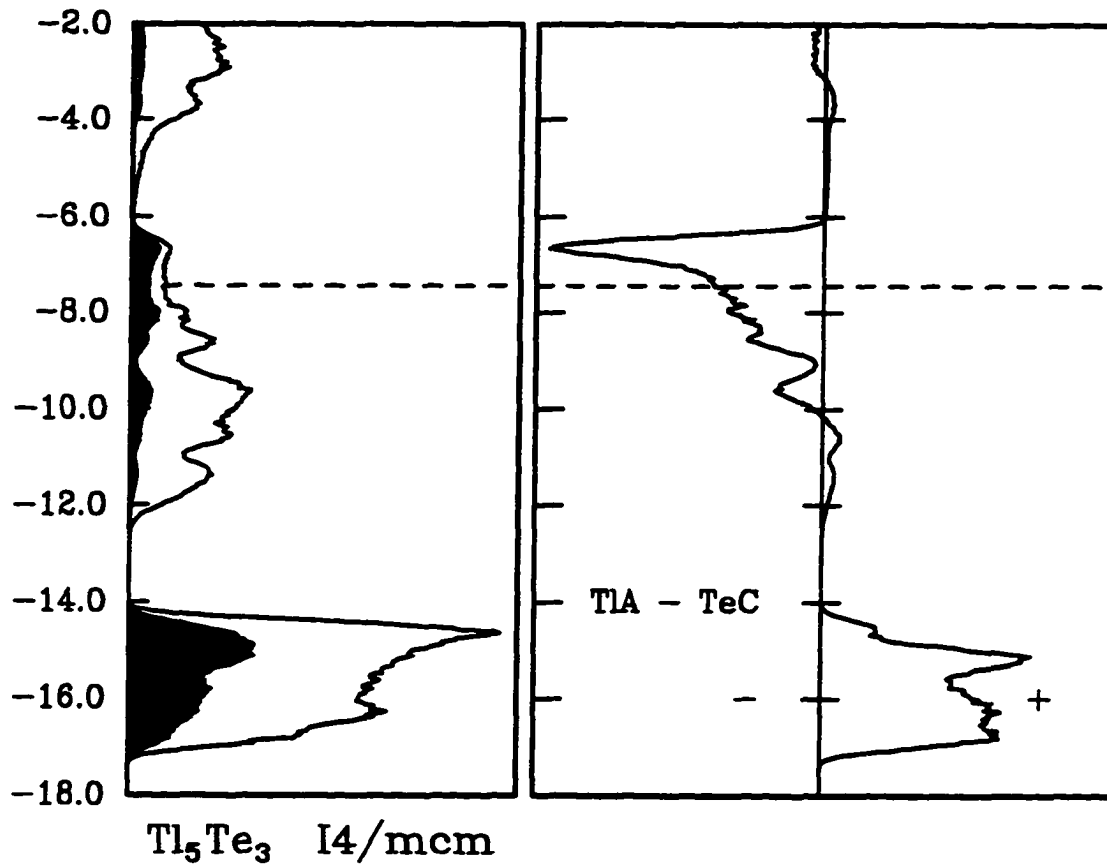


Figure 3: (a) The total DOS of Tl_5Te_3 with the Tl(A) and Te(C) states contributing to the shaded regions. The Fermi energy is highlighted by the dotted line at -7.45eV . (b) The COOP curve for the Tl(A) - Te(C) interactions with the right side (+) of the center line representing the bonding states, and the left side (-) the antibonding states.

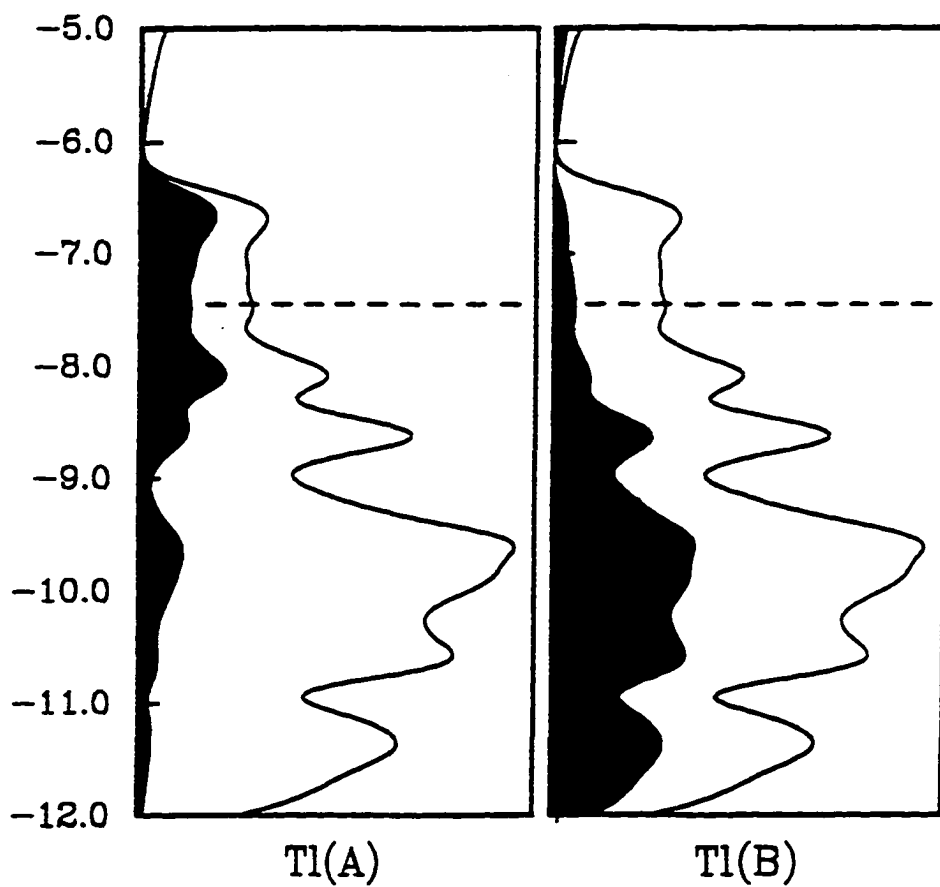


Figure 4: Expanded DOS curves for Tl₅Te₃ with states associated with Tl(A) (left), and Tl(B) (right) highlighted. Notice that the Tl(B) states lie lower in energy than most of the Tl(A) states, supporting the assignment of Tl(A)⁺², and Tl(B)⁺¹.

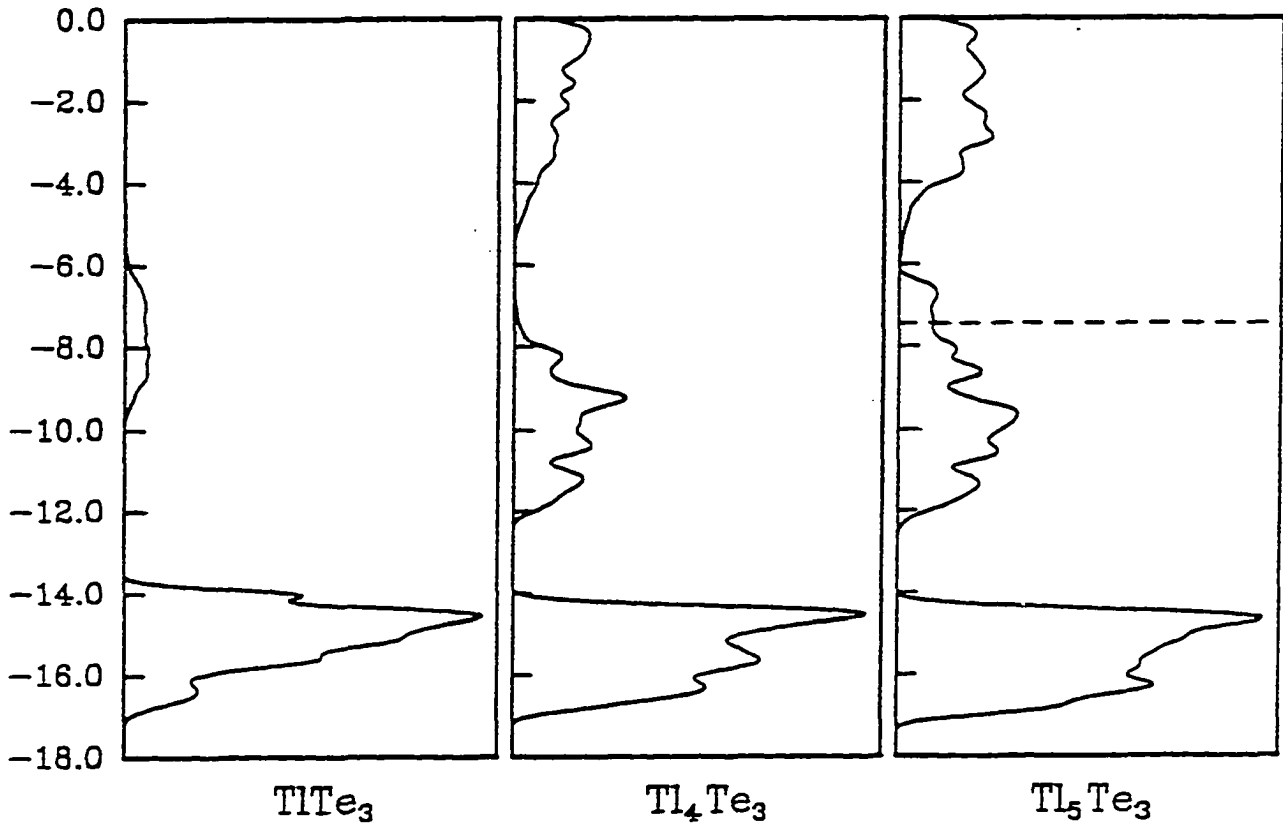


Figure 5: (left) The DOS curve for the partial structure Tl(A)Te_3 . (middle) The DOS curve for the partial structure $\text{Tl(B)}_4\text{Te}_3$. Both partial structures contain the tellurium framework, whose states are mainly contained in the large band from -17.0 to -14.0 eV. (right) The total DOS for the complete Tl_5Te_3 structure, which resembles a combination of the other two curves.

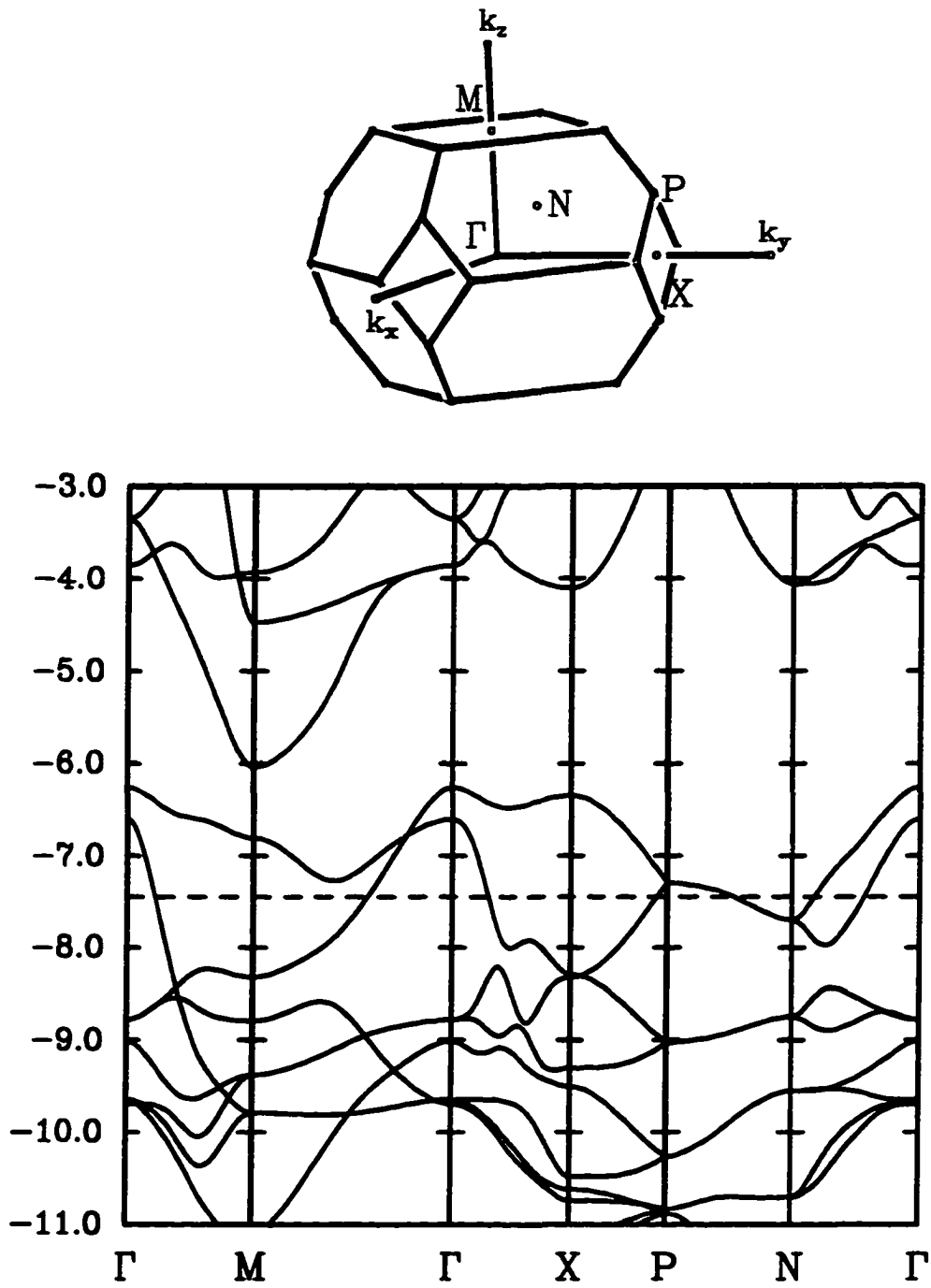


Figure 6: (top) The first Brillouin zone for a tetragonal cell, with special points labeled.
 (bottom) The electronic band structure of Tl_5Te_3 from $\Gamma (0,0,0) \rightarrow M (\frac{1}{2}, -\frac{1}{2}, \frac{1}{2}), (-\frac{1}{2}, \frac{1}{2}, \frac{1}{2}) \rightarrow \Gamma (0,0,0) \rightarrow X (\frac{1}{2}, 0, 0) \rightarrow P (\frac{1}{4}, \frac{1}{4}, \frac{1}{4}) \rightarrow N (0, \frac{1}{2}, 0) \rightarrow \Gamma (0,0,0)$.

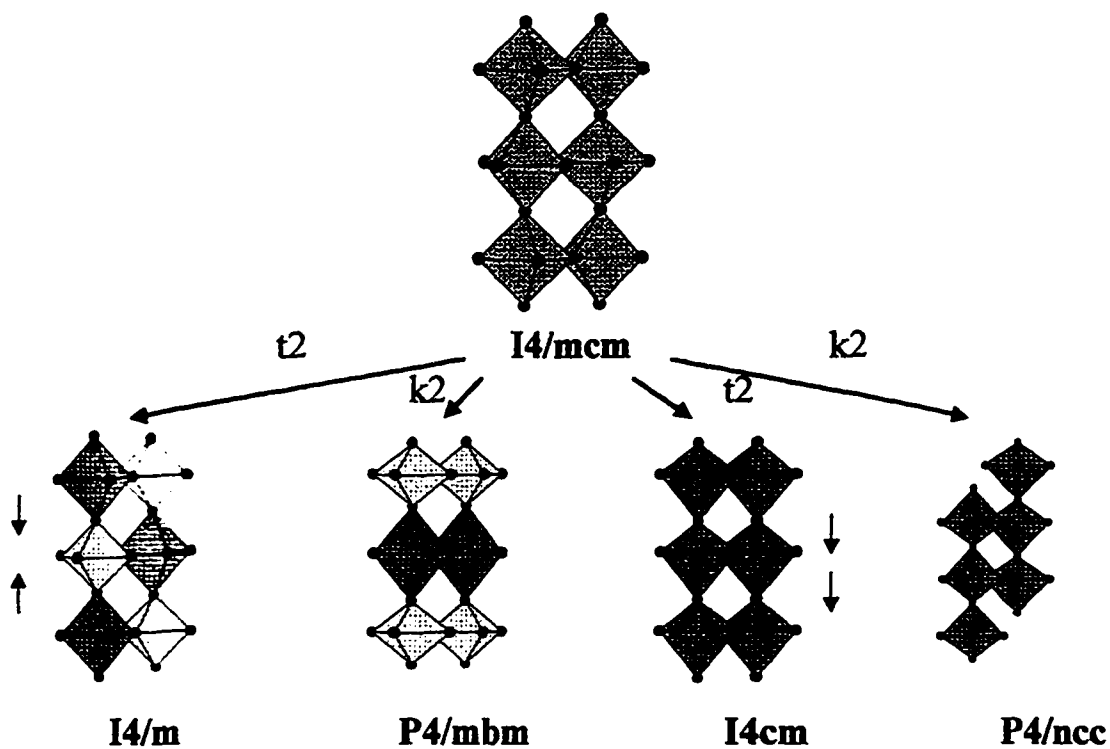


Figure 7: Representations of the four hypothetical structures based on the distortion of the Te(C) position of the I4/mcm structure. The distortion in I4/m and P4/mbm results in alternating compressed and elongated octahedra. The distortion in I4cm and P4/ncc results in unsymmetrically compressed octahedra.

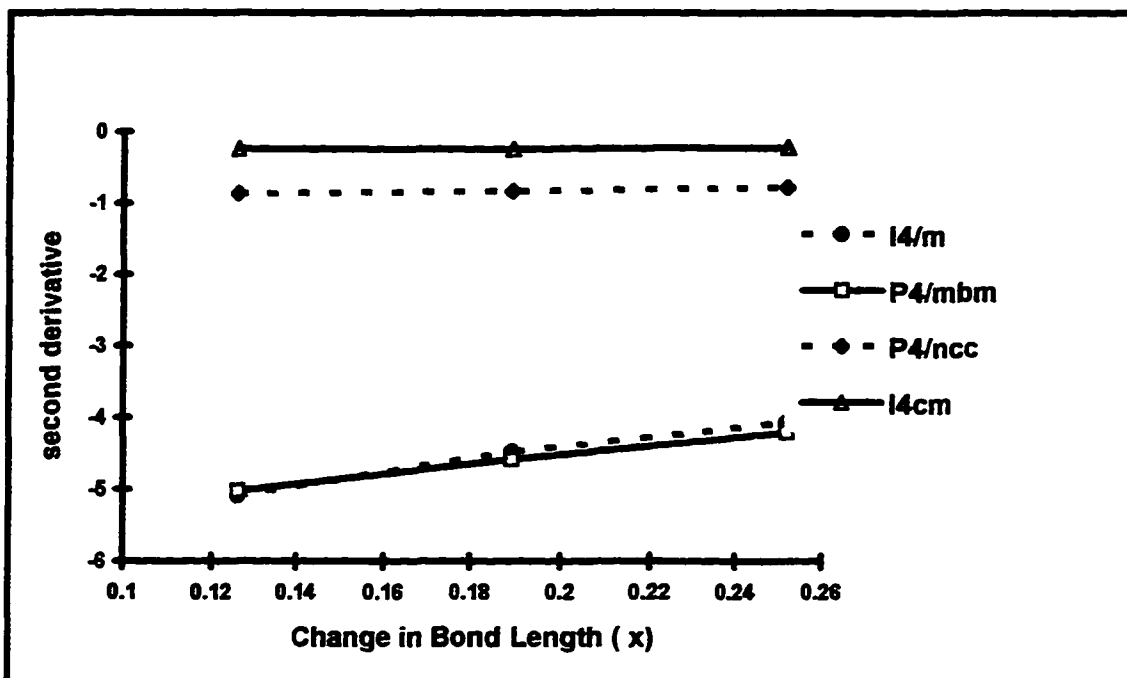


Figure 8: The second derivative (d^2E/du^2) for the 4 distortions plotted versus the change in the Tl(A) - Te(C) bond length.

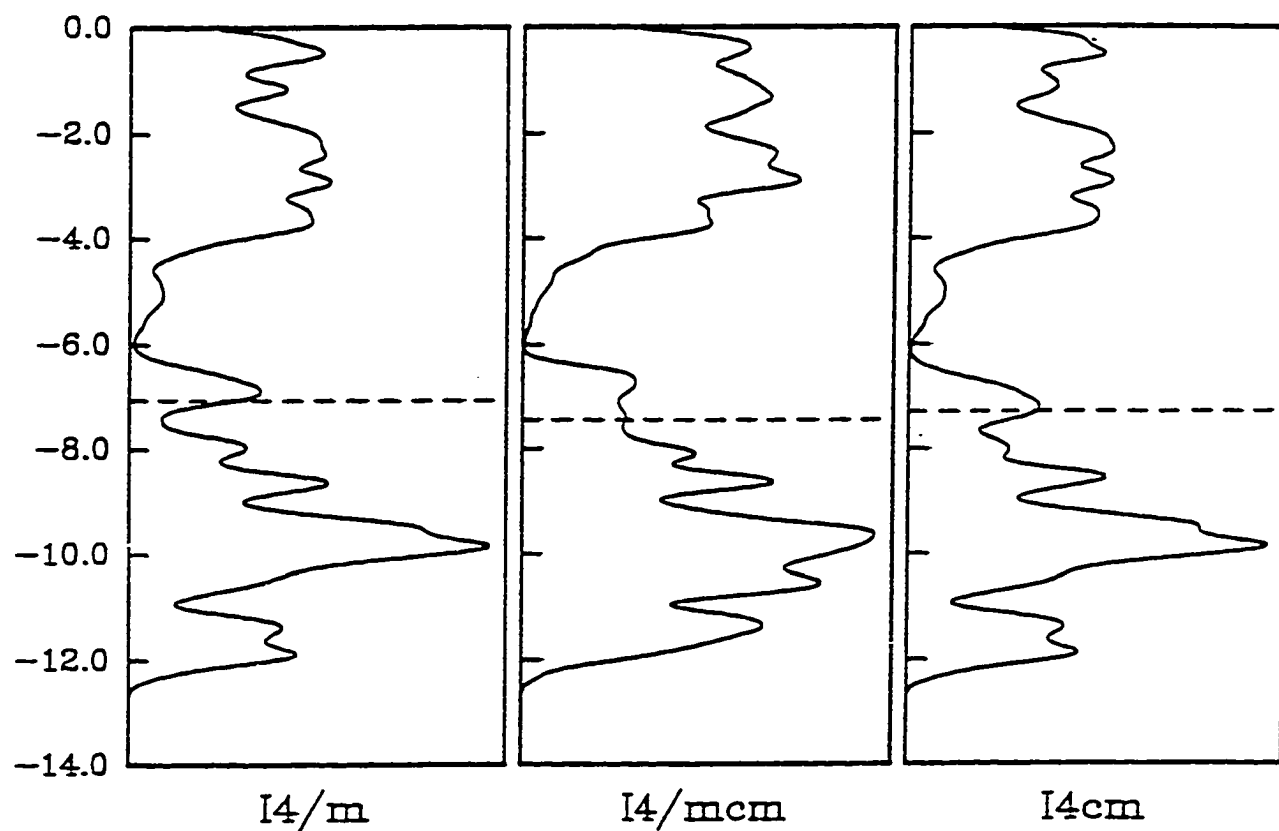


Figure 9: Three total DOS curves for the undistorted $I4/mcm$ structure and two of the distorted structures $I4/m$ and $I4cm$ are shown with the dotted lines representing the Fermi energies for each structure calculated with identical electron counts.

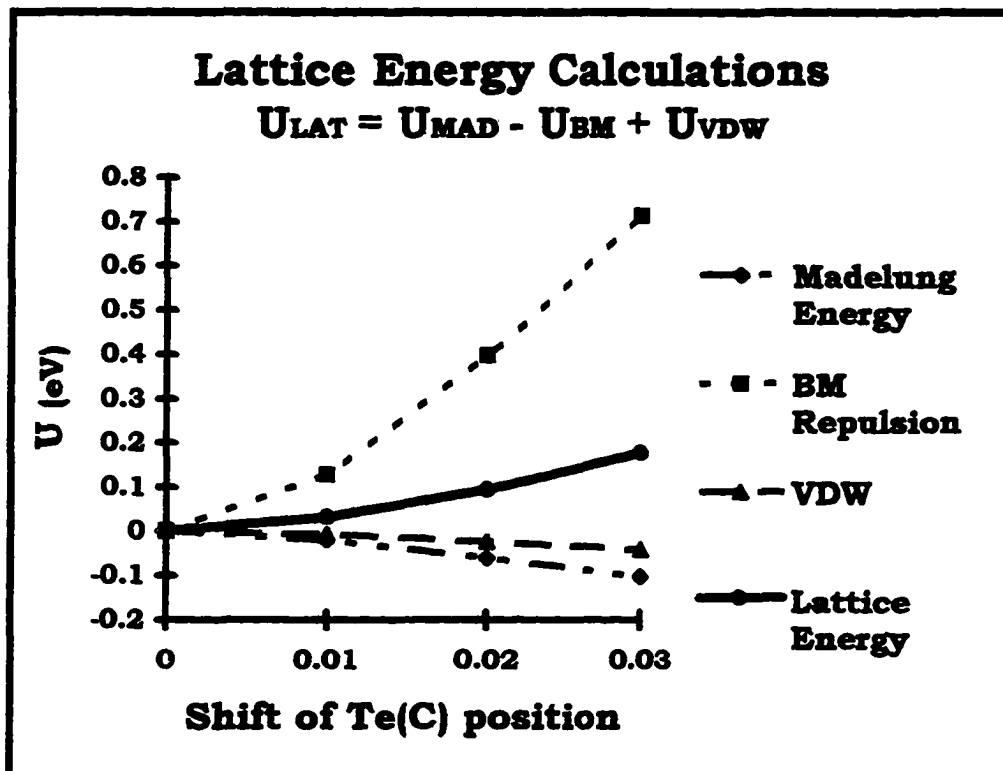


Figure 10: The four curves represent the four terms in the lattice energy equation, and are plotted as changes in energy (eV) vs. changes in the Te(C) position. In each case the greater the distortion of the Te(C) position, the greater the energy change.

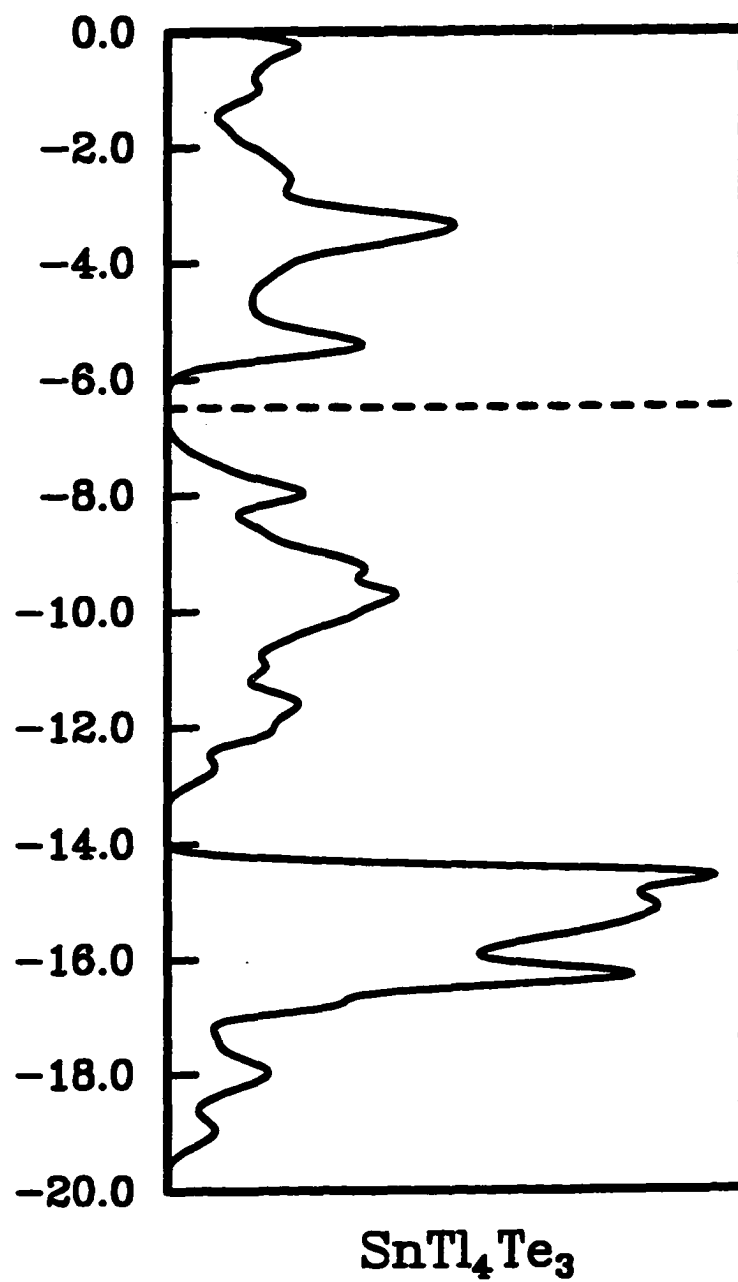


Figure 11: The total DOS curve for SnTl_4Te_3 in which all the Sn atoms are in the Tl(A) positions. Note the Fermi energy (dotted line, -6.5 eV) falls in a gap in the DOS.

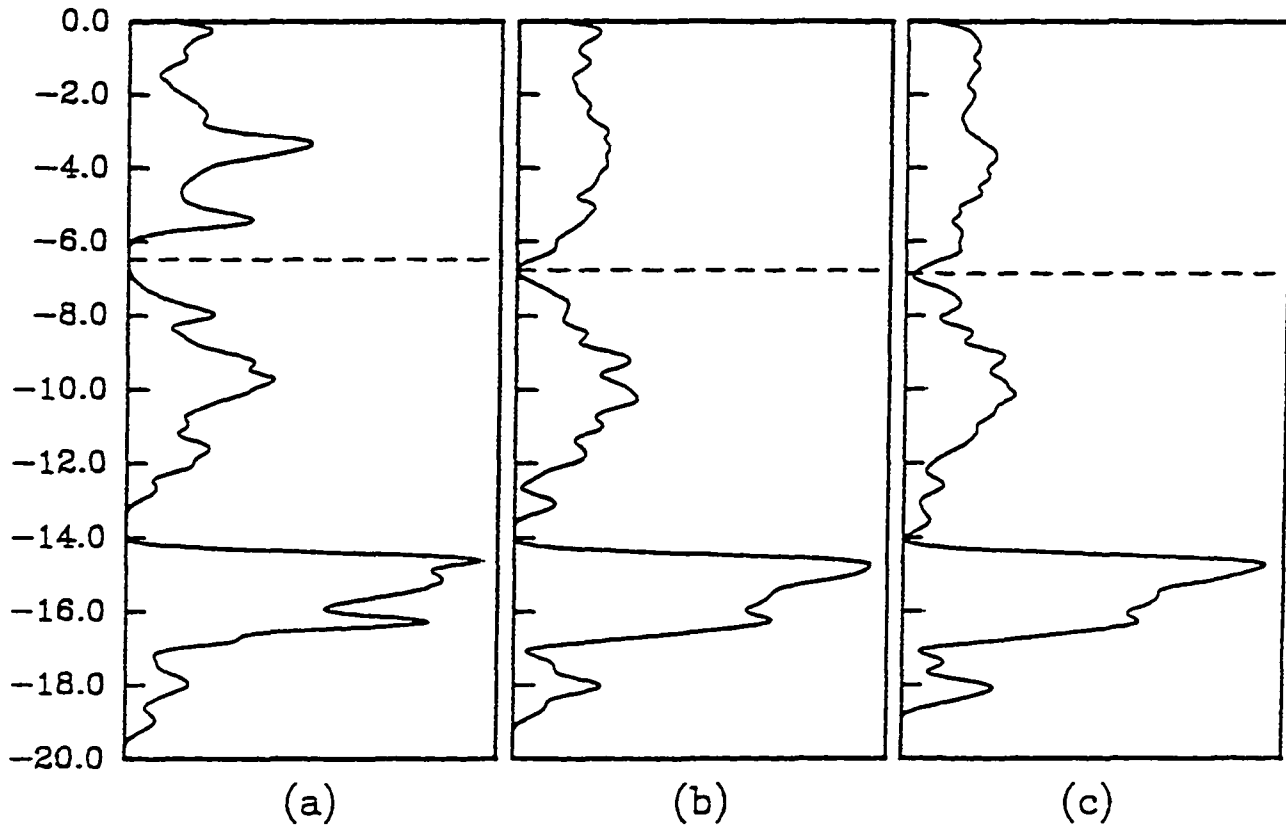


Figure 12 : (a) The total DOS curve for SnTl_4Te_3 , in which all the Sn atoms are located on the Tl(A) sites. The Fermi energy (-6.50 eV) is highlighted by the dotted line and falls in a gap in the DOS.

(b) The total DOS curve for $\text{Sn}_{0.75}\text{Tl}_{0.25}(\text{Sn}_{0.25}\text{Tl}_{3.75})\text{Te}_3$ where 1/4 of the tin atoms have substituted onto the Tl(B) sites.

(c) The total DOS curve for $\text{Sn}_{0.5}\text{Tl}_{0.5}(\text{Sn}_{0.50}\text{Tl}_{3.5})\text{Te}_3$ where 1/2 of the tin atoms have substituted onto the Tl(B) sites. Notice the gap which existed at the Fermi energy in (a) and (b) is gone in this curve.

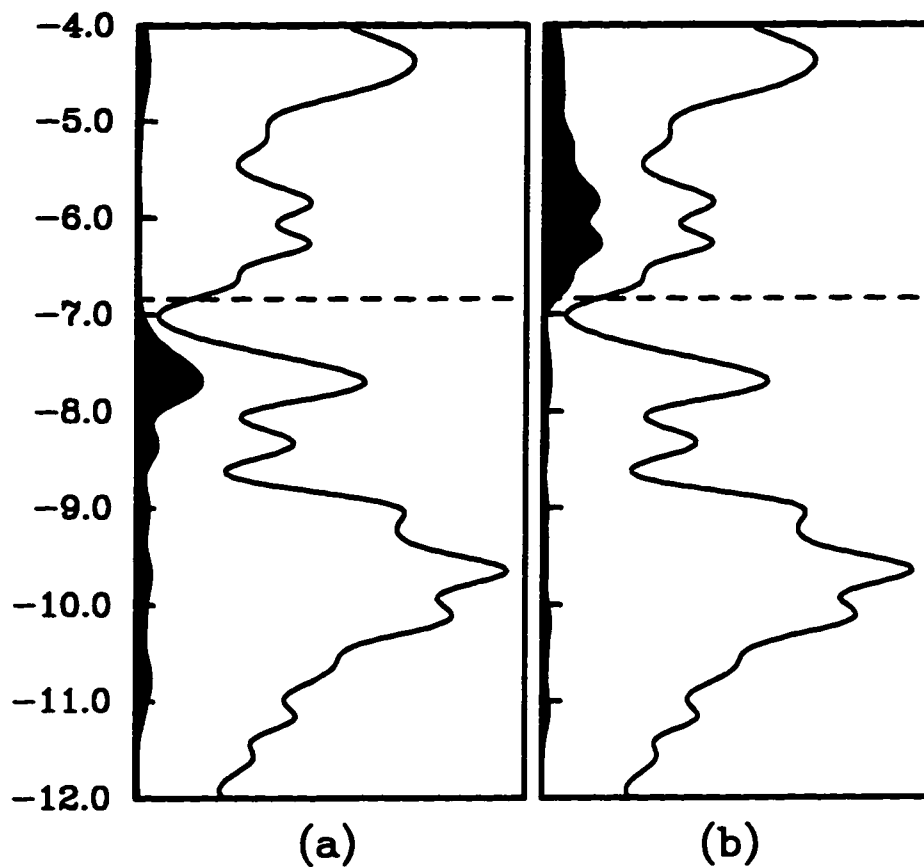


Figure 13: (a) Expanded DOS curve for $(\text{Sn}_{0.5}\text{Tl}_{0.5})(\text{Tl}_{3.5}\text{Sn}_{0.5})\text{Te}_3$ with Tl(A) states shaded. These states contribute to the peak near -7.0 eV just below the Fermi level (-6.84 eV).

(b) Expanded DOS curve for $(\text{Sn}_{0.5}\text{Tl}_{0.5})(\text{Tl}_{3.5}\text{Sn}_{0.5})\text{Te}_3$ with states of Sn(B) character which lie just above the Fermi level shaded.

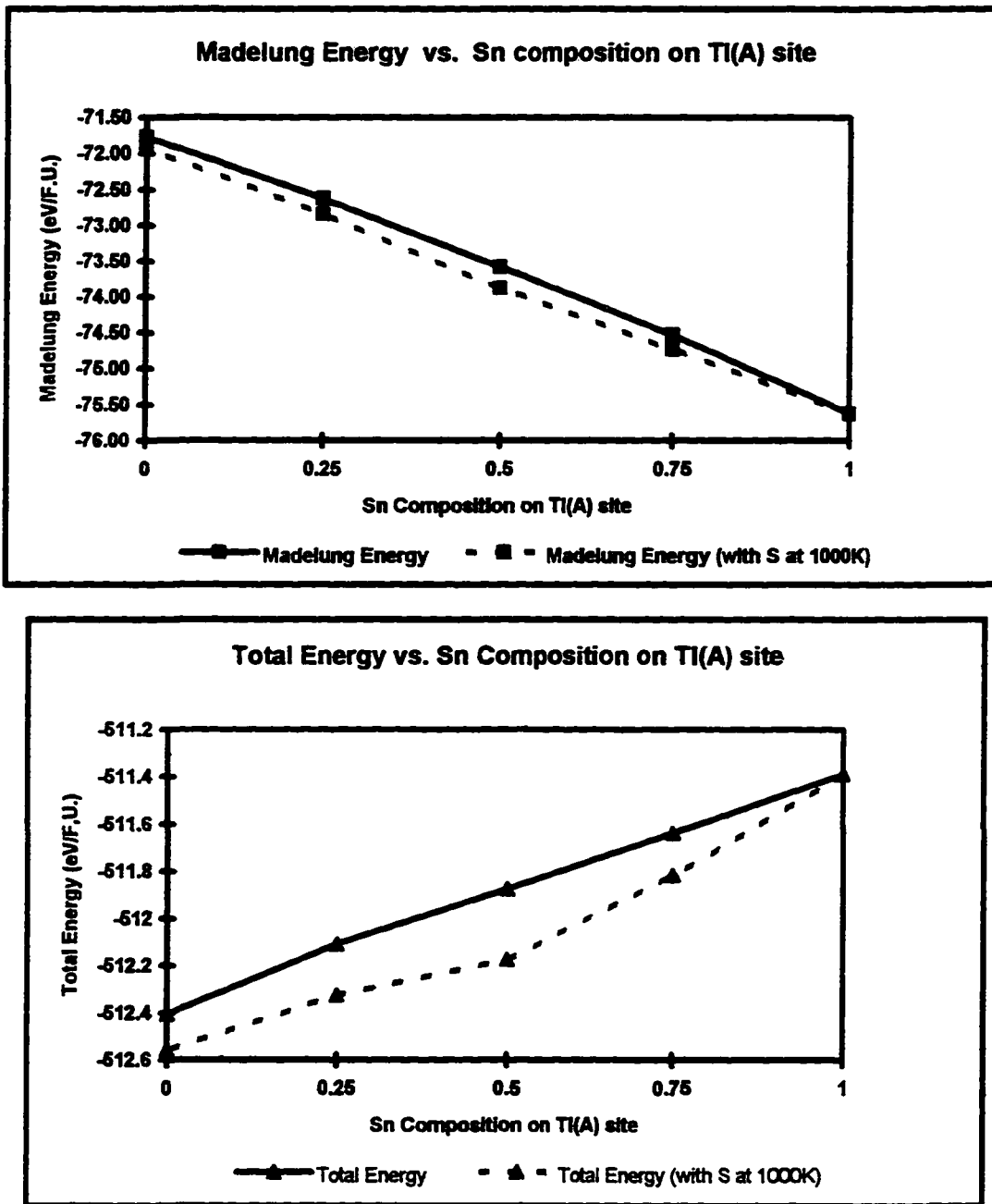


Figure 14: (top) The Madelung energy is plotted versus the Sn composition on the Tl(A) site. The negative slope of the curve indicates that it is unfavorable to move Sn from the Tl(A) to the Tl(B) site. The dotted line below the solid line is the energy with a configurational entropy term included at 1000 K. (bottom) The total energy plotted versus the Sn composition on the Tl(A) site. This curve has a positive but smaller slope than the top curve indicating that while the total energy decreases as Sn is moved from the Tl(A) to the Tl(B) position, the Madelung energy has the greater effect.

REFERENCES CITED

- [1] D.F. Shriver, P.W. Atkins, C.H. Langford, *Inorganic Chemistry*, W.H. Freeman and Company, New York, (1990); F.A. Cotton, G. Wilkinson, *Advanced Inorganic Chemistry*, 5th ed. , John Wiley & Sons Inc., New York, (1988).
- [2] K.A. Gschneidner Jr., *Theory of Alloy Phase Formation*, ed. L.H. Bennett, Proceedings of the 108th AIME Annual Meeting, (1979).
- [3] L.Brewer, *High-Strength Materials*, ed. V.F. Zackay, John Wiley & Sons Inc. New York, (1965); L. Brewer, *Phase Stability in Metals and Alloys*, eds. P.S. Rudman, J. Stringer, R.I. Jaffe, McGraw-Hill Books Co., New York, (1967).
- [4] W.B. Pearson, *The Crystal Chemistry and Physics of Metals and Alloys*, Wiley - Interscience, New York, (1972).
- [5] H. Stadelmaier, "Historical Developments in the Understanding of Alloy Phases", *JOM* 41, 21 (1989).
- [6] W. Hume-Rothery, *J. Inst. Metals* 35, 295 (1926); W. Hume-Rothery, *The Metallic State*, Oxford: Clarendon, 328, (1931); W. Hume-Rothery, G.V. Raynor, *The Structure of Metals and Alloys*, London: The Inst. of Metals, 1st ed. (1936).
- [7] A.J. Bradley, J. Thewlis, *Proc. Roy. Soc. A* 112, 678 (1926); A.J. Bradley, *Phil. Mag.* 6, 878 (1926).
- [8] A.F. Westgren, G. Phragmén, *Z. Metallkunde* 18, 279 (1926).
- [9] J.D. Bernal, *Ann. Rept. Progr. Chem.* 30, 387 (1933).
- [10] T.B. Massalski, H. Okamoto, P.R. Subramanian, L. Kacprzak, eds. *Binary Alloy Phase Diagrams*, American Materials Information Society, 2nd ed., Materials Park, Ohio, (1990).
- [11] C. Barrett, T.B. Massalski, *Structure of Metals*, Pergamon Press, 3rd ed. 248 (1980).
- [12] E. Zintl, *Naturwiss.* 17, 782 (1929).
- [13] E. Zintl, G. Woltersdorf, *Z. Electrochem.*, 41, 876 (1935); E. Zintl, *Angew. Chem.* 1, 52 (1939); W. Klemm, E. Busmann, *Z. Anorg. Allgem. Chem.*, 319, 297 (1963); W. Klemm, *Proc. Chem. Soc. London*, 329 (1958); H. Schäfer, B. Eisemann, W. Müller,

Angew.Chem. **85**, 742, (1973); *Angew. Chem. Intl. Ed.* **12**, 694 (1973); H. Schäfer, *Ann. Rev.Mater.Sci.* **15**, 1 (1985) and references therein.

- [14] R. Hoffmann, *Solids and Surfaces: A Chemist's View of Bonding in Extended Structures*, VCH, 3 (1988).
- [15] G. Miller, *Chemistry, Structure, and Bonding of Zintl Phases and Ions*, VCH, 1 (1996), and references therein.
- [16] D. Jiles, *Introduction to the Electronic Properties of Materials*, Chapman & Hall, London, (1994).
- [17] A.K. Cheetham, P. Day, eds. *Solid State Chemistry Compounds*, Oxford Science Publications, Oxford, (1992); A.K. Cheetham, P. Day, eds, *Solid State Chemistry Techniques*, Oxford Science Publications, Oxford, (1987).
- [18] K.A. Gschneidner Jr., V.K. Pecharsky, S.K. Malik, *Advances in Cryogenic Engineering*, Vol.42, L.T. Summers, ed., Plenum Press, New York, 423, 465, 475 (1996).
- [19] R. Nesper, *Angew. Chem. Intl. Ed. Engl.* **30**, 789 (1991).
- [20] D. Emin, T. Aselage, C. L. Beckel, I.A. Howard, C. Wood, (eds.) *Boron-Rich Solids*, AIP Conference Proceedings 140, Albuquerque, NM, (1985); D. Emin, T. Aselage, C. L. Beckel, I.A. Howard, C. Wood, (eds.) *Boron-Rich Solids*, AIP Conference Proceedings 213, Albuquerque, NM, (1990).
- [21] J. Corbett, *Chemistry, Structure, and Bonding of Zintl Phases and Ions*, VCH, 139 (1996), and references therein; W. van der Lugt, *Chemistry, Structure, and Bonding of Zintl Phases and Ions*, VCH, 211 (1996), and references therein; J. Corbett and S. Sevov, *Inorg. Chem.* **30**, (1991) 4876; C. Belin and M. Tillard-Charbonnel, *Prog. Solid State Chem.* (1993) 59.
- [22] B. Eisemann, G. Cordier, *Chemistry, Structure, and Bonding of Zintl Phases and Ions*, VCH, 61 (1996), and references therein.
- [23] L. Brewer, *J. Phys. Chem.*, **94**, 1196 (1990).
- [24] *CRC Handbook of Chemistry and Physics*, 62nd., eds. R. Weast, M. Astle, CRC Press, Inc., Boca Raton, FL, (1981-1982).
- [25] N.N. Greenwood, A. Earnshaw, *Chemistry of the Elements*, Oxford, Pergamon Press, (1990).

- [26] N.N. Greenwood, A. Earnshaw, *Chemistry of the Elements*, Oxford, Pergamon Press, 252 (1990).
- [27] E. Clementi and C. Roetti, *At. Data Nucl. Data Tables* **14**, (1974) 177; S. Alvarez, *Tables of Parameters for Extended Hückel Calculations*, Barcelona, (1995), and references within.
- [28] A.I. Goldman, D.J. Sordelet, P.A. Thiel, J. M. Dubois, (eds.), *New Horizons in Quasicrystals, Research and Applications*, World Scientific, London, (1996).
- [29] D. Shoemaker, R. Marsh, F. Ewing, L. Pauling, *Acta Cryst.* **5**, 637 (1952).
- [30] I. Felner, I. Nowik, *J. Phys. Chem Solids* **40**, 1035 (1979).
- [31] I. Felner, *J. Less Comm. Metals* **72**, 241 (1980).
- [32] K.H.J. Buschow, J.H.N. Van Hucht, W.W. Van Den Hoogenhof, *J. Less Comm. Metals* **50**, 145 (1976).
- [33] S. Lee, *J. Am. Chem. Soc.* **113**, 101 (1991); S. Lee, L. Hoistad, *J. Alloys Compds.* **229**, 66 (1995); D.G. Pettifor, *Bonding and Structure of Molecules and Solids*, Oxford Science, New York (1995) p. 77-106; J.K. Burdett, *Chemical Bonding in Solids*, Oxford University Press, New York, (1995) p. 270 - 300, and references therein.
- [34] G. Cordier, E. Czech, H. Ochmann, H. Schäfer, *J. Less Comm. Metals* **99**, 173 (1984).
- [35] G. Cordier, G. Dorsam, R. Kniep, *J. Magn. and Magn. Mater.* **76&77**, 653 (1988).
- [36] G. Cordier, G. Dorsam, R Henseleit, *J. Alloys Compds.* **186**, 161 (1992).
- [37] U. Rauchschwalbe, U. Gottwick, U. Ahlheim, H.M. Mayer, F. Steglich, *J. Less Comm. Metals* **111**, 265 (1993).
- [38] O.V. Zhak, B.M. Stel'makhovich, Yu.B. Kuz'ma, *J. Alloys Compds* **224**, 225 (1995).
- [39] G. Cordier, E. Czech, G. Dorsam, R Henseleit, A. Mehner, S. Thies, C. Geibel, *J. Less Comm. Metals* **169**, 55 (1991).
- [40] P.Villars, L.D. Calvert, *Pearson's Handbook of Crystallographic Data for Intermetallic Phases*, 2nd ed., ASM International, Metals Park OH, (1991).
- [41] G. Cordier, E. Czech, H. Schafer, *J. Less Comm. Metals*, **108**, 225 (1985).
- [42] G. Cordier, E. Czech, H. Schafer P. Woll, *J. Less Comm. Metals*, **110**, 327 (1985).

- [43] G.M. Sheldrick, in *Crystallographic Computing 3*, (Eds. G.M. Sheldrick, C. Kruger, R. Goddard), Oxford University Press, Oxford, 175, (1985). SHELXTL-93, Siemens Industrial Automation, Inc., Madison, WI, USA.
- [44] J.I. Goldstein, D.E. Newbury, P. Echlin, D.C. Joy, A.D. Pomig, Jr., C.E. Lyman, C. Fiori, E. Lifshin, *Scanning Electron Microscopy and X-ray Microanalysis*, 2nd. ed., Plenum Press, New York, (1992).
- [45] N.W. Ashcroft, N.D. Mermin, *Solid State Physics*, Saunders College Publishing, Orlando, (1976).
- [46] G. Bruzzone, *J. Less Comm. Metals*, **25**, 353 (1971).
- [47] J.E. Huheey, *Inorganic Chemistry: Principles of Structure and Reactivity*, Harper & Row, New York, (1972).
- [48] R. Hoffmann, W.N. Lipscomb, *J. Chem. Phys.*, **1962**, *36*, 2179, 3489; R. Hoffmann, *J. Chem. Phys.*, **1963**, *39*, 1397; J.H. Ammeter, H.B. Bürgi, J.C. Thibeault, R. Hoffmann, *J. Am. Chem. Soc.*, **1978**, *100*, 3686; M.-H. Whangbo, R. Hoffmann, R.B. Woodward, *Prog. Roy. Soc.*, **1979**, *A366*, 23.
- [49] T.A. Albright, J.K. Burdett, M.H. Whangbo, *Orbital Interactions in Chemistry*, John Wiley & Sons, New York, (1985).
- [50] J.K. Burdett, *Chemical Bonding in Solids*, Oxford University Press, New York, (1995).
- [51] J.K. Burdett, *Molecular Shapes*, John Wiley & Sons, New York, (1980).
- [52] The Cu and Y atomic orbital parameters were adjusted self-consistently based on charge. This procedure involves the three atomic orbital energies which are determined by fitting a quadratic relationship between charge and orbital energies.
- [53] B.M. Gimarc, *J. Am. Chem. Soc.* **1983**, *105*, (1979).
- [54] (a) J.K. Burdett, G.J. Miller, *Chem. Mater.*, **2**, 12 (1989); C. Zheng, R. Hoffmann, *Z. Naturforsch.*, **41B**, 292 (1986); (b) C. Zheng, R. Hoffmann, *Z. Naturforsch., Teil B*, **41**, 292 (1986); (c) G.J. Miller in *Chemistry, Structure, and Bonding of Zintl Phases and Ions*, (Ed. S.M. Kauzlarich), VCH, New York, (1996), pp. 1- 59.
- [55] In BaAl₄, *vec* is calculated per Al atom.
- [56] A. H. Gomes de Mesquita, K.H.J. Buschow, *Acta Cryst.* **22**, 497 (1967); K.A. Gschneidner Jr., F.W. Calderwood, *Bull. Alloy Phase Diagrams*, **9**, 686 (1988).

- [57] a) F. Hulliger, *J. Alloys Compds*, **218**, 255 (1995); b) F. Hulliger, H.U. Nissen, R. Wessicken, *J. Alloys Compds*, **206**, 263 (1994); c) K.J. Nordell, G.J. Miller, to be published.
- [58] Y.N. Grin, P.Rogl, K.Hiebl, F.E. Wagner, H.Noël, *J. Solid State Chem.*, **70** 168 (1987).
- [59] This result is confirmed by LMTO calculations on identical models.
- [60] S. Lee, *J. Am. Chem. Soc.* **113**, 101 (1991).
- [61] S. Lee, L. Hoistad, *J. Alloys Compds*. **229**, 66 (1995).
- [62] J. K. Burdett, *Struct. Bond.*, **65**, 29 (1987).
- [63] D.G. Pettifor, *Bonding and Structure of Molecules and Solids*, Oxford Science, New York (1995) p. 77-106.
- [64] *Early applications of sms*; D.G. Pettifor, R. Podloucky, *Phys. Rev. Lett*, **53**, 1080 (1984); J.K. Burdett, S. Lee, *J. Am. Chem. Soc.* **107**, 3063 (1985).
- [65] J.K. Burdett, *Chemical Bonding in Solids*, Oxford University Press, New York, (1995) p. 270 - 300, and references therein.
- [66] S. Lee, *J. Am. Chem. Soc.* **113**, 8611 (1991).
- [67] S. Lee, L. Hoistad, *J. Am. Chem. Soc.* **113**, 8216 (1991).
- [68] M.L. Fornasini, *J. Less Comm. Metals*, **25**, 329 (1971).
- [69] D. Givord, F. Givord, R. Lemaire, *J. Less Comm. Metals*, **29**, 389 (1972).
- [70] A. Streitwieser, *Molecular Orbital Theory for Organic Chemists*, Wiley, New York, (1967).
- [71] E.T. Teatum, K.A. Gschneidner, Jr., J.T. Waber, *Compilation of Calculated Data Useful in Predicting Metallurgical Behavior of the Elements in Binary Alloy Systems*, Los Alamos Scientific Laboratory, New Mexico, (1968).

ACKNOWLEDGMENTS

*“The Lord by wisdom founded the earth;
by understanding He established the heavens;
by His knowledge the deeps broke open.
My child, do not let these escape from your sight...
and they will be life for your soul.”*

- Proverbs 3: 19-22

I want to express my sincere thanks to Gordon Miller for his patience, encouragement, and commitment to me and my graduate research experience. It has been my pleasure to have Gordie as an advisor as I've learned and discovered more than I could have imagined.

I want to acknowledge many people whose help was invaluable to my learning and success at Iowa State. Thanks to Bob Jacobson for the generous use of the X-ray diffractometers, Jerry Ostenson for magnetic measurements, Jim Anderegg for XPS measurements and X-ray support, Scott Chumbley for help with the SEM, Laura Hoistad for teaching me the second moment scaling calculation programs, and Victor Young and Len Thomas for helpful suggestions regarding crystallography. Thanks to many of the chemistry and material science & engineering faculty members for helpful discussions about my research, and my career in chemistry.

I have enjoyed working with the members of the Miller group, and thank you all for keeping things in the lab running smoothly, and for helping make much of my time in the lab both fun and productive.

I thank Mark for his creativity, skill, and insight, but mostly for his sense of humor and faithful friendship.

Many thanks to other friends here in Ames, who have taken me away from the lab once-in-a-while. Finally, thanks to my family, for the love and encouragement which have provided a foundation of self-confidence and love of learning for which I will always be grateful.